Project No. 12-3456

Testing of Sapphire Optical Fiber and Sensors in Intense Radiation Fields When Subjected to Very High Temperatures

Fuel Cycle Research and Development

Thomas Blue
The Ohio State University

Frank Goldner, Federal POC,
James K. Jewell, Technical POC

NEUP Nuclear Energy University Programs
U.S. Department of Energy

FINAL REPORT

Project Title: Testing of Sapphire Optical Fiber and Sensors in Intense Radiation Fields, when Subjected to Very High Temperatures

Project Number: NEUP 12-3456

Covering Period: September 30, 2016 through September 30, 2017

Principle Investigators:

Dr. Thomas E. Blue (OSU)
(614) 292-0629
blue.1@osu.edu

Dr. Wolfgang Windl (OSU)
windl.1@osu.edu

Organization:

The Ohio State University
Nuclear Engineering Program
201 West 19th Avenue
Columbus, OH 43210

Industrial Collaborators:

Lambda Instruments, Inc.
Jon Greene
jgreene@lambdainc.com

TechOpp Consulting, Inc.
Robert Fielder
Bob.Fielder@techoppconsulting.com

Project Objective: The primary objective of this project was to determine the optical attenuation and signal degradation of sapphire optical fibers & sensors (temperature & strain), in-situ, operating at temperatures up to 1500°C during reactor irradiation through experiments and modeling. The results will determine the feasibility of extending sapphire optical fiber-based instrumentation to extremely high temperature radiation environments. This research will pave the way for future testing of sapphire optical fibers and fiber-based sensors under conditions expected in advanced high temperature reactors.

Abstract

The work that is to be performed for this project is important for the development of in-pile instrumentation that supports the DOE goal of understanding the behavior and predicting the performance of nuclear fuel systems at a microstructural level using fiber optic techniques. Due to the high melting point of optical fiber materials (alumina melts at ~2050°C), sapphire fiber optic sensors are promising candidates for in-pile instrumentation to support fuel cycle research and development, provided they can survive continuous irradiation at very high temperatures.

In the computational portion of this project, multi-scale modeling was performed to determine the effects of neutron radiation and thermal annealing at extremely high temperatures on the broadband optical attenuation in sapphire fibers. We have characterized the radiation field in the Ohio State University Research Reactor (OSURR) in standard terms, including the neutron flux energy spectra and the displacement damage rates (displacement damage and ionization rates due to both neutrons and gamma rays). Neutron-PKA interactions were modeled using both the MCNP and SPECTER-ANL software code packages to determine the distributions of primary knock-on atom (PKA) position, energy, and direction, as well as the PKA generation rates in the sapphire fibers. PKA transport and defect generation modeling was performed using the TRIM and Marlowe software code packages. Defect evolution modeling will be performed to predict the effects of annealing time and temperature on the various defect concentrations. Ab-initio electronic structure calculations are being performed using the Vienna Ab-initio Simulation Package (VASP) to determine defect formation energies as well as the optical properties of the defect structures.

In the experimental portion of this project, broadband (450-2200 nm) optical attenuation in sapphire optical fibers was continuously monitored, in-situ, as the sapphire fibers were exposed to: 1.) temperatures up to 1500 °C, 2.) gamma radiation with simultaneous heating to temperatures up to 1000 °C, and 3.) reactor radiation with simultaneous heating to temperatures up to 1000 °C. In addition to the transmission testing, sapphire optical fiber sensors were tested in-situ in: 1.) temperatures up to a 1000 °C, 2.) gamma radiation and 3.) reactor radiation.

Heated optical transmission experiments were performed at temperatures up to 1500 °C. During the initial experiments, the light transmission in the sapphire fiber continued to diminish across all wavelengths, without reaching a steady-state value, as the fiber was heated at temperatures above 1300 °C. We discovered that the sapphire fiber was interacting with water vapor in the air at high temperatures and forming a type of aluminum hydroxide on the surface of the fiber. Heated optical transmission tests were performed in an inert environment up to 1500 °C and the transmission results showed very minimal added attenuation in the IR range and a small (5 dB) steady state increase in the visible light range at 1500 °C.

An optical transmission experiment was performed in a high gamma ray environment, while a portion of one of the fibers was heated to temperatures up to 1000 °C. Gamma radiation caused a seemingly broadband increase in the fiber attenuation that saturated at ~4-5 dB after accumulating an absorbed dose of ~9 MRad. Heating a portion of one of the fibers to 200 °C decreased the radiation-induced attenuation. Heating to higher temperatures, while continuing to accumulate dose, resulted in a slight increase in the attenuation. This increase was likely due to a combination of continued accumulation of dose, and possibly thermally-induced attenuation at higher temperatures.

Sapphire transmission experiments were also conducted in the Ohio State Research Reactor. The heated reactor irradiation experiments consisted of in-situ measurements of the optical transmission in commercially available 100 μm diameter sapphire optical fibers during exposure to reactor irradiation at various reactor power levels and at various temperatures. During

the heated reactor irradiation experiment, sapphire fibers were irradiated at reactor power levels of 10, 30, and 90% reactor power and temperatures, including room temperature, of 300, 600, and 1000 °C. In general, during reactor irradiation, the added attenuation showed a linear increase with increasing time at constant reactor power for each of the temperatures that were tested. The rate of increase of the added attenuation during constant power reactor irradiation monotonically decreased with increasing temperature up to 1000 °C, with the most significant decrease occurring between 300 and 600 °C. The added attenuation at 1300 and 1550 nm remained less than ~1 dB for the sapphire fibers throughout the entire experiment.

For the sapphire fiber sensing portion of this project, Lambda Instruments, Inc., an industrial partner on this project, was supposed to develop a sensor readout system, a software application and 16 sapphire fiber-based Fabry-Perot temperature and strain sensors. The system and sensors were never made or delivered by Lambda Instruments Inc. OSU had to than complete the sapphire sensors portion of the project and instead of doing sapphire Faby-Perot point sensing, they developed a new type of sapphire fiber that would allow for distributed temperature sensing. OSU developed a method of creating a near single mode sapphire optical fiber which enabled the sapphire optical fiber to produce distributed temperature measurements using the OFDR sensing technique. With a single mode sapphire fiber created, OSU inscribed Bragg gratings every 6 cm along the entire fiber to act as high temperature sensors. These sapphire sensors were tested under the following environments: during heating in the absence of radiation up to 1000 °C, during Co-60 gamma irradiation at room temperature and finally during reactor irradiation at room temperature.

The sapphire Bragg grating sensors were ramped to 1000 °C, in 100 °C steps, in a tube furnace. The sapphire Bragg gratings were able to produce stable and accurate temperature measurements at every temperature tested. The gratings showed zero degradation in regards to their reflected backscatter amplitude to temperatures up to 1000 °C. The sapphire Bragg grating sensors have great potential for producing accurate temperature measurements at temperatures higher than a 1000 C, unfortunately, time restrictions caused a reduction in the scope of our testing. Tests to higher temperatures and a more accurate calibration of the sapphire Bragg gratings is recommended for future work.

Following the high temperature tests, the cladded sapphire fiber with inscribed Bragg gratings was tested for its radiation survivability. The sapphire fiber sensors were placed into the Co-60 irradiator and irradiated for a total of 5 full days. Over the 5 days of irradiation, the sapphire sensors accumulated approximately 2.82 MRads. The sapphire Bragg gratings were unaffected by the gamma rays as their reflective amplitude never changed over the course of the experiment and the gratings produced a constant temperature measurement. The accuracy and precision of the sapphire temperature measurements in the gamma irradiator were not fully investigated and would be a good future work idea.

Following the irradiations in the gamma irradiator, the sapphire fiber sensors were transferred into the Central Irradiation Facility (CIF) dry tube located in the Ohio State Research Reactor. The sapphire Bragg gratings appeared to have survived the irradiations in the OSURR and produced reasonable temperature measurements. The sapphire Bragg gratings were able to survive 1 GRad of gamma dose and a neutron fluence of 10^{18} n/cm^2 without showing degradation of the gratings. The lead in silica fiber did exhibit darkening which affected our results during the third day but recalibrating the fiber helped with ensuring accurate sapphire sensor measurements. The survivability testing of the sapphire sensors was successful but the accuracy and precision of these sensors still needs to be determined.

Table of Contents

List of Tables

List of Figures

Publications and Information Released

1. Brandon A. Wilson, Christian M. Petrie, Thomas E. Blue, "High Temperature Effects on the Light Transmission through Sapphire Optical Fiber", Journal of the American Ceramic Society, to be published
2. Brandon A. Wilson and Thomas E. Blue, "Creation of an Internal Cladding in Sapphire Optical Fiber Using the $^{6}Li(n,\alpha)^{3}H$", IEEE Sensors Journal, to be published
3. Brandon A. Wilson, Kelly M. McCary, Neil R. Taylor, Andrew Kauffman, Thomas E. Blue and Raymond Cao, "The Creation of a High Temperature Irradiation Facility in the Ohio State Research Reactor" Transactions of the American Nuclear Society 117 (2017)
4. B. Wilson, Ph.D. dissertation: "Evaluation of Optical Fiber Sensors in High Temperature and Nuclear Reactor Environments," The Ohio State University, Columbus, 2017.
5. C. Petrie, T.E. Blue "In-situ thermally-induced attenuation in sapphire optical fibers heated to 1400 oC". J. Am. Ceram. Soc., Vol 98 (2015), pp. 483-489.
6. Christian M. Petrie, Brandon Wilson and Thomas E. Blue, "In Situ Gamma Radiation-Induced Attenuation in Sapphire Optical Fibers Heated to 1000°C", Journal of Non-Crystalline Solids Volume 97, Issue 10, pages 3150–3156, October 2014
7. D. Hawn, C. Petrie, T. Blue, and W. Windl, "In-situ Gamma Radiation-Induced-Attenuation in Silica Optical Fiber Heated up to 600 °C", Journal of Non-Crystalline Solids 379 (2013) 192-200.
8. T. Wood Jr., B. Blake, T. E. Blue, C. Petrie and D. Hawn, "Evaluation of the Performance of Distributed Temperature Measurements with Single-mode Fiber using Rayleigh Backscatter up to 1000 °C", IEEE Sensors Journal, to be published.
9. C. Petrie, D. Hawn, and T. Blue, "In-situ Reactor Irradiation of Silica Optical Fiber Heated to 1000 °C", Transactions of the American Nuclear Society 108 (2013) 315-318.
10. T. Wood Jr., B. Blake, T. Blue, and C. Petrie, "Distributed Temperature Measurements with Single-mode Fiber using Rayleigh Backscatter up to 750 °C", Transactions of the American Nuclear Society 108 (2013) 323-325.
11. B. Reinke, T. Garcia, T. Wood, C. Petrie, A. Kumar, T. Blue, and W. Windl, "Temperature Controlled Cryostat for Electrical and Optical Reactor Irradiation Experiments", Transactions of the American Nuclear Society 108 (2013) 274-277.
12. T. W. Wood, Jr. MS thesis: "Evaluation of Single-Mode and Bragg Grating Optical Fibers Interrogated with an Optical Backscatter Reflectometer (OBR) in High Temperature Environments for Advanced Instrumentation in Nuclear Reactors," The Ohio State University, Columbus, 2013.
13. D. P. Hawn, Ph.D. dissertation: "The Effects of High Temperature and Nuclear Radiation on the Optical Transmission of Silica Optical Fibers," The Ohio State University, Columbus, 2012.
14. B. P. Blake. MS thesis: "Initial Testing of Single-Mode Optical Fibers Interrogated with an Optical Backscatter Reflectometer at High Temperatures and in Radiation Environments for Advanced Instrumentation in Nuclear Reactors," The Ohio State University, Columbus, 2012.
15. C. Petrie, D. Hawn, T. Blue, and W. Windl, "In-Situ Performance of Optical Fibers Heated to 1000°C", Transactions of the American Nuclear Society 106 (2012) 616-617.
16. D. Hawn, C. Petrie, T. Blue, and W. Windl, "In-Situ Performance of Optical Fibers Heater to 600°C during Gamma Irradiation", Transactions of the American Nuclear Society 106 (2012) 614-615.
17. C. Petrie, T. Blue, and J. Kulisek, "Modeling High Temperature Radiation Damage to Optical Fibers", Transactions of the American Nuclear Society 104 (2011) 269-270.

18. H. Govindarajan, R. Mishra, and W. Windl, “Atomic-Scale Modeling of the Effects of Irradiation on the Optical Properties of Silica Glass Fibers”, Transactions of the American Nuclear Society 104 (2011) 33-34.
19. D. Hawn, B. Blake, C. Petrie, and T. Blue, “Initial Testing of a High-Temperature Low-Activation Furnace”, Transactions of the American Nuclear Society 104 (2011) 308.
20. D. P. Hawn. Presentation: “High-Temperature Low-Activation Optical Fiber Irradiation Facility,” 2011 Test, Research, & Training Reactors Annual Meeting.
21. H. Govindarajan. MS thesis: "Atomic-Scale Modeling of the Effects of Irradiation on Silica Optical Fibers," The Ohio State University, Columbus, 2011.
22. Govindarajan, Harish. Poster presentation: “Atomic-scale modeling of the effects of Irradiation on Silica Optical Fibers.” 2011 OSU Institute for Materials Research Conference. Columbus, Ohio.
23. D. Hawn, C. Petrie, T. Blue, and R. Winningham, “Design and Analysis of a High-Temperature Low-Activation Furnace”, Transactions of the American Nuclear Society 103 (2010) 302.

Chapter 1. Introduction

1.1 Motivation and Objectives

The work that is to be performed for this project is important for the development of in-pile instrumentation that supports the DOE goal of understanding the behavior and predicting the performance of nuclear fuel systems at a microstructural level using fiber optic techniques. Due to the high melting point of optical fiber materials (alumina melts at ~2050°C), sapphire fiber optic sensors are promising candidates for in-pile instrumentation to support fuel cycle research and development, provided they can survive continuous irradiation at very high temperatures.

Optical fibers have a small diameter, small mass (and therefore fast response time), and they are naturally high temperature materials that are immune to electromagnetic interference. These qualities make them ideal candidates for measurements on the surface of fuel pins and inside fuel pins, where space is limited and temperature and radiation levels are highest. It may be ultimately possible to integrate sapphire optical fiber-based sensors within fuel pins, although there would certainly be challenges including attachment to curved surfaces, Coefficient of Thermal Expansion (CTE) mismatch between materials, and fiber routing to the pin under test. Each of these issues could potentially be addressed with proper design and some technological development efforts in the areas of welding/joining of fibers to the fuel pins and development of robust sapphire fiber coatings. The first step in determining the suitability of using sapphire fiber-based instrumentation inside or at the surface of fuel pins is to determine whether the sapphire fibers and/or sapphire fiber-based sensors can survive continuous irradiation at the extremely high fuel temperatures expected in advanced nuclear reactors.

The objective of this project is to characterize, by comparison of measured and modeled results, the performance of sapphire optical fibers and sensors in intense radiation fields, when subjected to very high temperatures. More specifically, the goals of the proposed project are to 1.) Develop validated multi-scale models for radiation damage from neutrons and gammas in sapphire fibers at high temperatures (~1500°C), 2.) Determine the optimum wavelength region for sapphire fiber-based sensors based on broadband (300-2400 nm) transmission measurements in a high temperature, high radiation environment and 3.) Evaluate the performance of sapphire fiber-based Fabry-Perot interferometric temperature and strain sensors subjected to intense neutron and gamma radiation at high temperatures (~1500°C). The multi-scale models will predict the resulting damage and structure evolution as a function of temperature, time, and absorbed dose (both ionization dose and displacement damage dose) for short and extended time scales. This research will pave the way for future testing of sapphire optical fibers and sapphire-based sensors under conditions expected in future reactors such as the next generation nuclear plant (NGNP).

1.2 Summary of Tasks and Associated Deliverables

This work that is to be performed for this project includes both computational modeling and experiments. This section provides a very brief summary of both the computational and experimental work that is to be performed, including a breakdown of the work by task.

The computational modeling will start with neutronics simulations of an experimental facility at the Ohio State University Research Reactor (OSURR), in which the sapphire fibers will be

irradiated. The models will include the furnace and rig that will be used to heat the sapphire fibers during irradiation. Neutronics modeling will determine the flux energy spectra in the sapphire fibers and the distributions of the position, energy, and direction of the primary knock-on atoms (PKAs) that are generated in the fibers via collisions of energetic neutrons with atoms in the crystalline lattice of the fibers. Further models will be developed to simulate the transport of PKAs throughout the fiber, the formation of defect structures, and the evolution of those defect structures due to thermal annealing at various temperatures. The results of these models will give defect concentrations as a function of irradiation conditions, including neutron flux, irradiation time, and temperature. Ab-initio simulations will be performed in order to determine the optical properties of the various defect structures resulting from neutron radiation-induced damage. The optical properties of the defect structures will be combined with the computationally determined defect concentrations to predict the optical attenuation as a function of neutron flux, irradiation time, and temperature.

The experimental portion of the work will include broadband optical transmission experiments of sapphire fibers and experiments involving sapphire fiber-based Fabry-Perot interferometric temperature and strain sensors. During the optical transmission experiments, the broadband transmission through the sapphire fibers will be continuously monitored, in-situ, while the fibers are: 1. Heated up to 1500 °C in the absence of radiation, 2. Heated during irradiation with Co-60 gamma rays to temperatures up to 1000 °C, and 3. Heated during irradiation with reactor neutrons and gamma rays up to temperatures of 1000 °C. The sapphire fiber-based sensors will first be tested to determine the functional performance of temperature sensors heated in the absence of radiation to temperatures up to 1500 °C. Survivability of the sensors will then be determined while they are irradiated with reactor radiation and Co-60 gamma rays.

The experimental and computational work performed for this project was broken down into eight tasks (Task A through Task H), each with its own deliverables. Tasks A through D (summarized in Table 1) are related to the computational portion of the work. Tasks E through H (summarized in Table 2) are related to the experimental portion of the work. The summaries shown in Table 1 and Table 2 include the timelines and the deliverables associated with each task. More details regarding the progress toward completing Task A through Task H are provided in Chapter 2 through 9, respectively.

Table 1: Summary of the computational tasks, their timelines, and the deliverables associated with each task.

Task	Description	Timeline	Deliverables
A	Neutron and PKA interaction Modeling	9/15/2012 to 9/30/2013	• MCNP model of the sapphire fiber irradiation furnace inside the OSURR • Neutron flux energy spectra in the sapphire fibers • Dosimetric characterization of the OSURR • Prediction of the PKA source term
B	Damage Creation Modeling	4/1/2013 to 9/30/2013	• Locations of the various defects resulting from damage cascades of PKAs
C	Damage Evolution Modeling	10/1/2013 to 12/30/2015	• Defect concentrations resulting from reactor irradiation and thermal annealing as a function of irradiation time and temperature

D	Predictive Optical Attenuation Modeling	4/1/2014 to 12/30/2015	• Optical properties of the various defects in sapphire • A predictive model for the broadband optical attenuation as a function of irradiation time and temperature

Table 2: Summary of the experimental tasks, their timelines, and the deliverables associated with each task.

Task	Description	Timeline	Deliverables
E	Design and Fabrication of High Temperature Irradiation Furnaces	9/15/2012 to 9/30/2013	• A high temperature, low-activation furnace suitable for operation in the OSURR at temperatures up to 1500 °C • A high temperature furnace suitable for operation in the OSU Co-60 gamma irradiator at temperatures up to 1000 °C
F	High Temperature Irradiations of Sapphire Fibers	4/1/2013 to 3/31/2014	• Optical attenuation in sapphire fibers due to high temperatures (1500 °C) • Optical attenuation in sapphire fibers due to gamma irradiation at high temperatures (1000 °C) • Optical attenuation in sapphire fibers due to reactor irradiation at high temperatures (1000 °C)
G	Design and Fabrication of Equipment for Performing Sensor Experiments	7/1/2013 to 12/30/2015	• A sensor readout system for testing multiple Fabry-Perot interferometric temperature and strain sensors • A functional test rig for testing sapphire Fabry-Perot interferometric strain sensors at temperatures up to 1500 °C
H	High Temperature Functional Performance Testing and Irradiation Survivability Testing of Sapphire Fiber-Based Sensors	7/1/2014 to 9/30/2017	• Functional performance of sapphire Fabry-Perot interferometric strain sensors up to 1500 °C • Survivability of sapphire Fabry-Perot interferometric temperature and strain sensors irradiated with Co-60 gamma rays • Survivability of sapphire Fabry-Perot interferometric temperature and strain sensors irradiated with reactor neutrons and gamma rays

Chapter 2. Task A - Neutron and PKA interaction Modeling

2.1 Deliverables

- A MCNP model of the sapphire fiber irradiation furnace located inside of the OSURR
- Neutron flux energy spectra in the sapphire fibers
- A dosimetric characterization of the OSURR
- Prediction of the PKA source term

2.2 Timeline and Task Status

- Start Date: 9/15/2012
- Planned Completion Date: 9/30/2013
- Task Status: 100%

2.3 Progress Toward the Completion of Deliverables

2.3.1 MCNP Model of the Sapphire Fiber Irradiation Furnace

In order to simulate radiation damage in the sapphire optical fibers, a MCNP model needed to be developed that includes the sapphire fibers loaded inside the fiber irradiation furnace (shown as both a CAD model and with labeled photographs in Figure 1 and Figure 2, respectively) located in the 7 inch diameter dry tube facility of the OSURR. The OSURR staff previously developed a MCNP model of the reactor core. Figure 3 shows a picture of the OSURR from a top down view, along with a MCNP Vised representation of the model of the reactor core. This model was modified to include the fiber irradiation furnace (see Figure 4). The sapphire fibers were modeled as an annulus on the inside of the furnace heating element in order to increase the number of neutrons passing through the fiber cells during MCNP simulations. Increasing the number of neutrons passing through the fiber cells improves the uncertainties in the simulated fluence tallies. Of course, all results of the MCNP simulations that were not by default on a per unit volume or per unit mass basis were scaled to the actual volume or mass of fiber loaded inside the furnace.

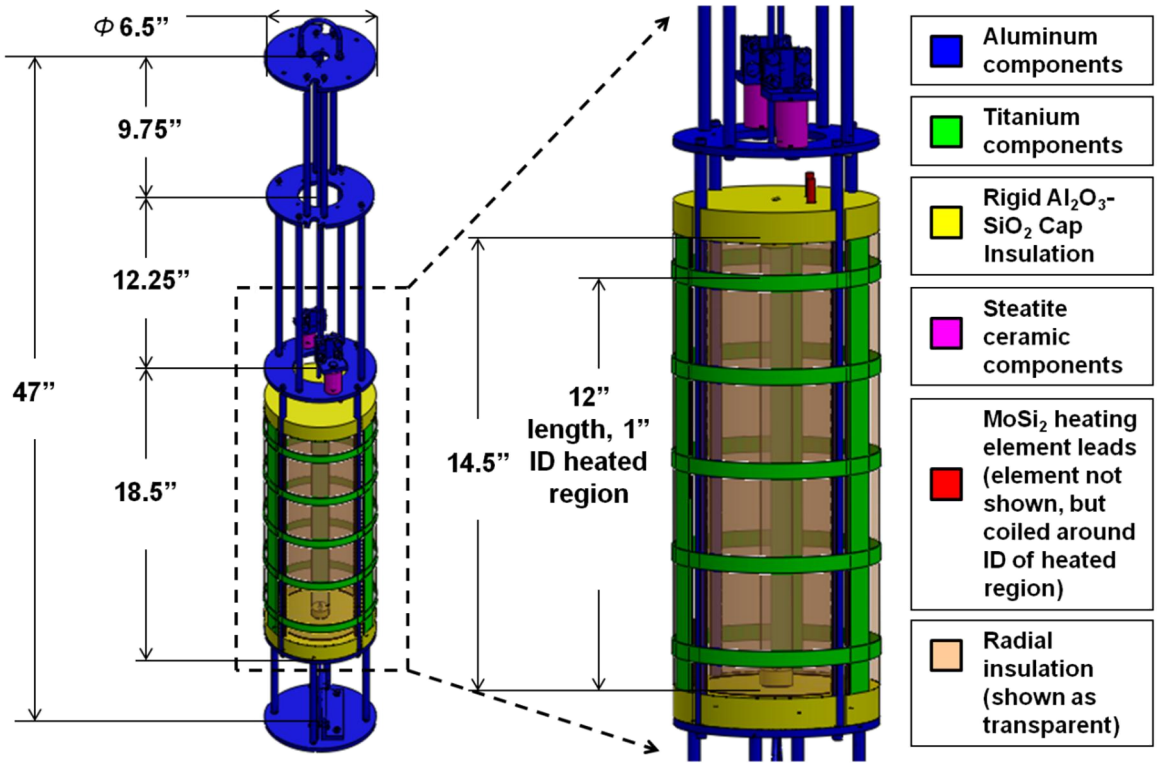

Figure 1: CAD model of the sapphire fiber irradiation furnace.

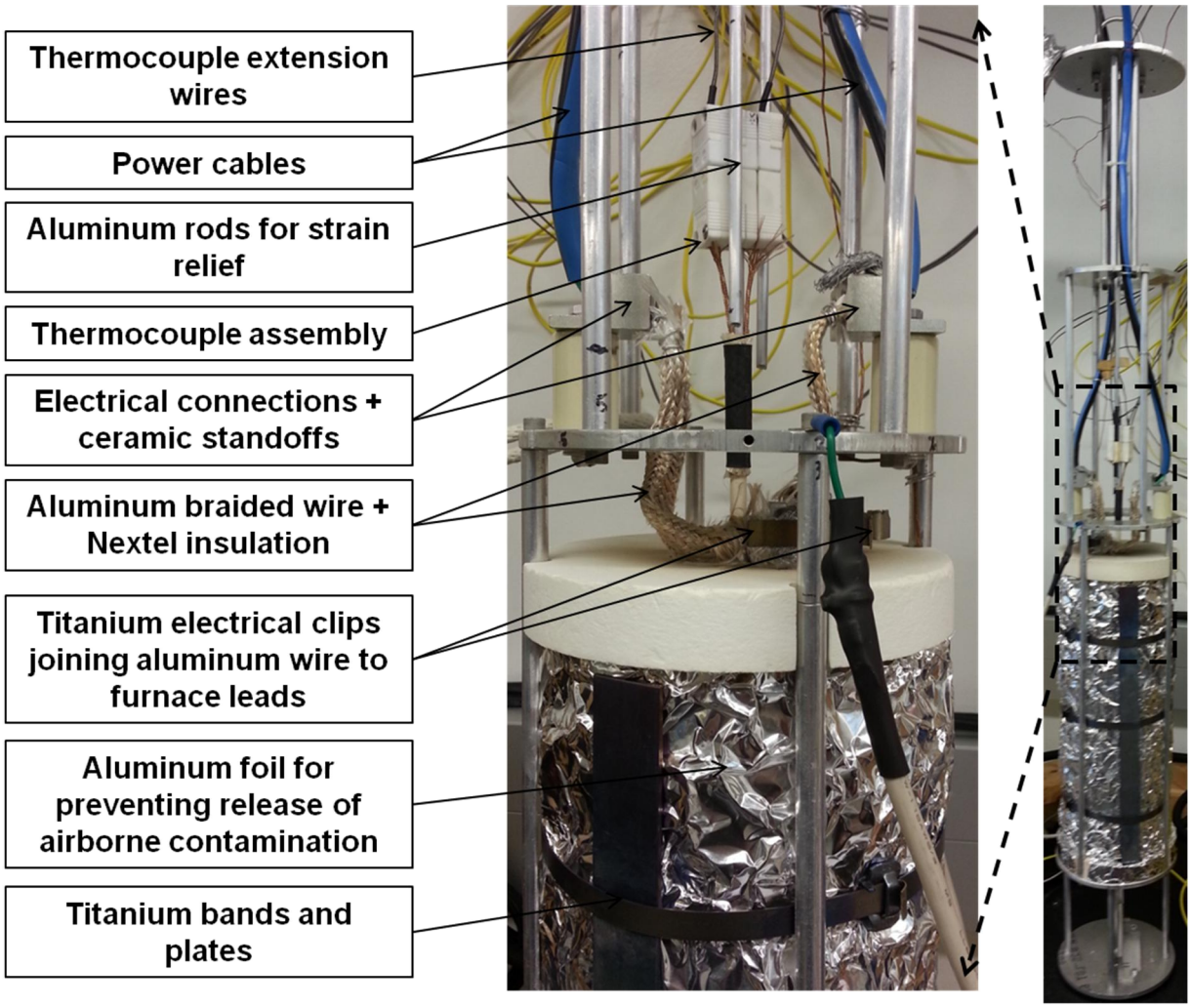

Figure 2: Labeled picture showing the components that make up the sapphire fiber irradiation furnace.

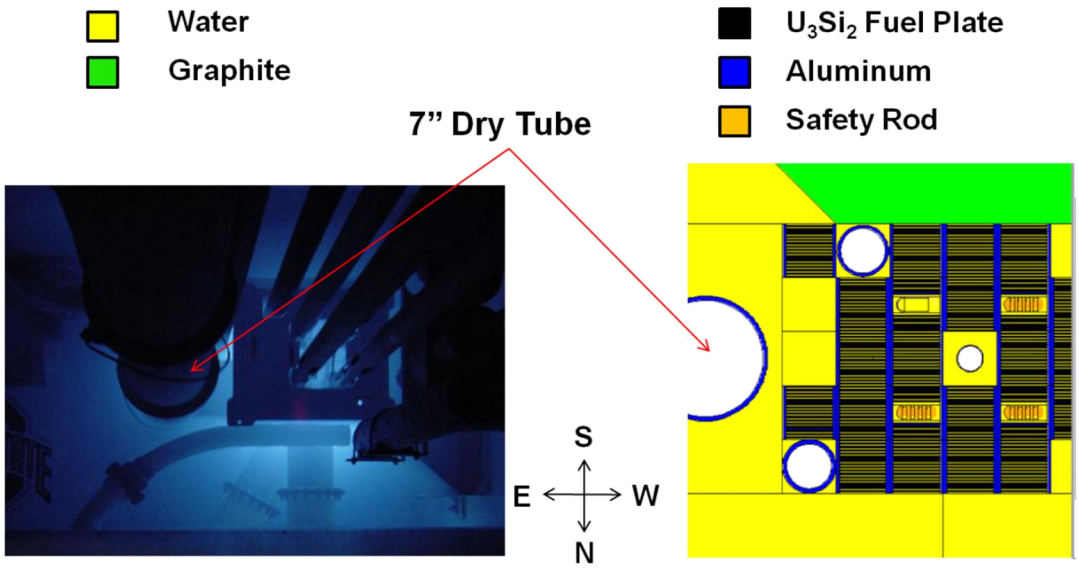

Figure 3: Top-down view of the OSURR core showing the 7 inch diameter dry tube facility as both a picture (left) and as MCNP Vised output (right).

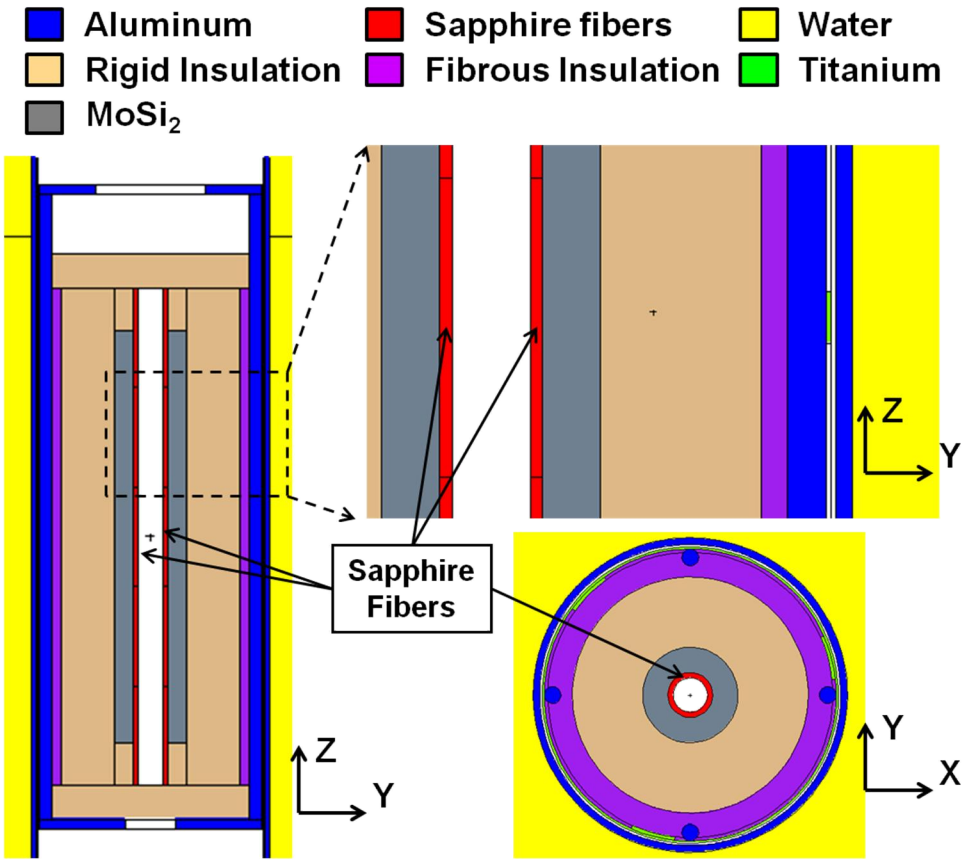

Figure 4: MCNP Vised output of the model of the sapphire fiber irradiation furnace located inside the 7 inch diameter dry tube facility of the OSURR.

2.3.2 Neutron Flux Energy Spectra in the Sapphire Fibers

Neutron flux energy spectra in the sapphire fibers were determined by MCNP simulations using the model described in section 2.3.1. F4 tallies of the neutron fluence in the sapphire fibers per MCNP source particle were normalized to the neutron source rate (using the appropriate reactor power). In order to validate the MCNP simulations, foil activation experiments were performed inside the 7 inch dry tube facility. The SAND-II software code package was used to unfold the neutron flux energy spectrum from the foil activation measurements. Figure 5 shows the neutron flux energy spectra obtained from the SAND-II code package along with the spectra obtained from MCNP simulations inside the voided 7 inch dry tube. The two spectra compare very well, particularly in the high energy region, which contributes most of the displacement damage in the fibers.

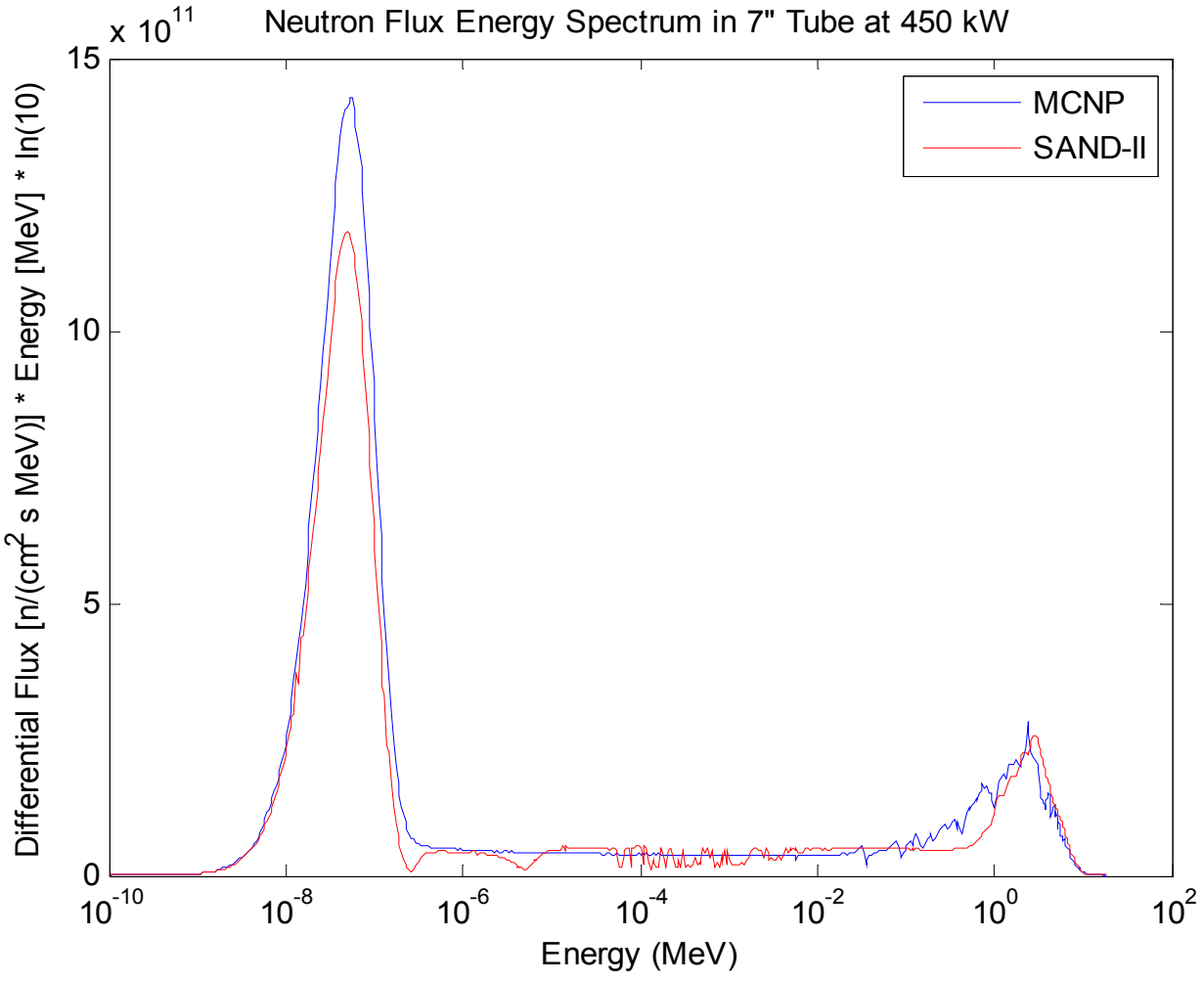

Figure 5: Neutorn flux energy spectra in the voided 7 inch dry tube facility of the OSURR obtained from MCNP simulations and unfolding of foil activation measurements using the SAND-II software code package.

Making foil activation measurements inside of the sapphire fiber irradiation furnace would be difficult to do and would also cause significant neutron activation of the furnace before the actual fiber irradiation experiments could be performed. Activation of the furnace would make loading fibers into the furnace particularly difficult without accumulating a significant radiation dose. Therefore, we decided to compare the results of MCNP simulations with and without the furnace to determine whether the neutron flux energy spectra in the fibers are significantly perturbed due to the furnace materials. Figure 6 shows the neutron flux energy spectra ($\phi(E)$ is the differential neutron flux as a function of energy E) in the voided 7 inch dry tube and in the sapphire fibers loaded inside of the furnace (with the furnace also located inside the 7 inch dry tube facility). The flux energy spectra compare very well. Small differences in the thermal neutron flux do not significantly affect the displacement damage rates in the fibers as will be shown later in this section.

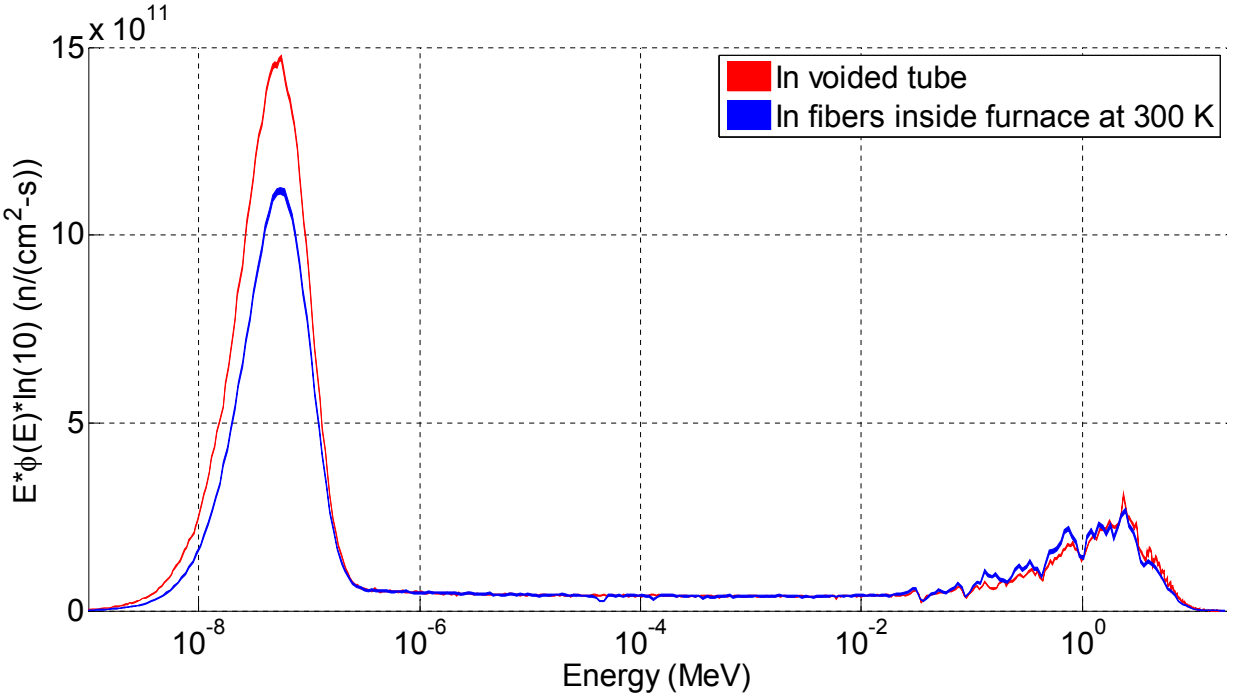

Figure 6: Neutron flux energy spectra obtained from MCNP simulations in the voided 7 inch dry tube facility of the OSURR and in the sapphire fibers loaded inside the fiber irradiation furnace (the furnace is located inside the 7 inch dry tube facility).

Figure 6 shows that the furnace materials, at room temperature, do not significantly perturb the neutron flux energy spectra compared to the flux energy spectra in the voided 7 inch dry tube. However, elevated temperatures could cause increased neutron absorption in the fibers, which could affect the neutron flux energy spectra and the displacement damage rates in the fibers. To determine the effects of temperature, we performed additional MCNP simulations with the furnace materials and the fibers at 2500 K, which is a conservative temperature for the simulations because the maximum temperature of the proposed experiments is 1600 °C, or 1873 K. In addition, all of the furnace materials will not be at such a high temperature. For example, the exterior insulation of the furnace and the titanium materials surrounding the furnace will certainly be at a lower temperature than the interior of the furnace. Figure 7 shows the neutron flux energy spectra in the

sapphire fibers at the center of the furnace at both 300 K and 2500 K. From Figure 7, one can see that elevated temperatures decrease the thermal neutron flux, but do not significantly perturb the fast neutron flux.

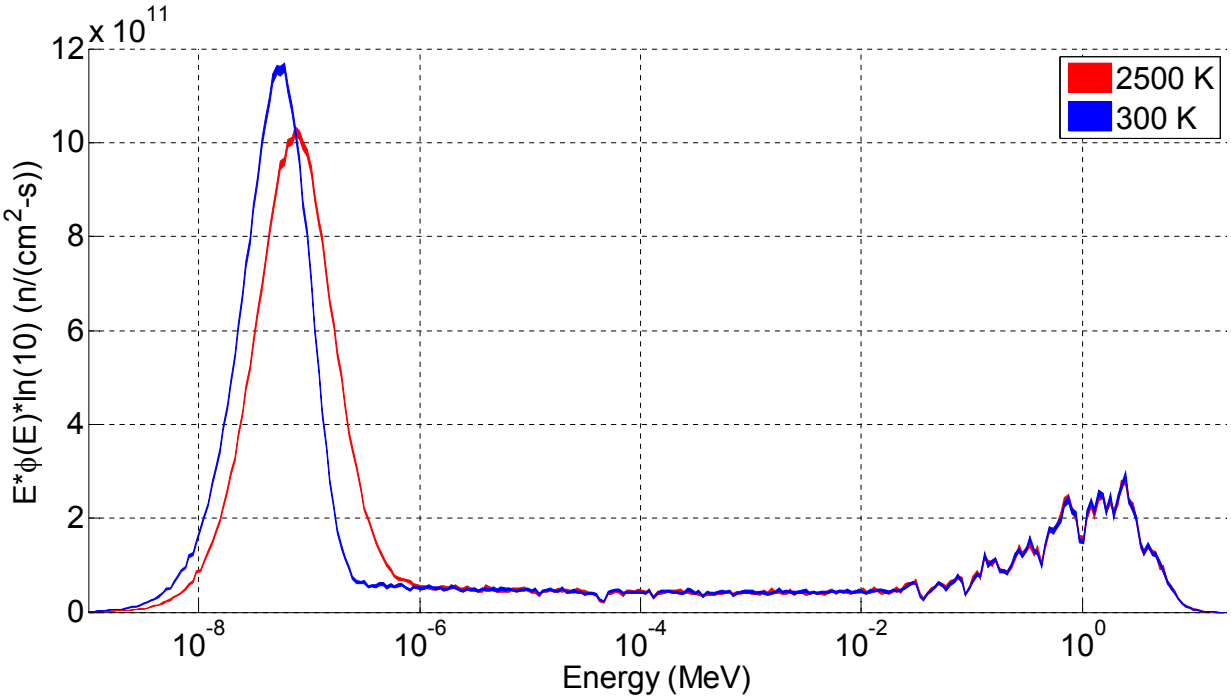

Figure 7: Neutron flux energy spectra in the sapphire fibers loaded inside the furnace determined from MCNP simulations with all materials at 300 K and 2500 K.

Figure 8, Figure 9, and Figure 10 show, as a function of distance from the center of the furnace, the total neutron flux, the total energy deposition rate (both displacement and ionization), and the portion of the energy deposition rate contributing to displacement damage in the sapphire fibers, respectively. The total neutron flux, total energy deposition rates, and displacement energy deposition rates were determined using MCNP with F4 tallies, F6 tallies, and F4 tallies with a displacement damage flux modifier card (FM 444), respectively. In these three figures, results are shown both at 300 K and 2500 K. In all three figures, results at 300 K and 2500 K are essentially the same at all locations. Therefore, it is safe to assume that temperature does not affect the displacement damage rate in the fibers, and, based on the results of foil activation measurements, our MCNP simulations give a good estimate for the displacement damage rates in the fibers.

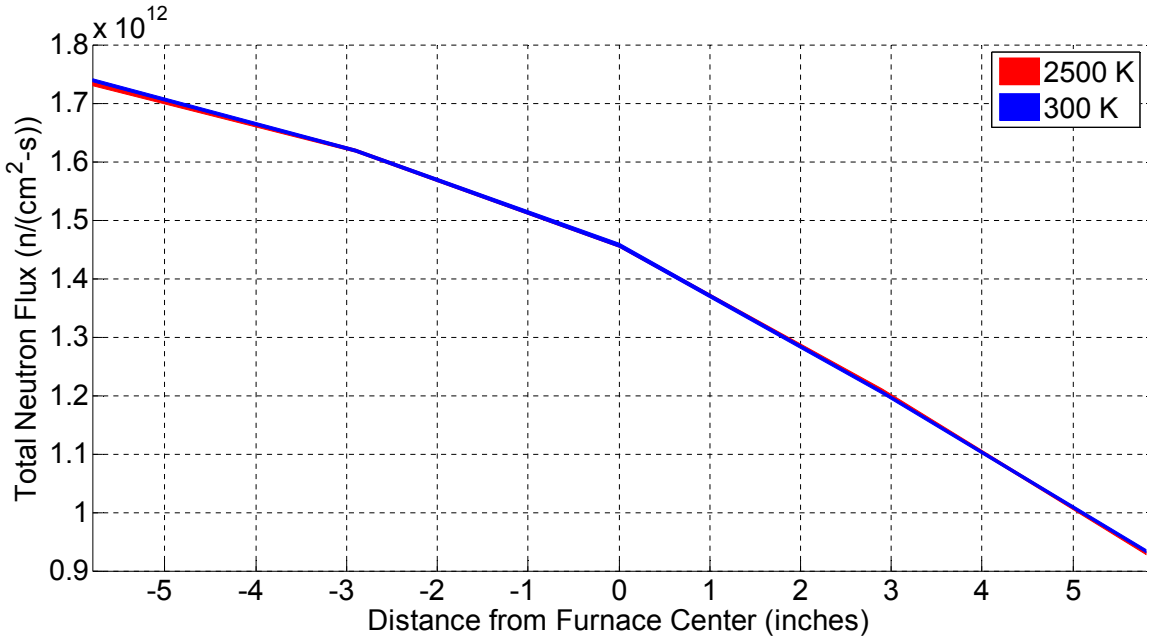

Figure 8: Total neutron flux in the sapphire fibers as a function of distance from the center of the furnace determined from MCNP simulations with all materials set to temperatures of 300 K and 2500 K.

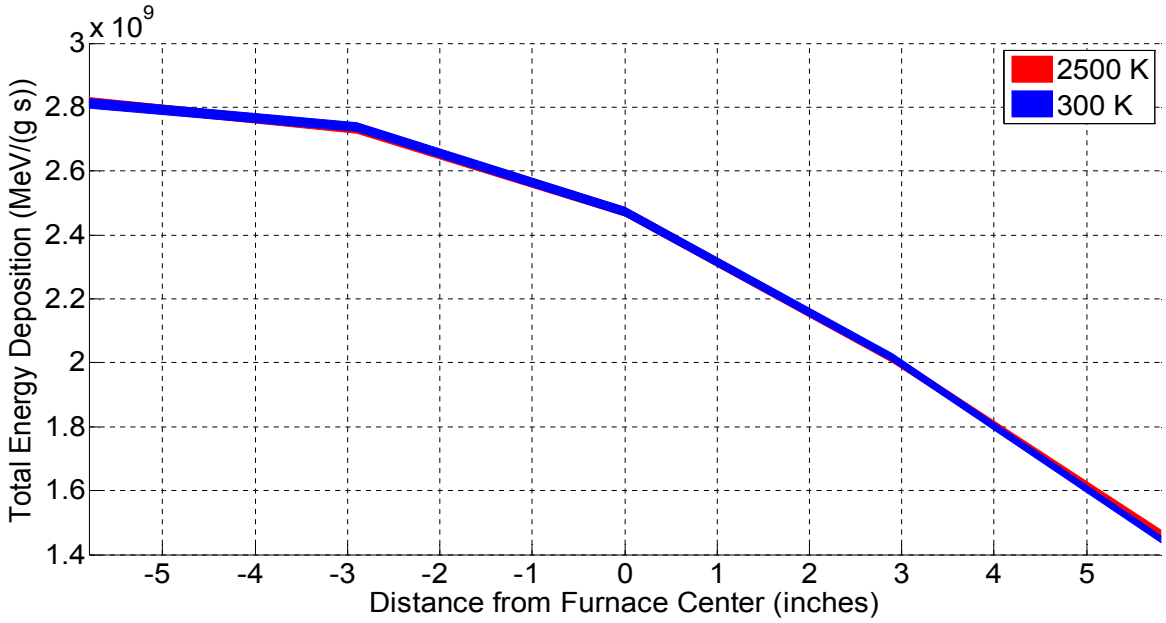

Figure 9: Total energy deposition rate in the sapphire fibers as a function of distance from the center of the furnace determined from MCNP simulations with all materials set to temperatures of 300 K and 2500 K.

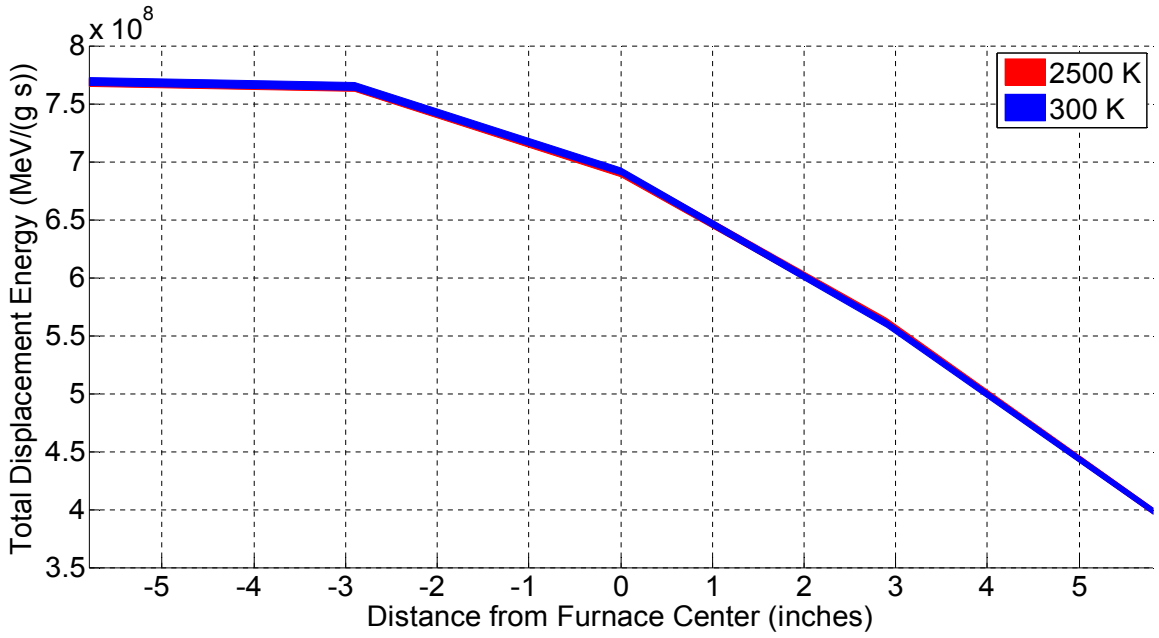

Figure 10: Displacement energy deposition rate in the sapphire fibers as a function of distance from the center of the furnace determined from MCNP simulations with all materials set to temperatures of 300 K and 2500 K.

2.3.3 Dosimetric Characterization of the OSURR

In order to properly characterize the dosimetry of the 7 inch dry tube facility of the OSURR (where the experimental irradiations are to be performed), we had to determine the energy deposition rates in the sapphire fibers from both neutrons and gamma rays. As mentioned in section 2.3.2, the energy deposition rates from neutrons can be determined using F6 tallies in MCNP. Damage energy deposition rates from neutrons can be determined using F4 tallies in MCNP with the FM 444 displacement damage flux modifier card. Ionization energy deposition rates from neutrons can be determined by subtracting the displacement energy deposition rate from the total energy deposition rate.

In addition to determining the energy deposition rates from neutrons using tallies in MCNP, MCNP also allows the user to track individual neutron entering a given cell using the PTRAC feature. We used the PTRAC feature to track all events occurring in the sapphire fiber cells. Using conservation of momentum and energy equations, we calculated the energy and direction of all PKAs using the energy and direction of the neutrons before and after any collision that occurs within any of the fiber cells. The fractions of energy that contribute to displacement and ionization were determined using the Lindhard partition function, which is a function of the mass and atomic number of both the PKA and the atoms of the target material, as well as the PKA energy. Since sapphire is a binary compound, an elemental averaged atomic number and mass were used.

Table 3 shows the displacement and ionization energy deposition rates (in units of MeV/g/NPS, where in NPS is the number of particles simulated in MCNP) in the sapphire fibers as well as their ratios as a function of distance from the center of the furnace. Results obtained using both MCNP tallies and the MCNP PTRAC feature are shown. The results obtained using the two

methods are in good agreement, thus verifying the method of post-processing the output of the PTRAC feature in MCNP to determine PKA information.

Table 3: Displacement and ionization energy deposition rates (in units of MeV/g/NPS, where in NPS is the number of particles simulated in MCNP) in the sapphire fibers as well as their ratios as a function of distance from the center of the furnace. Results obtained using both MCNP tallies and the MCNP PTRAC feature are shown.

Distance from Furnace Center (inches)	MCNP Tallies			MCNP PTRAC		
	Displacement Energy Deposition Rate (MeV/g/NPS)	Ionization Energy Deposition Rate (MeV/g/NPS)	Ratio of Displacement to Ionization Energy Deposition Rates	Displacement Energy Deposition Rate (MeV/g/NPS)	Ionization Energy Deposition Rate (MeV/g/NPS)	Ratio of Displacement to Ionization Energy Deposition Rates
-5.8	2.03E-08	5.39E-08	0.376	2.05E-08	4.85E-08	0.422
-2.9	2.02E-08	5.20E-08	0.388	2.07E-08	4.81E-08	0.430
0.0	1.82E-08	4.69E-08	0.389	1.87E-08	4.36E-08	0.428
2.9	1.48E-08	3.84E-08	0.385	1.54E-08	3.59E-08	0.428
5.8	1.05E-08	2.77E-08	0.380	1.10E-08	2.62E-08	0.418

MCNP simulations were used to determine the displacement and ionization energy deposition rates from neutrons. However, energy deposition rates from gamma rays cannot be easily simulated using MCNP. Fortunately, we are capable of measuring the gamma dose rate in the reactor using a Mg-walled ion chamber that has very low sensitivity to neutrons. In addition to the low sensitivity of the ion chamber to neutrons, the contribution to the total energy deposition rate from neutrons is expected to be at least an order of magnitude less than the contribution from gamma rays. Even though gamma rays contribute most of the energy deposition resulting from reactor irradiation, the majority of the gamma ray energy deposition causes ionization of the material, as opposed to displacement damage. It is still important to measure the gamma energy deposition because even though displacement damage is expected to be the largest contributor to the radiation-induced optical attenuation in the sapphire fibers, ionization effects can still have some contribution.

The Mg-walled ion chamber used to measure the gamma dose rate was first calibrated in a Co-60 gamma irradiation facility (located in the OSU Nuclear Reactor Laboratory) with a known gamma dose rate. The ion chamber was then inserted into the 7 inch dry tube facility of the OSURR at the location of the peak thermal neutron flux (estimated to be the peak location of the gamma

dose rate). Measurements were taken at reactor power levels of 0%, 0.6%, 2.0%, 6.0%, and 20.0% of full power (500 kW). The planned irradiations of sapphire fibers are to be performed at 90% power (450 kW). Ion chamber measurements were not made at higher powers in order to avoid significant neutron activation of the chamber and to avoid the significant gamma heating that occurs at higher powers and could affect the ion chamber measurements. Figure 11 shows the steady-state dose rate (absorbed dose in Al_2O_3 in units of krad/hr) as a function of reactor power. The data is well approximated by a linear fit (R^2 = 0.9994), indicating that an extrapolation can be performed to estimate the gamma dose rate at 450 kW with minimal error. The predicted gamma dose rate at 450 kW, based on extrapolation of the data shown in Figure 11, is 7518 krad/hr. Note that the maximum displacement, ionization, and total energy deposition rates from neutrons (shown in Table 3), when converted to units of krad/hr at 450 kW, are 45.5, 118.4, and 163.8 krad/hr, respectively. The maximum total energy deposition rate from neutrons (163.8 krad/hr) is more than an order of magnitude smaller than the predicted energy deposition rate from gamma rays (7518 krad/hr).

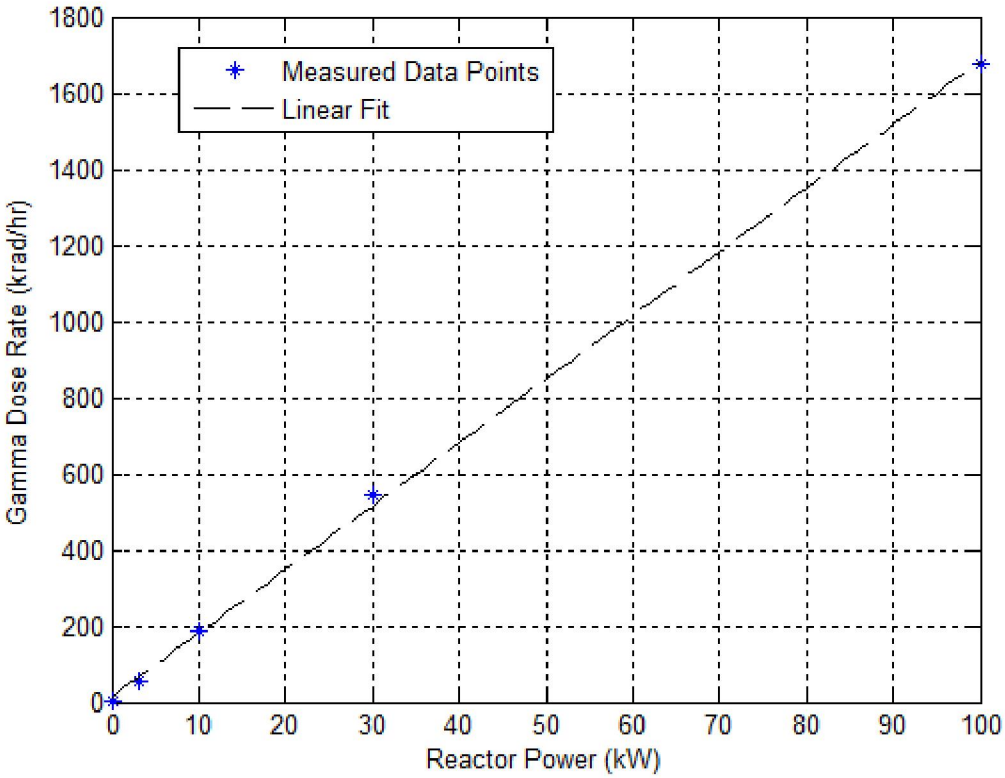

Figure 11: Steady-state gamma dose rate (dose in Al_2O_3 in units of krad/hr) in the 7 inch dry tube facility of the OSURR as a function of reactor power.

2.3.4 Prediction of the PKA Source Term

In order to determine the transport of PKAs throughout the sapphire fibers and the formation of point defects, the PKA source term must first be determined. This source term includes the distributions of PKA position, direction, and energy, and also the PKA generation rate. As mentioned in section 2.3.3, the MCNP PTRAC feature was used to track all neutrons entering the

fiber cells so that the PKA position, direction, and energy could be determined using conservation of momentum and energy equations for all neutron collisions within the fiber cells. The validity of using this method was confirmed by comparing energy deposition rates obtained using this method to the results of MCNP tallies. With the information obtained from the PTRAC method, we were able to generate statistical distributions of PKA position, direction, and energy. Figure 12 and Figure 13 show the distributions of PKA position and direction, respectively. The numbers shown in these figures are not normalized per MCNP source particle, so their absolute values are not meaningful. Positions in the Z-direction (the vertical direction as indicated on the figure) are with respect to the axial mid-plane of the core. Note that the furnace is not completely centered with the axial mid-plane of the core. This is because the sapphire fibers have to be bent 180 degrees below the furnace at a sufficiently large bend radius. An approximately 6 inch standoff is located below the furnace to allow the fibers room to be bent. There are steel plates at the bottom of the 7 inch dry tube facility, which limit how low the furnace can be inserted into the tube. Therefore, the position of the furnace inside the dry tube is constrained and the center of the heated region of the furnace is approximately 3 inches above the axial mid-plane of the core.

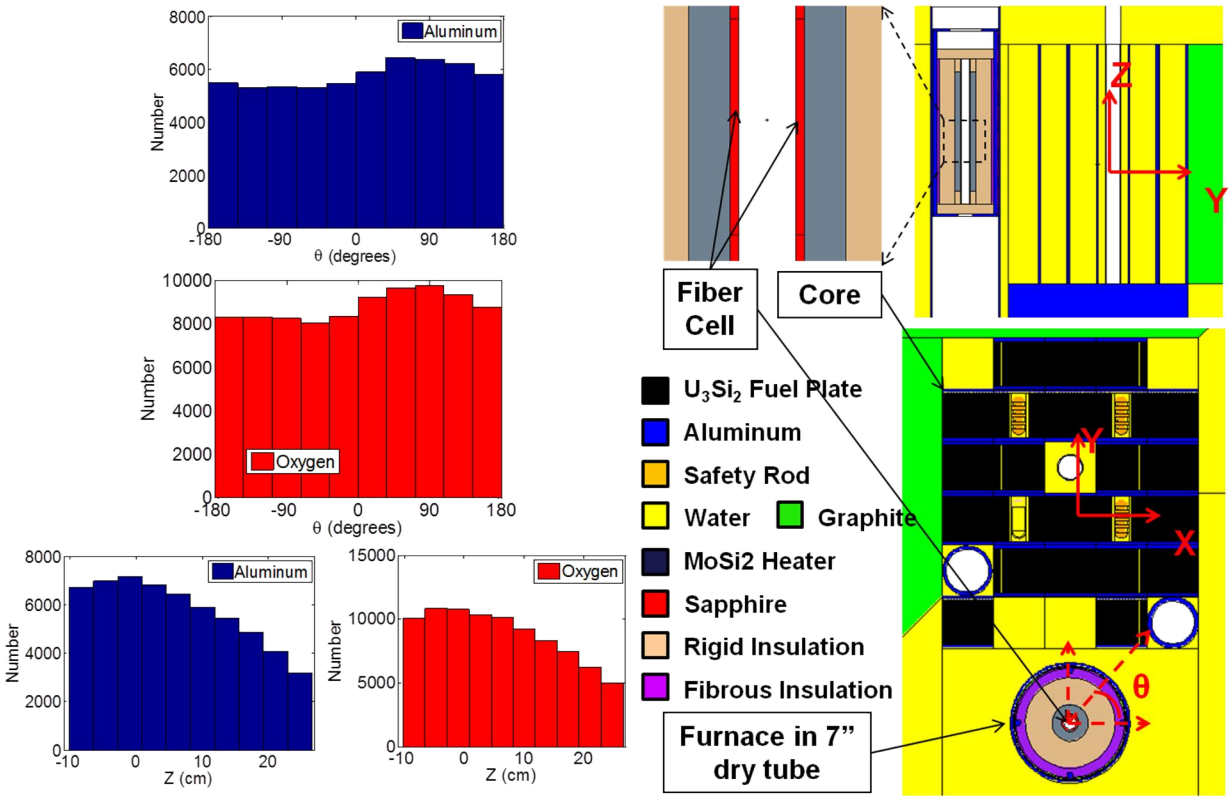

Figure 12: Distributions of PKA position with respect to the reactor core.

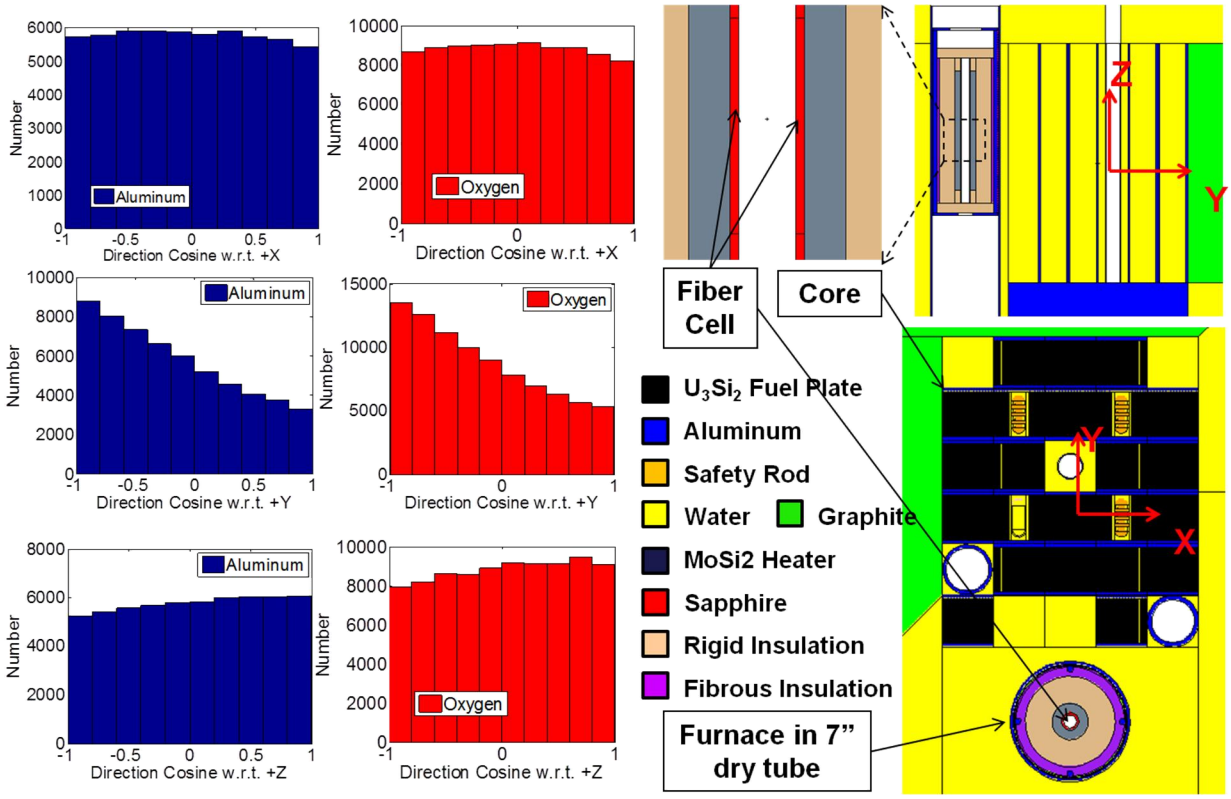

Figure 13: Distributions of PKA direction with respect to the reactor core.

In Figure 12, the angle θ is the azimuthal angle of the fibers relative to the X-direction (as indicated in the figure). Slightly more PKAs are located closer to the core (+90 degrees) as opposed to further away from the core (-90 degrees), which makes sense intuitively. However, this information is not particularly useful since the fibers will not actually be coiled on the inside surface of the heating element. Instead, they will travel straight down through the furnace at a radial position that is ~0.31 inches (0.79 cm) from the center of the furnace. The peak axial location of the PKAs is at Z=0 cm, which corresponds to the core axial mid-plane. In Figure 13, the PKA directions with respect to the X-axis are relatively uniform, with a slight peak near zero. Directions with respect to the Y-axis are skewed very much toward the negative direction as more neutrons are traveling away from the reactor core, as opposed to toward the reactor core. In the Z direction, more neutrons are traveling upward as opposed to downward. This is due to the fact that neutron direction is averaged over the entire heated region of the sapphire fibers. More of the heated region is located above the core as opposed to below the core, since the axial center of the furnace is above the core mid-plane. Therefore, the distribution of PKA direction in the Z-direction is slightly skewed in the positive direction because more neutrons entering the fibers above the core mid-plane would be traveling in the positive Z-direction to get above the core mid-plane.

The PKA generation rate and the distributions of PKA energy were also obtained using MCNP with the PTRAC feature. This information was also obtained using the SPECTER-ANL software code package (hereafter referred to as SPECTER). SPECTER uses displacement damage cross sections to determine displacement per atom (DPA) rates and PKA energy spectra with the group values for the neutron flux as an input. We used SPECTER to determine the PKA energy spectra to compare with the results of MCNP using the PTRAC feature. We also determined the PKA

generation rate (to compare with the results from MCNP with the PTRAC feature) using the spectrum averaged DPA cross sections and the average damage energy per PKA per unit time generated by SPECTER. Figure 14 shows PKA energy spectra (differential PKA rate [PKAs/(cm^3 MeV s)] * PKA Energy [MeV] * ln(10)) in the sapphire fibers at the center of the furnace at a reactor power of 450 kW for aluminum and oxygen atoms generated using MCNP with the PTRAC feature and SPECTER-ANL. The spectra obtained using the two different methods show very good agreement for both aluminum and oxygen PKAs.

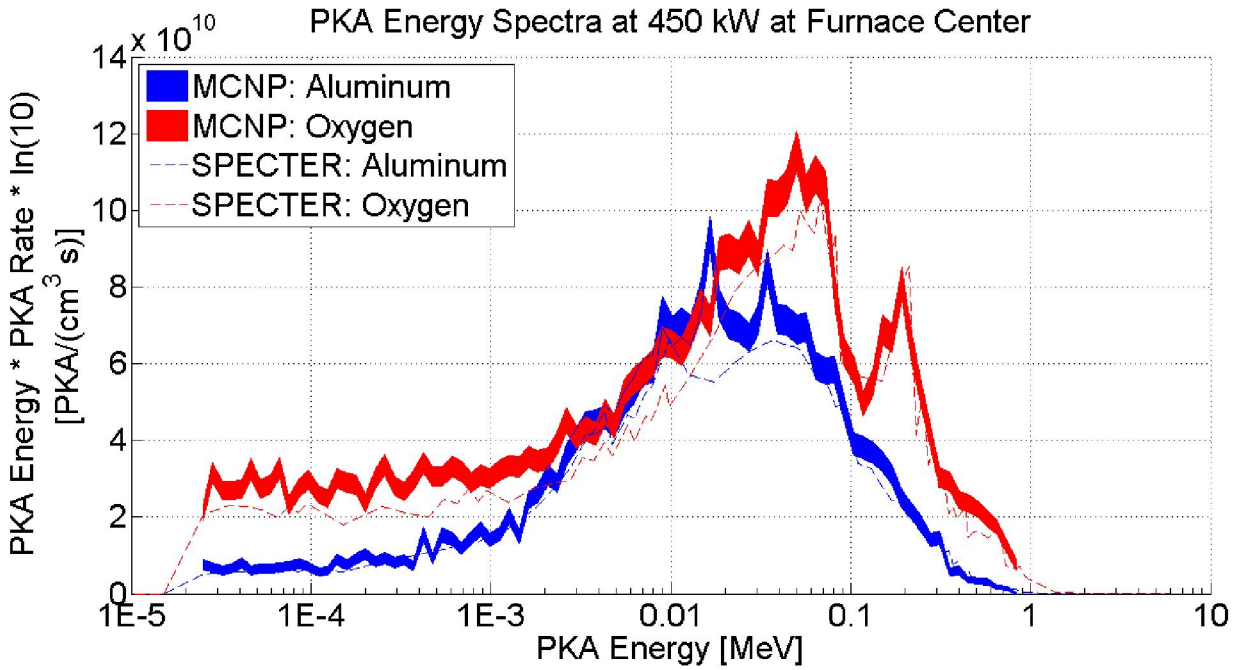

Figure 14: PKA energy spectra (differential PKA rate [PKAs/(cm^3 MeV s)] * PKA Energy [MeV] * ln(10)) in the sapphire fibers at the center of the furnace at a reactor power of 450 kW for aluminum and oxygen atoms generated using MCNP with the PTRAC feature and SPECTER-ANL.

Table 4 shows the PKA generation rates in the sapphire fibers at the center of the furnace at a reactor power of 450 kW for aluminum and oxygen PKAs and their sums as determined using MCNP with the PTRAC feature and SPECTER-ANL. The PKA generation rates obtained using the two different methods are almost identical for aluminum and oxygen PKAs as well as their sums.

Table 4: PKA generation rates in the sapphire fibers at the center of the furnace at a reactor power of 450 kW for aluminum and oxygen PKAs and their sums as determined using MCNP with the PTRAC feature and SPECTER-ANL.

Method	PKA Generation Rate [10^{10} PKAs/(cm^3 s)]		
	Aluminum PKAs	Oxygen PKAs	Total PKAs
MCNP with PTRAC	6.04	9.47	15.5
SPECTER-ANL	6.10	9.24	15.3

Chapter 3. Task B - Damage Creation Modeling

3.1 Deliverables

- Locations of the defects resulting from damage cascades of PKAs

3.2 Timeline and Task Status

- Start Date: 4/1/2013
- Planned Completion Date: 9/30/2013
- Task Status: 100%

3.3 Progress Toward the Completion of Deliverables

3.3.1 Locations of the Defects Resulting from Damage Cascades of PKAs

This task is devoted to modeling the transport of PKAs throughout the sapphire fiber material and the generation of point defects prior to any thermal annealing of the defects. The input to these models is the PKA source term discussed in section 2.3.4. We considered three codes for damage creation modeling:

- LAMMPS: A Molecular Dynamics (MD) code that, if implemented with an accurate interatomic potential, gives the most accurate results, however it is computationally expensive, particularly for large cell simulations that are required for modeling high energy damage cascades.
- SRIM/TRIM: A Monte Carlo-based code that gives relatively accurate results for a wide range of target materials and ions. Due to the binary collision approximation (BCA), SRIM/TRIM offers fast run times, but it is limited to amorphous materials and does not give positions of interstitials. SRIM/TRIM allows the user to explicitly input displacement threshold energies.
- Marlowe: Another BCA-based based code that can be relatively accurate, but typically requires tuning of parameters to match results of other codes or experiments, as the displacement threshold energies cannot be explicitly input. Marlowe offers fast run times, the ability to model crystalline materials, and it gives positions of both vacancies and interstitials.

Originally we had planned to use LAMMPS to model low energy PKA damage cascades and these simulations would account for immediate elastic relaxation and short term thermal annealing. The LAMMPS models may or may not account for electronic stopping effects, however these effects are not extremely significant at lower PKA energies. The interatomic potential that is implemented in a MD simulation is extremely important. These potentials often use a closed-form equation fitted to empirical data in order to reduce computation times. Of course, the accuracy of the simulation will only be as accurate as the interatomic potential that is implemented. Ab-initio, or quantum mechanical potentials utilizing density functional theory, for example, can be implemented; however, such quantum mechanical modeling is prohibitively expensive

computationally. Some empirical potentials may reproduce material properties at room temperature and/or equilibrium lattice spacing, however they may or may not be accurate when lattice spacing is altered due to the introduction of defect structures, for example. It is difficult to say for certain that any interatomic potential is suitable for performing dynamic simulations of radiation damage cascades, which represent a highly non-equilibrium process.

The best way to evaluate the suitability of interatomic potentials for performing radiation damage simulations are to compare the defect formation energies determined using the interatomic potential with defect formation energies determined using ab-initio simulations. However, even ab-initio simulations have large disparity in the calculated defect formation energies in sapphire. For sapphire, the most common defects whose formation energies are reported in the literature are Shottky defects (aluminum and oxygen vacancies generated in a stoichioetric ratio, i.e. 2 aluminum vacancies and 3 oxygen vacancies) and Frenkel defects (aluminum or oxygen vacancy/interstitial pairs). The concentration of a specific type of defect is proportional to $\exp(\frac{-E_f}{kT})$, where E_f is the defect formation energy of the defect, k is the Boltzmann constant, and T is the absolute temperature. The temperatures that are to be tested in the experiments performed for this project range from approximately 300 to 1873 K. As an example, consider two defects with formation energies of 4 and 5 eV. Neglecting differences in the proportionality constants of the two defects (which will only differ by a factor of 3/2 for sapphire), the ratio of the concentration of the defect with a 4 eV formation energy to the concentration of the defect with a 5 eV formation energy would be $6.3*10^{16}$ and 491 at temperatures of 300 and 1873 K, respectively. Therefore, even small differences in defect formation energies will determine which defects will be dominant, especially at lower temperatures.

Previous work has shown wide variability in the range of calculated defect formation energies in sapphire. Table 5 shows some of the values that have been calculated for these defects and the methods that were used in each of the calculations. The values listed for Shottky defects range from 4.01 to 5.86 eV, while the values listed for aluminum and oxygen Frenkel defects range from 4.95 to 10.0 eV and 3.79 to 7.0 eV, respectively.

Table 5: Calculated defect formation energies in sapphire and the methods that were used in each of the calculations.

Type of Calculation	Formation Energy per Defect (eV)			Reference
	Shottky	Aluminum Frenkel	Oxygen Frenkel	
Emperical Potentials	5.70	10.00	7.00	[1]
Emperical Potentials	4.70	6.47	4.06	[2]
Emperical Potentials	5.86	6.30	5.79	[3]
Emperical Potentials	5.17	6.59	4.87	[4]
Emperical Potentials	5.15	7.22	5.54	[5]
Semi-Emperical Potentials	4.18	5.22	3.79	[6]
Semi-Emperical Potentials	4.91	6.43	5.13	[7]
Density Functional Theory with Generalized Gradient Approximation	4.01	4.95	6.52	[8]

Other works have used ab-initio methods to calculate the defect formation energies of various defects as a function of chemical potential and Fermi level, but the results are not entirely consistent. Besides the wide variability in formation energies for each defect, there is also no consensus as to which defect is dominant (which defect has the lowest formation energy). Xu et al. [9] and Sokol et al. [10] used density functional theory (DFT) with the local density approximation (LDA) to determine formation energies of oxygen vacancies (5.83 eV) and interstitials (4.0 to 6.15 eV depending on the type of interstitial), respectively. Tanaka et al. used DFT with the generalized gradient approximation (GGA) to determine defect formation energies for neutral oxygen vacancies for the limiting cases of oxygen-rich (7.08 eV) and oxygen-poor (1.63 eV) environments [11]. Liu et al. performed similar DFT calculations with the GGA to determine formation energies of oxygen vacancies in an oxygen poor environment as a function of the Fermi level [12]. Hine et al. determined defect formation energies of aluminum and oxygen vacancy and interstitial defects as a function of both Fermi level and oxygen chemical potential using DFT with the LDA [13]. Weber et al. used DFT with the LDA [14] and a screened hybrid-functional proposed by Heyd, Scuseria, and Ernzen-hof (HSE) [15] to determine defect formation energies of aluminum and oxygen vacancies as a function of Fermi level for the oxygen-rich and oxygen-poor limits.

For this project, we plan to determine defect energies of aluminum and oxygen vacancies, interstitials, and antisites in various charge states using DFT with HSE hybrid functionals. This work will be performed in Task D. With so much uncertainty in the published defect formation energies, we have decided to temporarily abandon attempts to use MD to simulate radiation damage cascades and focus more on simulations that implement the BCA. If we are able to find an interatomic potential that gives defect energies that are consistent with the calculations that are to be performed by us in Task D, then we may revisit the idea of performing dynamic simulations of radiation damage cascades using MD. Others such as Iguchi et al. [16], Lee and Farnum [17], and Mota et al. [18] have used codes based on the BCA (Marlowe and TRIM) to perform radiation damage simulations in sapphire.

We decided to first perform TRIM calculations of aluminum and oxyen PKA damage cascades in Al_2O_3 with varying energy over the range of PKA energies predicted by the neutronics modeling performed in Task A. TRIM allows for the input of experimentally determined displacement threshold energies and is generally considered to give reasonably accurate results for most materials. Even though sapphire is a crystalline material and SRIM/TRIM does not give the locations of interstitials in the material, we decided to perform simulations in TRIM to determine the PKA range, electronic energy loss, and the number of aluminum and oxygen defects generated for each PKA energy. Similar simulations were performed in Marlowe, which does allow for simulations of crystalline materials and does give the locations of interstitial defects, although experimentally determined values for the displacement threshold energies cannot be explicitly input. Simulation parameters in Marlowe (such as binding energies and cutoff energies below which cascade atoms are no longer followed) were varied until the results (PKA range, electronic energy loss, and number of defects per PKA) from Marlowe matched the results from TRIM. The ZBL potential was used to describe the elastic scattering in Marlowe. This is the same potential that is used in TRIM.

Figure 15 and Figure 16 show the PKA range and the fraction of energy loss to ionization (or to electronic stopping), respectively, as a function of PKA energy for both aluminum and oxygen PKAs (or ions). PKA range and fraction of energy loss to ionization both generally show very good agreement between the results obtained using TRI and Marlowe for both aluminum and oxygen PKAs over all PKA energies. One exception is that Marlowe predicts lower values for the fraction of energy loss to ionization. However, this effect is significant only at lower PKA energies (below ~1000 eV). Lower energy PKAs obviously contribute less to the total displacement damage than

higher energy PKAs, and the PKA energy spectra shown in Figure 14 indicate that there are significantly more PKAs generated from the neutron flux energy spectrum in the OSURR having energies greater than 1000 eV compared to those generated with energy less than 1000 eV.

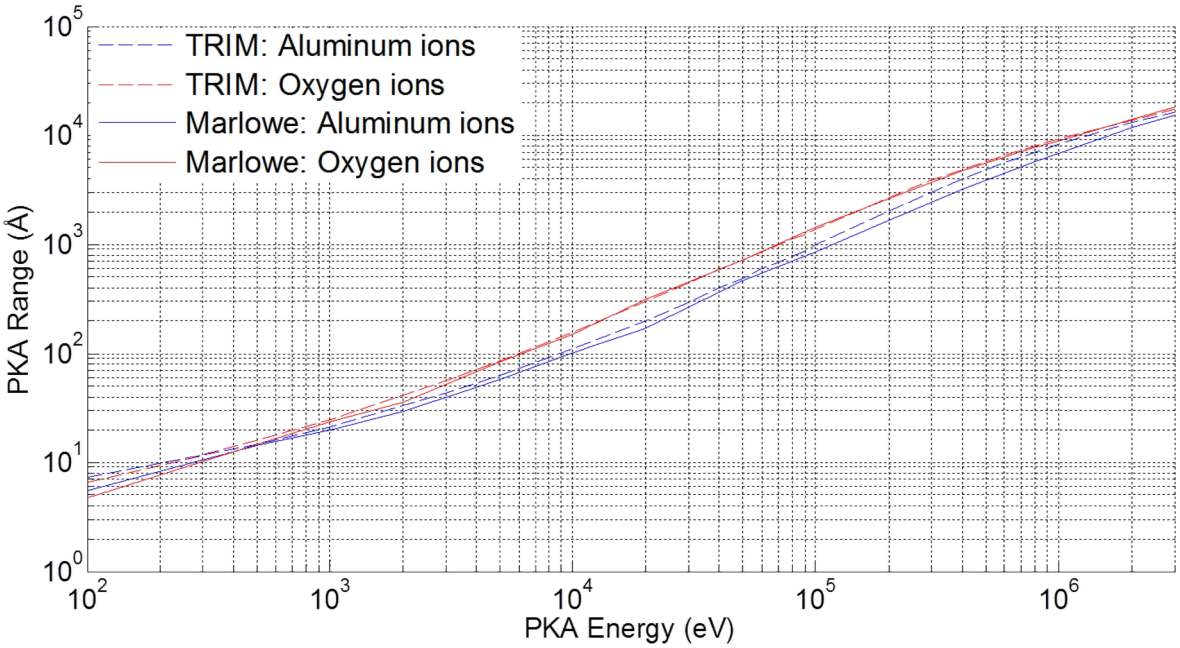

Figure 15: PKA range vs. PKA energy for both aluminum and oxygen ions determined using TRIM and Marlowe.

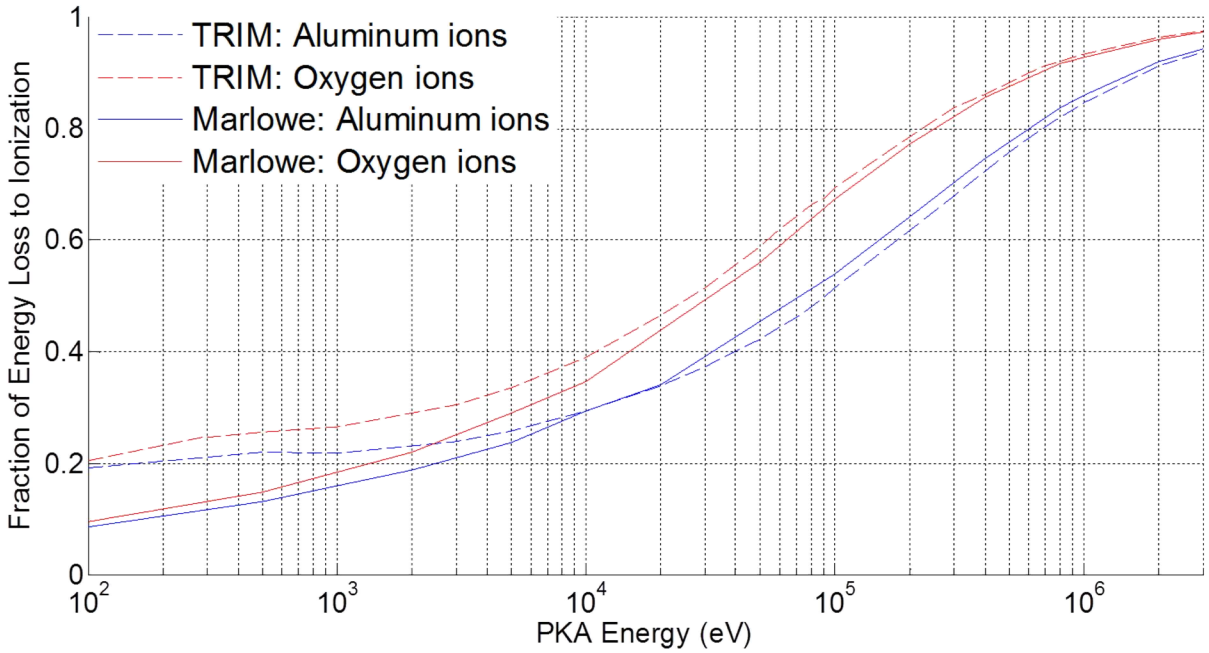

Figure 16: Fraction of energy loss contributing to ionization vs. PKA energy for both aluminum and oxygen ions determined using TRIM and Marlowe.

Figure 17 shows the number of defects (aluminum and oxygen defects) generated per aluminum PKA vs. aluminum PKA energy as determined using both TRIM and Marlowe. Figure 18 shows the number of defects (aluminum and oxygen defects) generated per oxygen PKA vs. oxygen PKA energy as determined using both TRIM and Marlowe. Similar to Figure 15 and Figure 16, the plots showing the number of defects vs. PKA energy (Figure 17 and Figure 18) show good agreement between the data generated using TRIM and Marlowe, with some disagreement at lower PKA energies.

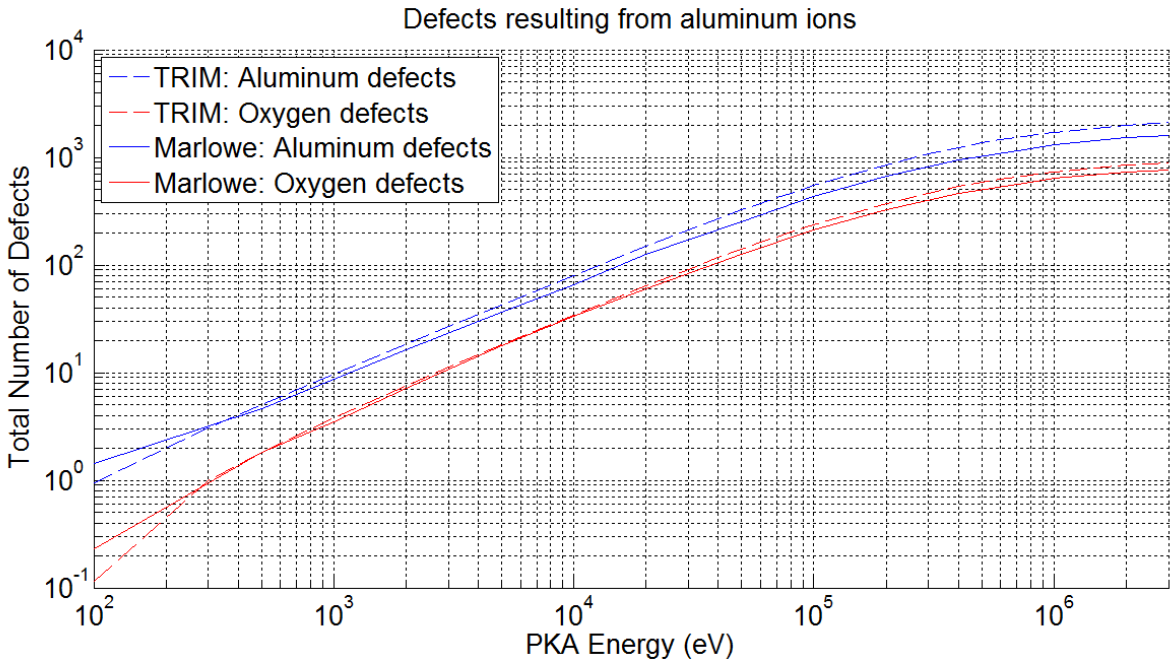

Figure 17: Number of defects (aluminum and oxygen defects) generated per aluminum PKA vs. aluminum PKA energy as determined using both TRIM and Marlowe.

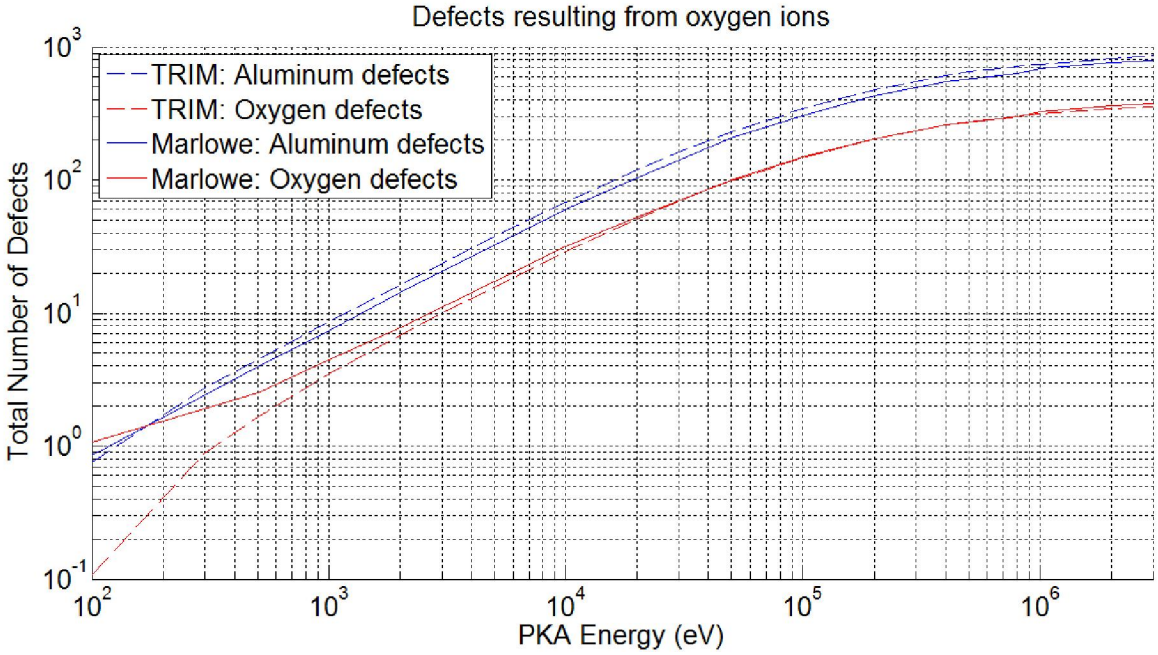

Figure 18: Number of defects (aluminum and oxygen defects) generated per oxygen PKA vs. oxygen PKA energy as determined using both TRIM and Marlowe.

The output of Marlowe includes the positions of vacancy and interstitial defects as well as the separation of each vacancy-interstitial pair (or Frenkel pair). With this information, one can determine the number of defects with separation less than or equal to some distance. This distance can be thought of as a recombination radius, within which Frenkel defects will recombine. Recombination radii for aluminum and oxygen Frenkel pairs can be determined using ab-initio simulations or these radii can be used as fitting parameters when fitting results to experimental data. We determined the effect of varying the recombination radii on the number of stable defects as a function of PKA energy. Figure 19 through Figure 22 show the number of stable defects as a function of PKA energy with recombination radius (or recombination distance) as a parameter. Figure 19 through Figure 22 show results for aluminum defects resulting from aluminum ions, oxygen defects resulting from aluminum ions, aluminum defects resulting from oxygen ions, and oxygen defects resulting from oxygen ions, respectively.

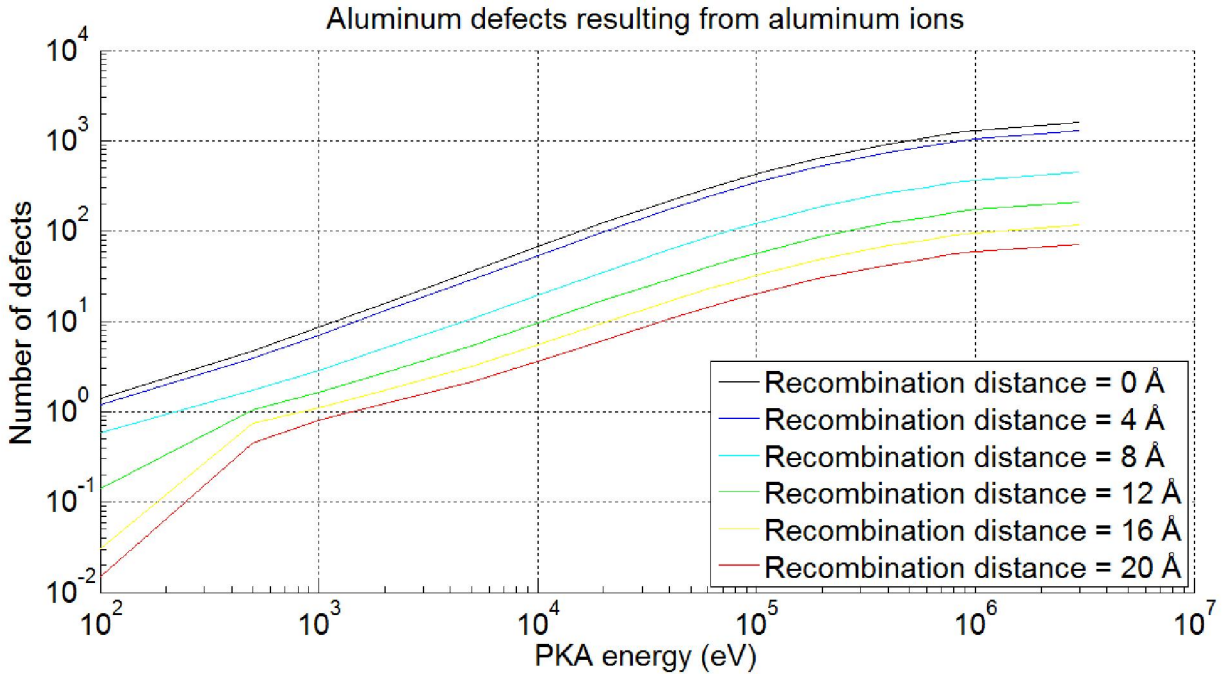

Figure 19: Number of stable aluminum defects resulting from aluminum ion cascades as a function of aluminum ion energy with defect recombination distance as a parameter.

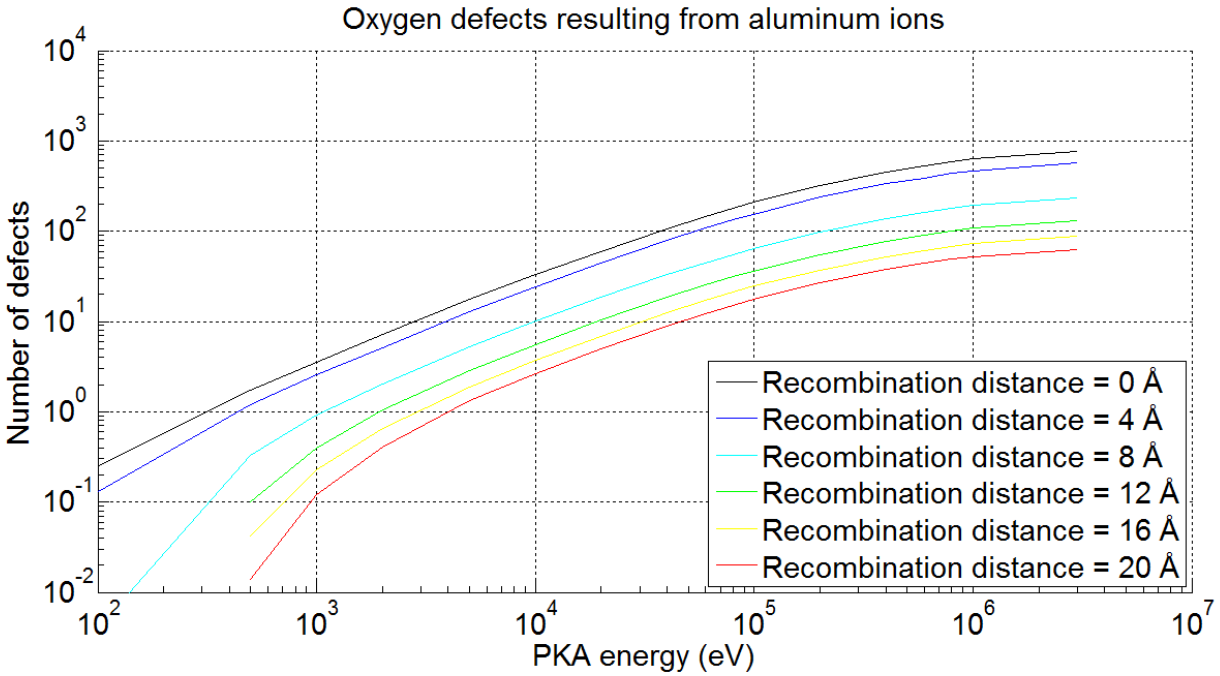

Figure 20: Number of stable oxygen defects resulting from aluminum ion cascades as a function of aluminum ion energy with defect recombination distance as a parameter.

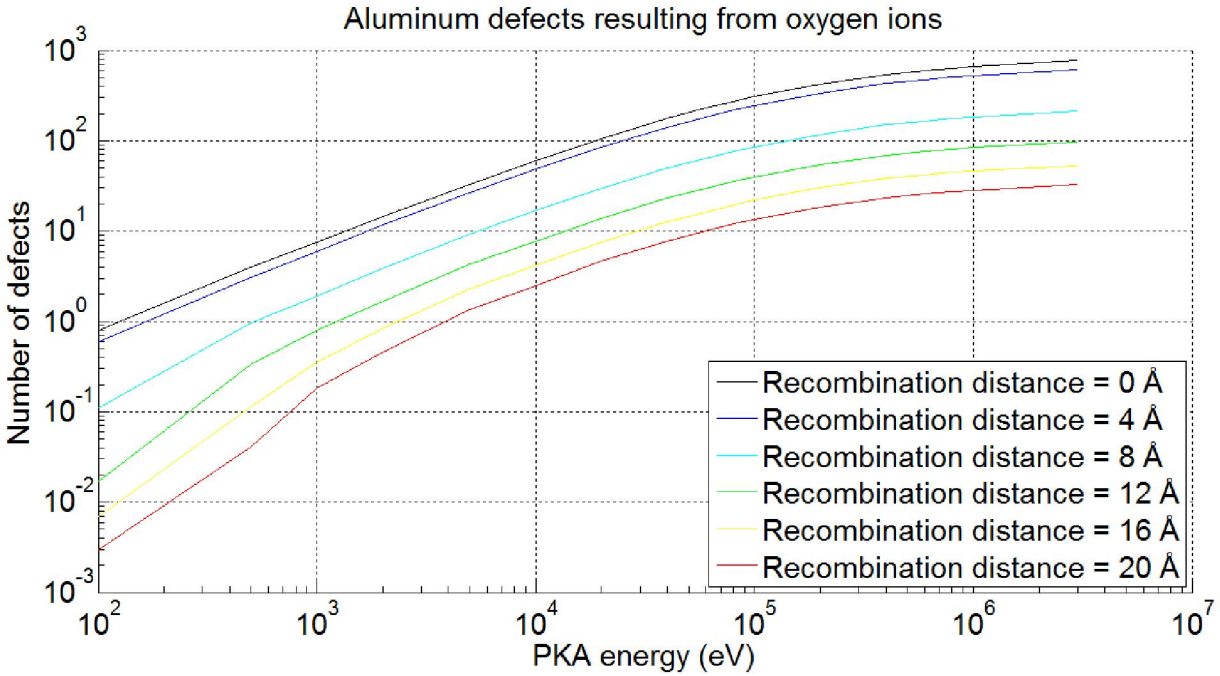

Figure 21: Number of stable aluminum defects resulting from oxygen ion cascades as a function of oxygen ion energy with defect recombination distance as a parameter.

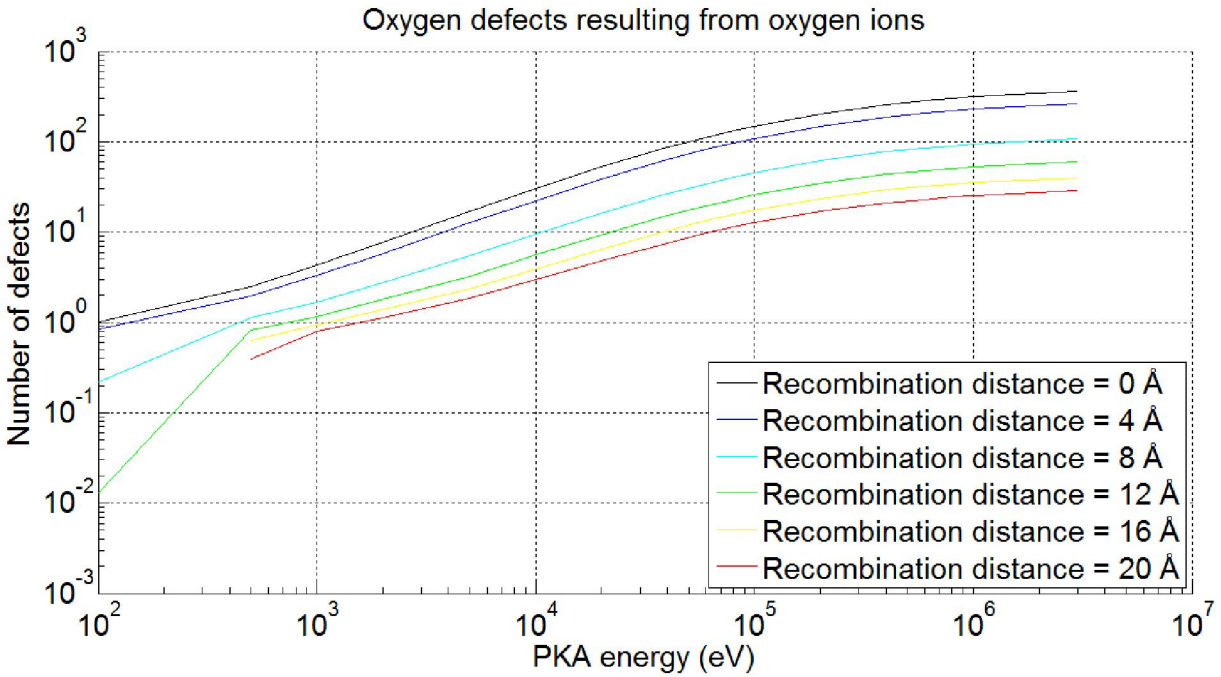

Figure 22: Number of stable oxygen defects resulting from oxygen ion cascades as a function of oxygen ion energy with defect recombination distance as a parameter.

We determined the distributions of PKA position and energy, as well as the PKA generations rates in Task A, and the number of defects generated per PKA as a function of PKA energy (and type, i.e. aluminum or oxygen) and recombination radius in Task B. Combining all of this information, we can determine the distribution of aluminum and oxygen defects (Frenkel pairs) in the sapphire fiber as a function of position and recombination radius (vacancy-interstitial recombination radius) by integrating over all PKA energies. Figure 23 shows defect (aluminum and oxygen Frenkel pairs) generation rates in the sapphire fibers at a reactor power of 450 kW vs. distance from the center of the furnace with the defect recombination radius, R, as a parameter. This plot shows a peak damage region in the fibers at approximately 4 to 5 inches below the axial center of the furnace. This is approximately equal to the location of the reactor core axial mid-plane. The damage rates at the top and bottom of the furnace are approximately 39% and 89% of the damage rates at the peak damaged region, respectively. The effects of recombination radius can also be seen in this plot as the defect generation rates decrease significantly with increasing recombination radius.

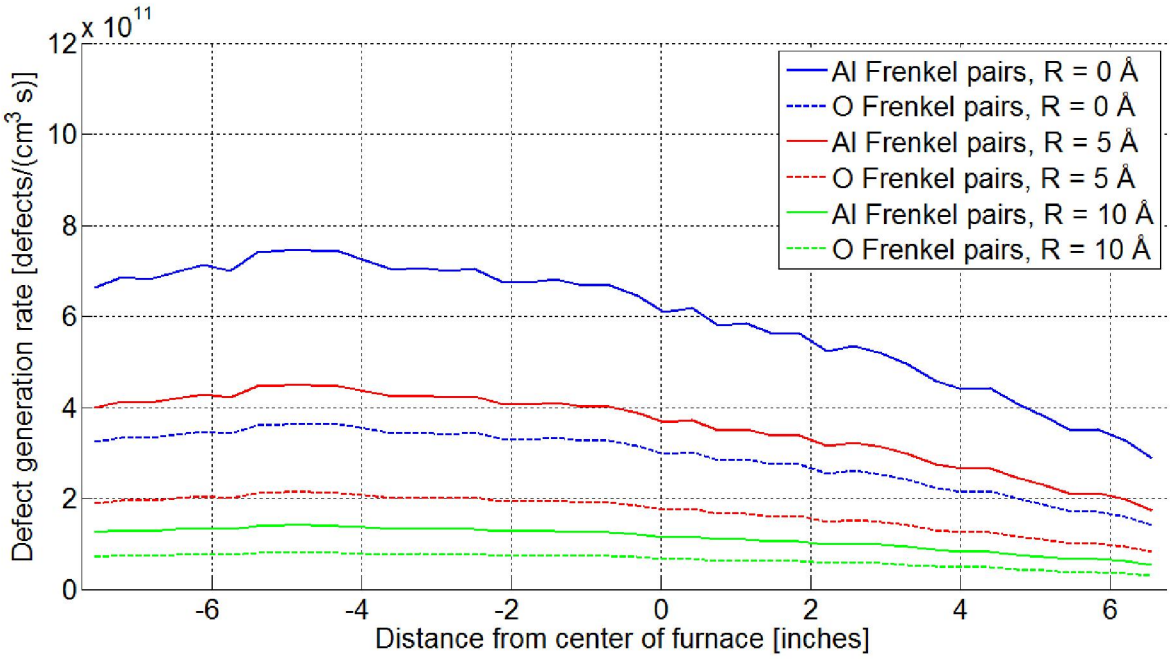

Figure 23: Defect (aluminum and oxygen Frenkel pairs) generation rates in the sapphire fibers at a reactor power of 450 kW vs. distance from the center of the furnace with the defect recombination radius, R, as a parameter.

Chapter 4. Task C - Damage Evolution Modeling

4.1 Deliverables

- Defect concentrations resulting from reactor irradiation and thermal annealing as a function of irradiation time and temperature

4.2 Timeline and Task Status

- Start Date: 10/1/2013
- Planned Completion Date: 12/30/2015
- Task Status: 100%

4.3 Progress Toward the Completion of Deliverables

4.3.1 Defect Concentrations Resulting from Reactor Irradiation

In order to calculate the post-irradiation concentration rates of various point defects in sapphire, we have developed a damage evolution model within the diffusion-reaction rate modeling code ALAMODE [19] to study how those defects evolve as a function of time and temperature. Our model assumes a fiber with a diameter of 100 μm that has undergone neutron radiation for 8 hours, comparable to experiments carried out in Task F. We have input values for the initial concentrations of defects formed from fast-neutron irradiation based on the data shown in Figure 23. An average of the values between distances of -4 and -2 inches from center, and for capture radii of 0 and 5 Å were used. We then made the assumptions that the displaced Frenkel pairs consisted of equal concentrations of interstitial and vacancy defects, and that all other defect species would evolve from these Frenkel pairs through solid-state reactions.

Before we used our diffusion-rate equation to determine the defect evolution in a sapphire fiber, a calculation of the formation energies of each defect as a function of temperature and stoichiometry first had to be made. To gain a full understanding of the point defect content in sapphire, a total of 8 different point defect species were considered throughout this section. The formation energies of the oxygen vacancy (V_O), aluminum vacancy (V_{Al}), oxygen interstitial (O_i), aluminum vacancy oxygen interstitial defect (AVOID) pair, aluminum antisite (Al_O), and aluminum interstitial (Al_i) in both O-rich and Al-rich sapphire were calculated as a function of Fermi energy using the constitutional defect method. For the O-rich case, the AVOID pair was found to be the constitutional defect, while for the Al-rich case, the constitutional defect was found to switch between the $V_{2O,c}$ and V_O, depending on the Fermi level. Plots of defect formation versus Fermi energy for the O-rich and Al-rich cases are shown below in Figures 24 and 25, respectively.

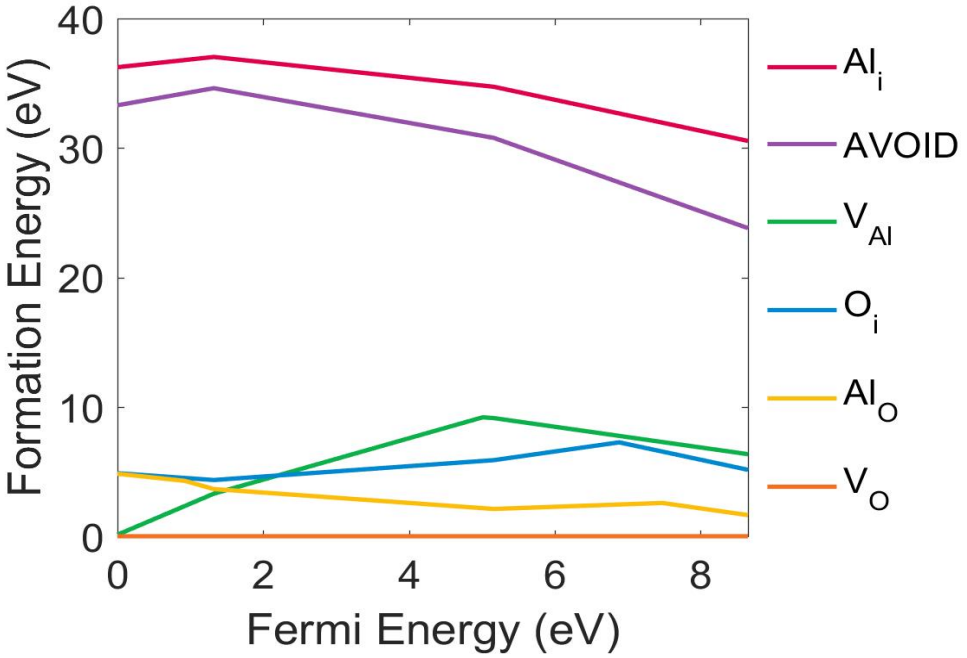

Figure 24. Formation energy as a function of Fermi energy for V_O, V_{Al}, O_i, AVOID, Al_O, and Al_i defects in O-rich sapphire using the constitutional defect method. A Fermi energy of 0 eV indicates the valence band maximum, while 8.6 eV indicates the conduction band minimum.

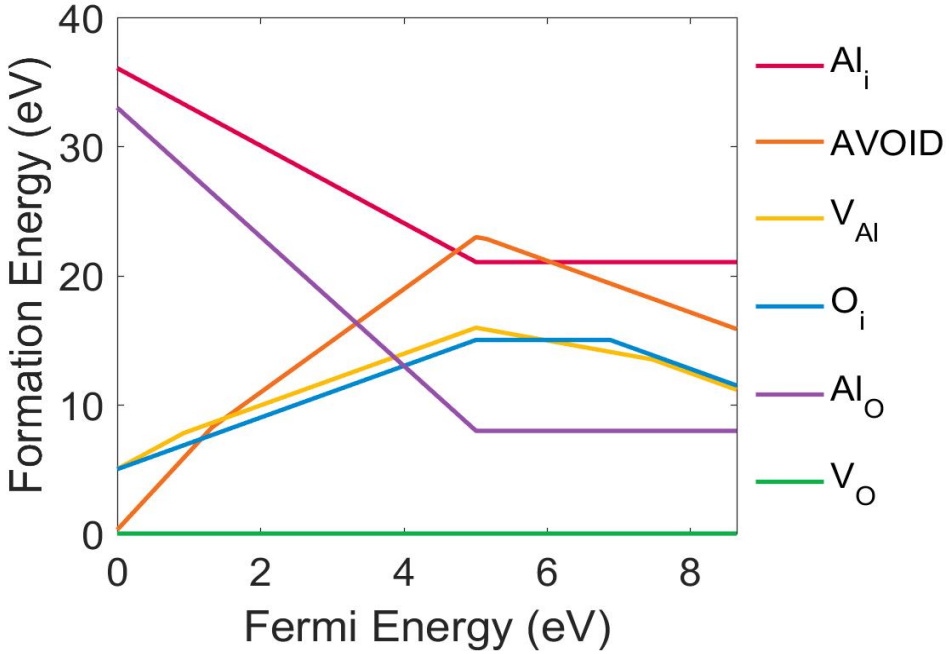

Figure 25. Formation energy as a function of Fermi energy for V_O, V_{Al}, O_i, AVOID, Al_O, and Al_i defects in O-rich sapphire using the constitutional defect method. A Fermi energy of 0 eV indicates the valence band maximum, while 8.6 eV indicates the conduction band minimum.

With the AVOID pair being the constitutional defect for the O-rich case, the VAl is the next most likely defect to form with a formation energy of 2.45 eV. The oxygen interstitial, vacancy, and divacancy pairs have moderately higher formation energies ranging from 5.53 to 16.65 eV, while the AlO and Ali have very high formation energies of 31.64 and 35.24 eV, respectively. For the Al-rich case, the VO is the constitutional defect for Fermi energies between the valence band maximum (VBM) and 3.42 eV, and then switches to the V2O,b up to the conduction band minimum (CBM). At mid-gap, however, the V2O,b is the constitutional defect, with the VO and V2O,c also likely to form with low formation energies of 0.88 and 2.32 eV, respectively. The Oi, VAl, AlO, and AVOID pairs have moderately high formation energies of 12.70, 13.20, 13.72, and 17.92 eV, respectively. Similarly to the O-rich case, the Ali has the highest formation energy (24.49 eV) of all considered defects for the Al-rich case. At mid-gap, the chemical potential of O in the O-rich sapphire is -7.91 eV, while the chemical potential of Al in the Al-rich sapphire is -3.63 eV.

The formation energies of the 8 considered defects were also calculated using the heat of formation method, for comparison purposes. For the O-rich case, μ_O was set equal to half of the energy of an oxygen molecule in vacuum, and for the Al-rich case, μ_{Al} was set to the energy of a single Al atom in FCC Al. Using these chemical potentials, defect formation energies were calculated as a function of Fermi energy for the O-rich and Al-rich cases, and are shown below in Figures 26 and 27, respectively.

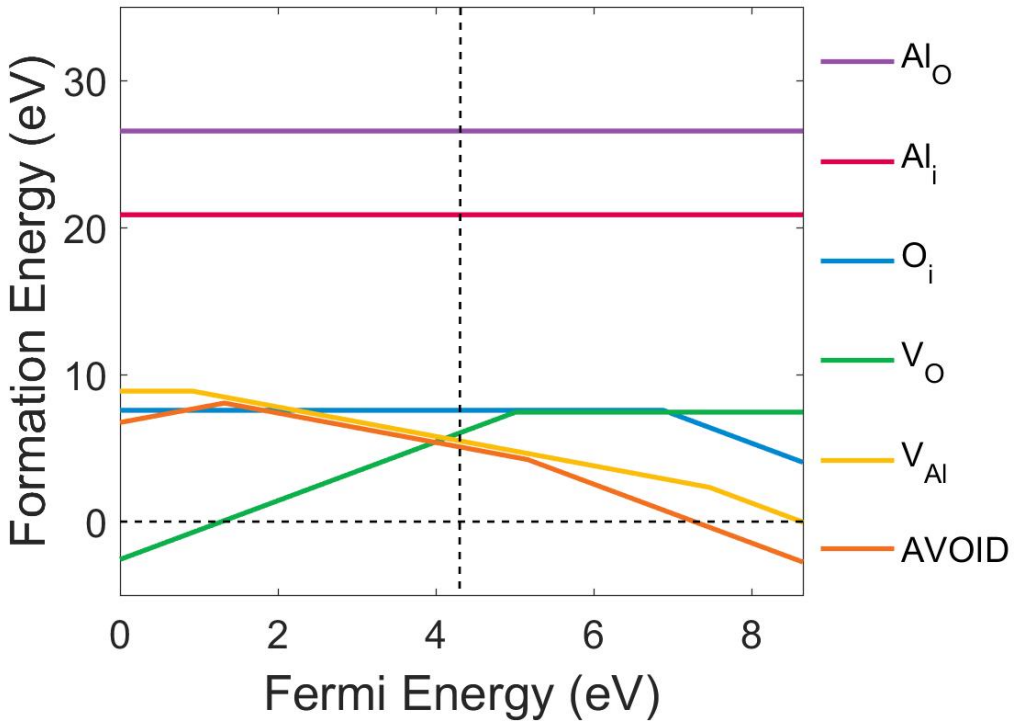

Figure 26. Formation energy as a function of Fermi energy for VO, VAl, V2O,b, V2O,c, Oi, AVOID, AlO, and Ali defects in O-rich sapphire using the heat of formation method. A Fermi energy of 0 eV indicates the valence band maximum, while 8.6 eV indicates the conduction band minimum.

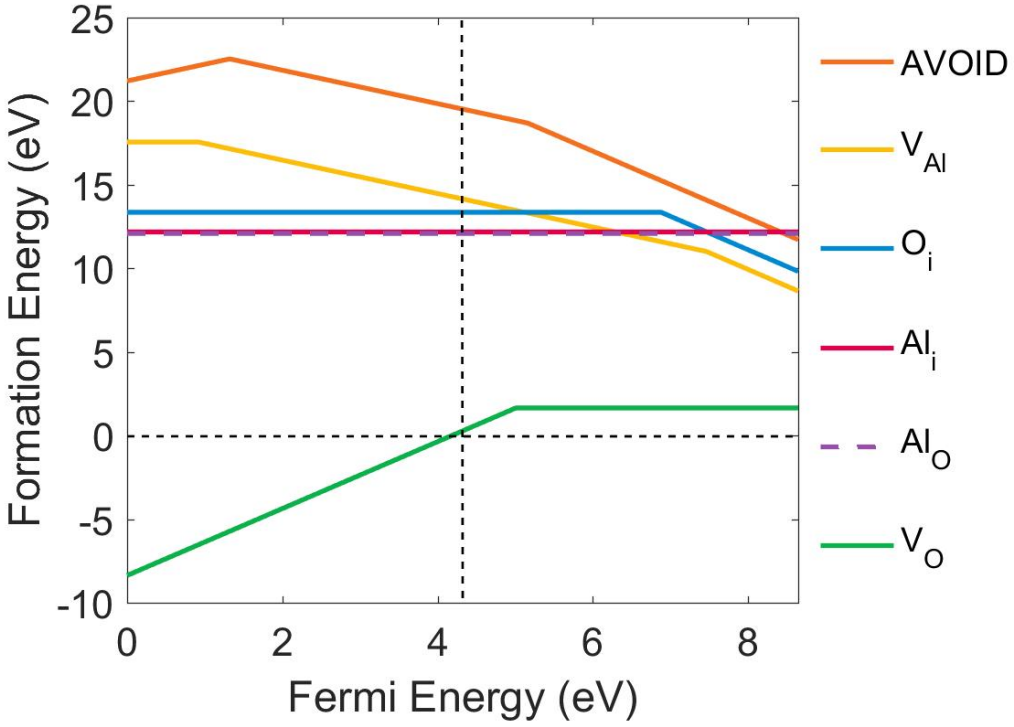

Figure 27. Formation energy as a function of Fermi energy for V_O, V_{Al}, $V_{2O,b}$, $V_{2O,c}$, O_i, AVOID, Al_O, and Al_i defects in Al-rich sapphire using the heat of formation method. A Fermi energy of 0 eV indicates the valence band maximum, while 8.6 eV indicates the conduction band minimum.

Using the heat of formation method, the AVOID pair is the most dominant defect in O-rich sapphire, with a formation energy of 5.07 eV. The V_{Al} and V_O are the next likely defects to form, having formation energies of 5.50 and 6.03 eV, respectively. The O_i, $V_{2O,b}$, and $V_{2O,c}$ have moderately high formation energies of 7.56, 10.27, and 12.50 eV, respectively. Similar to the results from the constitutional defect method, the Al_O and Al_i are the highest energy defects, having formation energies of 26.56 and 32.20 eV, respectively. Though none of the formation energies are negative at a Fermi energy of 4.3 eV, the V_O formation energy is negative between the VBM and 1.28 eV, while the AVOID pair has negative formation energy values between 7.27 eV and the CBM. For the Al-rich case, the most dominant defect, the $V_{2O,b}$, shows a negative formation energy of -1.31 eV. Though the next two most stable defects, the V_O and $V_{2O,c}$, show positive formation energies of 0.24 and 1.01 eV, respectively, both defects exhibit negative formation energies just below mid-gap. The Al_O, O_i, and V_{Al} have moderately high formation energies of 12.09, 13.35, and 14.18 eV, respectively, with the AVOID pairs and Al_i being the least stable with formation energies of 19.55 and 23.51 eV, respectively.

Comparing the results of the two methods shown in Figures 24-27, it is apparent that the constitutional defect method holds the advantage of not producing unphysical, negative formation energies. For the heat of formation method, this is not the case. As seen in the Al-rich case, this method predicts a negative formation energy for the most stable defect at mid-gap. This is a troubling result, since a negative formation energy indicates that a crystal with a defect is more stable than a perfect one and should be thermodynamically unstable.

The defect formation energies in stoichiometric sapphire were also considered and are should be considered the typical sapphire fiber state; formation energies of the 8 considered point defects are calculated for stoichiometric sapphire using the CCCP method. In Figure 28, the calculated defect formation energies in stoichiometric sapphire are shown as a function of the Fermi energy, where zero Fermi energy is equivalent to the valence band maximum (VBM). Considering intrinsic sapphire, point defects should be analyzed only at the mid-gap state (~ 4.3 eV).

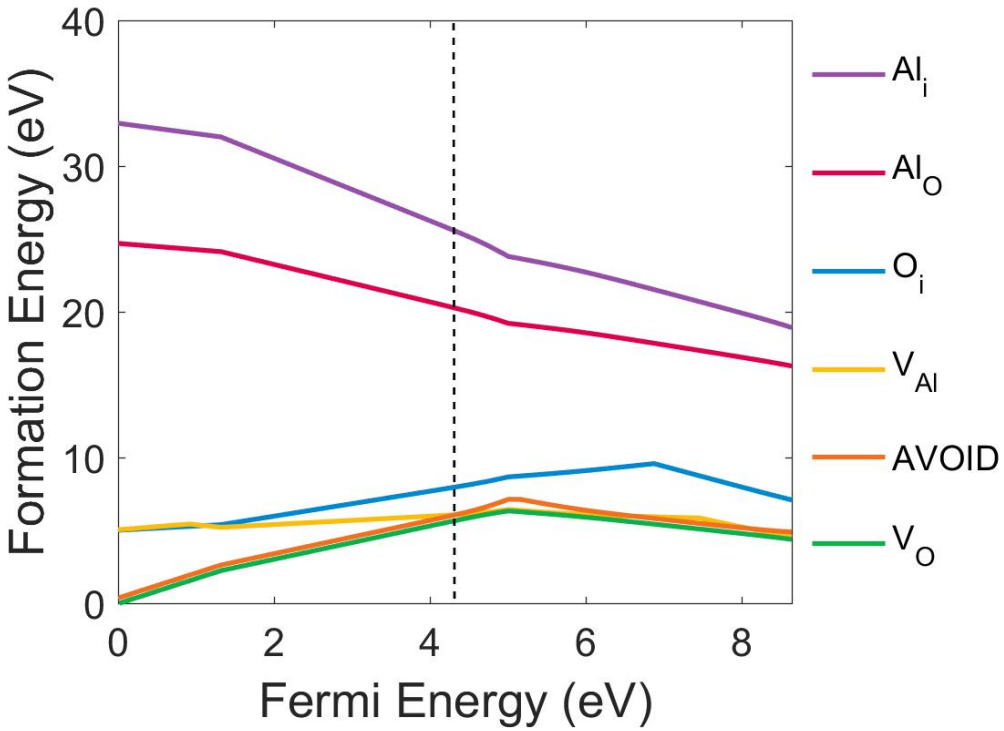

Figure 28. Formation energy as a function of Fermi energy for V_O, V_{Al}, $V_{2O,b}$, $V_{2O,c}$, O_i, AVOID, Al_O, and Al_i defects in stoichiometric sapphire using the CCCP method. A Fermi energy of 0 eV indicates the valence band maximum, while 8.6 eV indicates the conduction band minimum.

As is the case with the results for nonstoichiometric sapphire, the point defect with the lowest formation energy is the most likely to form. Unlike the constitutional defect method, however, there will be more than one dominant defect species, since a single species cannot maintain stoichiometry, and they will have a non-zero formation energy. From the data in Figure 28, the dominant point defects in stoichiometric sapphire are a combination of V_O, V_{Al}, and AVOID pairs, having formation energies of 5.64, 6.07, and 6.04 eV, respectively. These defects are within 0.43 eV in formation energy, and at high temperatures, can all form. The O_i and the $V_{2O,b}$ and $V_{2O,c}$ pairs have formation energies of 7.95, 9.52 eV, and 11.84 eV, respectively. Despite their higher formation energies, these defects can still be feasibly generated under very high temperature and irradiation exposure. The basal orientation of oxygen divacancy is more energetically favorable than the *c*-axis orientation. Furthermore, in forming a basal oxygen divacancy from a pair of isolated V_O, there is a net reduction in energy of 0.89 eV per vacancy, or a binding energy of 1.78 eV. The Al_O and Al_i have formation energies of 25.60 and 31.62 eV, respectively, which are considerably larger than any other point defect. These defects are not expected to easily form, even under extreme conditions.

Additionally, the formation energies of the point defects were calculated using the heat of formation method, with fixed chemical potentials. This is done using a method of linear interpolation between the nonstoichiometric limits to determine the elemental chemical potentials in sapphire. This method has been proposed by Torpo et al. [20] to study defects in the 4H-SiC system. Defect formation energies in an approximated stoichiometric sapphire are shown as a function of Fermi energy below, in Figure 29.

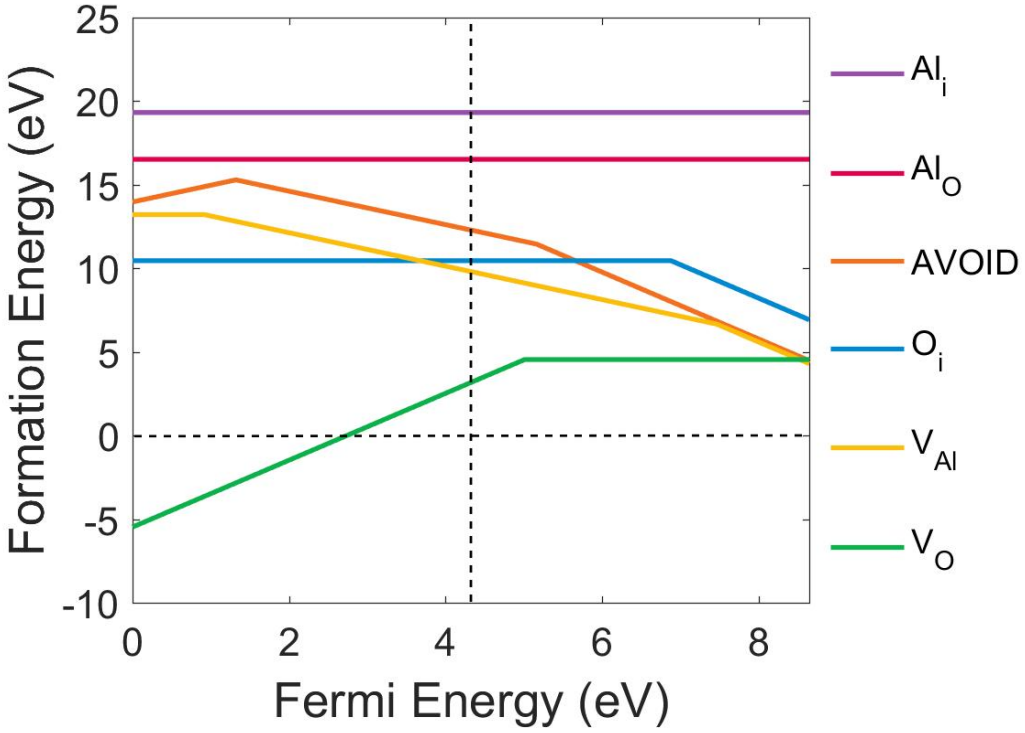

Figure 29. Formation energy as a function of Fermi energy for V_O, V_{Al}, O_i, AVOID, Al_O, and Al_i defects in stoichiometric sapphire using linear interpolation of the heat of formation method. A Fermi energy of 0 eV indicates the valence band maximum, while 8.6 eV indicates the conduction band minimum.

The V_O is shown to be the dominant defect in this case, with both orientations of the oxygen divacancy being the next likely to form. The V_{Al}, O_i, and AVOID pairs have moderately high formation energies with both the Al_O and Al_i having significantly higher formation energies. At mid-gap, all defect species have a positive formation energy, but moving towards the VBM, the formation energies of the oxygen vacancy and divacancies turn negative. Additionally, the dominant and other lower energy defect species can never combine to preserve stoichiometry. The oxygen vacancies and divacancies, when combined, can only contribute an oxygen deficiency in sapphire, making the material Al-rich.

The main difference between the CCCP and heat of formation methods are the elemental chemical potentials used. A comparison of the chemical potentials of O and Al as calculated by the CCCP and used in both the averaged "stoichiometric" and nonstoichiometric limiting heat of formation methods is shown below in Figure 30.

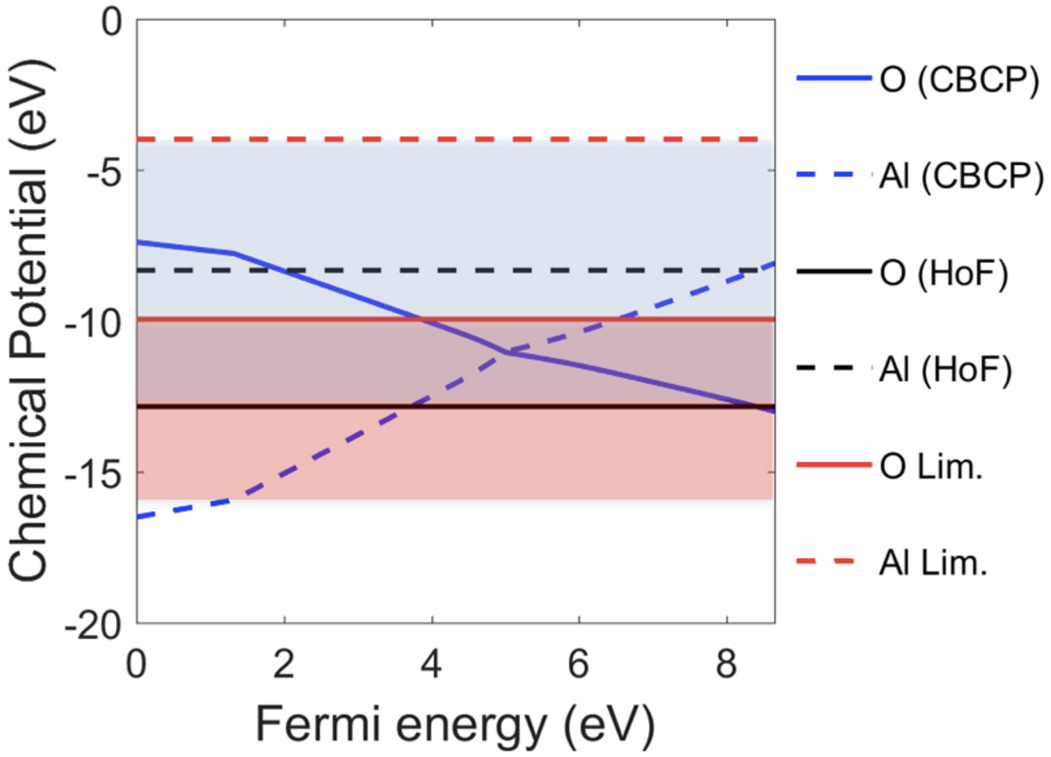

Figure 30. Calculated chemical potentials of oxygen and aluminum in sapphire from both the CCCP and heat of formation (HoF) methods.

Comparing the chemical potentials calculated using the CCCP method to the values used in both the O-rich and Al-rich limiting cases, it can be determined that that there is a significant range of Fermi energy ($0 < E_F < 3.8$ eV) where the CCCP chemical potential of oxygen is higher in energy than the O-rich limited value. This signifies that the energy per atom of oxygen in sapphire is higher than an atom of oxygen in its gas form, and that the oxygen would experience an energetic driving force to leave the material. Two interpretations are possible for this finding. First, it could mean that sapphire in the p-type range for $E_F < 3.8$ eV is indeed thermodynamically unstable, consistent with previous assumption. Second, it is evident that the energy per atom of aluminum in sapphire is significantly lower than that of bulk FCC aluminum. One could argue now that the trade-off could be dominated by the aluminum, which experiences a larger energetic driving to stay bonded in sapphire than the oxygen does to leave the material. What can be said in either case is that the averaged stoichiometric heat of formation method only agrees with the CCCP result for highly n-doped sapphire (Fig. 30).

Temperature-dependent formation free energies in stoichiometric sapphire were then calculated for the 6 point defects. Using DFT to calculate the formation energies of point defects is important for determining which defects will be the most likely to form, but this only holds true at 0 K. In order to understand the formation of point defects in high-temperature environments, the thermal lattice vibrations, or phonon frequencies must be calculated as well. Using the small displacement method in conjunction with the PHON code, the phonon frequency spectra for the

various defect structures were calculated, which were then used to calculate the Helmoltz free energies of those structures. These free energies were then combined with the 0 K defect formation energies above to calculate the formation free energies of the various defect species as a function of temperature. The formation free energies of all considered defects, except the Al_O, as a function of Fermi energy at 400, 600, 800, 1400, 1600, and 1800 K are shown below in Figures 31 – 36.

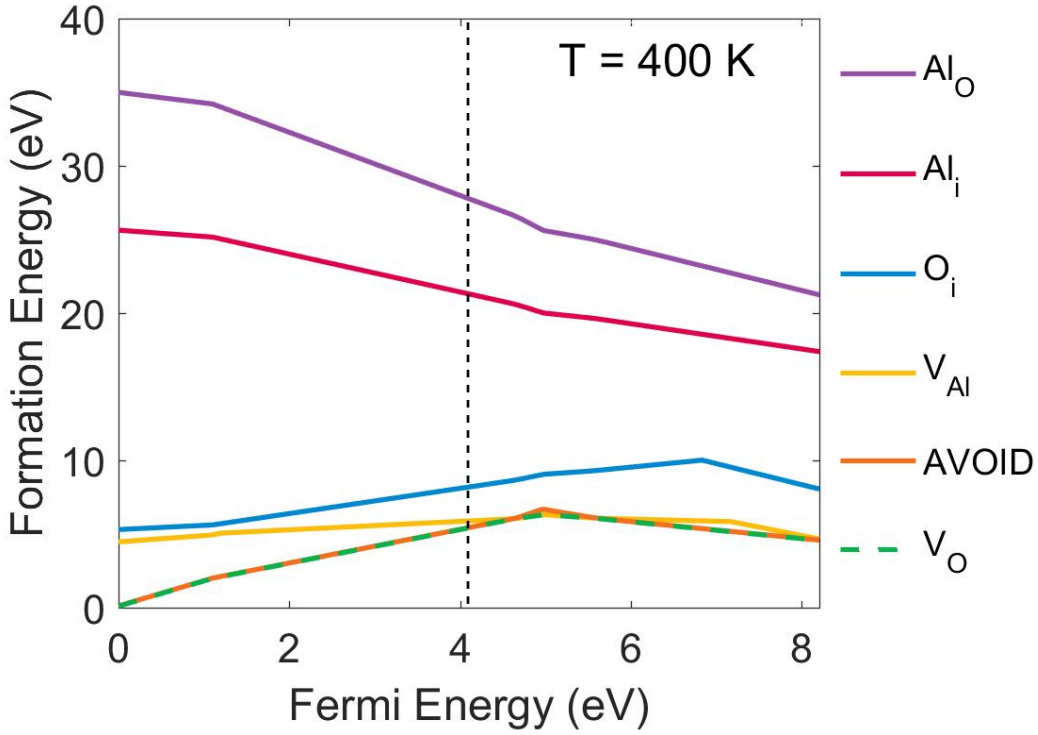

Figure 31. Formation free energy as a function of Fermi energy at 400 K for V_O, V_{Al}, $V_{2O,b}$, $V_{2O,c}$, O_i, AVOID, and Al_i defects in stoichiometric sapphire using the CCCP method. A Fermi energy of 0 eV indicates the valence band maximum, while 8.21 eV indicates the conduction band minimum.

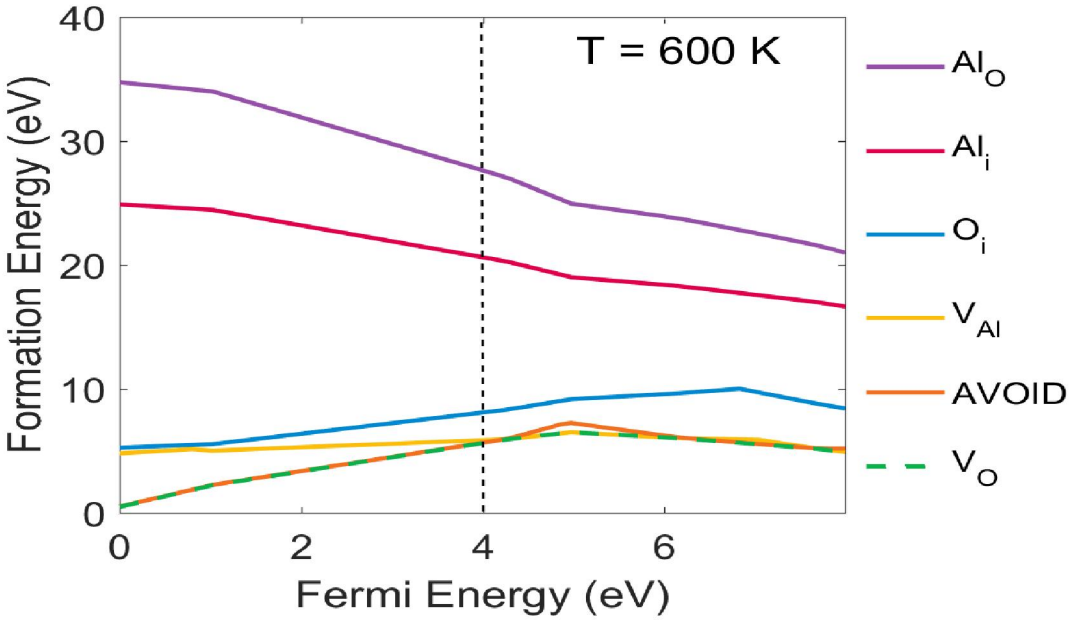

Figure 32. Formation free energy as a function of Fermi energy at 600 K for V_O, V_{Al}, $V_{20,b}$, $V_{20,c}$, O_i, AVOID, and Al_i defects in stoichiometric sapphire using the CCCP method. A Fermi energy of 0 eV indicates the valence band maximum, while 7.99 eV indicates the conduction band minimum.

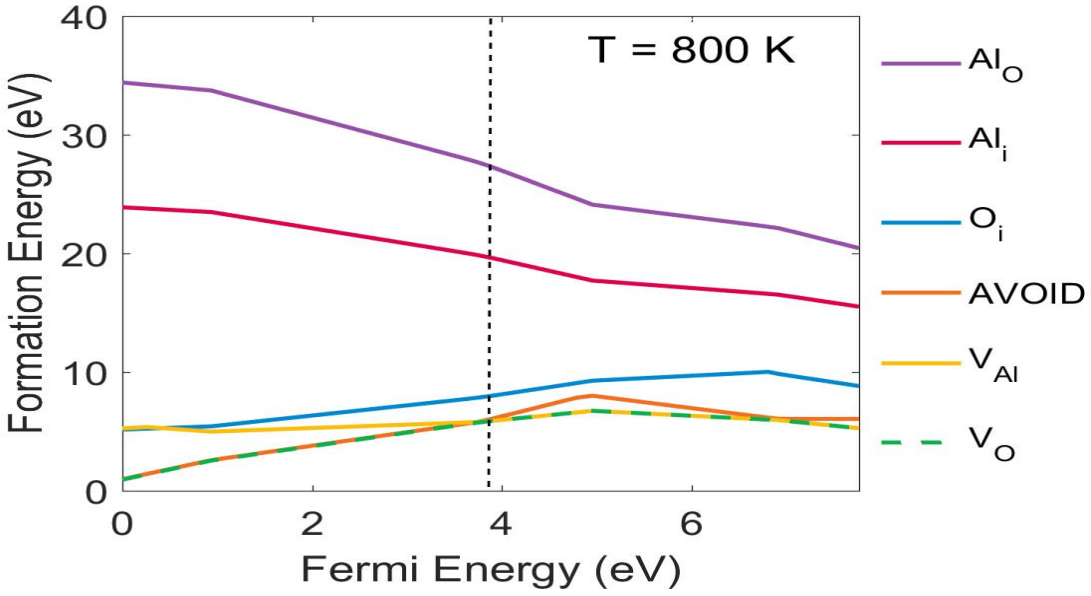

Figure 33. Formation free energy as a function of Fermi energy at 800 K for V_O, V_{Al}, $V_{20,b}$, $V_{20,c}$, O_i, AVOID, and Al_i defects in stoichiometric sapphire using the CCCP method. A Fermi energy of 0 eV indicates the valence band maximum, while 7.77 eV indicates the conduction band minimum.

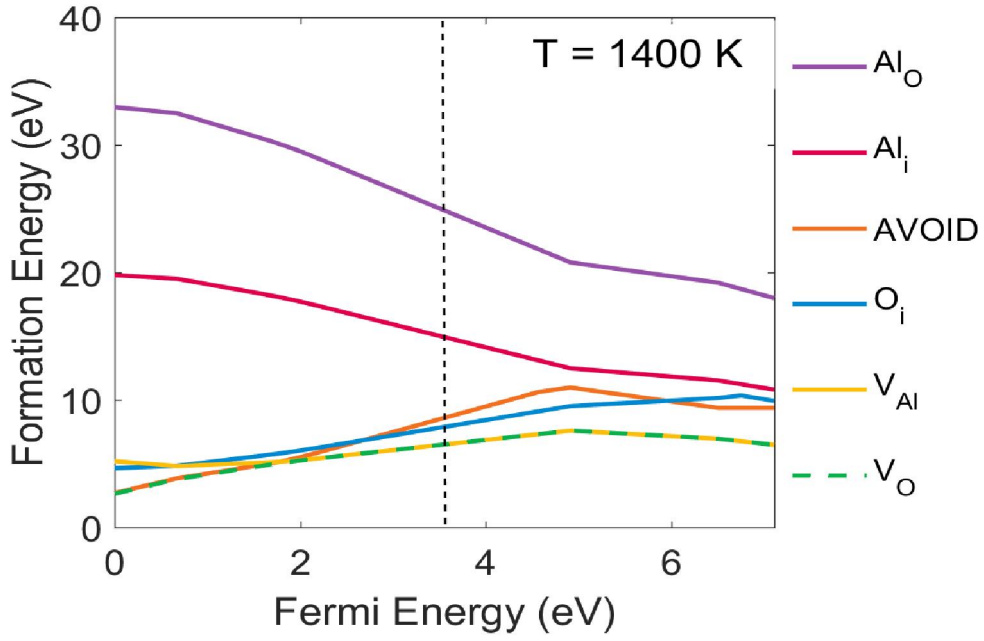

Figure 34. Formation free energy as a function of Fermi energy at 1400 K for V_O, V_{Al}, $V_{20,b}$, $V_{20,c}$, O_i, AVOID, and Al_i defects in stoichiometric sapphire using the CCCP method. A Fermi energy of 0 eV indicates the valence band maximum, while 7.11 eV indicates the conduction band minimum.

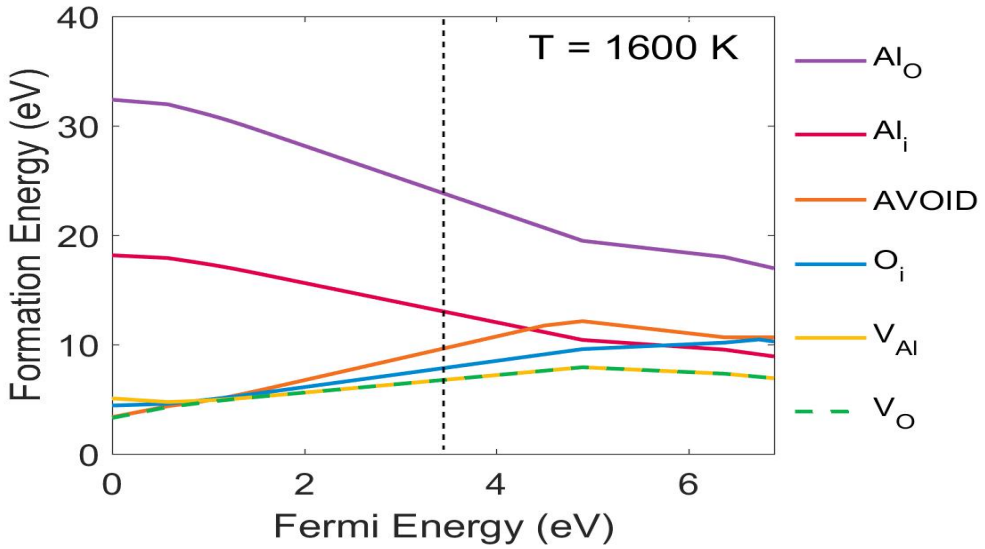

Figure 35. Formation free energy as a function of Fermi energy at 1600 K for V_O, V_{Al}, $V_{20,b}$, $V_{20,c}$, O_i, AVOID, and Al_i defects in stoichiometric sapphire using the CCCP method. A Fermi energy of 0 eV indicates the valence band maximum, while 6.88 eV indicates the conduction band minimum.

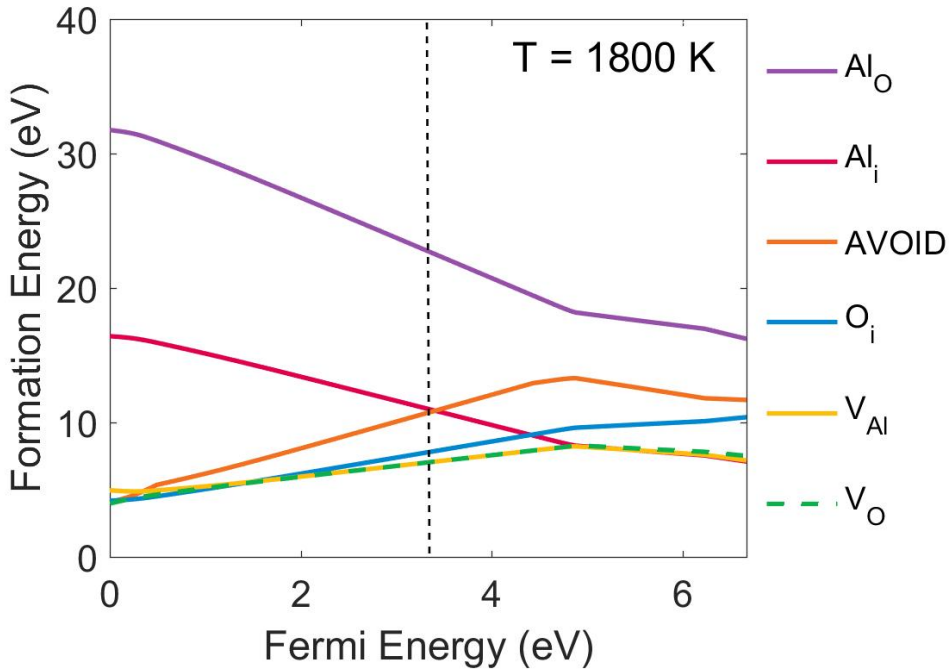

Figure 36. Formation free energy as a function of Fermi energy at 1800 K for V_O, V_{Al}, $V_{2O,b}$, $V_{2O,c}$, O_i, AVOID, and Al_i defects in stoichiometric sapphire using the CCCP method. A Fermi energy of 0 eV indicates the valence band maximum, while 6.66 eV indicates the conduction band minimum.

As is the case for the earlier results, the defects with the lowest formation free energy will be the most likely to form, and will be dominant in the material at that given temperature. From the data in Figures 31-36, the dominant defects up to 800 K are combinations of V_O and AVOID pairs. The V_{Al} is the next likely defect to form, with the oxygen interstitials being even less likely with moderately higher formation energies. Both the Al_i and Al_O are unlikely to form, having significantly higher formation energies. At 800 K, there is a third dominant defect introduced, having V_O, AVOID pairs, and V_{Al} all being dominant in a stoichiometric relation. Transitioning above 800 K, the dominant defects shift to being combinations of V_O and V_{Al}, with the formation energy of the AVOID pairs increasing. This behavior holds steady through 1800 K, with both the oxygen and aluminum interstitials becoming more stable due to decreasing formation energies. Around 1800 K, the Al_i becomes as favorable as the AVOID pair, while the Al_O remains the most energetically unfavorable point defect species.

The results DFT calculations used to produce the defect formation energies in sapphire were used as inputs into our diffusion-reaction rate model to determine the evolution of the defects as a function of temperature and location. Our diffusion-reaction modeling considers all possible diffusion and reaction events and combines them into a system of partial differential equations [21]. From our own calculations in the previous section, we determined the relevant defects to be oxygen vacancies (V_O), oxygen di-vacancy pairs (V_{O2}), oxygen interstitials (I_O), aluminum vacancies

(V_{Al}), and aluminum interstitials (I_{Al}). Aluminum antisite defects were determined to have an exceedingly high formation energy, and were therefore not included in the model. The differential equations used in our model can be broken down into four different terms. First, there is a diffusion term of the form $\nabla(D\nabla C)$, which applies to mobile defects, where D is the diffusivity of the specific defect in the bulk material and C is the concentration of the defect. The mobile species we consider are both types of vacancies and interstitials. The second term describes the effects of a first-order chemical reaction of the form $A + B \leftrightarrow C$, and is implemented by adding $K^r C_A C_B - K^f C_C$ to the right hand side of the differential equation. In the reaction term, K^r is the rate constant of the reverse reaction and K^f is the rate constant for the forward reaction. The third term describes the bimolecular recombination of interstitial and vacancy species, and is implemented by the operator $K^r(C_I C_V - C_I^* C_V^*)$, where C^* is the equilibrium concentration of a certain defect type in the bulk material. The fourth term is surface recombination term, and is discussed below. Including the first three terms, the following rate equations were considered:

$$\frac{dC_{\mathrm{V_{Al}}}}{dt} = \nabla\left(D_{\mathrm{V_{Al}}}\nabla C_{\mathrm{V_{Al}}}\right) + k_1^r\left(C_{\mathrm{V_{Al}}}C_{\mathrm{O_i}}\right) - k_1^f C_{\mathrm{AVOID}} - k_2^r\left(C_{\mathrm{AVOID}}C_{\mathrm{V_O}}\right) + k_2^f C_{\mathrm{V_{Al}}} - k_{\mathrm{Al}}^{bimole}\left(C_{\mathrm{V_{Al}}}C_{\mathrm{Al_i}} - C_{\mathrm{V_{Al}}}^* C_{\mathrm{Al_i}}^*\right)$$

$$\frac{dC_{\mathrm{V_O}}}{dt} = \nabla\left(D_{\mathrm{V_O}}\nabla C_{\mathrm{V_O}}\right) + k_3^r C_{\mathrm{V_O}}^2 - k_3^f C_{\mathrm{V_{2O}}} + k_2^r\left(C_{\mathrm{AVOID}}C_{\mathrm{V_O}}\right) - k_2^f C_{\mathrm{V_{Al}}} - k_{\mathrm{O}}^{bimole}\left(C_{\mathrm{V_O}}C_{\mathrm{O_i}} - C_{\mathrm{V_O}}^* C_{\mathrm{O_i}}^*\right)$$

$$\frac{dC_{\mathrm{Al_i}}}{dt} = \nabla\left(D_{\mathrm{Al_i}}\nabla C_{\mathrm{Al_i}}\right) + k_4^r\left(C_{\mathrm{AVOID}}C_{\mathrm{Al_i}}\right) - k_4^f C_{\mathrm{O_i}} - k_{\mathrm{Al}}^{bimole}\left(C_{\mathrm{V_{Al}}}C_{\mathrm{Al_i}} - C_{\mathrm{V_{Al}}}^* C_{\mathrm{Al_i}}^*\right)$$

$$\frac{dC_{\mathrm{O_i}}}{dt} = \nabla\left(D_{\mathrm{O_i}}\nabla C_{\mathrm{O_i}}\right) + k_1^r\left(C_{\mathrm{V_{Al}}}C_{\mathrm{O_i}}\right) - k_1^f C_{\mathrm{AVOID}} - k_4^r\left(C_{\mathrm{AVOID}}C_{\mathrm{Al_i}}\right) + k_4^f C_{\mathrm{O_i}} - k_{\mathrm{O}}^{bimole}\left(C_{\mathrm{V_O}}C_{\mathrm{O_i}} - C_{\mathrm{V_O}}^* C_{\mathrm{O_i}}^*\right)$$

$$\frac{dC_{\mathrm{AVOID}}}{dt} = -k_1^r\left(C_{\mathrm{V_{Al}}}C_{\mathrm{O_i}}\right) + k_1^f C_{\mathrm{AVOID}} + k_2^r\left(C_{\mathrm{AVOID}}C_{\mathrm{V_O}}\right) - k_2^f C_{\mathrm{V_{Al}}} + k_4^r\left(C_{\mathrm{AVOID}}C_{\mathrm{Al_i}}\right) - k_4^f C_{\mathrm{O_i}}$$

$$\frac{dC_{\mathrm{V_{2O}}}}{dt} = -k_3^r C_{\mathrm{V_O}}^2 + k_3^f C_{\mathrm{V_{2O}}}$$

The surface of the fiber acts as a potential sink for point defects in the material, and therefore acts to allow the concentration of defects to reach their equilibrium values as time approaches infinity. We implemented a fourth term into our rate equations to calculate the surface recombination flux for the mobile species, as explained in the ALAMODE manual [19]. This term was applied to all mobile defect species. The equation for the example of an oxygen vacancy reads:

$$-\vec{n}\cdot\frac{dC_{\mathrm{V_O}}}{dt} = -K_{\mathrm{V_O}}^{\mathrm{surf}}\left(C_{\mathrm{V_O}} - C_{\mathrm{V_O}}^*\right)$$

In order to solve this system of differential equations, our model required input data for the formation energies of the defect species, diffusivities of those species in sapphire, initial concentrations of those defect species, and the migration energies of the mobile defect species. Defect formation energies for each of the species included in our model were supplied by our first principles calculation in the previous section for single point defects in sapphire. The diffusivities of the defect species were approximated by a Debye temperature scaling method that related the known diffusivities of species in silicon to those in sapphire. As described above, initial defect concentrations after fast-neutron irradiation were determined from the data in Figure 23. Migration energies were gathered for both species of interstitials and vacancies, per the results of Hine et. all [22].

The defect concentration profiles for the O_i, V_{Al}, V_O, AVOID pairs, and V_{2O} were determined for both nonstoichiometric limits in sapphire after an hour long anneal at 1327°C (1800 K). The defect formation energy values for the O-rich and Al-rich cases were taken from the constitutional defect methods. Plots of defect concentration as a function of position in the 100 μm sapphire fiber are shown below in Figures 37 and 38 for the O-rich and Al-rich cases, respectively. A radial position of zero represents the center of the sapphire fiber.

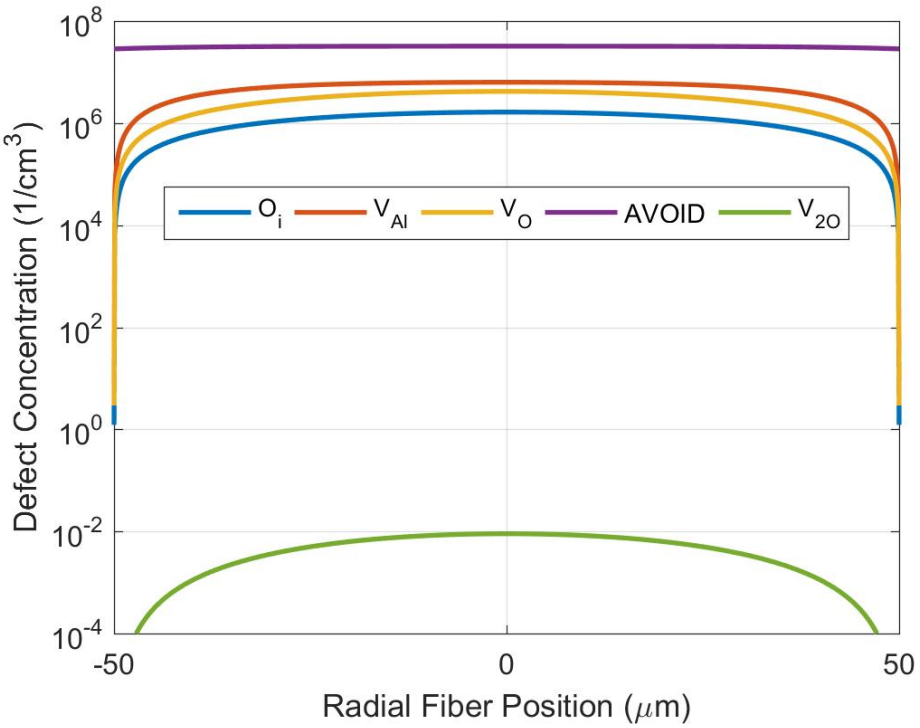

Figure 37. Calculated concentrations of defects in O-rich sapphire, as a function of radial position in the fiber, after annealing at 1327 °C (1800 K) for 1 hour. Annealing starts after initial fast-neutron irradiation for 8 hours, and includes constant generation of Frenkel defect pairs.

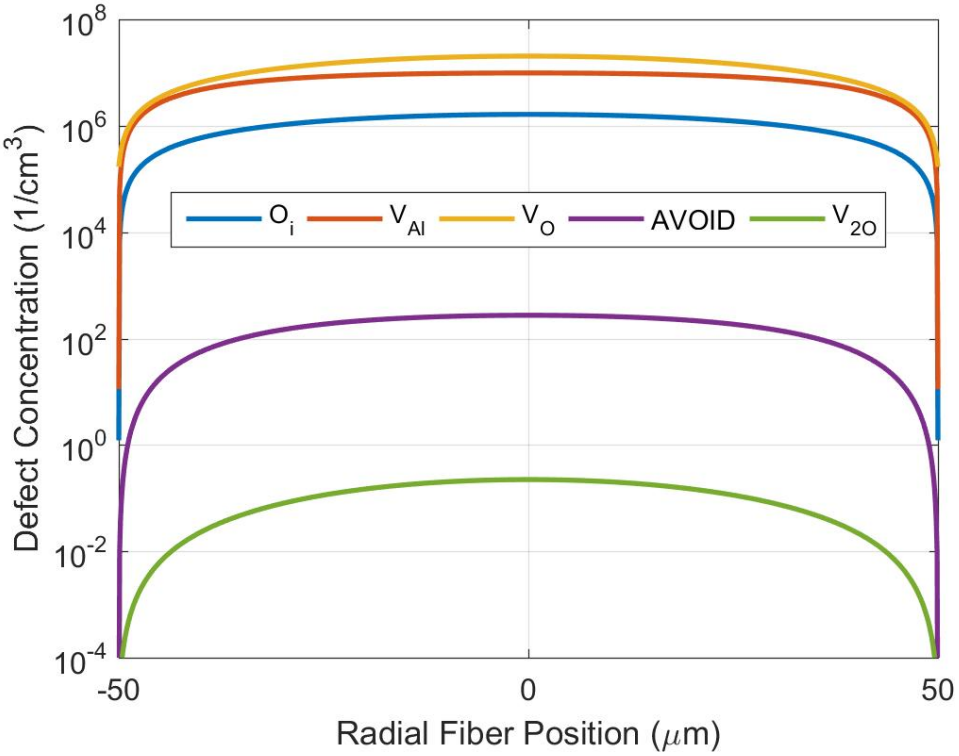

Figure 38. Calculated concentrations of defects in Al-rich sapphire, as a function of radial position in the fiber, after annealing at 1327 °C (1800 K) for 1 hour. Annealing starts after initial fast-neutron irradiation for 8 hours, and includes constant generation of Frenkel defect pairs.

The O-rich case shows the AVOID pairs being the most prevalent throughout the fiber cross-section, with a concentration of $3.21 \cdot 10^7$ 1/cm^3. The V_{Al}, V_O, and O_i are present in appreciable amounts showing concentrations of $6.31 \cdot 10^6$, $4.18 \cdot 10^6$, and $1.64 \cdot 10^6$ 1/cm^3 at the center of the fiber. Their concentrations profiles decrease towards the fiber surface, indicative of surface recombination. The V_{2O} is also present, but at negligible concentration. The dominant AVOID pairs introduce both and aluminum deficiency and an oxygen surplus to the material, confirming that the data represents an O-rich limiting case.

For the Al-rich case, the V_O is the most present defect species near the center of the fiber cross-section, with a concentration of $2.04 \cdot 10^7$ 1/cm^3. The V_{Al} and O_i are present in appreciable amounts showing concentrations of $9.84 \cdot 10^6$ and $1.64 \cdot 10^6$ 1/cm^3 at the center of the fiber. These three defect species have concentration profiles that decrease as they approach the fiber surface, and as they decrease, the V_O becomes less and less dominant. The V_{2O} is also present, but at negligible concentration. The dominant V_O introduces an oxygen deficiency to the material, but the combination of V_{Al} and O_i act to balance stoichiometry. The data above shows a ratio of missing oxygen atoms to aluminum atoms of 1.91, well over the stoichiometric value of 1.5, confirming that the data represents an Al-rich limiting case.

Defect concentration profiles were also calculated for the considered species in stoichiometric sapphire. Since these calculations are performed at a finite temperature, the temperature-dependent defect formation free energies were used as inputs for the stoichiometric case. A plot of the defect concentration profiles as a function of radial fiber position after an anneal at 1327 °C (1800 K) for 1 hour are shown below in Figure 39.

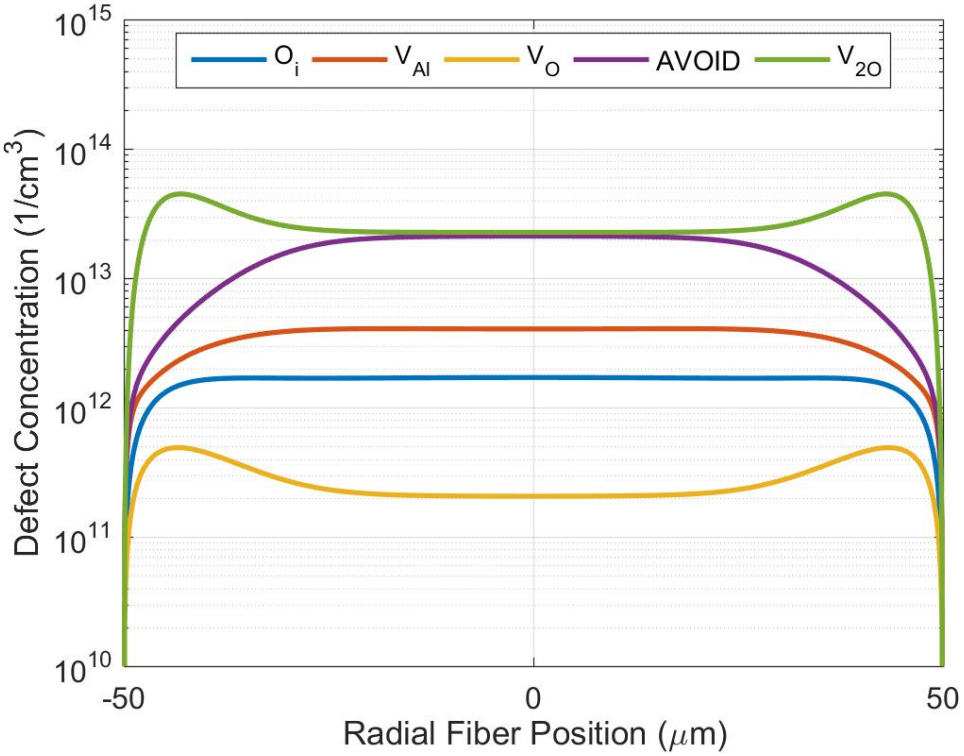

Figure 39. Calculated concentrations of defects present, as a function of radial position in the fiber, after annealing at 1327 °C (1800 K) for 1 hour. Annealing starts after initial fast-neutron irradiation for 8 hours, and includes constant generation of Frenkel defect pairs.

The data shows that both the V_{2O} and AVOID pairs are the most present species with concentrations of $2.26 \cdot 10^{13}$ and $2.11 \cdot 10^{13}$ $1/cm^3$ at the center of the fiber. While not as prevalent, the V_{Al}, O_i, and V_O are also present with concentrations of $4.05 \cdot 10^{12}$, $1.70 \cdot 10^{12}$, and $2.06 \cdot 10^{11}$ $1/cm^3$ at the center of the fiber. The concentration profiles of all defects follow the boundary conditions and tail off to the equilibrium concentration values at the fiber surface, but the oxygen vacancies and divacancy pairs exhibit an increase in concentration before this occurs. The peaks in concentration show that both the V_O and V_{2O} pairs actively migrate towards the surface of the fiber. A better understanding of this behavior could be gained by adapting the model to include a free boundary condition, where the concentration profiles are not constrained to their equilibrium values.

In conclusion, a rate theory modeling approach was described and used to calculate the evolution of the concentrations of various point defects in sapphire both as a function of temperature and spatial position in circular fiber cross-section. The formation energies and free energies presented in the previous section were used to calculate the concentration profiles of point defects in O-rich, Al-rich, and stoichiometric sapphire. The defect formation energies calculated using the constitutional defect method were used in the rate theory model to calculate the concentration profiles of the defects in O-rich and Al-rich sapphire after a thermal anneal at 1327°C (1800 K) for 1 hour. For the O-rich case, AVOID pairs have the highest concentration throughout the entire fiber cross-section, with Vo, V_{Al}, and O_i present in moderate concentrations, by comparison. The V_{2O} pairs are present, but at significantly lower concentrations. Shifting to the Al-rich case, the V_O is present in the highest concentration, followed closely by the V_{Al}. The O_i is present in a moderate concentration, while both the AVOID and V_{2O} pairs have significantly lower concentrations.

The defect formation free energies calculated using the CBCP method were used to accurately inform the calculation of concentration profiles of point defects in stoichiometric sapphire after a thermal anneal at 1327°C (1800 K) for 1 hour. Both the V_{2O} and AVOID pairs have the highest concentration through most of the fiber cross-section, with the V_{Al}, O_i, and V_O being present a lower, moderate levels. The oxygen vacancies and divcancy pairs exhibit a strong migration towards the surface, as evidenced by the peaks in concentration for both defects moving away from the center of the fiber cross-section. Such behavior could result in local changes in optical absorption near the surface of sapphire fibers operating at high temperature

Chapter 5. Task D - Predictive Optical Attenuation Modeling

5.1 Deliverables

- Optical properties of the various defects in sapphire
- A predictive model for the broadband optical attenuation as a function of irradiation time and temperature

5.2 Timeline and Task Status

- Start Date: 4/1/2014
- Planned Completion Date: 12/30/2015
- Task Status: 100%

5.3 Progress Toward the Completion of Deliverables

5.3.1 Optical Properties of the Various Defects in Sapphire

The last part of our sapphire optical modeling consists of determining the optical light attenuation in a sapphire fiber due to defects in the crystal lattice. Radiation bombardment can cause a change in the charge state of existing point defects, and create entirely new point defects in sapphire. Both of these outcomes can result in the shifting of appearance of trap states within the bandgap. With the change in or addition trap states in a fiber optic material under operating conditions; the device can experience an increase in light attenuation to and including the point of complete failure. To ensure that a sapphire fiber optic material is valid for use in a nuclear reactor environment, the change in optical absorption attributed to single point defects must be determined. Experimental procedures were implemented in the next section (section 7) to empirically determine the broadband absorption spectra associated with sapphire fiber in high temperature, radiation environments. Unfortunately, these techniques are not able to explicitly determine the contribution of individual point defect species. With the use of DFT (Density Functional Theory), the absorption spectra associated with the formation of a single point defect can be calculated. The spectra of all considered defects in the sapphire system can then be combined with the defect concentration data calculated using rate theory to determine the added absorption as a function of irradiation, temperature, and time.

The optical absorption of a structure can be calculating using DFT techniques. In VASP, this is called using the LOPTICS flag [23]. Turning this flag on enables the program to calculate the frequency-dependent dielectric function for the input structure. First, the imaginary portion of the dielectric function, ε_i, is calculated using a mathematical summation over the empty conduction band states in the electronic structure of the material. Using ε_i in conjunction with a mathematical transformation, the real portion of the dielectric function, ε_r, is calculated [24]. For these calculations to be accurate, the total number of bands included in the calculation must be significantly increased. Additionally, the subdivision of the energy, and therefore frequency, calculation grid must be especially fine. With both ε_i and ε_r calculated, the optical absorption coefficient, $\alpha(\lambda)$, can be calculated using the following equation:

$$\alpha(\lambda) = \frac{4\pi}{\lambda}\sqrt{\frac{\sqrt{\varepsilon_r^2 + \varepsilon_i^2} - \varepsilon_r}{2}}$$

where λ represents wavelength. This quantity can be used to determine the added optical attenuation, or loss of transmitted light intensity, along a sapphire optical fiber. In sapphire, attenuation of light can occur due to scattering and absorption effects. Considering two points along a sapphire optical fiber, 1 and 2, a length L apart, the optical attenuation per unit length A can be defined as

$$A(\lambda) = \frac{-10\log\frac{I_2(\lambda)}{I_1(\lambda)}}{L}$$

where $I_1(\lambda)$ and $I_2(\lambda)$ are the intensities of transmitted light at points 1 and 2, respectively. The optical attenuation gives a measure of signal loss as function of wavelength in units of dB per unit length. The optical attenuation can then be related to the absorption coefficient, using the relation

$$\frac{I_2(\lambda)}{I_1(\lambda)} = e^{-\alpha(\lambda)L}$$

The equations above can be combined to give a direct relationship between $A(\lambda)$ and $\alpha(\lambda)$, defined as

$$A(\lambda) = \frac{10}{\ln(10)}\alpha(\lambda)$$

This model focuses on the optical absorption attributed with the considered point defect species, and does not take thermal scattering effects into account. DFT calculations were again carried out using VASP for each of the considered point defect species. For the optical calculations, the energetics calculations consisted of a single point defect embedded in 270 atoms of sapphire. HSE hybrid functional mixing was also again employed to assure an accurate description of the electronic structure of the material. The frequency-dielectric function was calculated for each defect species, and from these data, both the optical absorption coefficient and attenuation spectra for each point defect species were calculated.

Attenuation spectra was calculated for both the perfect sapphire crystal, and for the V_O, V_{Al}, $V_{2O,c}$, $V_{2O,b}$, O_i, and AVOID pair defects. Both the Al_O and Al_i were not included due to their high formation free energies over a broad temperature range. In order to understand the changes in attenuation caused by each of the defect species, the added attenuation, or difference in attenuation between the defect and perfect cells, was calculated. Any non-zero value of added attenuation indicates a contribution from the point defect, while zero added attenuation refers to the intrinsic attenuation of the sapphire crystal. In Figures 40-45, below, the added attenuation is shown as a function of wavelength. The data sets have been scaled relative to one another, for comparison purposes, and only the stable charge states are included.

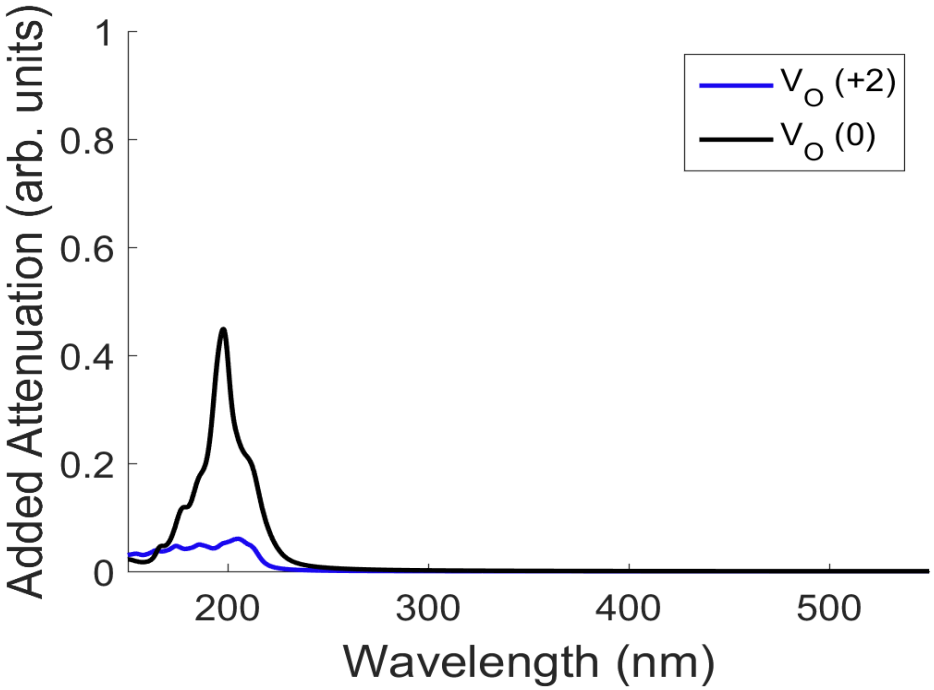

Figure 40. Added attenuation spectra, in arbitrary units, as a function of wavelength for +2 and neutral oxygen vacancies in sapphire.

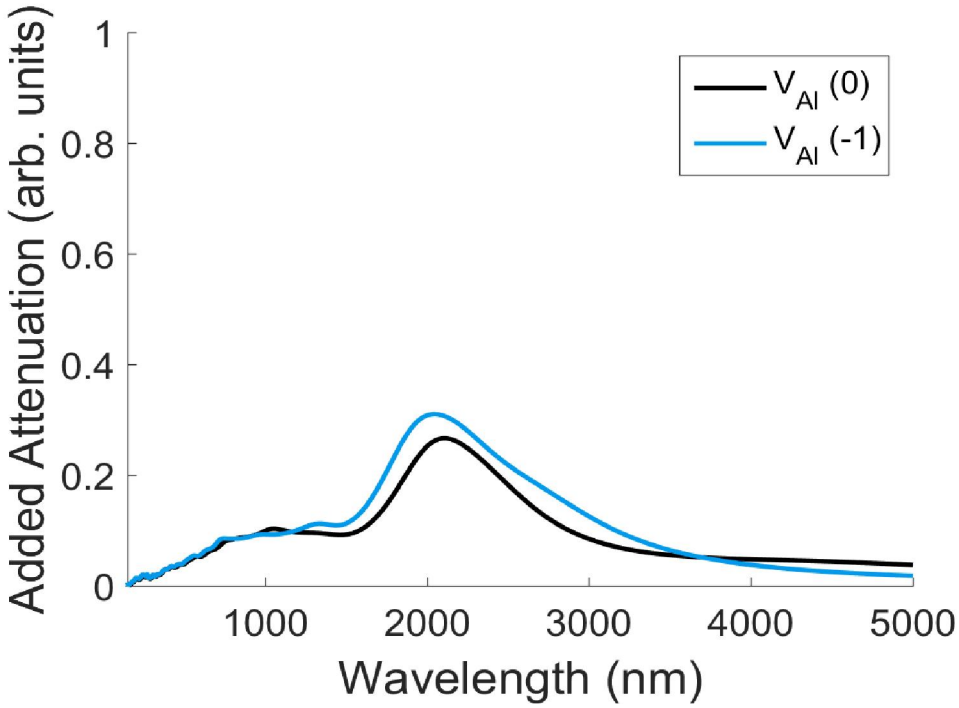

Figure 41. Added attenuation spectra, in arbitrary units, as a function of wavelength for neutral and -1 charged aluminum vacancies in sapphire. The extended wavelength range is to show the unique region of optical activity.

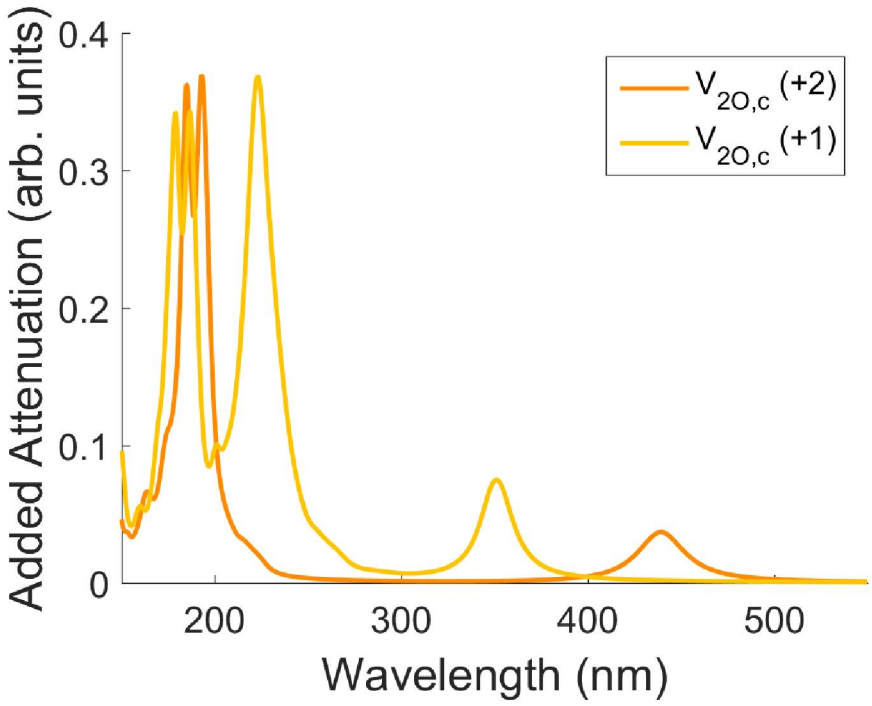

Figure 42. Added attenuation spectra, in arbitrary units, as a function of wavelength for +2 and +1 charged c-axis oriented oxygen divacancies in sapphire.

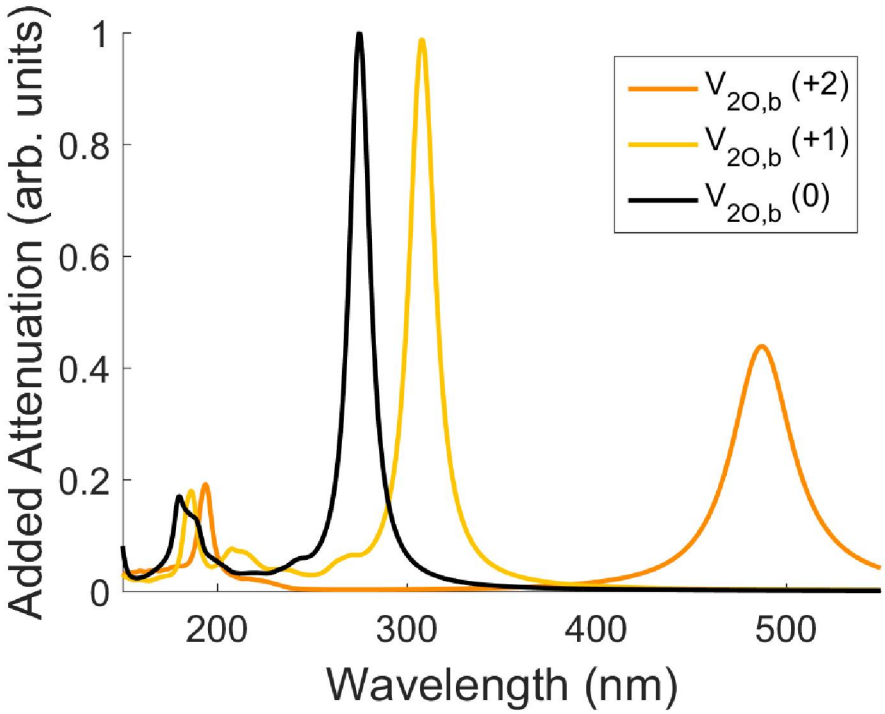

Figure 43. Added attenuation spectra, in arbitrary units, as a function of wavelength for +2 , +1 charged, and neutral basal oriented oxygen divacancies in sapphire.

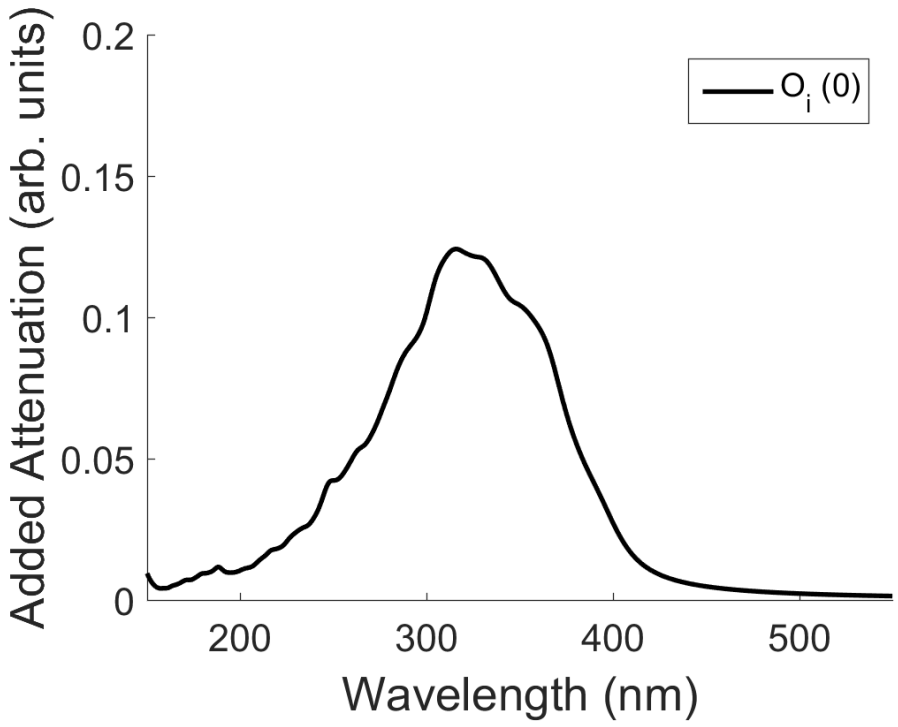

Figure 44. Added attenuation spectra, in arbitrary units, as a function of wavelength for neutral oxygen interstitials in sapphire.

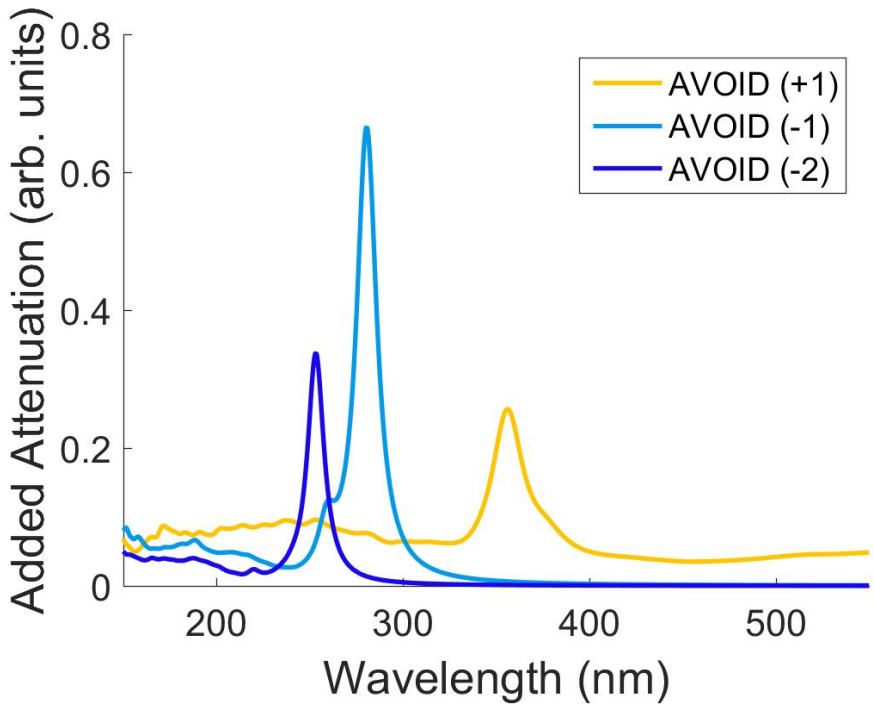

Figure 45. Added attenuation spectra, in arbitrary units, as a function of wavelength for +1, -1, and -2 charged AVOID pairs in sapphire.

The attenuation spectra show that all the considered defects, except for the V_{Al}, are optically active in the ultraviolet (UV) to low-visible wavelength range. The V_{Al} does not contribute much to the optical attenuation in this region, but both charge states do gradually increase, showing a peak in attenuation in the infrared (IR) near 2000 nm. The neutral charge state of V_O shows a discreet peak in attenuation at 198 nm, while the +2 state shows a broader, smaller increase in attenuation near the same position. The less stable +1 charge state, which is not shown here, was calculated to have a broad, double-crested peak with local maxima at 238 and 262 nm. Experimental results have shown peaks near 203-205 nm [25-27] for the neutral V_O, or F center, and peaks near 225-232 nm [25-26,28] and 258-260 nm [25-28] for the +1 charge state of V_O,, or F^+ center. The calculated data here compares extremely well with experimental data in the following section, giving validation to the results of defects previously undiscovered.

The $V_{2O,c}$ shows discreet peaks in added attenuation located at 179, 187, 223, and 351 nm for the +1 charge state, and at 185, 193, and 438 nm for the +2 charge state. The double-crested peaks between 179 and 193 nm are exhibited by both the +1 and +2 charge states, with a slight offset. Comparatively, the $V_{2O,b}$ shows discreet peaks of much larger magnitude, the largest of all considered point defects. The neutral state shows a large, discreet peak at 275 nm and a smaller, wider peak near 180 nm. The +1 charge state shows sharp peaks at 186 and 307 nm and a small, broad peak near 200 nm, while the +2 charge state shows sharp peaks at 194 and 488 nm. Both orientations of divacancy show peaks clustered near 200 and 450 nm, but the c-axis orientation shows larger magnitude peaks at lower wavelengths, while the basal orientation show larger magnitude peaks at higher wavelengths in the near-UV region. Experimental studies have shown absorption peaks at 300 nm [26-27] for the neutral oxygen divacancy, 355-379 nm [26-27,29] for the +1 charge state, and 450-550 nm [26-27, 29] for the +2 charge state. These studies have not attributed and peaks lower than 300 nm to the oxygen divacancy, but the calculated data here matches well with the higher wavelength peaks.

The neutral O_i shows a comparatively small and broad peak in attenuation centered near 325 nm, while the AVOID pairs show discreet peaks at 253, 280, and 356 nm attributed to the -2, -1, and +1 charge states, respectively. The 280 nm peak is the highest in magnitude, and has a smaller peak incorporated into its tail near 260 nm.

5.3.2 A Predictive Model for the Broadband Optical Attenuation

By summing the individual point defect added attenuation spectra, and normalizing this data against the concentration profiles presented in our previous reactor damage model (section 3), the full defect added attenuation spectra can be calculated as a function of temperature. Using the concentration values at the center of the fiber cross-section and the spectra presented in the previous section, total defect attenuation spectra were calculated at 800, 1400, 1600, 1800, and 2000 K. Figure 46 shows this spectra over a broadband range of 150-3000 nm, while Figure 47 shows the total spectra in the near-visible to IR range of 800-2000 nm. The range in Figure 47 highlights wavelengths that are commonly used in telecommunications.

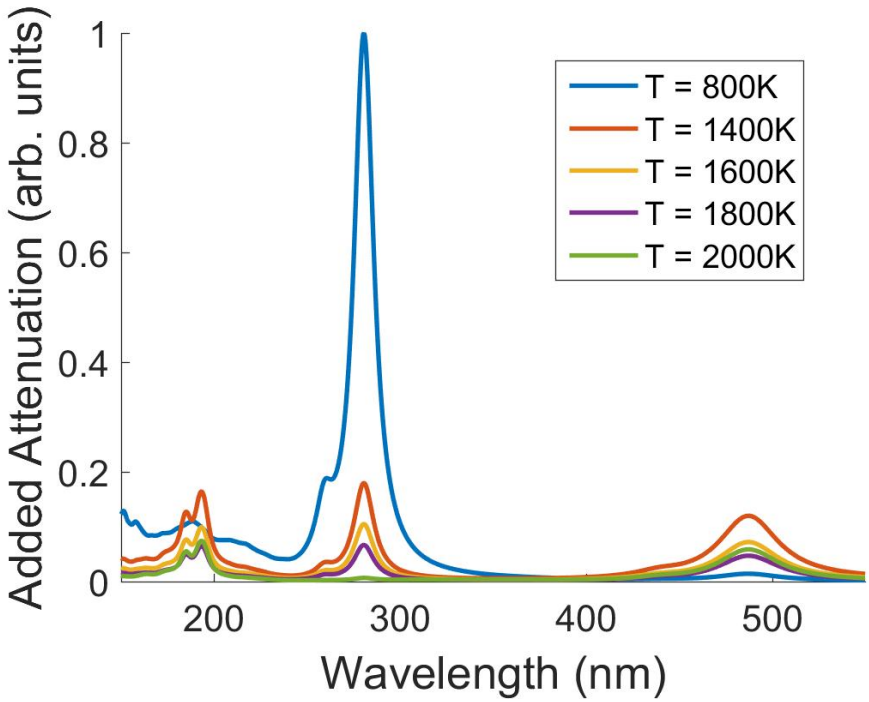

Figure 46. Added attenuation spectra for all point defects in sapphire, in arbitrary units, as a function of wavelength from 150-3000 nm at 800, 1400, 1600, 1800, and 2000 K.

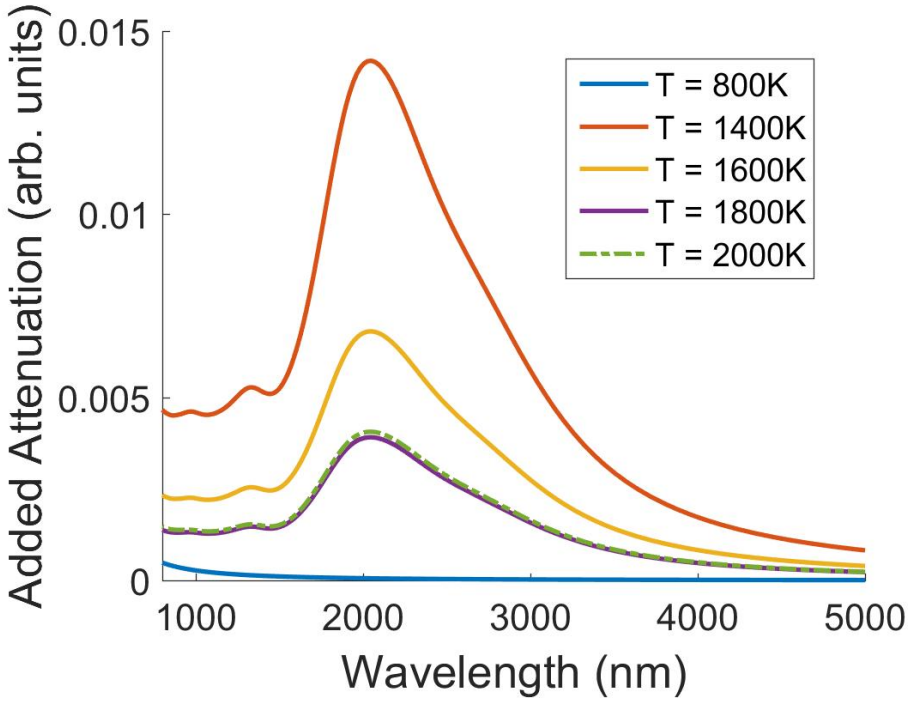

Figure 47. Added attenuation spectra for all point defects in sapphire, in arbitrary units, as a function of wavelength from 800-2000 nm at 800, 1400, 1600, 1800, and 2000 K.

The broadband spectra shows that the point defects are optically active mostly in the UV to low-visible range, with a large, sharp peak at 356 nm arising from a combination of the +2 $V_{2O,b}$ and +1 AVOID pair attenuation peaks. There are also smaller, less defined peaks near 187 and 280 nm. In the IR, a single peak centered near 2050 nm is present, and can be attributed to a combination of the tails of the +2 $V_{2O,b}$ and +1 AVOID pairs and the broad peak of the V_{Al}. The data also shows a temperature dependence on the defect added attenuation. As the temperature increases, the added attenuation attributes to the point defects decreases, indicating increasing annihilation and recombination of point defects due to thermal annealing. Large increases in added attenuation have been observed in heated sapphire at temperatures above 1300°C, with a more dramatic increase at and above 1500°C (see section 7). This data, however, shows a decrease in added attenuation due to absorption at point defect centers at higher and higher temperature. At these temperatures, the dominant defect species are changing. Also, all optical effects calculated in this work take only optical absorption into account. Increasing the scope of this research to include thermal scattering effects on the added attenuation could shed more light on this issue.

In conclusion, DFT calculations were used to calculate the optical absorption and added attenuation spectra attributed to single point defects in sapphire. Added attenuation spectra as a function of wavelength showed that all point defects are optically active in the UV to low-visible wavelength range, with the exception of the V_{Al}, which is active in the IR. The $V_{2O,b}$ and AVOID pairs showed the largest magnitude peaks in added attenuation, with the V_O, $V_{2O,c,}$ and V_{Al} showing peaks roughly a quarter to a half those values. The O_i exhibited a very weak, broad peak in added attenuation, and is not considered to contribute to loss in an operating fiber.

Additionally, the defect concentration profiles presented in our radiation damage evolution model (section 4) were used to calculate the added attenuation spectra of point defects in sapphire as a function of temperature. Full defect added attenuation spectra showed two main regions of optical activity. The first region is in the UV to low-visible range, with a large, sharp peak in attenuation at 280 nm. This peak is attributed to the combined effects of the +2 $V_{2O,b}$ and the +1 AVOID pairs. There are additional peaks of much lower magnitude centered near 187 and 475 nm. The second active region is in the IR, where a single peak is centered near 1300 nm. The tails of the individual +2 $V_{2O,b}$ and +1 AVOID pair peaks combined with the broad V_{Al} peak combine to account for the activity in the IR. A general trend is shown between decreasing added attenuation and increasing temperature, which is indicative of point defect annihilation and recombination from thermal annealing effects. The experimental results of the sapphire optical absorption spectra will be shown in the following sections (section 7) and our modeling results from this section can be used to determine the various optical spectra seen in the sapphire from high temperatures and radiation.

Chapter 6. Task E - Design and Fabrication of High Temperature Irradiation Furnaces

6.1 Deliverables

- A high temperature, low-activation furnace suitable for operation in the OSURR at temperatures up to 1600 °C
- A high temperature furnace suitable for operation in the OSU Co-60 gamma irradiator at temperatures up to 1000 °C

6.2 Timeline and Task Status

- Start Date: 9/15/2012
- Planned Completion Date: 9/30/2013
- Task Status: 100%

6.3 Progress Toward the Completion of Deliverables

6.3.1 A High Temperature, Low-Activation Furnace Suitable for Operation in the OSURR at Temperatures up to 1600 °C

In order to perform high temperature (1600 °C) reactor irradiations of sapphire fibers, we need a furnace that is capable of operating at these high temperatures, fits in the geometry of the 7 inch dry tube facility of the OSURR, and would have minimal neutron activation following use in the reactor facility. At the start of this project, we had a tube furnace from Micropyretic Heater International (MHI), Inc. that could be operated up to 1600 °C. This furnace consisted of a molybdenum disilicide heating element coiled around the 1 inch inner diameter of a right circular cylindrical annulus of a refractory ceramic insulation with an outer diameter of 5.25 inches and a total length of 14.5 inches. The actively heated region of the furnace is 12 inches in length. The furnace required several modifications in order to be used for high temperature irradiations of sapphire fibers. The modifications that were required are summarized in Table 6. A CAD drawing and a labeled photograph of the furnace and the rig that holds the furnace after the modifications have been made can be found in Figure 1 and Figure 2, respectively, in section 2.3.1.

Table 6: Required modifications to the MHI furnace it could be used for high temperature irradiations of sapphire fibers inside the 7 inch dry tube facility of the OSURR.

Modification Number	Description
1	Electrical connections required modification in order to fit the furnace inside the 7 inch dry tube facility
2	A thermocouple assembly needed to be fabricated in order to fit inside the 7 inch dry tube facility and monitor the temperature at several points inside the furnace (as opposed to just a single point)
3	New cap insulation pieces were required to reduce axial heat losses and allow penetrations for fibers and thermocouples

4	Steel band clamps, plates, and electrical clips required replacement with materials that would become quite so radioactive following irradiation
5	Fibrous insulation surrounding the furnace needed to be contained because it could become a source of airborne contamination if radioactive
6	A bend guide was required below the furnace to guide the sapphire fibers around a 180 degree bend at a sufficiently large bend radius

Most of these modifications were relatively straight-forward, and do not require much explanation. For example, in order to prevent the fibrous insulation of the furnace from becoming a source of airborne contamination once it becomes radioactive, the furnace was wrapped in high purity aluminum foil. Custom 1 inch thick alumina-silica based cap insulation pieces with penetrations for fibers and thermocouples were ordered from Zircar Ceramics, Inc. All steel components (band clamps, plates and electrical clips) were replaced with equivalent titanium components. The titanium sheets (ordred from OnlineMetals.com) have identical geometry to the steel plates that were replaced. The steel band clamps (purchased from Mabor Industrial Inc.) were replaced with titanium band and buckle systems, similar to those that are used for strapping street signs to metal poles. Commercially available titanium clips were purchased from Servi-Sure Corporation. A tear drop-shaped bend guide was fabricated by bending a small diameter aluminum rod in order to guide the sapphire fibers around a 180 degree bend below the furnace. The bend guide was shaped such that the fibers are bent at a radius no less than 2 inches, which is the minimum bend radius recommended for long-term optical fiber use by the ASTM E1614-94 standard. Each of these modifications (except for the bend guide) can be seen in Figure 2 of section 2.3.1.

Electrical connections for the MHI furnace were previously mounted to an aluminum plate above the furnace and they protruded outward from the outer diameter of the aluminum plate. With this mounting, the electrical connections would prevent the furnace from fitting inside of the 7 inch aluminum dry tube facility. New electrical connections were fabricated using two commercially available dual wire aluminum set screw lugs. The lugs were mounted to the aluminum plate above the furnace using threaded ceramic insulators. The lugs were mounted inside the outer diameter of the plug with a vertical orientation. The mounting of the new electrical connections can also be seen in Figure 2 of section 2.3.1.

A custom thermocouple assembly was fabricated in order to replace the original thermocouple used with the MHI furnace, which was inserted radially from the side of the furnace and would not allow the furnace to fit inside the 7 inch dry tube of the OSURR. The new thermocouple assembly contains three B-type thermocouples, which allows one to monitor the temperature inside the furnace at three axial locations. A labeled picture of the thermocouple assembly is shown in Figure 48. The heated region of the thermocouple wires are insulated with 1 inch length two-hole alumina ceramic insulators. Above the heated region the thermocouples are insulated with silica braided insulation. The heated portion of the thermocouple wires are inserted into a protective alumina ceramic tube. The thermocouple wires are attached to three thermocouple connectors at the top of the thermocouple assembly. The three connectors are joined together with extended-length nuts and bolts. The center connector clamps down on an aluminum tube, which is press fit into a larger diameter aluminum tube that is joined to the protective alumina tube with shrink tubing with Nextel packing on the inside.

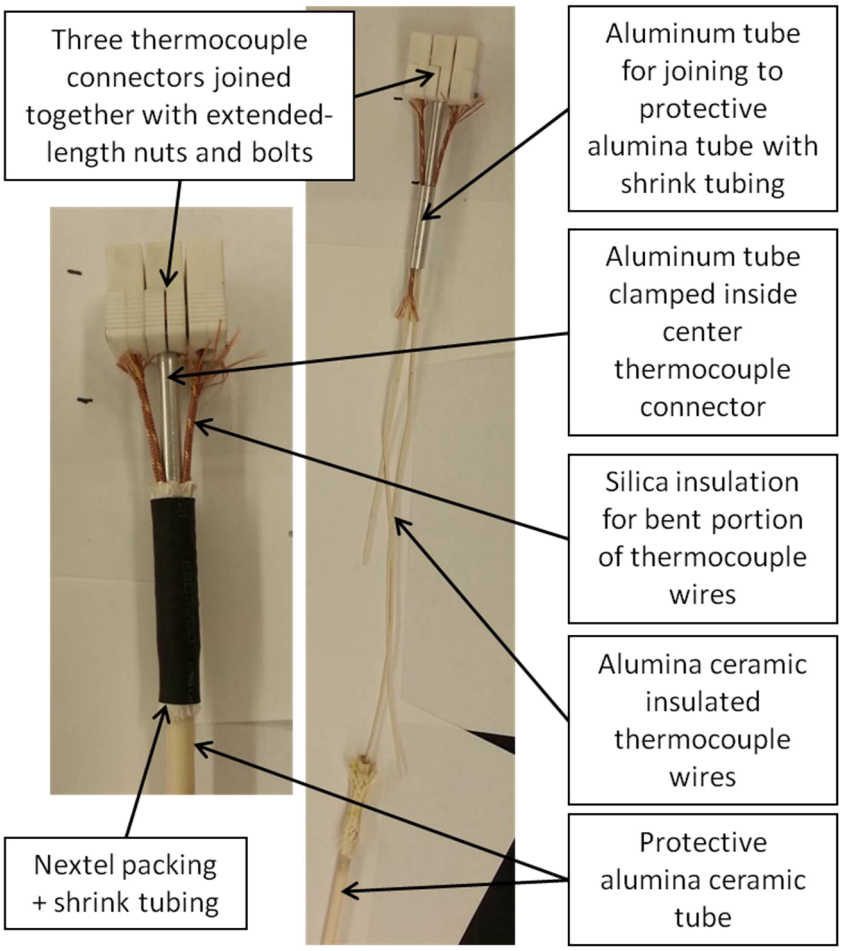

Figure 48: Labeled picture of the custom fabricated thermocouple assembly.

One of the three thermocouples located inside the protective tube of the thermocouple assembly is located at the center of the 12 inch length of the heated region of the furnace. The other two are located about 3 inches below the center of the heated region, and about 5 inches above the center of the heated region. Figure 49 shows the axial temperature profile of the furnace (when the peak temperature of the furnace was 1000 °C) from the top of the bottom cap insulation piece to the bottom of the top cap insulation piece. The actively heated region of the furnace is from 0 to 12 inches from the top of the bottom cap insulation piece. The locations of the three interior thermocouples (TC#1, TC#2, and TC#3) are also indicated in Figure 49.

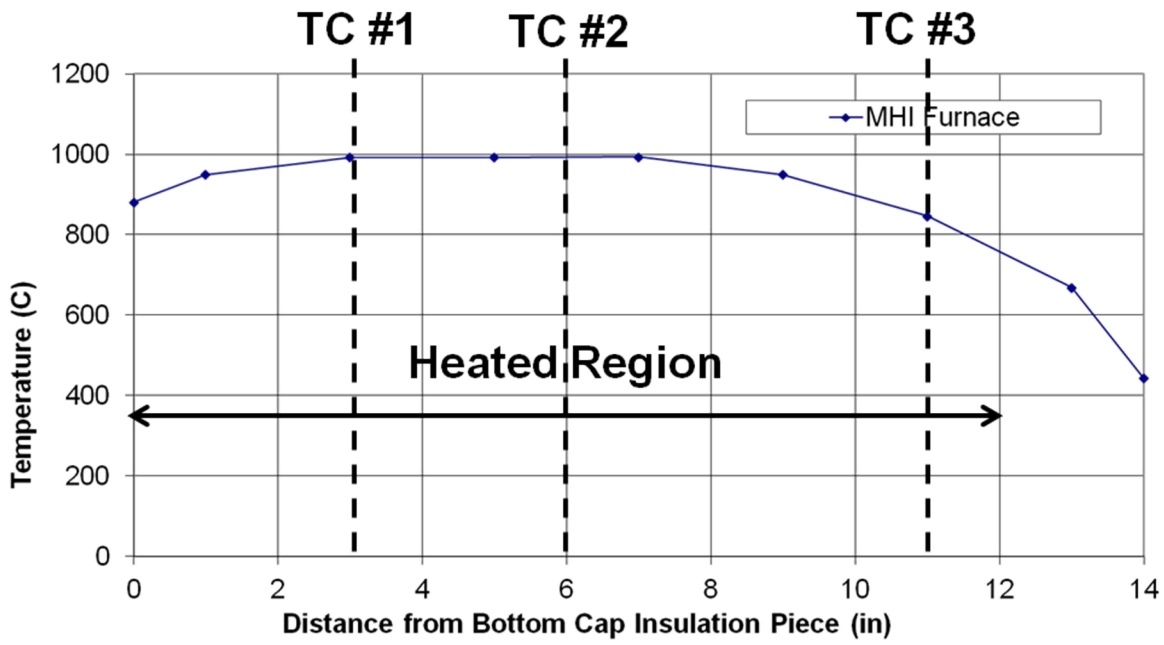

Figure 49: Axial temperature profile of the MHI furnace measured at a peak axial temperature of 1000 °C. The locations of the three B-type thermocouples (TC#1, TC#2, and TC#3) that will be used to monitor the temperature during an experiment are also shown.

Figure 50 shows the radial temperature of profile of the furnace at the axial center of the furnace. Note that the data shown in Figure 50 was obtained by inserting a thermocouple from the side of the furnace through a hole that was drilled in one side of the furnace insulation. Because this hole exists, there is a gap in the heating coil at the location of the hole. This gap explains why the radial temperature profile is skewed with a higher temperature in the negative direction, as indicated in Figure 50, than in the positive direction (the direction in which the hole in the furnace extends). The sapphire fibers will be located at approximately +/- 0.25 inches from the furnace centerline.

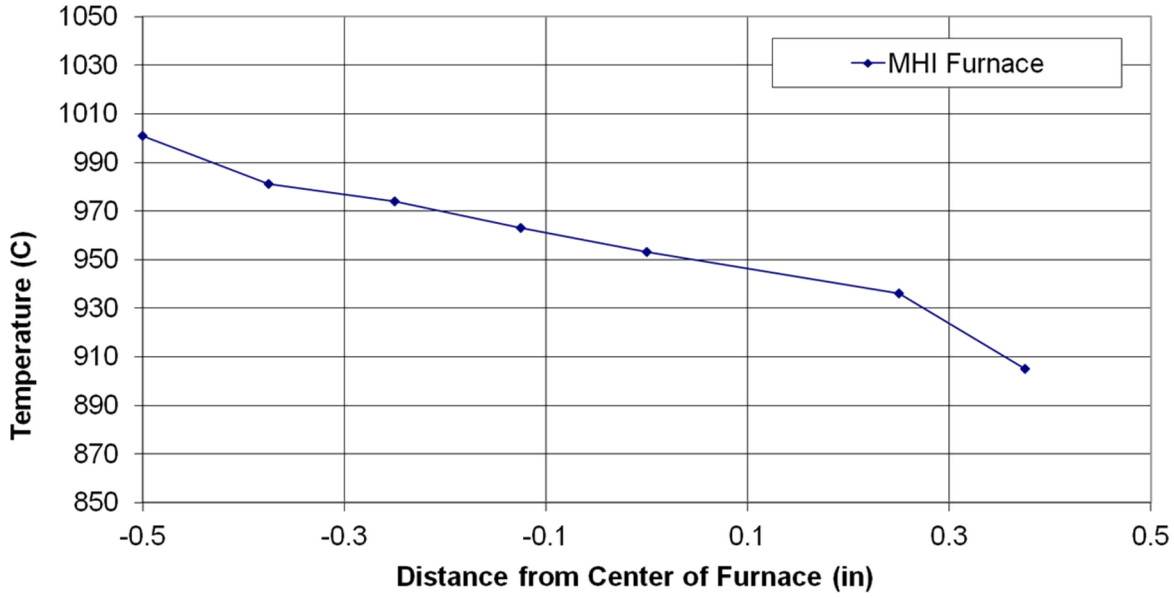

Figure 50: Radial temperature of profile of the furnace at the axial center of the furnace.

Once these modifications were made, a mock experiment was performed to see how the furnace would perform when placed inside of a 7 inch dry tube surrounded by water. The goals of this mock experiment were to: 1.) determine the temperature at the surface of the dry tube when the interior of the furnace reached the maximum temperature (1600 °C) for the planned reactor experiments, 2.) ensure that no boiling of water occurs at the maximum temperature, and 3.) ensure that we can successfully reach an interior temperature of 1600 °C with the dry tube surrounded by water without exceeding the maximum rated power of the heating element (2200 W).

First, a 7 inch dry tube was placed inside of a plastic trash can and the furnace was lowered into the dry tube. The furnace was heated to approximately 400 °C to determine the axial hot spot at the surface of the dry tube. The dry tube was instrumented at this location with a K-type thermocouple. The trash can was then filled with water and the furnace was gradually heated up to an interior temperature of 1600 °C. With stagnant water inside the trash can, we were able to reach an interior furnace temperature of 1600 °C with a steady-state furnace power of 1715 W. No boiling of water was observed and the temperature at the surface of the dry tube remained below 50 °C. Small bubbles were observed at the surface of the dry tube and the trash can, however this was due to dissolved oxygen coming out of solution at higher temperatures and was not due to boiling. Pictures of the dry tube instrumented with a K-type thermocouple and the dissolved oxygen coming out of solution at the surface of the dry tube and the trash can are shown in Figure 51.

Figure 51: Pictures of the dry tube instrumented with a K-type thermocouple and the dissolved oxygen coming out of solution at the surface of the dry tube and the trash can.

In order to get a more realistic prediction of the surface temperature of the dry tube during operation inside the 7 inch dry tube facility of the OSURR, water was simultaneously added and removed using a siphon to simulate flow inside the trash can. With flowing water, the steady-state furnace power required to maintain an interior temperature of 1600 °C remained about the same, but the dry tube surface temperature was reduced to approximately 25 °C.

For further reassurance that no boiling of water would occur, we submersed a cartridge heater in a bucket of 14 °C water and determined the heat flux required to initiate boiling. At 2.5 W/cm^2, no bubbles were observed. At 2.9 W/cm^2, a small amount of bubbles were detaching from the heater and were making it to the surface. It is likely that the bubbles observed at 2.9 W/cm^2 were actually dissolved oxygen coming out of solution, but to be conservative this was considered incipient boiling. Therefore, 2.5 W/cm^2 was chosen as a safe heat flux for the conditions below which boiling would not occur. The MHI furnace has a 12" tall heated zone. The maximum electrical power that can be provided to the heating element is 2200 W and the power required to reach 1600 °C, as mentioned previously, is ~1700 W. If one assumes that all the thermal energy is dissipated radially outward, then a 12" tall, 7" diameter surface would be in contact with water during the heated experiments that are to be performed in the 7 inch diameter dry tube facility at the OSURR. The thermal energy will actually be distributed over a larger surface area, so this area calculation is conservative. For this heated surface area, the maximum heat flux and the heat flux at 1700 W are calculated to be 1.29 and 0.99 W/cm^2, respectively. Based on the safe heat flux defined above, the factors of safety to boiling using the maximum power and the 1600 °C steady state power would be 1.93 and 2.52, respectively.

Before performing heated irradiation experiments in the OSURR, we would also like to know how much neutron activation to expect from the various furnace materials. With this knowledge, we can estimate how much personnel dose will be accumulated in servicing the furnace materials and which components we should avoid remaining in intimate contact with. Material samples of each of the furnace materials were irradiated in the OSURR in a "rabbit" facility. The irradiated samples were then analyzed using gamma spectroscopy to determine the activation products of the materials and predict what the activation would be for a longer, higher power irradiation of materials with larger mass. The rabbit facility has a similar neutron flux energy spectrum to the 7 inch dry tube facility, but the total neutron flux in the rabbit is slightly larger than the 7 inch dry tube facility so our predictions will be conservative. The most radioactive components, as predicted by extrapolation of the results from the sample irradiation experiments, are summarized in Table 7. The most active components are some steel bolts that are used to hold the thermocouple assembly together. Other relatively radioactive components include the $MoSi_2$ heating element, the various titanium components, and the electrical insulators. The dominant activation product of the $MoSi_2$ heating element has a relatively short half life (65 hours), so it likely will not be an issue after a few more weeks of decay. The steel bolts, titanium components, and electrical insulators can all be easily removed from the furnace (thus limiting the time during which we will accumulate dose while handling them), and they can all be disposed of following the experiment.

Table 7: Summary of the most radioactive components of the MHI furnace following reactor irradiation, as predicted by extrapolation of the results from sample irradiation experiments.

Component	Estimated Activity After 4 Week Decay (μCi)	Dominant Activation Product (Half life)	Decay Mode
Steel bolts	4100	Cr-51 (28 days)	Electron caputre + a 320 keV gamma with a ~10% yield
$MoSi_2$ heating element	575	Mo-99 (65 hours)	133 & 443 keV average energy β particles + low-energy, low-yield gammas
Titanium components	381	Sc-46 (84 days)	112 keV average energy β particles + 0.9 & 1.1 MeV energy gamma photons
Electrical insulators	368	Ba-131 (11.5 days)	Electron capture + gamma photons with energy generally below ~500 keV, but as high as 1.34 MeV

6.3.2 A High Temperature Furnace Suitable for Operation in the OSU Co-60 Gamma Irradiator at Temperatures up to 1000 °C

At the start of this project, the only functioning furnace that we had that was capable of operating in the Co-60 gamma irradiation facility at the OSU Nuclear Reactor Lab was designed for heating coiled optical fiber to temperatures up to 600 °C. This furnace is shown with and without insulation in Figure 52. The MHI furnace described in section 6.3.1 has an outer diameter of ~6.75 inches, and therefore would not fit in the nominally 6 inch diameter dry tube of the Co-60 irradiator. Clearly, in order to reach 1000 °C inside the Co-60 irradiation facility, we would need to fabricate another furnace.

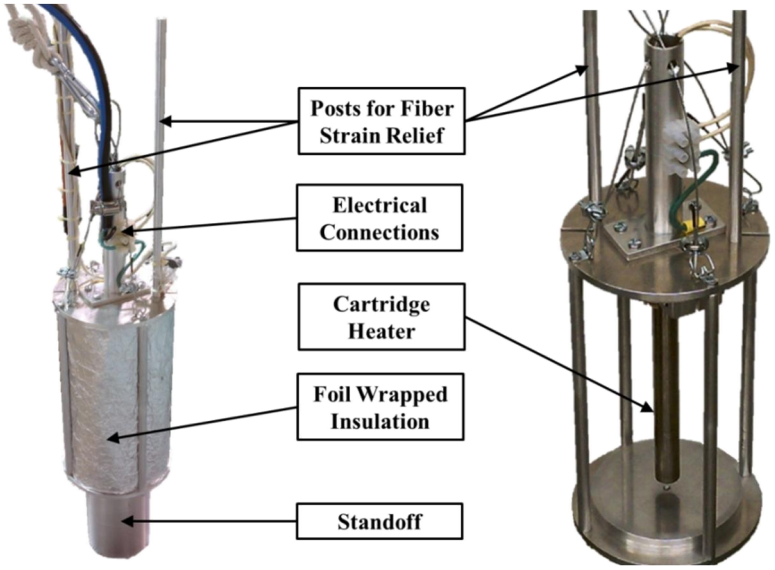

Figure 52: Previous furnace (both with and without insulation shown) used for heated gamma irradiations of coiled silica optical fiber heated up to temperatures of 600 °C.

We decided to purchase a furnace with geometry as close to the MHI furnace as possible in order to practice loading the fiber and running an experiment in a gamma irradiator before we proceed to the reactor irradiation experiments. The hope was that any mistakes in the design of the experiments would be identified and corrected during the gamma irradiation experiment (which will not result in neutron activation of components), rather than the reactor irradiation experiment, after which neutron activation of components makes repeating the experiments difficult. The furnace that was purchased is a tube furnace from Thermcraft, Inc. A picture and a labeled CAD model of the furnace are shown in Figure 53. The furnace consists of an iron-chrome-nickel wire wrapped around the 1 inch inner diameter of a right circular cylindrical annulus of vacuum-formed ceramic fiber insulation with an outer diameter of 3 inches and a total length of 15 inches. The heated length of the furnace is 12 inches. The furnace has a maximum temperature of 1100 °C and a maximum power rating of 1000 W, although the manufacturer cannot guarantee the furnace beyond 500 W. The geometry of the furnace, specifically the approximately 1.375 inch gap between the dry tube of the Co-60 irradiator and the outer surface of the furnace insulation, allows us to load a fiber on the outside of the furnace in addition to inside the furnace. This way, we can see the effects of gamma radiation on both heated and unheated sapphire fibers.

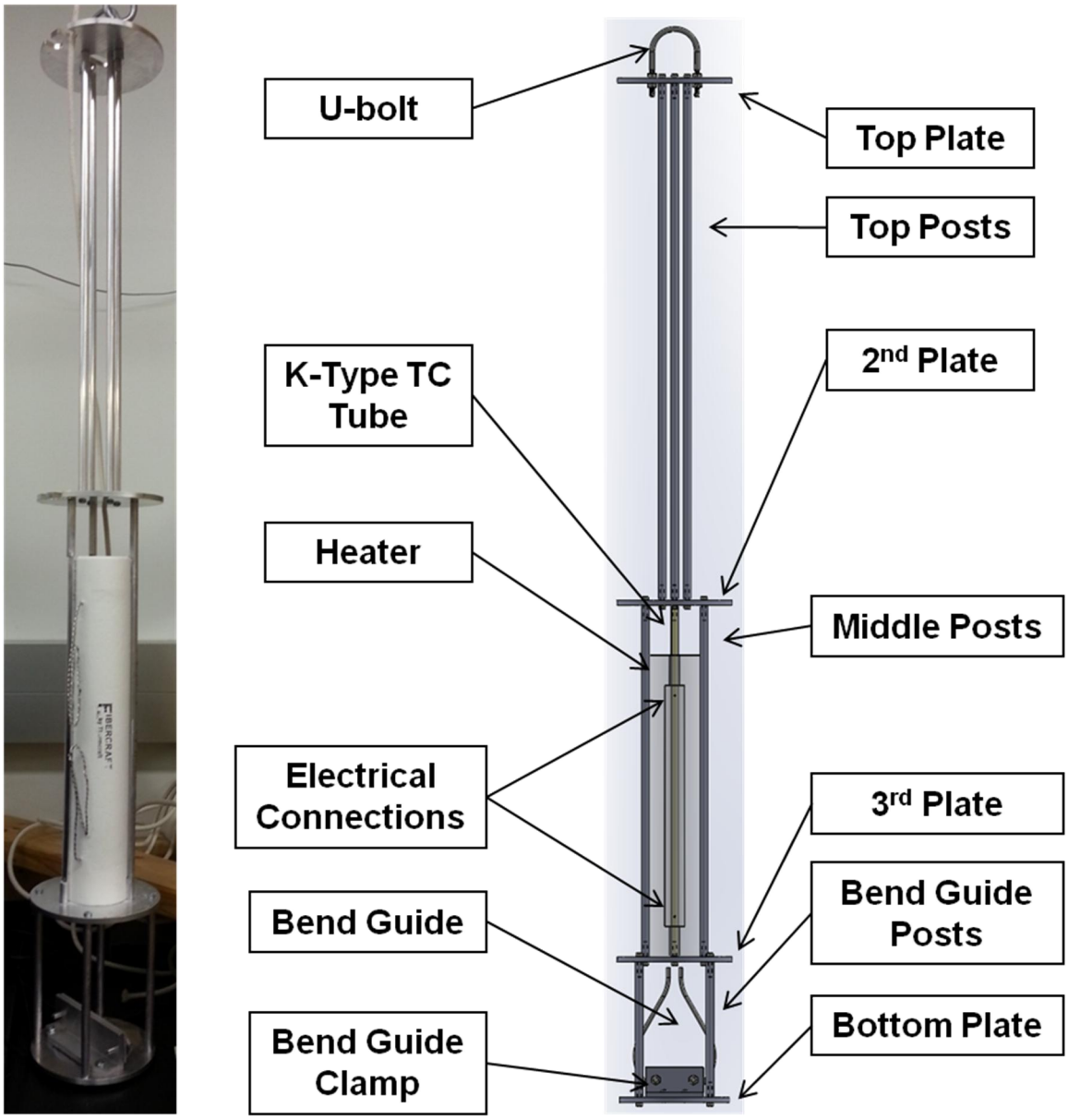

Figure 53: Picture and labeled CAD model of the gamma irradiation furnace that was fabricated in order to perform heated (up to 1000 °C) gamma irradiations of sapphire fibers in a Co-60 gamma irradiation facility.

We tested this furnace up to the maximum proposed temperature (1000 °C) for the gamma irradiations of sapphire fibers and determined the axial temperature profile inside the furnace. During the process of determining the axial temperature profile, we discovered that a convective loop in the furnace caused large heat losses and asymmetry in the temperature profile. Plugging the top of the furnace with Nextel insulation significantly improved the symmetry of the temperature profile and reduced heat losses. The axial temperature profiles of the gamma irradiation furnace both with and without the top hole of the furnace plugged are shown in Figure 54.

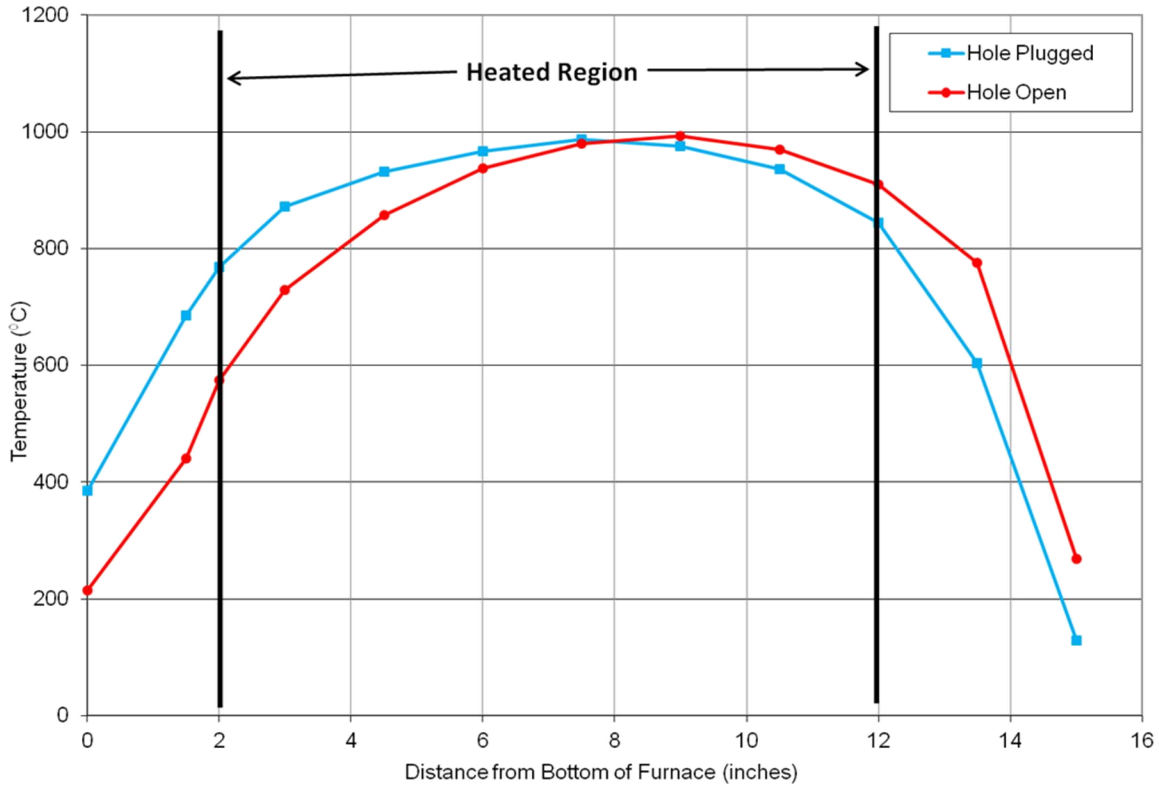

Figure 54: Axial temperature profile of the gamma irradiation at its maximum use temperature (1000 °C). Profiles are shown with and without the top hole of the furnace plugged to show how plugging the hole eliminates the asymmetry caused by a convective loop in the furnace.

Chapter 7. Task F - High Temperature Irradiations of Sapphire Fibers

7.1 Deliverables

- Optical attenuation in sapphire fibers due to high temperatures (1500 °C)
- Optical attenuation in sapphire fibers due to gamma irradiation at high temperatures (1000 °C)
- Optical attenuation in sapphire fibers due to reactor irradiation at high temperatures (1000 °C)

7.2 Timeline and Task Status

- Start Date: 4/1/2013
- Planned Completion Date: 3/31/2014
- Task Status: 100%

7.3 Progress Toward the Completion of Deliverables

7.3.1 Optical Attenuation in Sapphire Fibers Due to High Temperatures (1500 °C) in the Absence of Radiation

We first performed a heated optical transmission experiment with unprotected sapphire optical fiber. Approximately 0.61 meters of a 2 meter length of sapphire fiber was heated inside the MHI furnace, as shown in Figure 55, to temperatures up to 1500 °C.

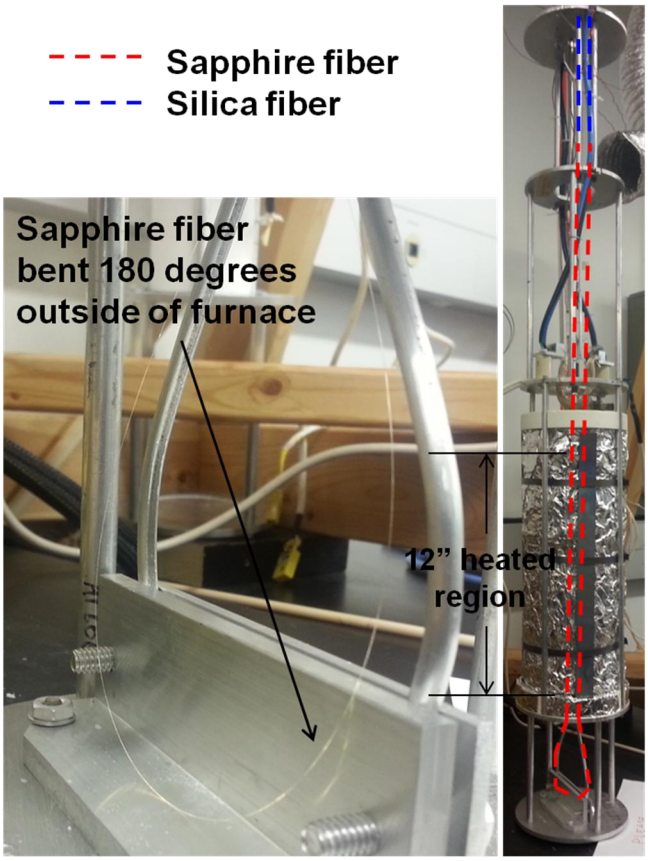

Figure 55: Pictures showing the MHI furnace with the sapphire fiber loaded inside the furnace and outside the furnace, where it is bent 180 degrees before passing back through the furnace. The sapphire fiber and silica lead fibers are shown schematically in the right figure with dashed lines.

The sapphire fiber was joined to silica lead fibers by fusion splicing the fibers together. This splicing was required because the sapphire fiber is extremely expensive (~$1100 for a 2 meter length), has very high intrinsic optical attenuation (thought to be on the order of several dB per meter), and it can only be manufactured in lengths up to 2 meters. The splicing process is difficult because sapphire and silica have very different melting temperatures and thermal expansion coefficients. We worked with OFS Fitel, LLC (from whom we purchased the fusion splicer) to optimize the splicing process by adjusting various splicer settings. We used small silica capillary tubing to protect the splices and used a small arc from the splicer to locally melt the capillary tubing onto the fibers on each end of the splice. Figure 56 shows pictures taken by cameras inside of the fusion splicer after splicing sapphire to silica in two different planes. Figure 57 shows a picture of one of the splices and the protective silica capillary tube that covers the splice. The optical attenuation resulting from two sapphire to silica splices, in addition to the optical attenuation in an approximately 2" length of sapphire fiber was estimated to be ~3.5 dB, or ~45% transmission.

Sapphire (left) to silica (right) splice in XZ plane

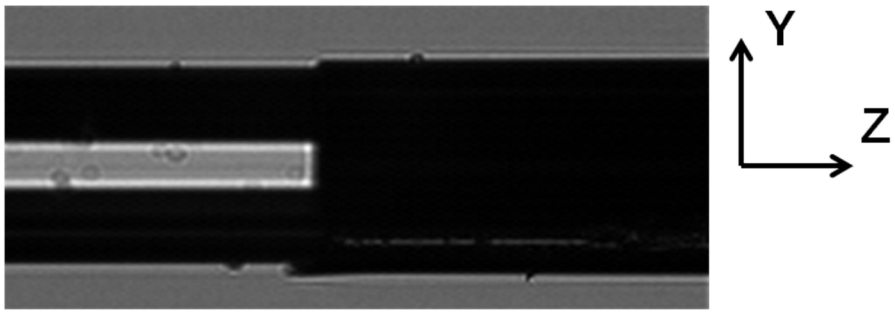

Sapphire (left) to silica (right) splice in YZ plane

Figure 56: Pictures taken in two different planes using cameras inside the fusion splicer showing a sapphire to silica splice following a successful splicing operation.

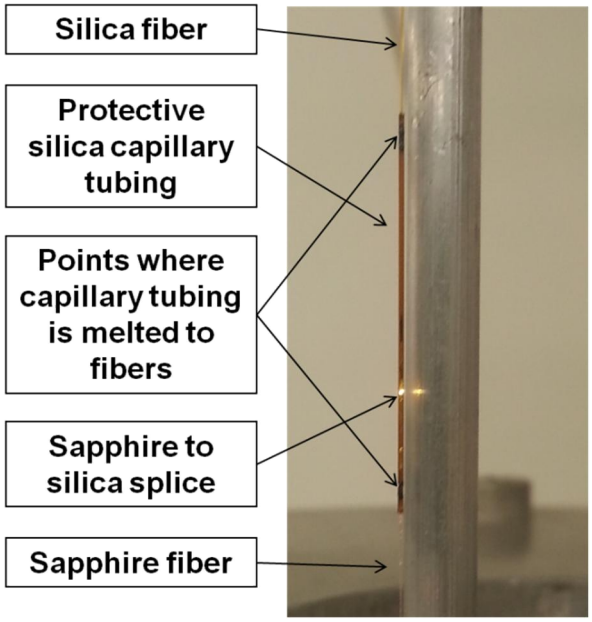

Figure 57: A picture of one of the sapphire to silica splices and the protective silica capillary tube that covers the splice.

After the sapphire fiber was spliced to silica lead fibers and loaded into the furnace as shown in Figure 55, the fiber was heated in steps of 100 °C up to 1500 °C. The temperature (at three locations inside the furnace, as measured by B-type thermocouples) vs. time profile during the first heated experiment is shown in Figure 58.

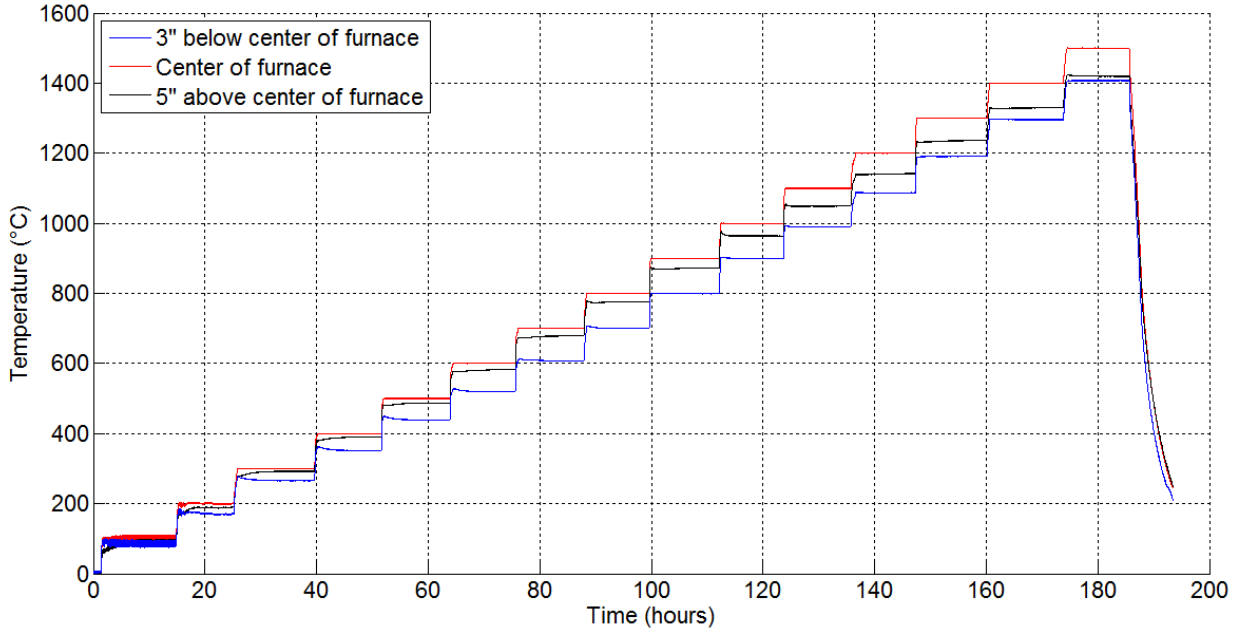

Figure 58: The temperature (at three locations inside the furnace, as measured by B-type thermocouples) vs. time profile during the first heated experiment.

The optical transmission through the sapphire fiber was continuously monitored throughout the experiment, in-situ. Background measurements (with the light source optically disconnected from the sapphire fiber) were made following each active measurement (with the light source coupled to the fiber) of the transmission through the sapphire fiber. Background measurements were subtracted from the active measurements. An unheated silica fiber was continuously interrogated throughout the experiment to serve as a control fiber. Background corrected transmission measurements made with the sapphire fiber were normalized to the background corrected transmission measurements and with the control fiber in order to account for fluctuations in the light source intensity and/or spectrometer sensitivities. Figure 59 shows the added attenuation in the sapphire optical fiber as a function of wavelength at the end of each period of time at each of the temperatures (up to 900 °C) indicated in the figure. The temperatures that are shown are the temperatures at the center of the furnace. Clearly, at temperatures of 900 °C and below, the sapphire optical fiber has negligible attenuation at all of the wavelengths shown. In fact, the optical transmission actually improves (as evidenced by negative added attenuation) with heating to temperatures of 900 °C and below at some wavelengths.

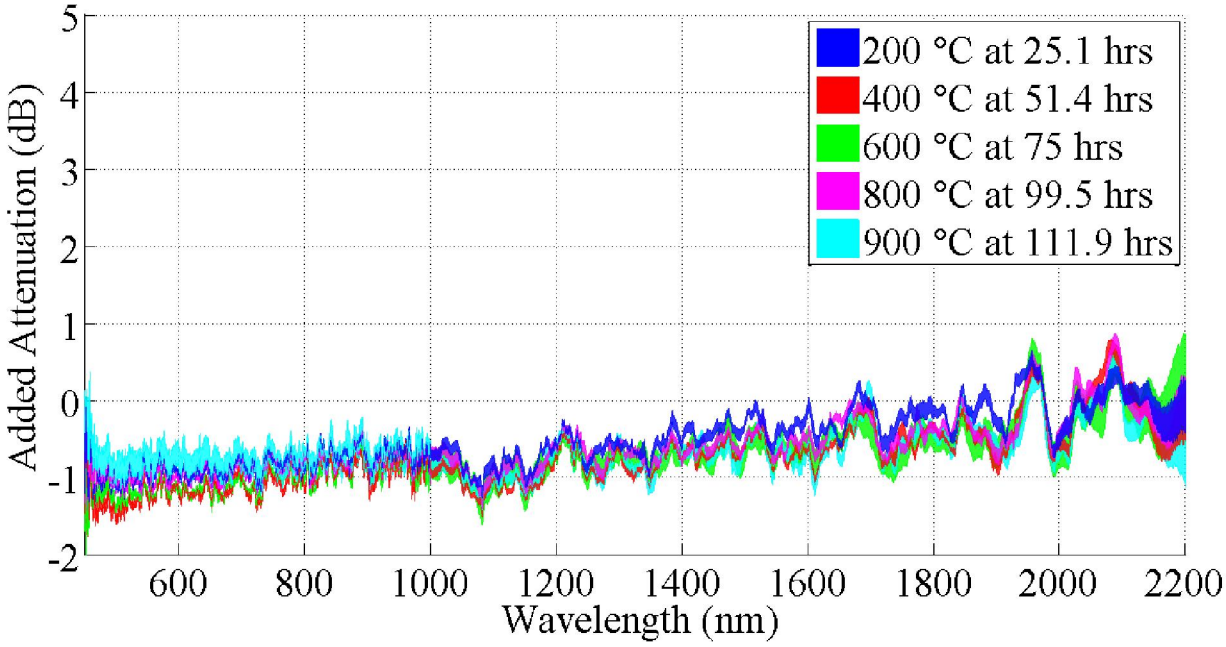

Figure 59: Added attenuation in the sapphire optical fiber as a function of wavelength at the end of each period of time at each of the temperatures (up to 900 °C) indicated in the figure.

Figure 60 shows the added attenuation at the wavelengths indicated in the figure as a function of time throughout the first heated experiment. The temperature at the center of the furnace is also shown in the figure as a function of time. Data is only shown up to 172 hours because beyond this time, after the fiber was heated to 1500 °C, the large uncertainties in the added attenuation data make the data difficult to analyze. Figure 60 shows that the added attenuation at all wavelengths continues to increase with time at all wavelengths, with no apparent trend toward reaching a steady-state. The rate of increase in the added attenuation also increases with increasing temperature.

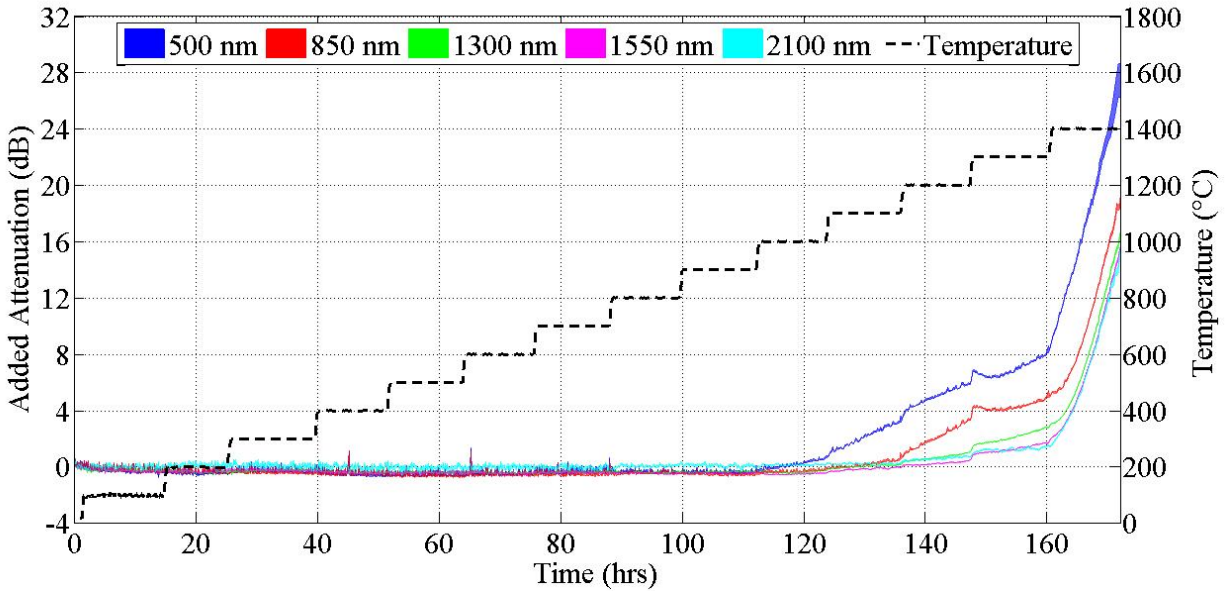

Figure 60: Added attenuation in the sapphire fiber at the wavelengths indicated in the figure as a function of time throughout the first heated experiment. The temperature at the center of the furnace is also shown in the figure as a function of time.

In addition to being unprotected, the sapphire fiber used in the first heated experiment also did not have enough strain relief above and below the furnace. For this reason, the slack in the fiber caused the fiber to drift toward the heating element of the furnace that is coiled on the inside diameter of the heated region. At high temperatures, the fiber stuck to the heating element, which caused the rapid increases in the added attenuation at 1000 °C and above. After the experiment, the fiber was broken while trying to remove the fiber from the furnace. Figure 61 shows several pictures of the sapphire fiber stuck to the heating element of the furnace. Figure 62 shows pictures obtained using an optical microscope showing damage at the location where the sapphire fiber stuck to the furnace (top) and the surface of the sapphire with (bottom left) and without (bottom right) small bubbles or "local spots" at the surface of the fiber.

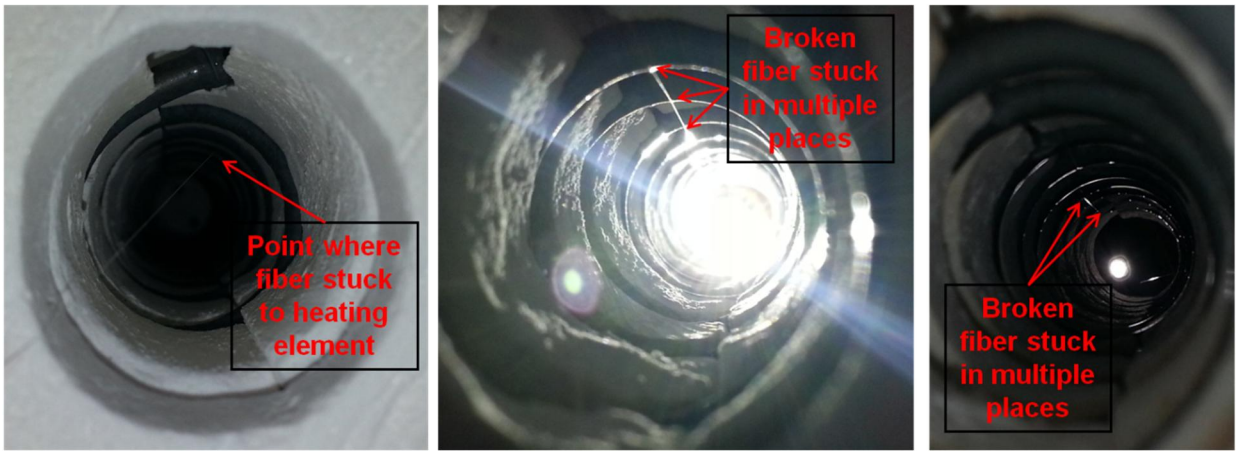

Figure 61: Pictures showing the sapphire fiber stuck to the heating element of the furnace after trying to remove the fiber from the furnace after the first heated experiment.

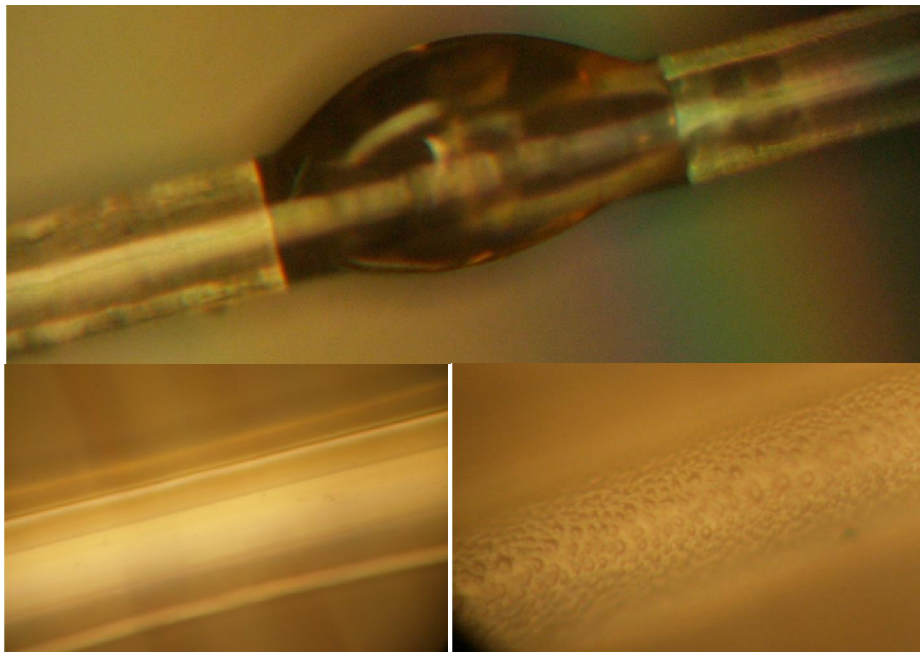

Figure 62: Pictures obtained using an optical microscope showing damage at the location where the sapphire fiber stuck to the furnace (top) and the surface of the sapphire with (bottom left) and without (bottom right) small bubbles or "local spots" at the surface of the fiber.

Because the lack of strain relief and protection of the sapphire caused the sapphire fiber to stick to the heating element of the furnace, we decided to perform a second heated experiment where the fibers were loaded inside a protective ceramic tube (to avoid the fibers contacting with the heating element of the furnace). During the second heated experiment, the fibers were first heated to 1000 °C (the temperature at which degradation was first observed during the first heated experiment). The fibers were then heated in increments of 100 °C up to 1500 °C. The temperature (at three locations inside the furnace, as measured by B-type thermocouples) vs. time profile during the second heated experiment is shown in Figure 63.

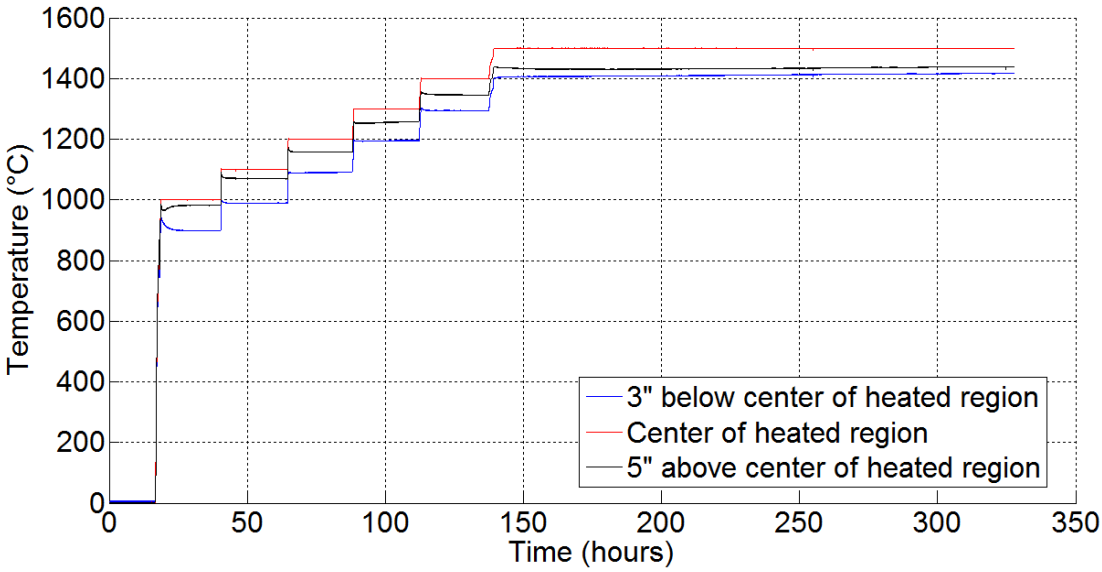

Figure 63: The temperature (at three locations inside the furnace, as measured by B-type thermocouples) vs. time profile during the second heated experiment.

Figure 64 shows the added attenuation at the wavelengths indicated in the figure as a function of time throughout the second heated experiment. The temperature at the center of the furnace is also shown in the figure as a function of time. Figure 64 shows that the added attenuation at all wavelengths increases with each step in temperature; however, the added attenuation seems to approach a steady-state at all temperatures, particularly at temperatures below 1400 °C. At 1400 °C, the added attenuation is likely approaching a steady-state, but it is difficult to say whether or not the added attenuation actually reached steady-state values. Figure 65 shows a zoomed in portion of the data in Figure 64 for times at which the temperature was maintained at 1400 °C. Note that the data acquisition system failed between approximately 128 and 137.8 hours. From the data shown in Figure 65, it seems that the added attenuation at 1400 °C did reach a steady-state, or at least was close to reaching a steady-state, at all wavelengths. Loses light

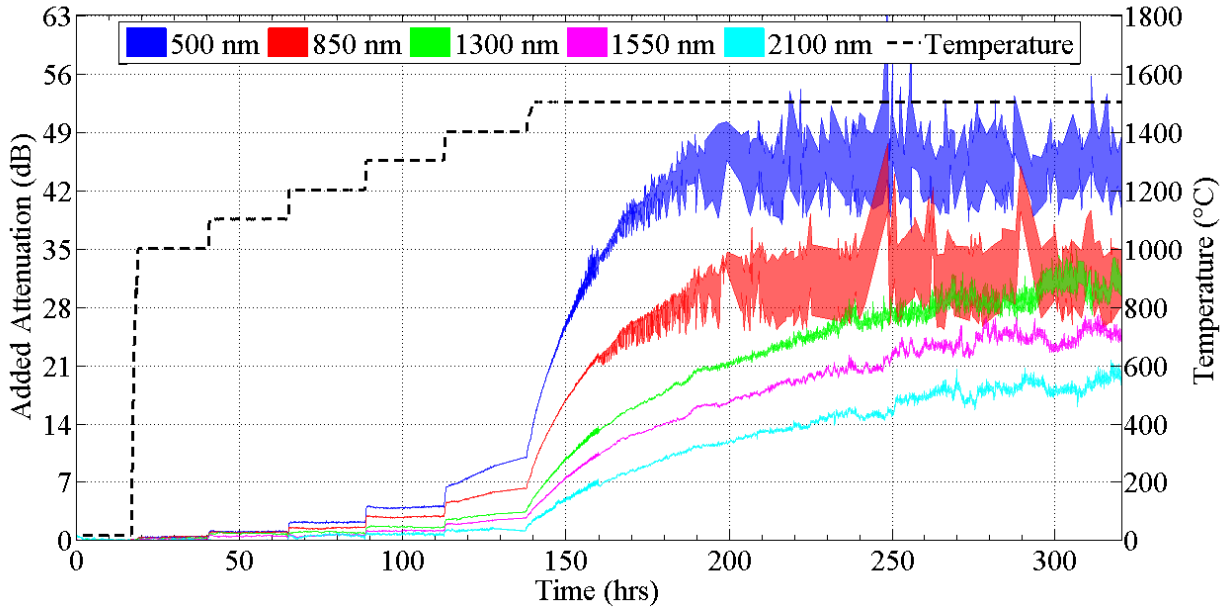

Figure 64: Added attenuation at the wavelengths indicated in the figure as a function of time throughout the second heated experiment. The temperature at the center of the furnace is also shown in the figure as a function of time.

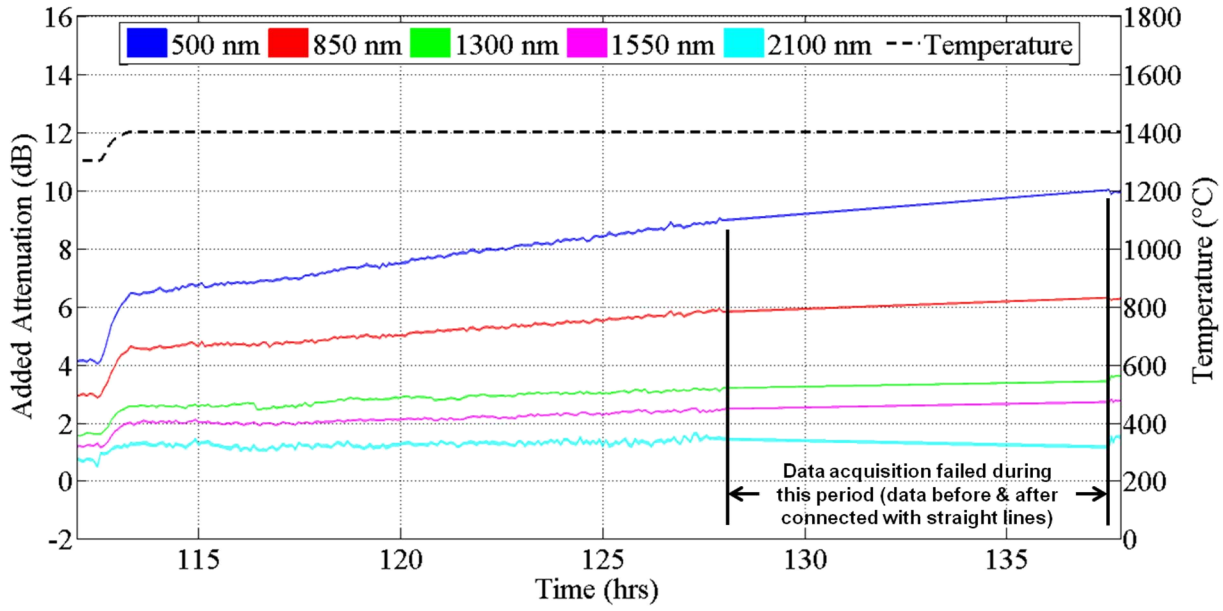

Figure 65: Added attenuation at the indicated wavelengths as a function of time during the period of time during which the fiber was heated to 1400 °C. Note that the data acquisition system failed between approximately 128 and 137.8 hours.

At 1500 °C the increase in the added attenuation was much larger than at any previous temperature. The added attenuation did eventually reach, or at least approach, steady-state values at all wavelengths after approximately 181 hours holding at 1500 °C. Figure 66 shows the added attenuation vs. wavelength at the end of each period of time holding at constant temperature at temperatures up to 1400 °C. Figure 67 is similar to Figure 66, except that the added attenuation is shown various times when the furnace temperature was held constant at 1400 and 1500 °C.

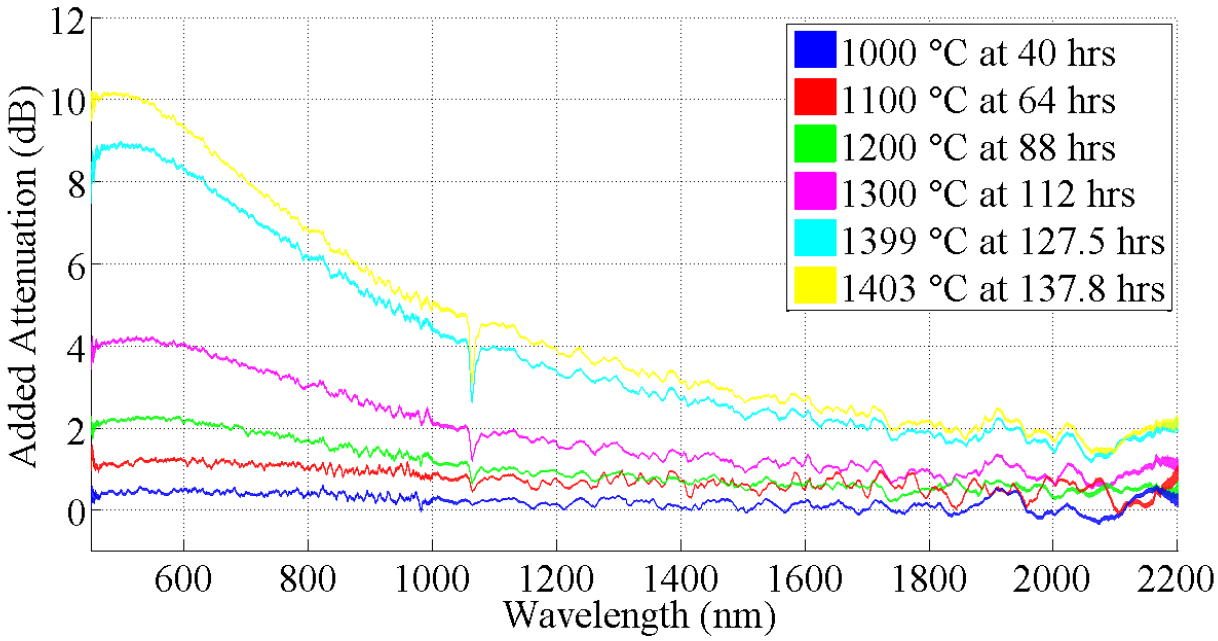

Figure 66: Added attenuation vs. wavelength at the end of each period of time holding at constant temperature at temperatures up to 1400 °C.

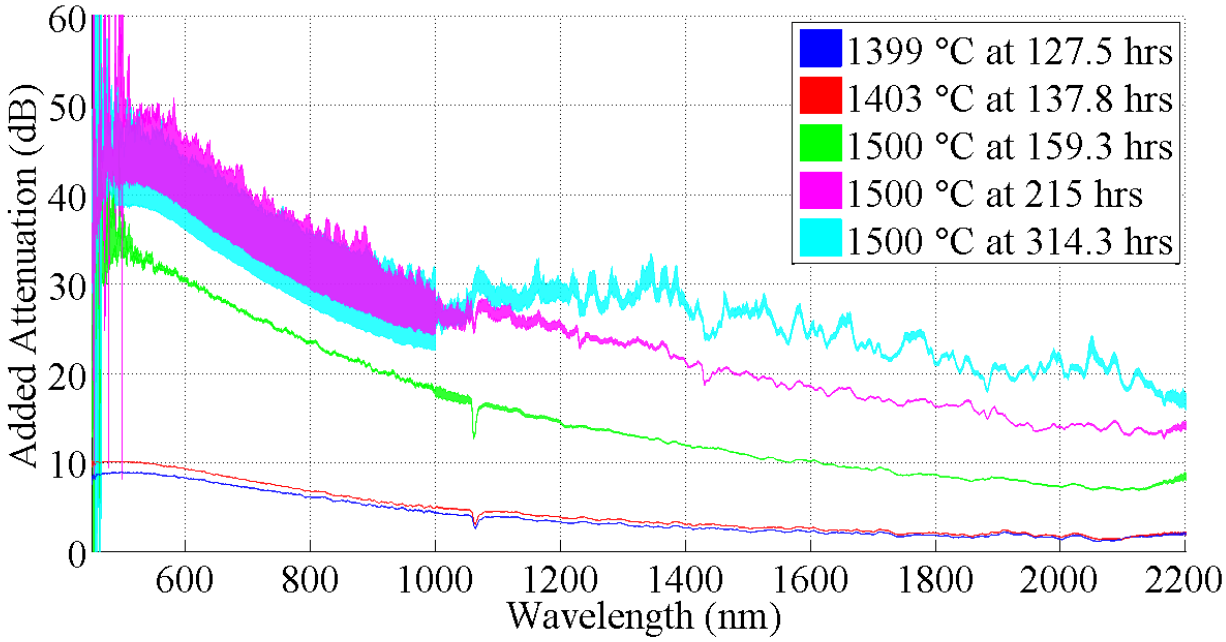

Figure 67: Added attenuation vs. wavelength at various times when the furnace temperature was held at 1400 and 1500 °C.

While the furnace was held at a temperature of 1500 °C, the sapphire fiber broke because the tape holding one of the alumina tubes protecting the sapphire fiber failed, causing the tube to drop through the furnace and snap the fiber. However, we were able to splice half of the sapphire fiber to silica fiber outside of the heated region of the furnace. With this new sapphire to silica splice, we were then able to observe how the attenuation in half of the heated sapphire fiber changed as the furnace was cooled from 1500 °C. Figure 68 shows the change in the attenuation from the end of heating at 1500 °C (called added attenuation in the figure) in one half of the heated portion of the sapphire fiber. The added attenuation and the temperature at the center of the furnace are shown as a function of time with wavelength as a parameter. Figure 69 shows the improvement in the cooled portion of the sapphire fiber as a function of wavelength at several times during cooling.

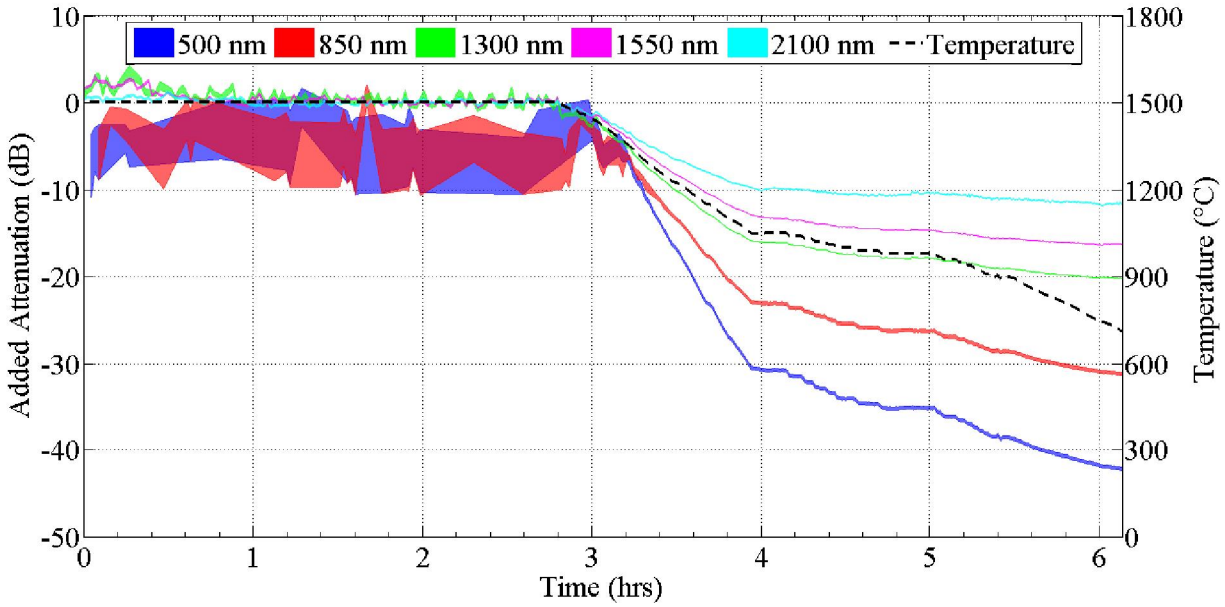

Figure 68: Change in the attenuation from the end of heating at 1500 °C (called added attenuation in the figure) in one half of the heated portion of the sapphire fiber. The added attenuation (with wavelength as a parameter) and the temperature at the center of the furnace are shown as a function of time.

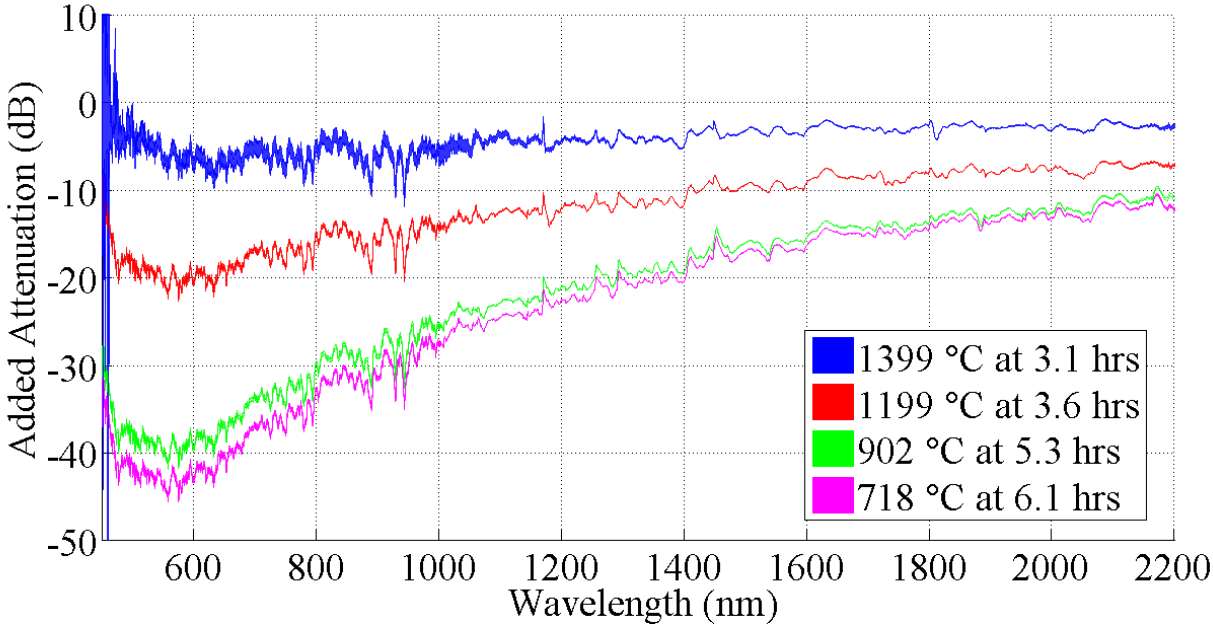

Figure 69: Change in the attenuation from the end of heating at 1500 °C in one half of the heated portion of the sapphire fiber as a function of wavelength at several times during cooling. The temperature at the center of the furnace is also indicated with each time.

The large negative added attenuation shown in Figure 68 and Figure 69 indicate that there is significant recovery of the sapphire fiber transmission when the fiber was cooled to temperatures of approximately 700 °C. While the sapphire fiber does appear to recover at low temperatures, the large attenuation losses in the fiber at high temperatures are a major obstacle in enabling sapphire sensors to operate effectively at high temperatures. The large losses in the light transmission would affect the signal to noise ratio of the sapphire sensor at high temperatures causing it to fail. To overcome this obstacle, we investigated the heated sapphire optical fiber with a variety of microscopy tools to determine the cause of the light attenuation in the sapphire fiber at high temperatures. The results of these tests are presented in Chapter 9; to avoid the large losses in light transmission, the gamma and reactor tests were held to temperatures under 1300 °C.

7.3.2 Optical Attenuation in Sapphire Fibers Due to Gamma Irradiation at High Temperatures (1000 °C)

The gamma irradiation furnace described in section 6.3.2 was lowered into a Co-60 irradiator located in the reactor bay of the Ohio State University Nuclear Reactor Laboratory (OSUNRL). The Co-60 irradiation facility consists of a 6 inch inner diameter aluminum dry tube surrounded by 14 Co-60 pins immersed in a pool of water that is approximately 20 feet deep. An approximately 1.56 meter length and a 2 meter length of 100 μm diameter sapphire fiber were both fusion spliced to ~19 meter lengths of jacketed silica fiber at each end, which serve as lead-in and lead-out fibers. The 1.56 meter length sapphire fiber assembly (with jacketed silica lead fibers) was loaded axially from the top of the furnace to the bottom of the furnace, bent 180 degrees at a radius of ~2 inches, and then passed back up through the bottom of the furnace to exit through the top of the furnace. The sapphire-to-silica splices were located above the furnace so that the silica lead fibers were not heated. The 1.56 meter length fiber was heated to 1000 °C prior to irradiation to ensure that no thermally-induced attenuation would occur as a result of heating to 1000 °C in the gamma irradiation furnace. During the course of the gamma irradiation experiment, the silica lead fibers that were fusion spliced to the sapphire fibers were subjected to some amount of gamma radiation. To account for changes in the transmission of the sapphire fiber assemblies due to attenuation in the silica lead fibers, a jacketed silica control fiber (of the same type as the lead fibers that were spliced to the sapphire fibers) was also loaded into the experiment. This control fiber was bent through 180 degrees at the location of the sapphire-to-silica splices and then passed back up to the top of the irradiation facility. A 2 meter length sapphire fiber assembly was loaded outside the furnace to determine the radiation-induced attenuation in a sapphire fiber that was not actively heated. The interior temperature of the furnace was monitored using 3 K-type thermocouples positioned at the axial center of the furnace and ~5 inches above and below the axial center of the furnace. An additional K-type thermocouple was positioned on the outside of the furnace at the axial center of the furnace, so that the temperature of the sapphire fiber that was loaded on the exterior of the furnace could be measured. The peak dose rate in the Co-60 irradiator at the OSUNRL at the time of the experiment was 38.3 krad/hr (dose rate in sapphire). Figure 70 shows the spatial profile (in the axial direction) of the normalized furnace temperature and normalized gamma dose rate. Values are normalized relative to the peak values (maximum temperature of 1000 °C and maximum gamma dose rate of 38.3 krad/hr). Indicators in Figure 70 also show the locations of the sapphire fibers (both heated and unheated regions), the silica fibers (including the control fiber and the lead fibers for the sapphire fiber assembly), and the three interior thermocouples. Note that the heated region could not overlap with the location of the peak dose rate, because the sapphire fibers had to be bent 180 degrees at the bottom of the dry tube at a

sufficiently large bend radius (~2 inches) in order to pass back through the furnace and return to the top of the irradiation facility through the top of the furnace.

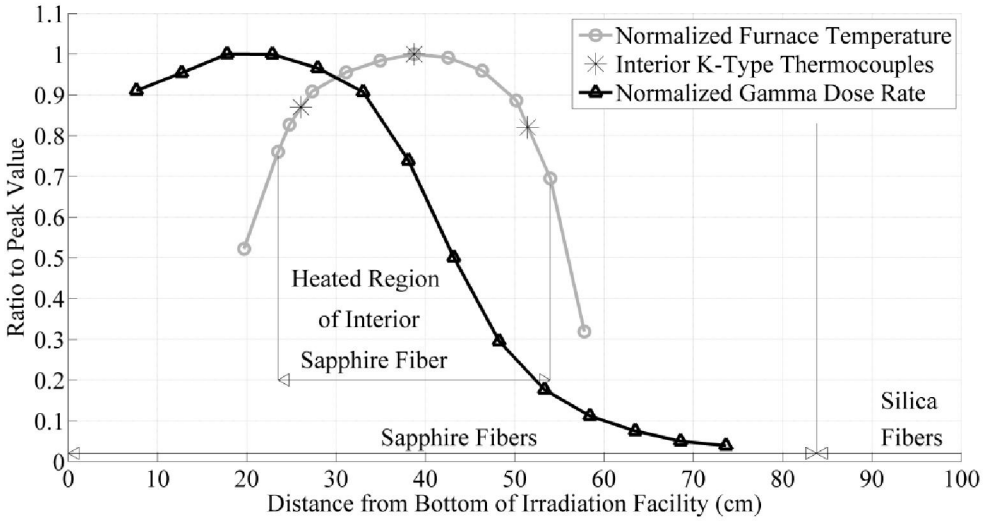

Figure 70: Spatial (in the axial direction) profile of the normalized gamma irradiation furnace temperature and normalized gamma dose rate. Values are normalized to the peak values. The locations of the sapphire and silica fibers are also shown, along with the K-type thermocouples located on the interior of the furnace.

The sapphire fibers were irradiated for a total of 233.1 hours, resulting in a total dose of 8.93 Mrad (dose in sapphire at the location of the peak dose rate). The time profile of the peak temperature of the furnace and the absorbed dose in sapphire at the location of the peak dose rate is shown in Figure 71.

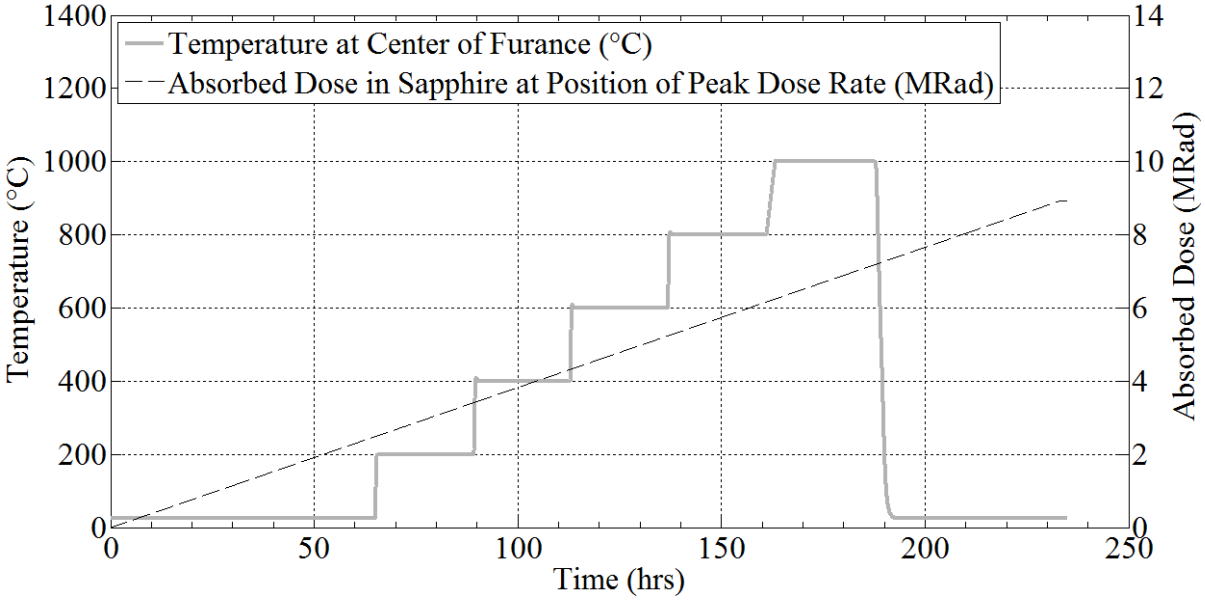

Figure 71: Time profile of the peak temperature of the gamma irradiation furnace and the absorbed dose in sapphire at the location of the peak dose rate during the heated Co-60 gamma irradiation of sapphire fiber.

Figure 72 shows the added attenuation at several discrete wavelengths, as indicated in the plots, throughout the entire experiment for the sapphire fibers loaded on the interior (top) and exterior (bottom) of the furnace. The wavelengths that are displayed are those that are most commonly used for commercial optical instrumentation (850 nm, 1300 nm and 1550 nm). The time profile of the temperature at the center (top) and exterior (bottom) of the furnace is also shown in Figure 72. For the unheated sapphire fiber, the temperature at the exterior of the furnace was not continuously logged throughout the experiment; however, measurements were taken at the end of each step in temperature. Therefore, the time profile of the temperature of the unheated sapphire fiber is simply shown in the bottom portion of Figure 72 as step changes in temperature using the known temperature measurements taken at the end of each step in temperature. The actual temperature profile of the unheated sapphire fiber would have had some delay in reaching a steady-state temperature with each step in the internal temperature of the furnace. Note that the data shown in Figure 72 between 35 and 64.5 hours are connected by straight lines. We were not able to log data during these times because the data acquisition software application crashed over the weekend when we did not have access to the OSUNRL so we could not reset the application.

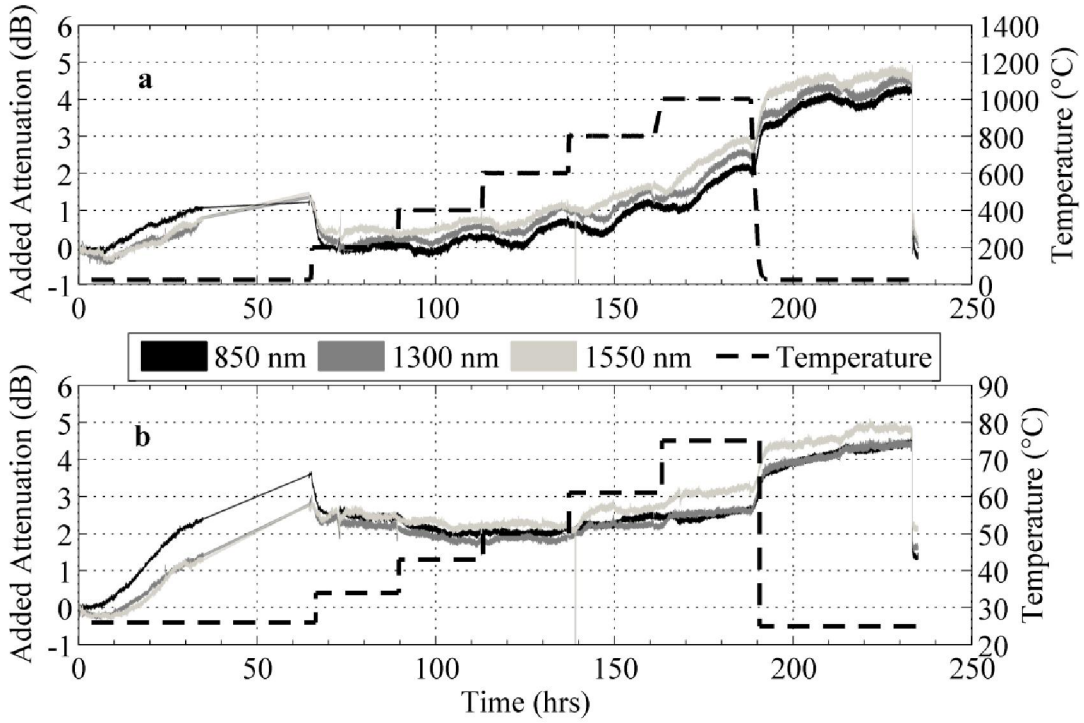

Figure 72: Added attenuation for the interior (a) and exterior (b) sapphire fibers as a function of time at various wavelengths during heated Co-60 gamma irradiation. The temperatures at the interior center (a) and exterior center (b) of the furnace are also shown as a function of time. The widths of the lines shown in this figure indicate one sigma uncertainties. Note that the experiment was removed from the Co-60 irradiator at 233.3 hours.

There is a periodic oscillation in the added attenuation data for the interior sapphire fiber (shown in the top portion of Figure 72) that occurs with a period of approximately 24 hours. This effect is due to diurnal fluctuations in the light source intensity and/or spectrometer sensitivities (due to diurnal fluctuations in the temperature of the OSUNRL reactor bay) that were only partially accounted for by normalizing the added attenuation data using the partially irradiated, but unheated silica control fiber described previously. The interior sapphire fiber was found to be more sensitive to fluctuations in the light source intensities and/or spectrometer sensitivities, so normalization using the data from the silica control fiber did not fully account for the fluctuations in the measurements made for the interior sapphire fiber. After normalization using the silica control fiber, the periodic oscillations in the added attenuation data for the interior sapphire fiber due to fluctuations in the light source intensity and/or spectrometer sensitivities have an amplitude of approximately 0.25 dB. These small oscillations do not prevent one from discussing the behavior of the added attenuation data for the interior sapphire fiber that are on the order of several dB. Oscillations in the added attenuation data for the exterior sapphire fiber (shown in the bottom portion of Figure 72) were not easily identifiable and are thought to be much less significant.

The added attenuation generally increases with time (and continued accumulation of dose) at constant temperature. It is difficult to say whether or not the added attenuation reaches a steady-state at elevated temperatures due to the periodic oscillations in the data resulting from light source intensity fluctuations. However, we can clearly see that increasing temperature from room

temperature to 200 °C (see Figure 72a) and 34 °C (see Figure 72b) causes the added attenuation to decrease. In fact, the added attenuation at 200 °C is approximately zero. The added attenuation in the exterior sapphire fiber stays relatively constant after heating to temperatures above 34 °C until the fiber is cooled back to room temperature. The added attenuation in the interior sapphire fiber generally increases as the temperature is increased up to 1000 °C. This increase could be due to continued accumulation of dose in the fiber (both heated and unheated portions of the fiber), or from thermally-induced attenuation that is not a consequence of radiation effects. Reducing the temperature of both fibers to room temperature causes the added attenuation to rapidly increase and approach a steady-state value of approximately 4-5 dB for all wavelengths. Because the added attenuation did not increase rapidly until the temperature was decreased, it is clear that elevated temperatures do in fact reduce the radiation-induced attenuation in sapphire fibers, however the amount of reduction may be less than the thermally-induced attenuation at some temperatures. When the fibers were removed from the Co-60 irradiator at 233.3 hours, the added attenuation in the fibers rapidly decreased. In fact, the interior sapphire fiber recovered to approximately zero added attenuation.

Figure 73 and Figure 74 show the broadband change in the optical attenuation for the sapphire fibers loaded on the interior (top portion of the figures) and exterior (bottom portion of the figures) of the furnace at several times throughout the experiment. In these figures, added attenuation was plotted as a function of wavelength at various times and both the temperature and the total absorbed dose at each time are indicated for each curve in the legends of the plots. The temperatures that are shown are either the temperatures at the axial center of the furnace (top portions of the figures) or the exterior of the furnace (bottom portions of the figures), and the values that are shown for the absorbed dose are the values at the position corresponding to the peak dose rate. The widths of the lines shown in these figures indicate one sigma uncertainties. Figure 73 shows added attenuation spectra at several times during heating of a portion of the interior sapphire fiber. Figure 74 shows added attenuation at several times at room temperature after cooling the furnace from 1000 °C. The data at 234.8 hours were obtained after the experiment was removed from the Co-60 gamma irradiator.

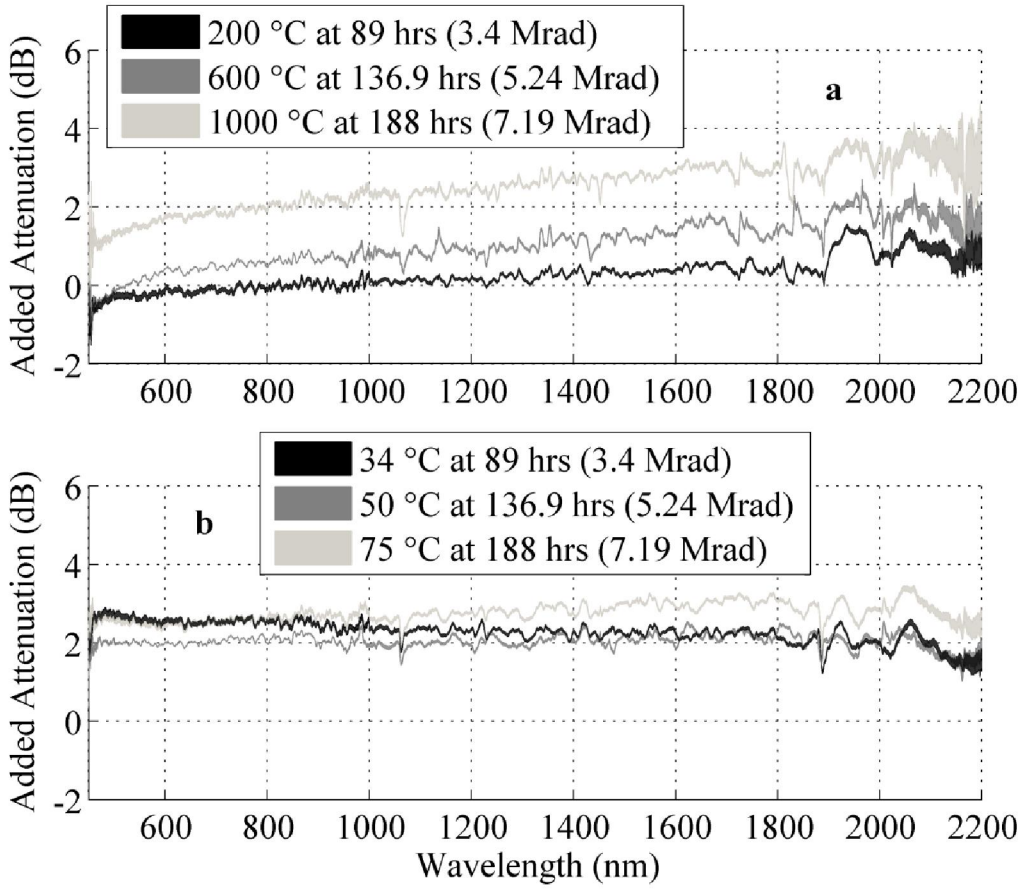

Figure 73: Added attenuation for the interior (a) and exterior (b) sapphire fibers as a function of wavelength at various times during heating of the interior fiber. The temperatures at the interior center (a) and exterior center (b) of the furnace and the value of the absorbed dose from Co-60 gamma rays at the position corresponding to the peak dose rate are indicated with each time. The widths of the lines shown in this figure indicate one sigma uncertainties.

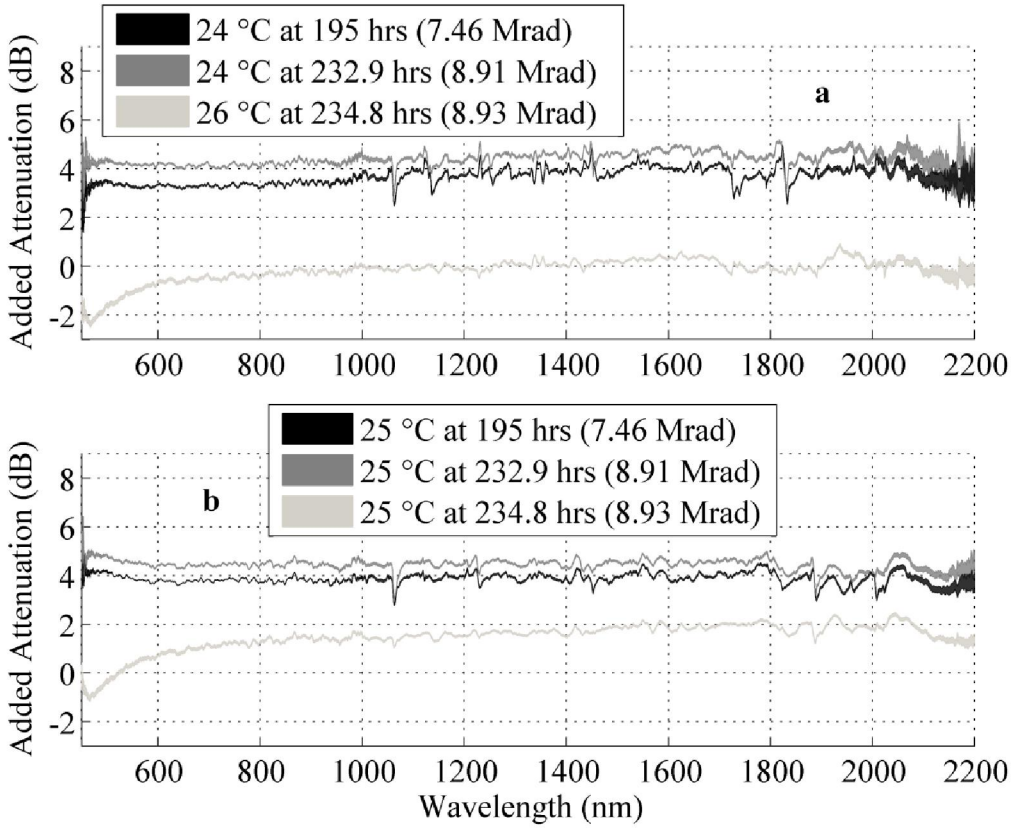

Figure 74: Added attenuation for the interior (a) and exterior (b) sapphire fibers as a function of wavelength at various times after the furnace cooled to room temperature. The temperatures at the interior center (a) and exterior center (b) of the furnace and the value of the absorbed dose from Co-60 gamma rays at the position corresponding to the peak dose rate are indicated with each time. The widths of the lines shown in this figure indicate one sigma uncertainties. Note that the experiment was removed from the irradiator at 233.3 hours.

Figure 74 shows that gamma radiation causes a seemingly broadband increase in the attenuation that saturated at between ~4-5 dB after accumulating an absorbed dose of almost 9 Mrad. Figure 73 shows that heating a portion of the interior sapphire fiber to temperatures above 200 °C, while continuing to accumulate dose, resulted in an increase in the attenuation, although the increase was more significant at higher wavelengths. This is most likely due to thermal annealing of defect centers with peak absorption at lower wavelengths.

7.3.3 Optical Attenuation in Sapphire Fibers Due to Reactor Irradiation at High Temperatures (1000 °C)

The heated reactor transmission experiments did not yield the results we hoped to obtain as our furnace to test the fiber to 1600°C failed after a day of irradiation. The electrical connection broke on the furnace due to an increase in gamma heating. A new furnace was quickly rigged to test reactor transmission experiments but had a lower temperature limit (~1000 °C) and so the following results are from the two reactor transmission experiments. A new experiment is currently underway to provide better results and we will update this section when they are done.

7.3.3.1 First Heated Reactor Irradiation Experiment

The first heated reactor irradiation experiment was performed in the molybdenum disilicide furnace at room temperature and at 300 °C. The sapphire fibers were irradiated at a reactor power of 10%, 30%, and 90%. Results are shown for one of the two sapphire fibers, since the results for the two sapphire fibers that were tested in this experiment were very similar. Figure 75 shows the added attenuation in the sapphire fibers at 600, 850, 1300, and 1550 nm as a function of time during the experiment. The temperature (at the center of the furnace) and the neutron flux (at the axial location of the peak neutron flux) are also shown as a function of time.

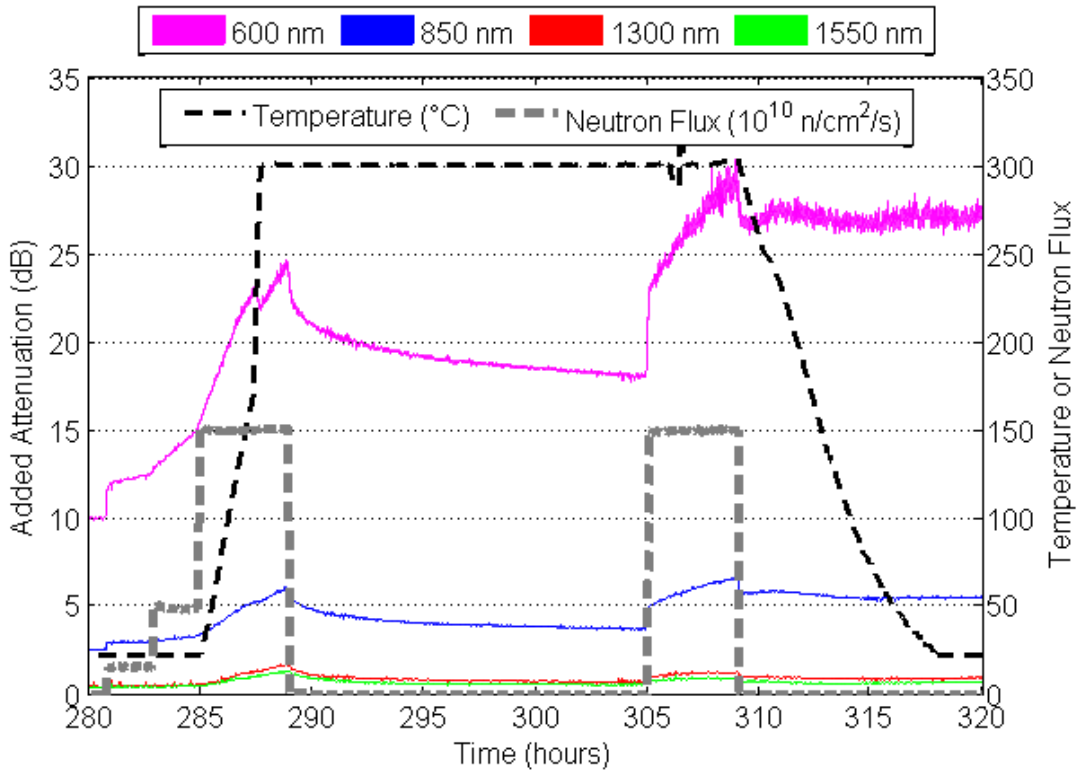

Figure 75: Added attenuation in the sapphire fiber at various wavelengths as a function of time during the first heated reactor irradiation experiment. The temperature (at the center of the furnace) and the neutron flux (at the axial location of the peak flux) are also shown as a function of time. The widths of the lines for the added attenuation data shown in this figure indicate one sigma uncertainties.

When the neutron flux was increased to 1.5×10^{12} n/cm^2/s near 285 hours, the increased gamma heating caused significant increases in temperature without any electrical heating. Therefore, a comparison of the added attenuation at a reactor power of 10%, 30%, and 90% is somewhat complicated by the fact that the temperature changed when the reactor power was increased to 90% power. At 287.4 hours, the furnace was powered in order to increase the temperature to 300 °C and to then maintain a constant temperature with electrical heating. The furnace temperature was maintained at 300 °C, after the reactor was shut down at 289 hours and after the reactor was restarted at 305 hours. The furnace failed near 306 hours, at which point the temperature fluctuated slightly, as shown in Figure 75. The gamma heating was able to maintain the temperature close to 300 °C until the reactor was eventually shut down near 309 hours.

A linear fit to the added attenuation data at 600 nm (the effects of reactor irradiation were most significant at this wavelength compared to the other wavelengths shown in Figure 75) was performed for each constant power reactor irradiation period to determine the slope of the increase in added attenuation as a function of reactor power. Data were fit during the first two hours of the 90% power irradiation that occured between 285 and 289 hours, so that the effects of increased temperature (due to gamma heating) would be minimized. Data was not fit between 305 and 309 hours, because the slope of the added attenuation appeared to be changing due to some transient effect.

Table 8 shows the slope of the added attenuation at 600 nm, the goodness of fit parameter for the linear fit, and the nominal reactor power (in percent of full power) for each constant power irradiation that was performed close to room temperature. The slope of the added attenuation at 600 nm increases, almost proportionally, with the reactor power. The ratio of the slope of the added attenuation during irradiation at 30% power to the slope during irradiation at 10% power (4.2:1) is larger than the ratio of the two reactor power levels (3:1). This could be because the slope of the added attenuation during irradiation at 10% power was small enough that it was significantly affected by noise in the measurement system (due to, for example, fluctuations in spectrometer sensitivities or light source intensity). The smaller value of the goodness of fit parameter during the irradiation at 10% power is evidence that the fit was not particularly accurate. The ratio of the slope of the added attenuation during irradiation at 90% power to the slope during irradiation at 30% power (3:1) is identical (within two significant figures) to the ratio of the two reactor power levels (3:1). Therefore, it appears that the slope of the added attenuation, at least at a wavelength of 600 nm, increases proportionally with the reactor power (or neutron flux). This is consistent with the idea that reactor irradiation causes displacement damage in the form of point defects, with very little defect recombination at room temperature.

Table 8: Results of the linear fits to the dynamic added attenuation data at 600 nm during the first heated reactor irradiation experiment. Data were fit for each constant power reactor irradiation period near room temperature.

Time Period (hours)	Nominal Reactor Power (percent)	Slope of Added Attenuation at 600 nm (dB/hr)	Goodness of fit parameter
281.2 to 282.8	10	0.26	0.877
283.1 to 284.9	30	1.1	0.991
285 to 286.6	90	3.3	0.997

7.3.3.2 Second Heated Reactor Irradiation Experiment

Because the molybdenum disilicide furnace failed during the first heated reactor irradiation experiment, the second heated reactor irradiation experiment was performed using the ThermCraft furnace. This furnace was used in the Co-60 irradiation experiments and it was not originally intended to be used as it has a Nickel, Chrome, Iron heating element which had a limit of 1000°C and activated heavily meaning that we could run only at a maximum of 30% power. In the second heated reactor irradiation experiment, the sapphire fibers were irradiated for two days, with approximately 8 hours spent each day at 10% reactor power. The temperature of the furnace was held constant during irradiation at four different temperatures for a period of about 4 hours at each

temperature. The tested temperatures included room temperature (with gamma heating up to 34 °C), and 300, 600, and 1000 °C. The exterior sapphire fiber (a fiber loaded outside of the furnace insulation) was irradiated under the same conditions as the interior (heated) fibers, except that the temperature remained less than 95 °C throughout the entire experiment.

Figure 76 shows added attenuation in the interior (Figure 76a) and exterior (Figure 76b) sapphire fibers at 650, 850, 1300, and 1550 nm as a function of time during the second heated reactor irradiation experiment. In addition to the added attenuation data, the temperature at the center of the furnace is also shown as a function of time in Figure 76a (for the interior sapphire fiber). The neutron flux (at the axial location of the peak neutron flux) is also shown as a function of time in Figure 76a and Figure 76b.

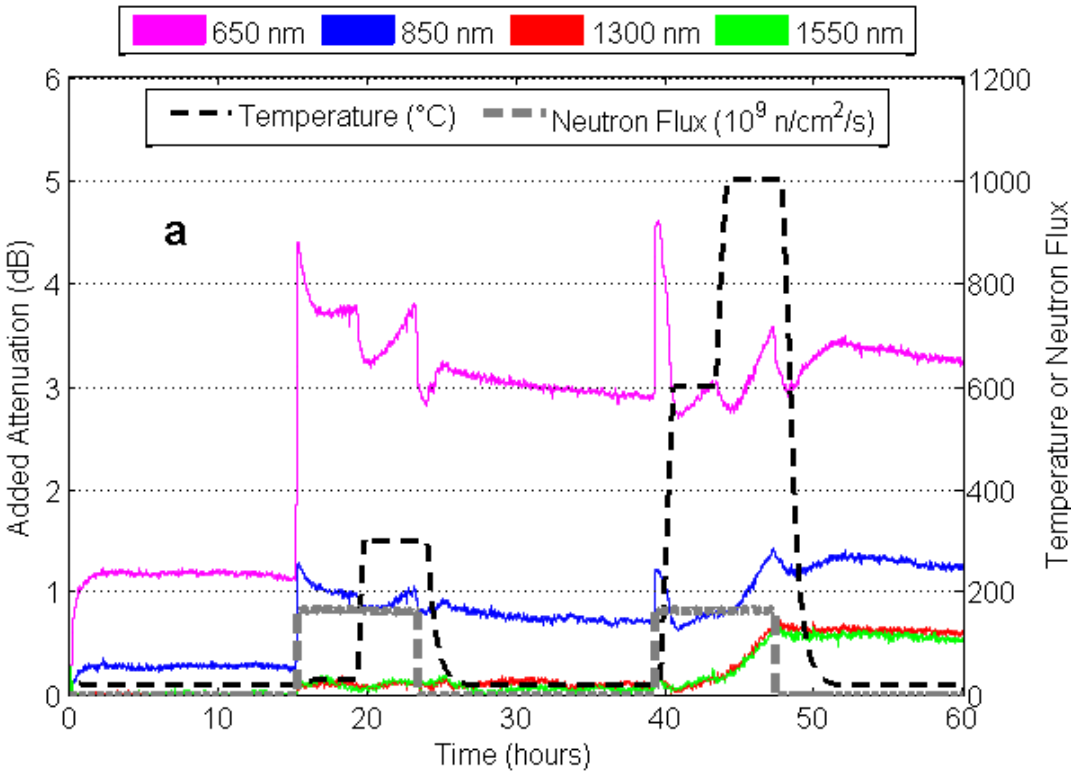

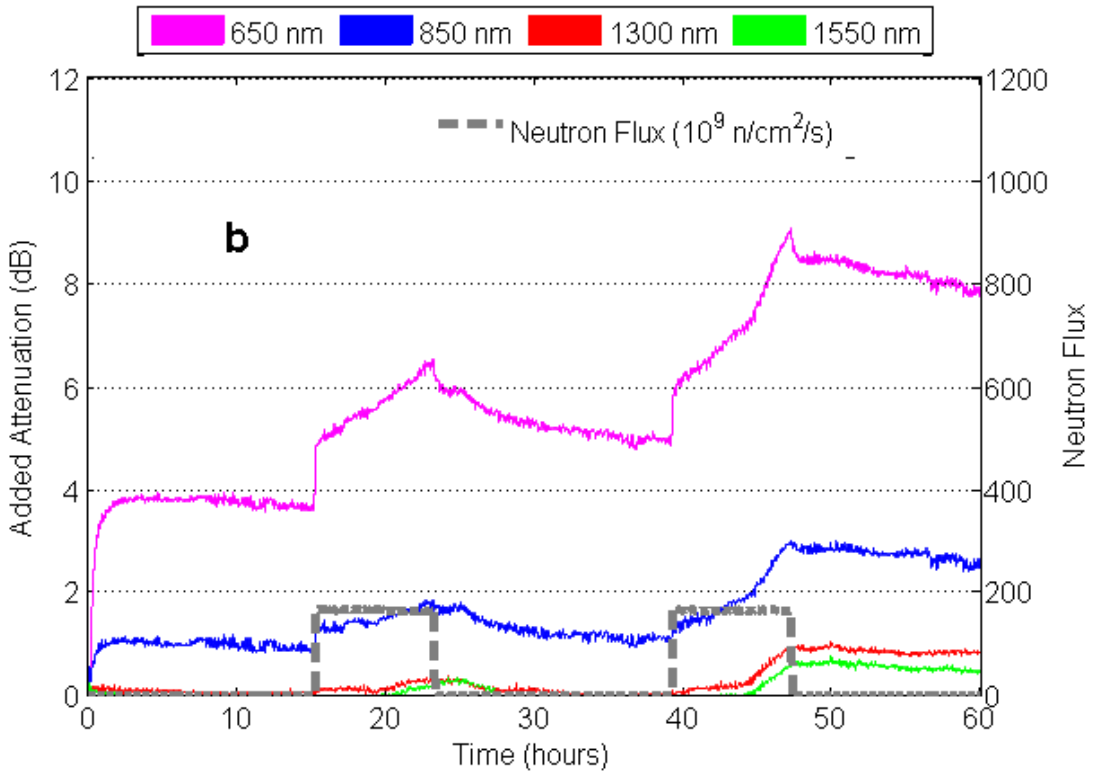

Figure 76: Added attenuation in the interior (Figure 76a) and exterior (Figure 76b) sapphire fibers at 650, 850, 1300, and 1550 nm as a function of time during the second heated reactor irradiation experiment. The temperature at the center of the furnace is shown as a function of time in Figure 76a (for the interior sapphire fiber), and the neutron flux (at the axial location of the peak neutron flux) is shown as a function of time in both Figure 76a and Figure 76b.

The results shown in Figure 76 are difficult to interpret because the periods of time during which the fibers were irradiated at constant temperature were relatively short. It appears as though there were transient effects taking place due to the combined effects of temperature and irradiation. The added attenuation increased rapidly in both the interior and exterior sapphire fibers, when the reactor irradiation first began at 15.3 hours. For the exterior fiber, the added attenuation increased linearly with continued irradiation beyond 15.3 hours, similar to what was observed in the unheated reactor irradiation experiment. The slope of the added attenuation in the exterior fiber generally remained approximately constant during each constant power irradiation period of the second heated experiment; however, the slope did increase near 44.8 hours, at which time the interior temperature of the furnace was being held constant at 1000 °C. It is proposed that the increase in the slope of the added attenuation in the exterior sapphire fiber near 44.8 hours was due to thermally-induced attenuation, as the temperature of the exterior of the furnace increased to approximately 95 °C when the interior furnace temperature was held constant at 1000 °C. The exterior sapphire fiber was not heated prior to irradiation. Previous heated experiments that were performed in the absence of radiation have shown thermally-induced increases in the attenuation of sapphire fibers at temperatures below 100 °C.

The added attenuation in the interior sapphire fiber decreased, during reactor irradiation prior to heating the fibers, immediately after the rapid increase at 15.3 hours. The explanation for this decrease is likely related to increased temperature of the interior sapphire fibers, due to the furnace insulation containing the heat generated by the gamma radiation emitted from the reactor.

The added attenuation reached a minimum near 17.6 hours, which was approximately the time when the temperature inside the furnace reached a dynamic equilibrium with a steady-state value of approximately 33.6 °C. With continued irradiation at 33.6 °C beyond 17.6 hours (between 17.6 and 19.3 hours), the added attenuation started to increase. It is likely that the slope of the added attenuation would have eventually reached a constant value if the irradiation at 33.6 °C were continued for a longer time before the temperature was increased to 300 °C.

Similar to what was observed when the irradiation was begun at 15.3 hours, increasing the temperature to 300 °C at 19.4 hours caused a transient decrease in the added attenuation of the interior sapphire fiber. The added attenuation reached a minimum near 20.3 hours, before increasing with continued irradiation at 300 °C beyond 20.3 hours. The slope of the added attenuation may have even reached a constant value before the end of the irradiation at 300 °C (at 23.3 hours); however, it is difficult to say for certain that the slope of the added attenuation would not have continued to change with continued irradiation at 300 °C, due to the short period of time that the fiber was irradiated at constant temperature.

During the second day of irradiation, more of the same dynamic behavior was observed in the added attenuation in the interior sapphire fiber during irradiation at 600 °C and 1000 °C. The added attenuation increased, when the irradiation first began at 39.3 hours, but then decreased significantly as soon as the temperature was increased. The added attenuation reached a minimum during irradiation at 600 °C at 40.8 hours, and then increased, before the temperature was increased (eventually up to 1000 °C), at 43.4 hours. During irradiation at 1000 °C, the added attenuation in the interior fiber at 650 nm initially decreased, reached a minimum near 44.4 hours, and then increased until the irradiation ended at 47.3 hours. At 850, 1300, and 1550 nm, the slope of the added attenuation increased when the temperature was increased to 1000 °C. It is possible that some thermally-induced increases in attenuation occurred when the temperature was increased to 1000 °C.

In general, the added attenuation in the interior sapphire fiber decreased significantly with increased temperature. The added attenuation at 1300 and 1550 nm remained less than ~1 dB in both the interior and exterior sapphire fibers throughout the entire experiment. It is difficult to predict the long-term performance of sapphire fibers, under irradiation at high temperature, based on the data presented in Figure 76. This is because the data shown in this figure are dominated by transient effects. For this reason, a third heated reactor irradiation experiment was performed during which the fibers were irradiated at constant power (30% reactor power) for approximately 8 hours for each temperature that was tested. The OSURR can only be operated continuously during normal business hours, so 8 hours represents the longest possible continuous irradiation time in this facility. The results of the third heated reactor irradiation experiment are presented in section 7.3.3.3.

7.3.3.3 Third Heated Reactor Irradiation Experiment

Two sapphire fibers were loaded again on the inside and outside of the ThermCraft furnace during the third heated reactor irradiation experiment (3rd reactor experiment overall, 2nd experiment using the ThermCraft furnace). This third test was run at 30% power and the results are shown for both the exterior and interior sapphire fiber on the following pages. Both fibers were subjected to the same irradiation conditions with the only difference being that the exterior fibers were not actively heated.

Figure 77 shows added attenuation in the interior (Figure 77a) and exterior (Figure 77b) sapphire fibers at 650, 850, 1300, and 1550 nm as a function of time during the experiment between 133 and 175 hours. During this time, the sapphire fibers were irradiated at 30% power, while the temperature of the furnace increased to 59 °C (due to gamma heating) and 300 °C (due to

electrical and gamma heating). In addition to the added attenuation data, the temperature at the center of the furnace is shown as a function of time in Figure 77a (for the interior sapphire fiber). The neutron flux (at the axial location of the peak neutron flux) is also shown as a function of time in both Figure 77a and Figure 77b.

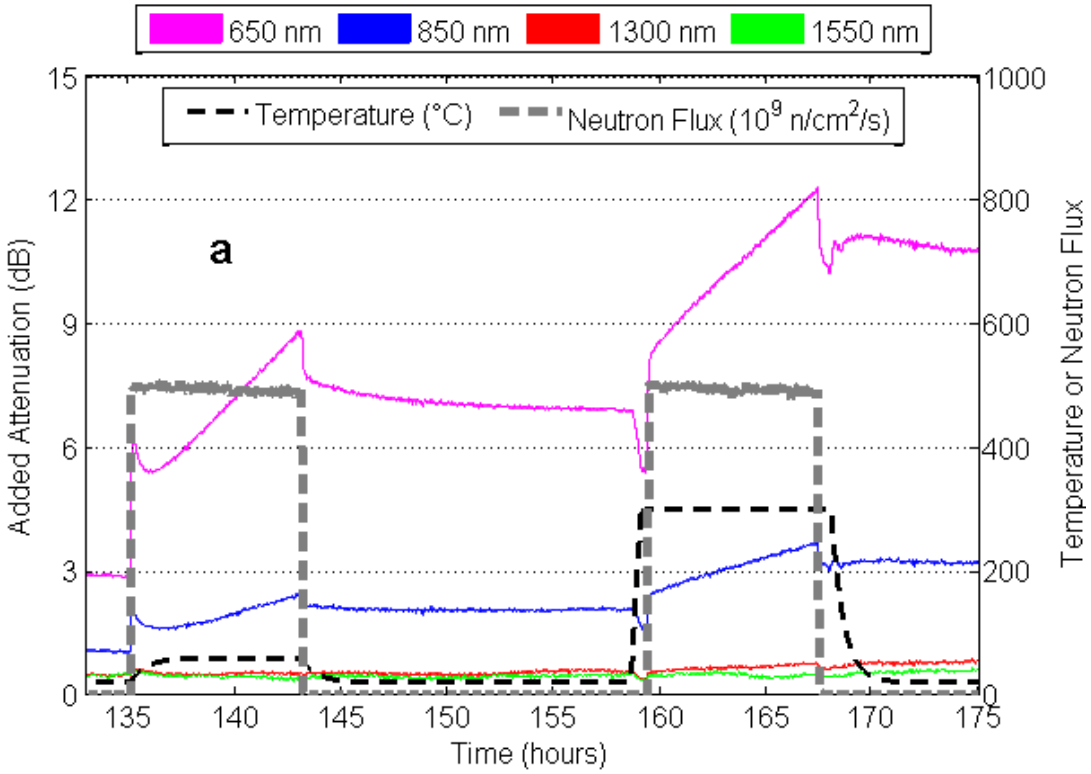

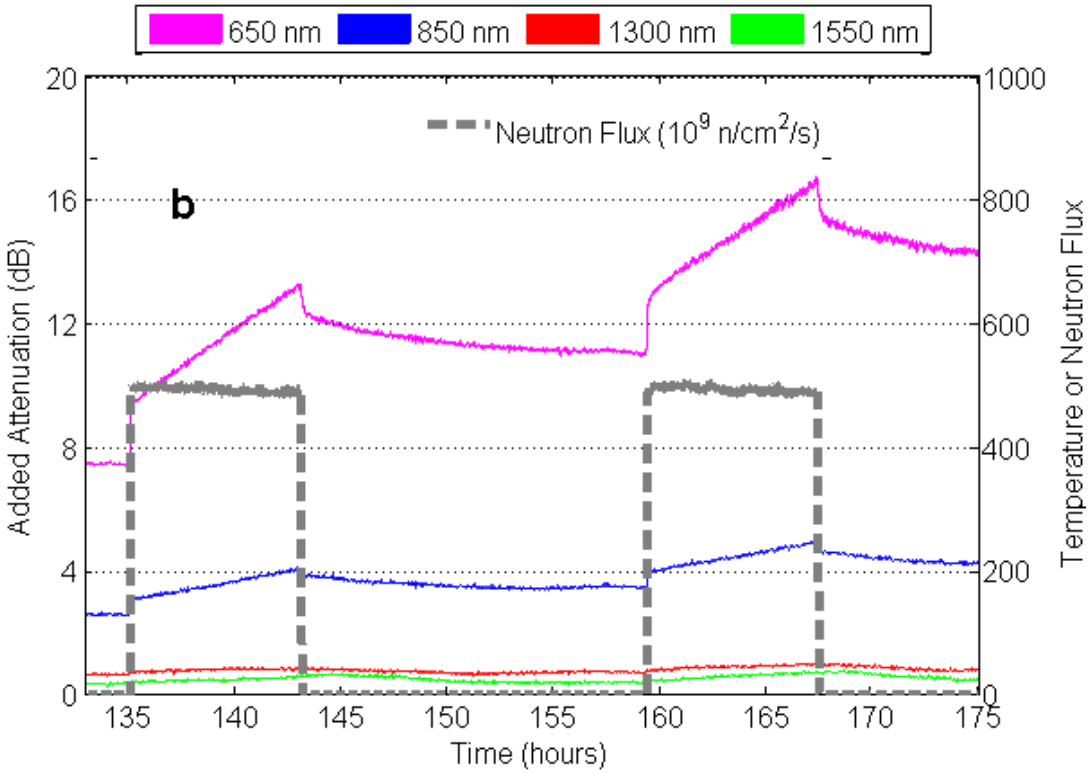

Figure 77: Added attenuation in the interior (Figure 77a) and exterior (Figure 77b) sapphire fibers at 650, 850, 1300, and 1550 nm as a function of time during the third heated reactor irradiation experiment between 133 and 175 hours. The temperature at the center of the furnace is shown as a function of time in Figure 77a (for the interior sapphire fiber), and the neutron flux (at the axial location of the peak neutron flux) is shown as a function of time in both Figure 77a and Figure 77b.

The added attenuation in the interior sapphire fiber between 133 and 175 hours (Figure 77a) shows dynamic behavior similar to what was observed at the start of the second heated irradiation experiment. When the irradiation was first started at 135.2 hours, the added attenuation increased rapidly, but then immediately started to decrease due to increased temperature that was caused by gamma heating inside the furnace insulation. The transient decrease in the added attenuation concluded by about 136.5 hours, after which the added attenuation increased with a constant slope. This transient behavior can likely be explained by rapid ionization of existing defect centers, when the irradiation first started, in competition with increased charge recombination when the temperature increased. Constant accumulation of defect centers via displacement damage, and their immediate activation (due to ionizing radiation), is responsible for the linear increase in added attenuation following the transient. The added attenuation decreased when the reactor was shut down at 143.1 hours. Increasing the temperature to 300 °C prior to the second day of irradiation caused a significant decrease in the added attenuation; however, as soon as the irradiation began at 159.5 hours, the added attenuation increased rapidly to values that were only slightly smaller than those observed at the end of the previous irradiation that was performed at 59 °C. This behavior can also be explained by a competition between ionization and charge recombination. The ionization rate decreased significantly, when the reactor was shut down, and rapidly increased when the reactor irradiation resumed. Charge recombination increased, when the temperature was increased, which explains the reduction in the added attenuation when the temperature increased to 300 °C. Constant power irradiation at 300 °C caused an increase in added

attenuation with a constant slope due to displacement damage from neutrons. When the reactor was shut down at 167.4 hours, the added attenuation decreased rapidly while the temperature was maintained at 300 °C. When the furnace was shut down and the temperature started to drop at 168 hours, the added attenuation increased temporarily and then approached a steady-state value, after the temperature reached room temperature near 171 hours. The dynamic behavior after the reactor was shut down at 167.4 hours can also be explained by competition between ionization and thermally-induced charge recombination.

Figure 78 shows added attenuation in the interior (Figure 78a) and exterior (Figure 78b) sapphire fibers at 650, 850, 1300, and 1550 nm as a function of time during the experiment between 180 and 230 hours. During this time, the sapphire fibers were irradiated at 30% power, while the temperature of the furnace was held constant at 600 and 1000 °C. In addition to the added attenuation data, the temperature at the center of the furnace is also shown as a function of time in Figure 78a (for the interior sapphire fiber). The neutron flux (at the axial location of the peak neutron flux) is also shown as a function of time both in Figure 78a and Figure 78b.

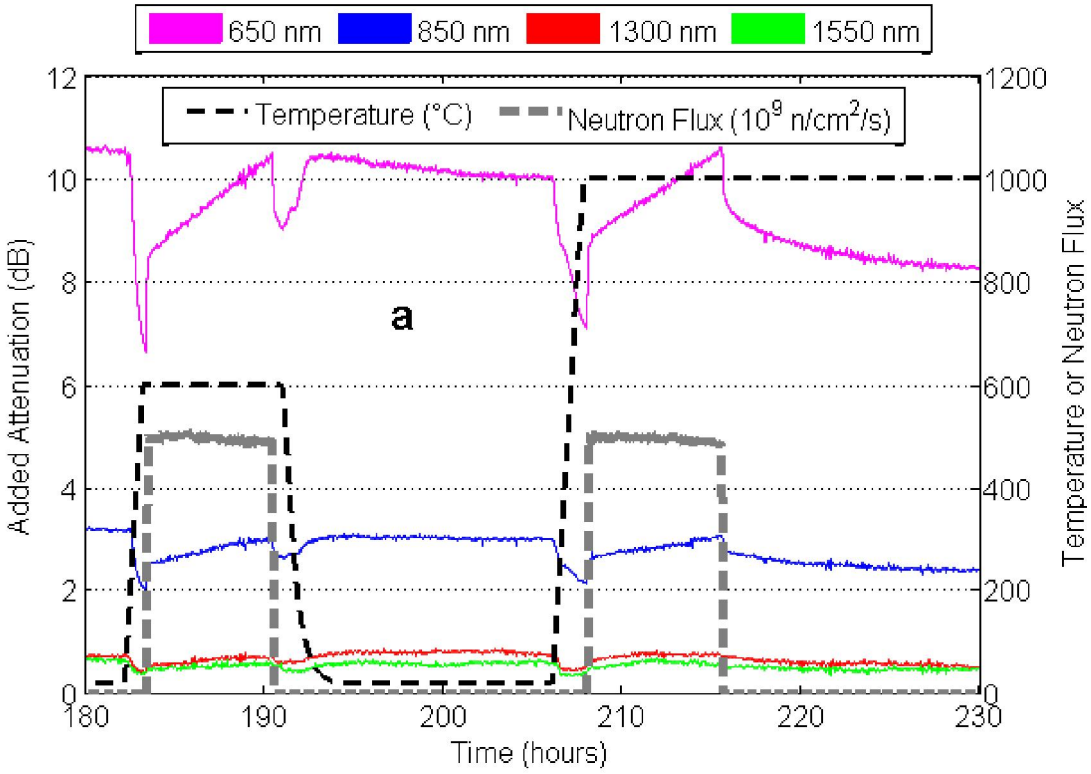

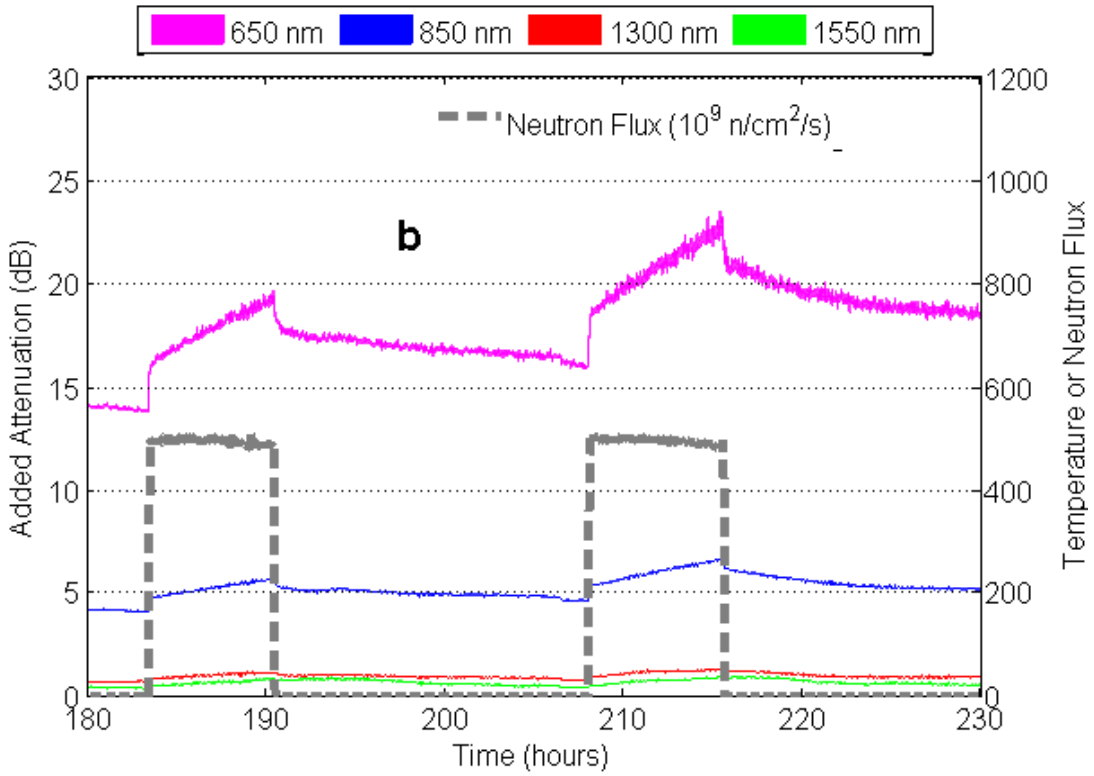

Figure 78: Added attenuation in the interior (Figure 78a) and exterior (Figure 78b) sapphire fibers at 650, 850, 1300, and 1550 nm as a function of time during the third heated reactor irradiation experiment between 180 and 230 hours. The temperature at the center of the furnace is shown as a function of time in Figure 78a (for the interior sapphire fiber), and the neutron flux (at the axial location of the peak neutron flux) is shown as a function of time in both Figure 78a and Figure 78b.

The added attenuation in the interior (Figure 78a) and exterior (Figure 78b) sapphire fibers between 180 and 230 hours generally show dynamic behavior similar to what was observed between 133 and 175 hours. However, the slope of the added attenuation data for the interior sapphire fiber during constant power irradiation at 600 and 1000 °C appears to be smaller than the slope during constant power irradiation at 59 and 300 °C. The added attenuation data in the interior sapphire fiber at 650 nm were fit for each constant temperature irradiation period to determine the slope of the added attenuation as a function of temperature for constant (30%) reactor power. Table 9 shows the slope of the added attenuation at 650 nm, the goodness of fit parameter for the linear fit, and the temperature for each data set that was fit.

Table 9: Results of the linear fits to the dynamic added attenuation data at 650 nm during the third heated reactor irradiation experiment. Data were fit for each constant temperature reactor irradiation at 30% reactor power.

Time period	Temperature (°C)	Slope of added attenuation at 650 nm (dB/hr)	Goodness of fit parameter

137 to 143 hours	56	0.52	0.999
160 to 167 hours	300	0.49	0.999
184 to 190 hours	600	0.27	0.990
208.5 to 215 hours	1000	0.23	0.993

Table 9 shows that increasing temperature caused a monotonic decrease in the slope of the added attenuation at 650 nm. This is consistent with the idea that increased temperature reduced the formation of optically active defect centers either by annealing of point defects, increased charge recombination at existing point defects, or some combination of both processes. The slope of the added attenuation decreased most significantly when the temperature during irradiation was increased from 300 to 600 °C. However, the ability to draw conclusions from the data presented in Table 9 is limited by the fact that only a portion of the interior sapphire fiber was heated. Because only a portion of the interior sapphire fiber was heated, there was a section of the interior sapphire fiber that was exposed to reactor irradiation at approximately room temperature, even when the furnace temperature was increased as high as 1000 °C. The slopes that were determined for the increase in added attenuation, during reactor irradiation at each temperature, include effects both in the heated portion of the fiber and the unheated portion of the fiber.

The separate effects of reactor irradiation on the heated and unheated portions of the interior sapphire fiber were estimated using a simple calculation. This calculation first assumed that during constant power reactor irradiation, the time derivative of the added attenuation per unit length of fiber is proportional to the neutron energy deposition rate. The neutron energy deposition rate is proportional to the neutron flux, so long as the neutron flux energy spectra do not vary significantly with location in the 7 inch dry tube facility. It was further assumed that the temperature was spatially constant over the heated region of the fiber (with the temperature equal to the measured temperature at the center of the furnace for each constant temperature irradiation period) and spatially constant over the unheated region of the fiber (with the temperature always equal to room temperature in this section of the fiber). These assumptions are summarized in Equation [1].

$$\frac{dA_T}{dt}(T) = \frac{dA_H}{dt}(T) + \frac{dA_{UH}}{dt}$$

$$\frac{dA_H}{dt}(T) = \int_{L_H} \frac{dA(x,T)}{dt}\, dx$$

$$\frac{dA_{UH}}{dt} = \int_{L_{UH}} \frac{dA(x,T = 22\ °\text{C})}{dt}\, dx$$

$$\frac{dA(x,T)}{dt} = f(T(x))\phi(x)$$

where:

A_T = Total (integrated over the entire length of the sapphire fiber) added attenuation at 650 nm (dB)

A_H = Added attenuation at 650 nm (dB) in the heated portion of the sapphire fiber

A_{UH} = Added attenuation at 650 nm (dB) in the unheated portion of the sapphire fiber

t = Time (seconds) during constant power reactor irradiation

T = Temperature (°C)

A = Added attenuation per unit length at 650 nm (dB m^{-1})

x = Position along the length of the sapphire fiber (m)

L_H = Length of the heated region of the sapphire fiber (m)

L_{UH} = Length of the unheated region of the sapphire fiber (m)

f = Response function accounting for temperature dependence of the radiation-induced attenuation (dB m^{-1} cm^2)

ϕ = Neutron flux (cm^{-2} s^{-1})

[1]

The results presented in section 7.3.3.1 showed that $\frac{dA_T}{dt}$ is proportional to the neutron flux during constant power reactor irradiation. Between 137 and 143 hours, both the heated and unheated sections of the fiber were irradiated at constant reactor power at close to room temperature (the temperature of the interior of the furnace increased to about 59 °C due to gamma heating, but these temperature effects are neglected in the present analysis). Between 137 and 143 hours, the following relations can be written.

$$\frac{dA_H}{dt}(T = 22\ ^\circ\mathrm{C}) = f(T = 22\ ^\circ\mathrm{C}) \int_{L_H} \phi(x)\, dx$$

$$\frac{dA_{UH}}{dt} = f(T = 22\ ^\circ\mathrm{C}) \int_{L_{UH}} \phi(x)\, dx$$

$$\frac{dA_T}{dt}(T = 22\ ^\circ\mathrm{C}) = f(T = 22\ ^\circ\mathrm{C})\left[\int_{L_H} \phi(x)\, dx + \int_{L_{UH}} \phi(x)\, dx\right]$$

$$\frac{\dfrac{dA_{UH}}{dt}}{\dfrac{dA_T}{dt}(T = 22\ ^\circ\mathrm{C})} = \frac{\displaystyle\int_{L_{UH}} \phi(x)\, dx}{\displaystyle\int_{L_H} \phi(x)\, dx + \int_{L_{UH}} \phi(x)\, dx}$$

$$\frac{\dfrac{dA_H}{dt}(T = 22\ ^\circ\mathrm{C})}{\dfrac{dA_T}{dt}(T = 22\ ^\circ\mathrm{C})} = \frac{\displaystyle\int_{L_H} \phi(x)\, dx}{\displaystyle\int_{L_H} \phi(x)\, dx + \int_{L_{UH}} \phi(x)\, dx} \qquad [2]$$

Using the relations shown in Equation [2], the following relations can be written for $\frac{dA_H}{dt}(T)$.

$$\frac{dA_H}{dt}(T) = \frac{dA_T}{dt}(T) - \frac{dA_{UH}}{dt}$$

$$\frac{dA_H}{dt}(T) = \frac{dA_T}{dt}(T) - \frac{dA_T}{dt}(T = 22\ ^\circ\mathrm{C}) \frac{\displaystyle\int_{L_{UH}} \phi(x)\, dx}{\displaystyle\int_{L_H} \phi(x)\, dx + \int_{L_{UH}} \phi(x)\, dx} \qquad [3]$$

The spatial profile (in the axial direction) of the neutron energy deposition rate (assumed to be proportional to $\phi(x)$) in the 7 inch dry tube facility was determined from MCNP simulations of the OSURR (see section 2 for more details regarding the MCNP model). Figure 79 shows the axial profile of the normalized neutron energy deposition rate (neutron energy deposition in sapphire) obtained from the MCNP simulations. The energy deposition rates presented in Figure 79 are normalized to the peak energy deposition rate in the facility. Also illustrated in Figure 79 are the locations of the heated (L_H) and unheated (L_{UH}) regions of the sapphire fibers.

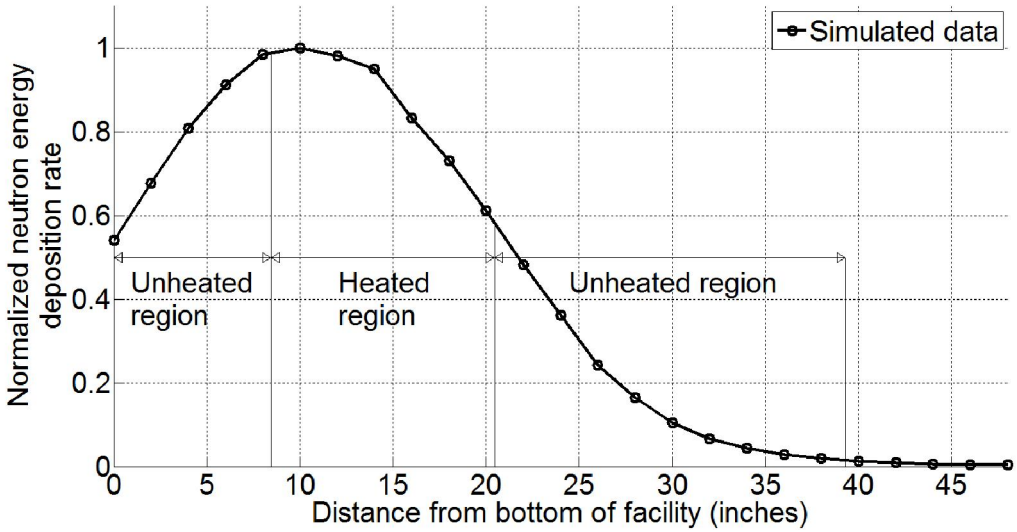

Figure 79: Spatial profile (in the axial direction) of the normalized neutron energy deposition rate (energy deposition in sapphire) in the 7 inch dry tube facility. Energy deposition rates were determined from MCNP simulations. The energy deposition rates were normalized to the peak energy deposition rate. The heated and unheated regions of the sapphire fiber used in the third heated reactor irradiation experiment are also indicated in the figure.

The data shown in Figure 79 were used to calculate $\frac{\int_{L_H} \phi(x)\,dx}{\int_{L_H} \phi(x)\,dx + \int_{L_{UH}} \phi(x)\,dx}$ and $\frac{\int_{L_{UH}} \phi(x)\,dx}{\int_{L_H} \phi(x)\,dx + \int_{L_{UH}} \phi(x)\,dx}$. These values were calculated to be 52% and 48%, respectively. Using these values and the data presented in Table 9 for $\frac{dA_T}{dt}(59\ ^\circ\mathrm{C})$ (assumed to be equal to $\frac{dA_T}{dt}(22\ ^\circ\mathrm{C})$), $\frac{dA_{UH}}{dt}(22\ ^\circ\mathrm{C})$ can be calculated using Equation [2] to be 0.48*0.52 dB/hr, or 0.25 dB/hr. Table 9 shows that $\frac{dA_T}{dt}(T = 600\ ^\circ\mathrm{C})$ and $\frac{dA_T}{dt}(T = 1000\ ^\circ\mathrm{C})$ are equal to 0.27 and 0.23 dB/hr, respectively. By subtracting $\frac{dA_{UH}}{dt}(22\ ^\circ\mathrm{C})$ from these values (see Equation [3]), $\frac{dA_H}{dt}(T = 600\ ^\circ\mathrm{C})$ and $\frac{dA_H}{dt}(T = 1000\ ^\circ\mathrm{C})$ are calculated to be 0.02 and -0.02 dB/hr, respectively. Therefore, according to the calculations presented above, essentially all of the increase in the added attenuation of the interior sapphire fiber that was observed at 650 nm during irradiation at 30% reactor power at temperatures of 600 and 1000 °C was due to reactor radiation-induced attenuation in the unheated portion of the sapphire fiber. In other words, the rate of

increase of the added attenuation at 650 nm in the heated portion of the sapphire fiber was essentially zero during 30% reactor power irradiation at temperatures of 600 and 1000 °C. While there is some amount of uncertainty in the analysis presented in this section, it appears that heating the interior sapphire fibers to temperatures of 600 °C or greater during 30% power reactor irradiation caused significant reduction (or possibly entire elimination) of the rate of growth of the added attenuation at 650 nm in the heated portion of the interior sapphire fiber.

7.3.3.4 Summary of Heated Reactor Irradiation Experiments

During the heated reactor irradiation experiments, in-situ measurements of the optical transmission in commercially available 100 μm diameter sapphire optical fibers were made during exposure to reactor irradiation at various reactor power levels and at various temperatures. During the first heated reactor irradiation experiment, sapphire fibers were first irradiated at approximately room temperature at reactor power levels of 10, 30, and 90% reactor power. The fibers were then irradiated at 90% power while holding the temperature constant at 300 °C. Fitting the slope of the added attenuation vs. time data showed that the slope of the linear increase in added attenuation during constant power irradiation increased proportionally with increasing reactor power. This finding is consistent with the idea that reactor irradiation generates displacement damage from high energy neutrons, and very little defect recombination is taking place near room temperature. The furnace that was used to heat the fibers during irradiation failed during the second day of the first heated reactor irradiation experiment, after operating at 300 °C during 90% power reactor irradiation for about an hour. For this reason, a second heated reactor irradiation experiment was performed using the ThermCraft furnace.

During the second heated reactor irradiation experiment, two sapphire fibers were irradiated for two days, with approximately 8 hours spent each day at 10% reactor power. The temperature of the furnace was held constant during irradiation at four different temperatures for a period of about 4 hours at each temperature. The tested temperatures included room temperature (with gamma heating of the furnace interior up to 34 °C), and 300, 600, and 1000 °C. One of the two sapphire fibers (referred to as the exterior sapphire fiber, which was loaded outside of the furnace insulation) was irradiated under the same conditions as the interior (heated) fiber, except at a much lower temperature. The results of the second heated irradiation experiment were difficult to interpret, because the periods of time during which the fibers were irradiated at constant temperature were relatively short. It appeared as though there were transient effects taking place due to the combined effects of temperature and irradiation. In general, during reactor irradiation, the increase in added attenuation in the interior sapphire fiber was significantly less than that observed in the exterior sapphire fiber. The added attenuation at 1300 and 1550 nm remained less than ~1 dB in both the interior and exterior sapphire fibers throughout the entire experiment. However, it was difficult to predict the long-term performance of sapphire fibers under irradiation at high temperature based on the data obtained in the second heated reactor irradiation experiment, since the data appeared to be dominated by transient effects.

Because of the significance of the transient effects that were observed during the limited time that the fibers were irradiated at constant reactor power and constant temperature during the second heated reactor irradiation experiment, a third heated reactor irradiation experiment was performed. During the third heated reactor irradiation experiment, the same two sapphire fibers that were used in the second heated reactor irradiation experiment were irradiated at constant power (30% reactor power) for approximately 8 hours for each temperature that was tested (59, 300, 600, and 1000 °C). The added attenuation in the interior and exterior sapphire fibers during the experiment generally showed dynamic behavior similar to what was observed in the first

heated reactor irradiation experiment. The added attenuation showed a linear increase with increasing time at constant reactor power for each of the temperatures that were tested. The added attenuation data in the interior sapphire fiber at 650 nm were fit for each constant temperature irradiation period, during the third heated irradiation experiment, to determine the slope of the added attenuation as a function of temperature, for constant (30%) reactor power. The rate of increase of the added attenuation during constant power reactor irradiation monotonically decreased with increasing temperature up to 1000 °C, with the most significant decrease occurring between 300 and 600 °C.

The ability to draw conclusions from the fitting was limited by the fact that only a portion of the interior sapphire fiber was heated. The separate effects of reactor irradiation on the heated and unheated portions of the interior sapphire fiber were estimated using a simple calculation that assumed that, for constant power reactor irradiation, the time derivative of the added attenuation is proportional to the neutron flux. Using data for the spatial (in the axial direction) profile of the neutron deposition rate in the 7 inch dry tube facility (determined from MCNP simulations), it was estimated that the heated and unheated regions of the sapphire fiber were exposed to 52% and 48% of the total neutron flux integrated over the entire region of the sapphire fiber, respectively. Using this approximation, it was found that the slope of the added attenuation in the interior sapphire fiber, during 30% power reactor irradiation at temperatures of 600 and 1000 °C, was approximately equal to the estimated contribution to the measured added attenuation, at room temperature, from effects in the unheated region of the sapphire fiber alone. Therefore, according to the calculations presented in this work, the majority of (if not all of) the increase in the added attenuation, of the interior sapphire fiber that was observed at 650 nm during irradiation at 30% reactor power at temperatures of 600 and 1000 °C, was due to reactor radiation-induced attenuation in the unheated portion of the sapphire fiber. While there was some uncertainty in the analysis presented in this section, it appears that heating the interior sapphire fibers, to temperatures of 600 °C or greater during 30% power reactor irradiation, caused significant reduction (or possibly entire elimination) of the rate of growth of the added attenuation at 650 nm in the heated portion of the interior sapphire fiber.

8 Task G - Design and Fabrication of Equipment for Sensor Experiments

8.1 Deliverables

- A sensor readout system for testing multiple Fabry-Perot interferometric temperature and strain sensors
- A functional test rig for testing sapphire Fabry-Perot interferometric strain sensors at temperatures up to 1500 °C

8.2 Timeline and Task Status

- Start Date: 7/1/2013
- Planned Completion Date: ?
- Task Status: 0% - Likely never to be completed

8.3 Progress Toward the Completion of Deliverables

8.3.1 A Sensor Readout System for Testing Multiple Fabry-Perot Interferometric Temperature and Strain Sensors

In the first quarter of this project, OSU submitted a purchase order to Lambda Instruments, Inc. (the industrial partner on this project) for the following equipment: 1. An optical interferometric sensor readout system operating at 1550 nm with software, 2. A 16-channel optical multiplexer, 3. Two 2 meter lengths of sapphire fiber fused to silica lead fibers (henceforth referred to as sapphire fiber assemblies), 4. Four sapphire fiber-based temperature sensors, and 5. Four sapphire fiber-based strain sensors. OSU has not received any of the items that were ordered as of Q20 and OSU does not expect the equipment to ever be delivered. Lambda Instruments has informed OSU that it cannot create the equipment and sensors that were to be tested for this project. Lambda Instruments has since filed for bankruptcy and changed their name. Without the sensors or readout system, OSU has had to improvise to complete the goals of this project. OSU has devised a way of making a sapphire fiber that is capable of making distributed temperature measurements using a sensing technique called Optical Frequency Domain Reflectometry. More information about this will be given in Chapter 9. To summarize, Lambda Instruments was unable to deliver the equipment that was to be tested for this project, and thus this deliverable will never be accomplished, but OSU has invented its own sapphire optical fiber sensors and the results of their testing can be seen in the proceeding chapter.

9 Task H - High Temperature Functional Performance Testing and Irradiation Survivability Testing of Sapphire Fiber-Based Sensors

9.1 Deliverables

- Functional performance of sapphire sensors up to 1500 °C
- Survivability of sapphire temperature sensors irradiated with Co-60 gamma rays
- Survivability of sapphire temperature sensors irradiated with reactor neutrons and gamma rays

9.2 Timeline and Task Status

- Start Date: 7/1/2014
- Planned Completion Date: 9/30/2017
- Task Status: 100%

9.3 Progress Toward the Completion of Deliverables

9.3.1 Determination of the Effects of High Temperature on Sapphire Optical Fiber Transmission

In Chapter 7, we discovered that the light transmission in sapphire optical fiber exhibits high losses at high temperatures across all the wavelengths that were tested (450-2300nm). The transmission results from the heated sapphire fiber experiment are shown in Figure 64. The results show small increases in light attenuation that reach a dynamic equilibrium with each step in temperature up to 1400 °C. At 1400 °C, the added attenuation in the sapphire optical fiber appears to increase across all light wavelengths without reaching equilibrium. This large increase in light attenuation would inhibit sapphire sensors from operating effectively at high temperatures. This issue must be addressed if sapphire sensors are to be used at temperatures over 1300 C.

Upon completion of the high temperature transmission experiments with sapphire optical fiber, the fiber was removed from the furnace and analyzed under an optical microscope. In Figure 80, three photos of the sapphire fiber are shown. The photo on the left was taken at 4x magnification and the middle and right photos were taken at 40x magnification. The photo on the left shows two fibers: a sapphire fiber that was heated to 1500 °C (top) and a virgin sapphire fiber (bottom). The heated fiber shows a brown discoloration and is visibly less transparent than the virgin fiber. The two other photos show 40x views of the virgin fiber (middle) and the heated fiber (right). The virgin fiber has a very smooth surface texture compared to that of the heated fiber. The heated fiber appears to have some kind of nucleation or bubbling occurring on the surface of the fiber. Because sapphire fibers rely on the fiber/air interface for maintaining total internal reflection, the non-uniform surface condition could cause increased leakage, which may have contributed to the observed increases in light attenuation.

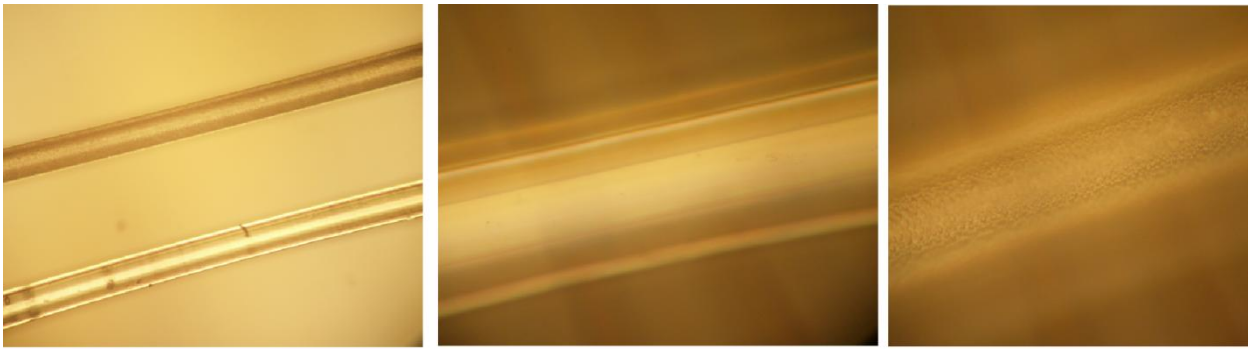

Figure 80: Pictures of sapphire fiber under various magnifications; (Left) 4x comparison of the virgin (bottom) and heated (top) sapphire fiber, (Middle) 40x image of virgin sapphire fiber and (Right) 40x image of heated sapphire fiber.

To further investigate the surface of the heated sapphire optical fiber, an analysis of the cross section of the sapphire fiber was conducted using electron microscopy. SEM images of the heated fiber surface are shown in Figure 81. The SEM images confirm the bubble nucleation on the surface of the heated sapphire fiber. These bubbles may have resulted from a chemical reaction between the sapphire fiber and the surrounding air at high temperatures. The bubbles vary in size, but they consistently cover the fiber, along the entire length of the heated section of the fiber.

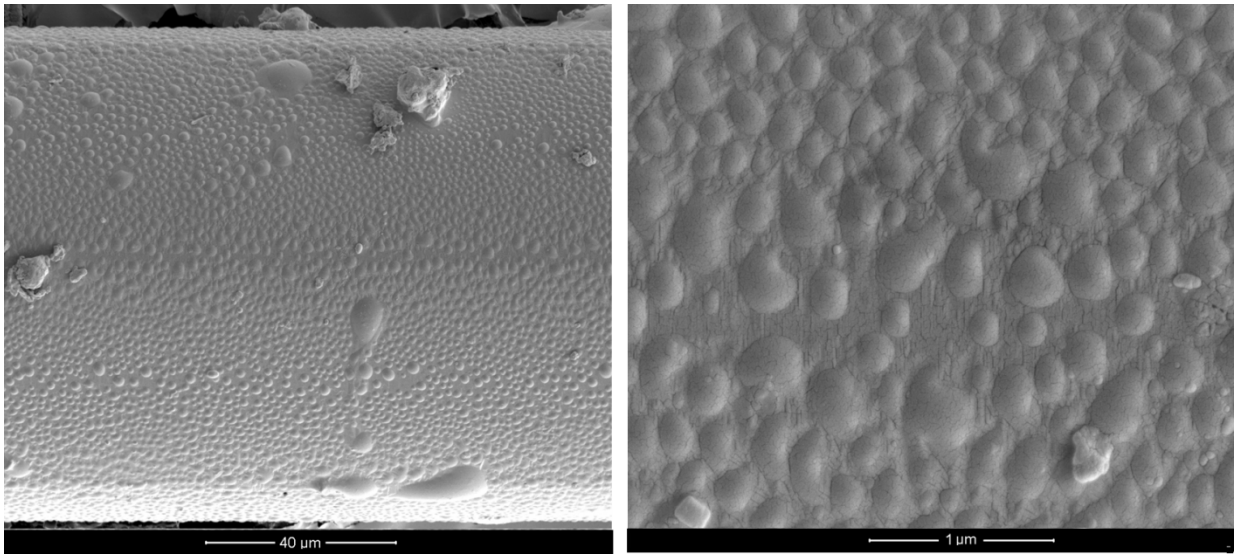

Figure 81: SEM images of the heated sapphire fiber under various magnifications.

To create a sample for TEM microscopy, the sapphire fiber was prepared using a Nova 600 Nano Lab DualBeam SEM / FIB. The Nova 600 was used to coat the sapphire fiber in gold and platinum and then mill a cross section of the fiber surface to an appropiate depth for TEM analysis (100 nm). TEM images of the cross section of the surface of a heated and a virgin sapphire fiber can be seen in Figure 82. The light area near the top of the images is the gold coating. The bright dendritic features in the middle of the images are the platinum coating and the dark area at the bottom of the image is the cross section of the sapphire fiber surface. The heated sapphire fiber

surface is much less uniform compared to the smooth, flat surface of the virgin sapphire fiber. There also appears to be a dark area on the surface of the heated sapphire fiber. A TEM image of this dark area with greater magnification can be seen in Figure 83. The dark area that can be observed in Figure 82 and Figure 83 is a surface effect that extends around most of the perimeter of the heated sapphire fiber. The darkness of the region indicates that it is less dense than the α-Al_2O_3 phase.

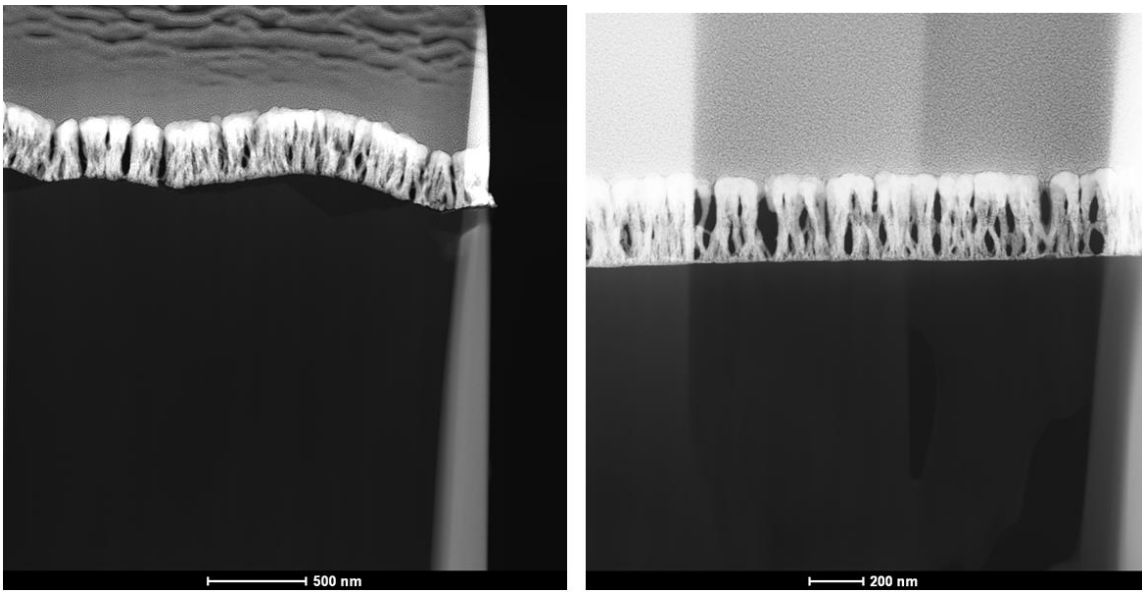

Figure 82: TEM images of the cross section of the surface of the heated sapphire fiber (Left) and the virgin sapphire fiber (Right).

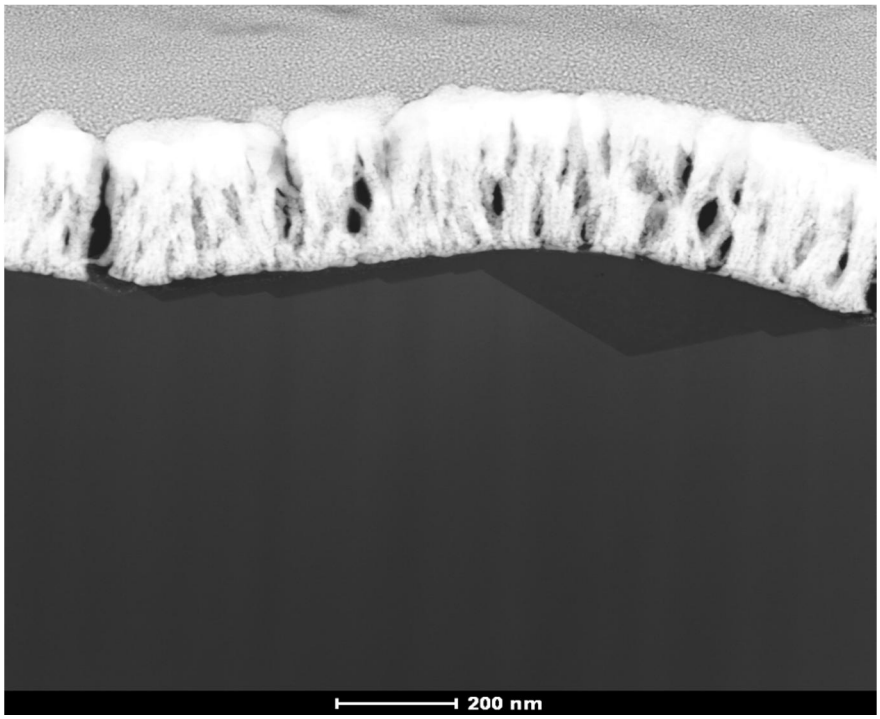

Figure 83: TEM image of the cross section of the surface of the heated sapphire fiber.

To investigate the composition of the unknown surface layer, an EDX measurement was made (see Figure 84). From the images in Figure 84, there appears to be a slight increase in the O:Al ratio on the surface of the fiber, corresponding to the darkened region seen in the TEM image. Although EDX is not typically used to resolve small quantitative changes in composition (particularly for elements with low atomic number), the EDX statistics show an increase of 7% in the O:Al ratio at the surface of the fiber compared to the O:Al ratio of the interior of the sapphire fiber. The uncertainty in the oxygen concentrations is ±1.2%. The EDX results also showed a 25% decrease in the density of the darkened region of the sapphire fiber compared to the normal sapphire lattice.

The lower density of the darkened region, it's higher O:Al ratio and its crystalline structure suggest that some form of aluminum hydroxide is forming on the surface of the sapphire fiber at high temperatures. Aluminum oxyhydroxide (AlO(OH)) is 25% less dense than sapphire, which matches the density measurement of the darkened region, but contradicts what the current literature predicts in regards to the species of aluminum hydroxide that should form. Opila [31] found that the surface of a sapphire wafer underwent a "rearrangement" in the presence of water vapor at temperatures above 1300 C. The surface rearrangement discovered by Opila was the formation of aluminum hydroxide in the form of $Al(OH)_3$. Water vapor could have interacted with the sapphire fibers in our experiment, as our tests occurred during the summer months when humidity in Ohio is relatively high. Contradictorily, $Al(OH)_3$ is 39% less dense than sapphire and the density we measured for the darkened region was only 25% less dense. Future work is needed to accurately identify the exact species of aluminum hydroxide that is forming on the fibers.

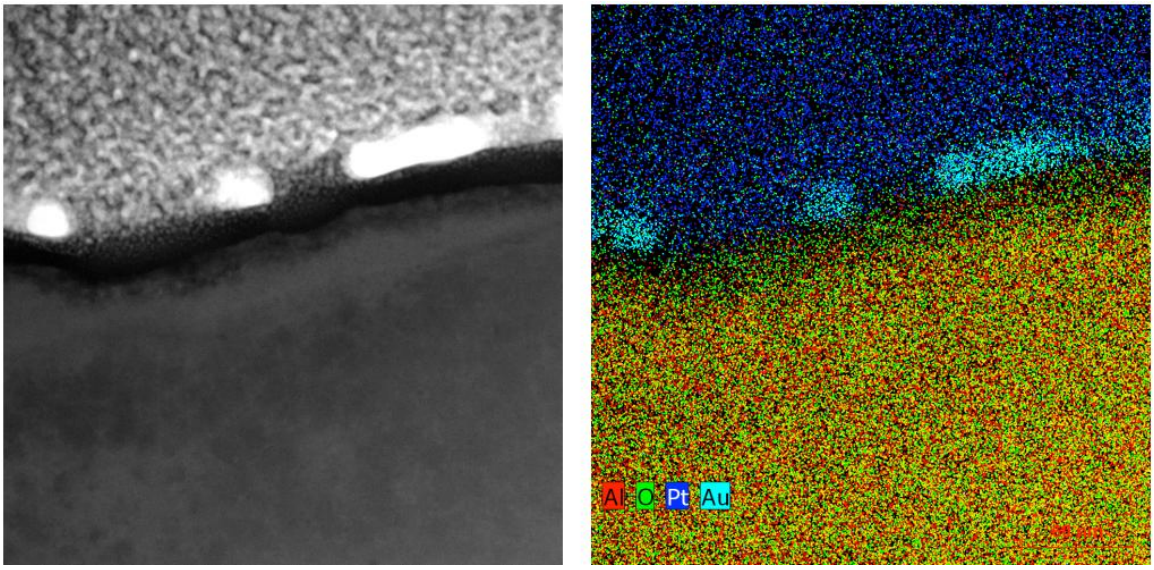

Figure 84: TEM image and EDX graph of the cross section of the surface of the heated sapphire fiber.

An additional experiment was performed to test the hypothesis that water vapor from the atmosphere is responsible for the increases in attenuation and the formation of a layer of aluminum hydroxide on the surface of the sapphire optical fiber at high temperatures. This second experiment was designed to duplicate the previous transmission experiment performed in air with the addition of an inert atmosphere surrounding the sapphire fiber. For this, a 0.5 meter length sapphire fiber was encapsulated in a pure alumina tube (99.8%) and backfilled with Argon. The fiber was loaded into the alumina tube in an argon-filled glovebox. The alumina was then sealed at both ends using a high-temperature, vacuum-rated epoxy (Loctite Stycast 2850FT) to ensure an inert atmosphere inside the tube. The ends of the sapphire fiber that protruded from the sealed ends of the alumina tube were fusion spliced to silica fiber. The silica fibers were connected to the broadband light spectrometry system similar to the previous test and the sapphire fiber/tube assembly was placed in the high-temperature tube furnace.

Light transmission through the sapphire fiber was continuously recorded every minute for the duration of the experiment. The furnace was ramped to 1000 °C and held at that temperature for about 12 hours. After 12 hours at 1000 °C, the temperature of the furnace was incrementally increased in steps of 100 °C every 12 hours until the temperature reached 1400 °C. The temperature was held at 1400 °C for 120 hours before it was finally stepped up to 1500 °C. The temperature was then held for 50 hours at 1500 °C.

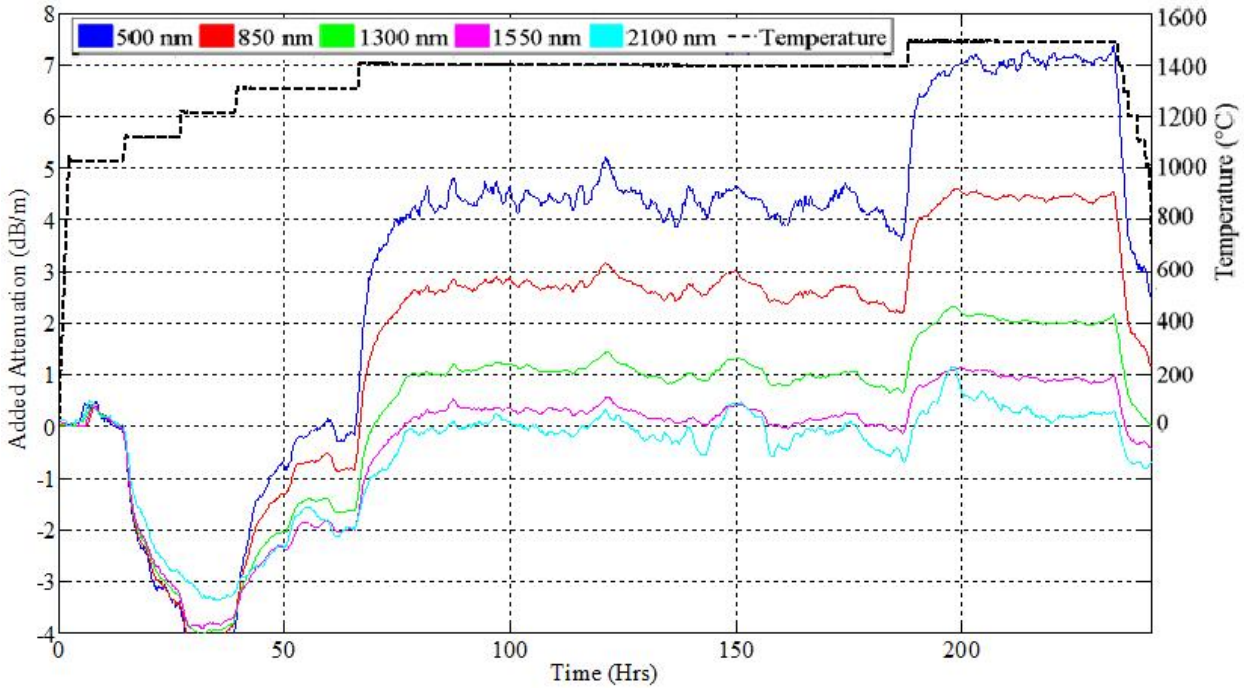

Figure 85: **Added attenuation in the light transmission through sapphire optical fiber as a function of time and temperature for select wavelengths. Line widths indicate ±1 sigma uncertainties.**

The results from the heated inert sapphire fiber experiment, shown in Figure 85, indicate that the inert atmosphere aided significantly in reducing the added light attenuation in the sapphire fiber at high temperatures. All of the wavelengths tested (450-2300 nm) showed much lower added attenuation when subjected to high temperatures. Furthermore, the steadily increasing light attenuation that was observed at temperatures above 1400 °C in air (Figure 64) was not observed in the argon environment. The fiber transmission improved (negative added attenuation) around 15 hours (i.e., at 1100 °C) indicating that more light was being transmitted through the fiber at that temperature than at room temperature. This improvement could be attributed to thermal annealing of defect centers that were formed in the fiber during fabrication. The operating wavelengths for most commercial optical fiber-based instrumentation, 1330 and 1550 nm, were nearly unaffected by high temperatures. The added attenuation at 1330 and 1550 nm remained below approximately 1 and 2 dB, respectively, over the entire duration of the experiment.

Upon completion of the inert high temperature transmission experiments, the sapphire fiber was removed from the furnace and analyzed under an optical microscope. In Figure 86, three photos of the sapphire fiber are shown under various magnifications. The images in Figure 86 show no signs of nucleation or bubbles that were observed following high temperature operation in air. The fiber surface largely appears the same as that of a virgin fiber. Upon inspection of the entire length of the heated inert sapphire fiber, zero bubbles were identified over the entire heated length of the fiber. These results indicate that the air atmosphere is indeed responsible for the chemical reaction on the surface of the sapphire fiber at high temperatures and the subsequent attenuation of the light.

Figure 86: Photos of the sapphire fiber that was heated in an inert atmosphere at 4x (Left), 10x (Center), and 40x (Right) magnification.

In conclusion, optical transmission was monitored in-situ in sapphire fibers while heating to temperatures as high as 1500 °C both in air and in an inert environment (argon). Heating in air resulted in large increases in attenuation that did not reach a dynamic equilibrium when the temperature was increased to 1400 °C and above. Examination of the fiber surface revealed nucleation of small bubbles and a thin surface layer with reduced density and perhaps an increase in the O:Al ratio. Electron microscopy suggested that some form of aluminum hydroxide may be forming due to reactions with water vapor at high temperature. Testing in an inert atmosphere showed much lower attenuation that did reach a dynamic equilibrium even at a temperature of 1500 °C. Furthermore, no bubbles were observed over the entire heated length of the fiber. These results provide conclusive evidence that sapphire optical fiber-based instrumentation operating at temperatures above 1400 °C would have to have an inert environment surrounding the fiber to ensure adequate transmission.

9.3.2 Functional Performance of Sapphire Fabry-Perot Interferometric Temperature Sensors up to 1500 °C

The Fabry-Perot sensors and readout system that was to be tested in this project will unfortunately not be tested. Lambda Instruments was supposed to build and deliver sapphire Fabry-Perot sensors and a readout system for this project but have been unable to. The company has 'thrown in the towel' on the completion and delivery of this vital piece of equipment that is needed for the remaining experiments. Without the delivery of this equipment, the remaining tasks cannot be completed as they were originally designed to be. Ohio State has tried to find another vendor that could build this equipment but have been unsuccessful. A company in England called Oxsensis claimed to be able to produce the equipment and sensors needed for this project. Unfortunately, upon review of the Oxsensis sensor, a fatal flaw was discovered that would have caused the sensor to fail early in our tests. Besides Oxsensis, no other company was found to be able to produce sapphire Fabry-Perot sensors and readout system needed to finish this project.

Ohio State decided to build their own sapphire sensors and use a piece of equipment they had from another project, a Luna Innovations Optical Backscatter Reflectometer (OBR), as a readout system. The OBR only works if the light in an optical fiber is of a single modal nature and sapphire fiber has a multimodal nature in regards to light transmission. An optical cladding is needed on the sapphire fiber to reduce the amount of light modes in the fiber. OSU invented a method of cladding the sapphire optical fiber to reduce the amount of light modes in the sapphire. By creating this cladded sapphire fiber, OSU can create a sapphire fiber capable of making distributed temperature measurements along the entire length of the fiber. This sensor would far surpass the original Fabry-Perot sensor as multiple temperature measurements could be made

instead of just one. The following section will cover the details of the cladding process and the ability of the sapphire fiber to perform distributed sensing.

9.3.3 Creation of a Cladding on Sapphire Fiber to enable Distributed Temperature Measurements using Optical Frequency Domain Reflectometry

Due to the delays in the delivery of the sapphire optical fiber readout system by Lambda Instruments, OSU researched sapphire optical fiber sensors as a secondary plan in the event Lambda never delivered on their part of the project. OSU decided to look at distributed temperature sensing using Optical Frequency Domain Reflectometry instead of Lambda's approach using Fabry-Perot point sensors. OSU currently has a fiber optic system that can make distributed temperature measurements along an optical fiber (the Luna Innovations OBR 4600) and so the only thing needed would be to invent a sapphire fiber that can be used with this readout system.

Sapphire optical fiber has a disadvantage in that it is a single crystal (instead of a glass) and a reflective cladding cannot be put on it during the manufacturing process. Sapphire employs the air around it as its reflective cladding so if any substance (dirt, dust, oil etc.) gets on the fiber, the light will leak out due to a mismatch in the refractive index. The lack of a cladding makes sapphire fiber have a high light attenuation and also makes the light highly multimodal (i.e. the light is not confined to one wave form). In order to make distributed temperature measurements using the sensing technique of the OBR (Optical Frequency Domain Reflectometry), light has to be near single mode. Optical Frequency Domain Reflectometry (OFDR) is a distributed measurement technique that works on the principles of injecting light into an optical fiber and measuring the reflected light off reflection points caused by natural defects or intentionally inscribed defects in the fiber. First, a 'map' of the reflection points within the fiber is made at a known temperature (usually room temperature). As temperature or stress causes the fiber to expand or contract, the location of these reflection points moves. The measurement of their movement can be correlated to temperature or strain. Presently, only silica optical fibers are used with the OFDR technique, because they can be made to support only a single light mode and because they have inherent reflection points within them that are due to defects and density changes of the amorphous silica glass structure. Sapphire fiber's multimodal nature, due to its large core and the lack of a cladding, along with the deficiency of defects in sapphire, due to its crystalline structure, makes the interference based OFDR sensing technique fail with normal sapphire fiber.

To create a reflective cladding in sapphire optical fiber, OSU decided to try and create an internal reflective cladding by means of creating a layer of high density displacement defects in the crystal. The internal cladding idea came from a group of researchers at the State University of New York at Albany whom used an accelerator to create an ion implanted waveguide in a sapphire wafer [32]. The ion damage survived up to 1600 °C and maintained its wave guiding properties over the entire range of temperatures. The internal cladding idea seemed more reasonable compared to an external cladding on the fiber as thermal expansion mismatches from a surface cladding material could stress and break the sapphire fiber.

To create an internal cladding in sapphire fiber using ion implantation, OSU decided to invent a new method of implanting ions. The sapphire fiber would be surrounded by a thin annulus of Li-6 enriched lithium carbonate powder and irradiated in a nuclear reactor. The ${}^{6}_{3}Li(\mathrm{n},\alpha){}^{3}_{1}H$ reaction,

$$ {}^{6}_{3}Li + {}^{1}_{0}n \rightarrow {}^{4}_{2}He + {}^{3}_{1}H + 4.8MeV $$

creates high energy alpha particles and tritons that irradiate the fiber simultaneously along the entire periphery of the sapphire fiber. The ${}^{6}_{3}Li(\mathrm{n},\alpha){}^{3}_{1}H$ reaction creates an alpha particle that has an energy of 2.05 MeV and a triton that has an energy of 2.73 MeV. The alpha particle has a range of 4 micrometers in sapphire, while the triton has a range of 24 micrometers. The large depth of the triton implantation reduces the core size of the sapphire fiber, which helps reduce the multimodal characteristics of the sapphire. In addition to creating the cladding from ion irradiation via the ${}^{6}_{3}Li(\mathrm{n},\alpha){}^{3}_{1}H$ reaction, which is induced mostly by thermal neutrons, the reactor irradiation also created displacement damage throughout the sapphire fiber core, as a consequence of fast neutron interactions with the nuclei of the aluminum and oxygen atoms composing the fiber. Consequently, by using the OSURR reactor, we simultaneously created a cladding within the fiber via the ${}^{6}_{3}Li(\mathrm{n},\alpha){}^{3}_{1}H$ reaction and defects in the sapphire fiber core via fast neutron induced displacement damage. Because the reaction rate for the ${}^{6}_{3}Li(\mathrm{n},\alpha){}^{3}_{1}H$ reaction far exceeds the reaction rate for the creation of Primary Knock-on Atoms (PKAs) by fast neutron interaction with the sapphire, the radiation damage to the periphery of the fiber that created the fiber clad far exceeded the radiation damage to the fiber core that was created by fast neutron induced PKAs. The fast neutron induced damage in the fiber core can be viewed as being beneficial, because it was not substantial enough to greatly degrade transmission through the fiber, but was still large enough to create a Rayleigh backscatter signature within the fiber core. This backscatter signal provided the reflected light that was necessary for the functioning of the Luna OBR-4600. OSU developed this method, because using an accelerator to create a cladding on the periphery of a sapphire fiber, along the entire length of the fiber, would take an unreasonably long time and would be consequently very expensive.

Before OSU ran the Li-6 experiment, theoretical models were made to make sure that the cladding would reduce the multimodal characteristics of sapphire fiber. Distributed sensing using OFDR only works when the light is single mode and or close to single mode. A single mode fiber ensures that the light that is scattered due to defect reflections head straight back down the fiber. Any light reflections in the fiber that aren't close to 180 degrees are absorbed in the cladding. With only the reflected light that reflects parallel with the fiber reaching the OBR, it allows a time of flight measurement to be made and thus a distance can be calculated between the reflections in the fiber. The numerical aperture (NA) of a fiber is a dimensionless number that characterizes the range of angles of a light cone that can propagate in an optical fiber. In Figure 87 below, a diagram, equations and a table for the NA of different fibers are shown.

Fiber Type	NA	Max θ (degrees)
Single Mode Silica fiber	0.14	5.5
Multimode Silica fiber	0.22	8.6
Sapphire	1.43	55.1
Sapphire with an ion damaged clad	0.247	8.2

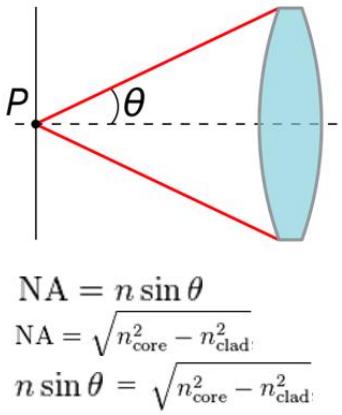

Figure 87: (Left) A table showing the various numerical apertures for different types of fibers. (Right) A diagram depicting the cone of light that is admissible in a certain optical fiber with the relevant equations below it

The equations in Figure 87 show that the angle of light (θ) that can be transmitted in a fiber depends on the refractive index (n) of the core and clad of the fiber. The smaller the difference between the cladding and the core, the smaller the angle of light that can be transmitted and the more single mode a fiber is. Since sapphire does not have a cladding on it, the air that surrounds the fiber acts as its reflective cladding. The problem lies in the fact that the difference between the index of refraction between air and sapphire (n_{air} = 1.0 and $n_{sapphire}$ = 1.75) is much larger than traditional silica fiber (n_{core} = 1.5 and n_{clad} = 1.43) that the equations in Figure 87 allow for a large angle in which the light can be transmitted. Looking at the table above, it shows that sapphire fiber is extremely multimodal in nature and that a cladding could make it more like traditional optical fiber. The idea behind using crystal damage in the fiber as a reflective cladding stems from the fact that alpha and triton particles create large displacement defects in sapphire. These displacement defects are giant holes in the crystal lattice which reduce the index of refraction by a small amount. By bombarding the fiber with $5x10^{15}$ particles per cm^2, an internal cylindrical annulus of damaged fiber is created that has an index of refraction that is slightly smaller than that of normal sapphire and has characteristics that are very similar to that of traditional silica optical fiber.

Transmission models of the light propagating through an optical fiber were also conducted and can be seen below in Figure 88. The diagrams show a cross section of a fiber and the normalized percent of the light being transmitted through the fiber. These models represent what the light transmission through the fiber would be for different fibers and are a big indicator of how modal the light is in a fiber. For the silica single mode and multimode fiber, most of the light was centered in the middle of the fiber in one distinct mode. The sapphire fiber did not have one distinct mode as the light tended to focus in different areas along the fiber.

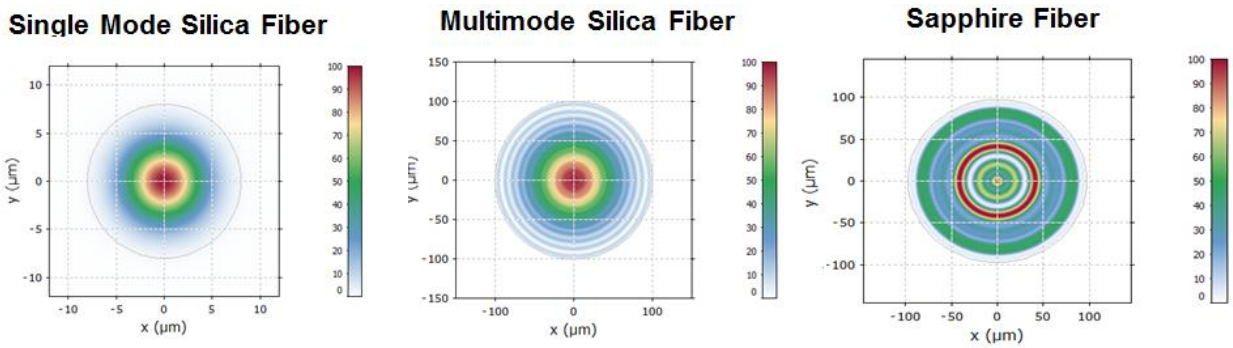

Figure 88: Simulations depicting the light transmission through an optical fiber using a cross sectional view and a normalized intensity.

Upon completion of the theoretical models, OSU decided to go ahead and make the internal cladding in a sapphire fiber using the Li-6/neutron reaction. A VISED image of the cross section of the Li-6 carbonate/sapphire fiber irradiation assembly is shown in Figure 89. Sapphire optical fiber, with an outer diameter of 100 micrometers that was purchased from MicroMaterials Inc., was radially centered in an aluminum capillary tube (henceforth called the irradiation tube) that had an internal diameter of 1 mm. Lithium-6 carbonate powder was packed into the irradiation tube surrounding the sapphire fiber. The Li-6 carbonate had a Li-6 enrichment of 95.8 atomic percent and a (experimentally determined) density of approximately 0.7 g/cc. The ends of the irradiation tube were crimped to ensure that Li-6 powder would not fall out in the reactor and, to ensure safety, the crimped irradiation tube was placed in another aluminum tube (henceforth called the carrier tube)that was sealed with vacuum epoxy to create an air tight vessel. The carrier tube was then lowered into the CIF dry well facility of the OSURR core and irradiated for 5.5 hours at 450 kW for a total neutron fluence of (6.1 ± 0.6)E+17 n/cm^2 at the axial mid-plane of the OSURR core, which was also the approximate axial midpoint of the sapphire fiber. After irradiation, the sealed ends were snipped off the carrier tube and pliers were used to un-crimp the irradiation tube. The irradiation tube was placed in a fume hood and the tritium gas that was produced in the irradiation was allowed to vent for an hour. After the venting process, the irradiation tube was placed in water to dissolve all of the Li-6 carbonate powder around the fiber. The fiber was then pulled from the irradiation tube and tested to see if an internal cladding was created.

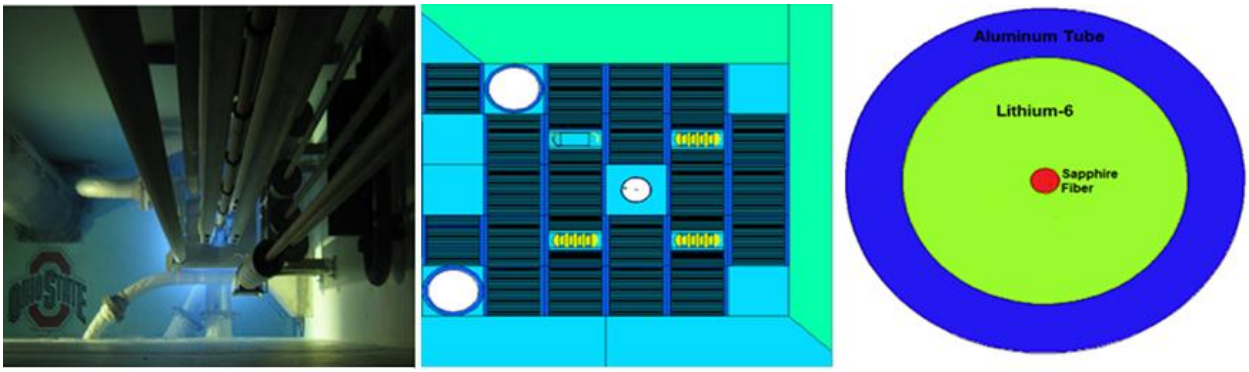

Figure 89: (Left) Photograph of the OSURR core in water filled reactor pool; (Middle) VISED transverse cross-sectional image of the OSURR core at the core vertical mid-plane, including the CIF facility into which the Li-6 carbonate/sapphire fiber irradiation assembly was placed. (Right) VISED transverse cross-sectional image of the Li-6 carbonate/sapphire fiber irradiation assembly.

To test the sapphire fiber to confirm whether a cladding was made in it and to verify the theoretical models, a dark box optical transmission system was built to measure the light transmission coming through the optical fibers. The set up can be seen below in Figure 90. They transmission system contained an optics table with a dark box around it to make sure that all ambient light was blocked. A fiber chuck was placed in front of an IR camera (Thorlabs BP-209 IR) to capture the beam profile of the light exiting the fiber. A 1550 nm laser was attached to other end of the fiber. The IR camera also came with a software package that allowed the data from the transmission data to be analyzed in a variety of ways. Three fibers were tested in this system: a silica fiber, a virgin sapphire fiber and the cladded sapphire fiber.

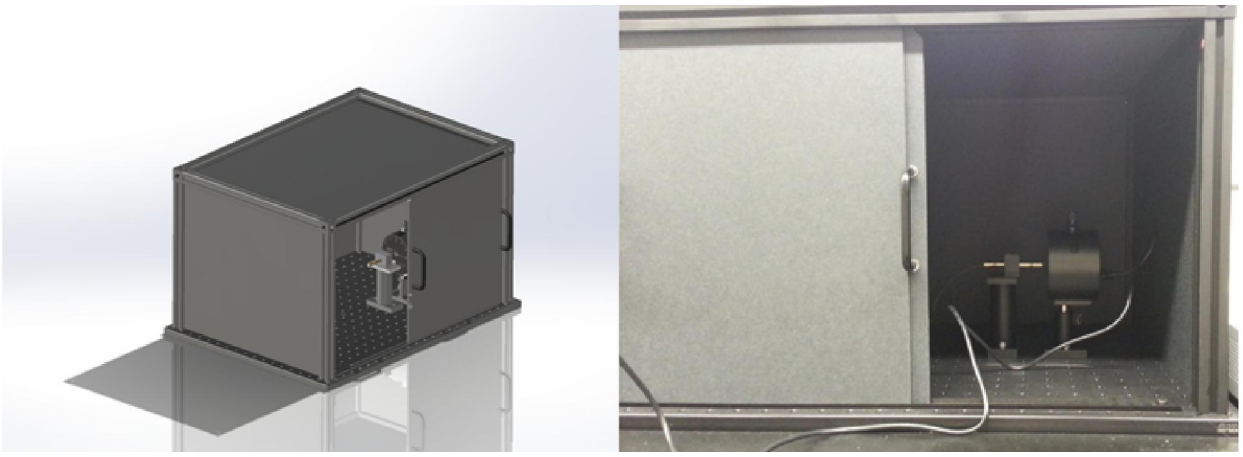

Figure 90: A Solidworks diagram and a picture of the dark box and fiber optic transmission experiments set up.

The transmission data through the various fibers can be seen below in 2-d and also 3-d in Figure 91. The silica fiber (leftmost image) had a transmission pattern with one distinct transmission peak in the center of the fiber that resembled a gaussian shape. The virgin sapphire fiber (middle image) did not have the same pattern. The light transmission was very multimodal and the light modes changed from picture to picture. The light transmission pattern appeared to have a shape that was more nearly a plateau than a gaussian distribution and the light intensity did not have a central peak as it did for the silica fiber. The rightmost images in Figure 91 show the light transmission pattern with our sapphire fiber with the cladding in it. It appears that the cladding is effective, because the transmitted light intensity has a central peak. The beam profile was not circular, which could be caused by either a bad endface and/or a lopsided cladding in the fiber. The nearly single mode light tranmsission characteristic of our internally cladded sapphire fiber prompted us to test the fiber's distributed temperature sensing capability

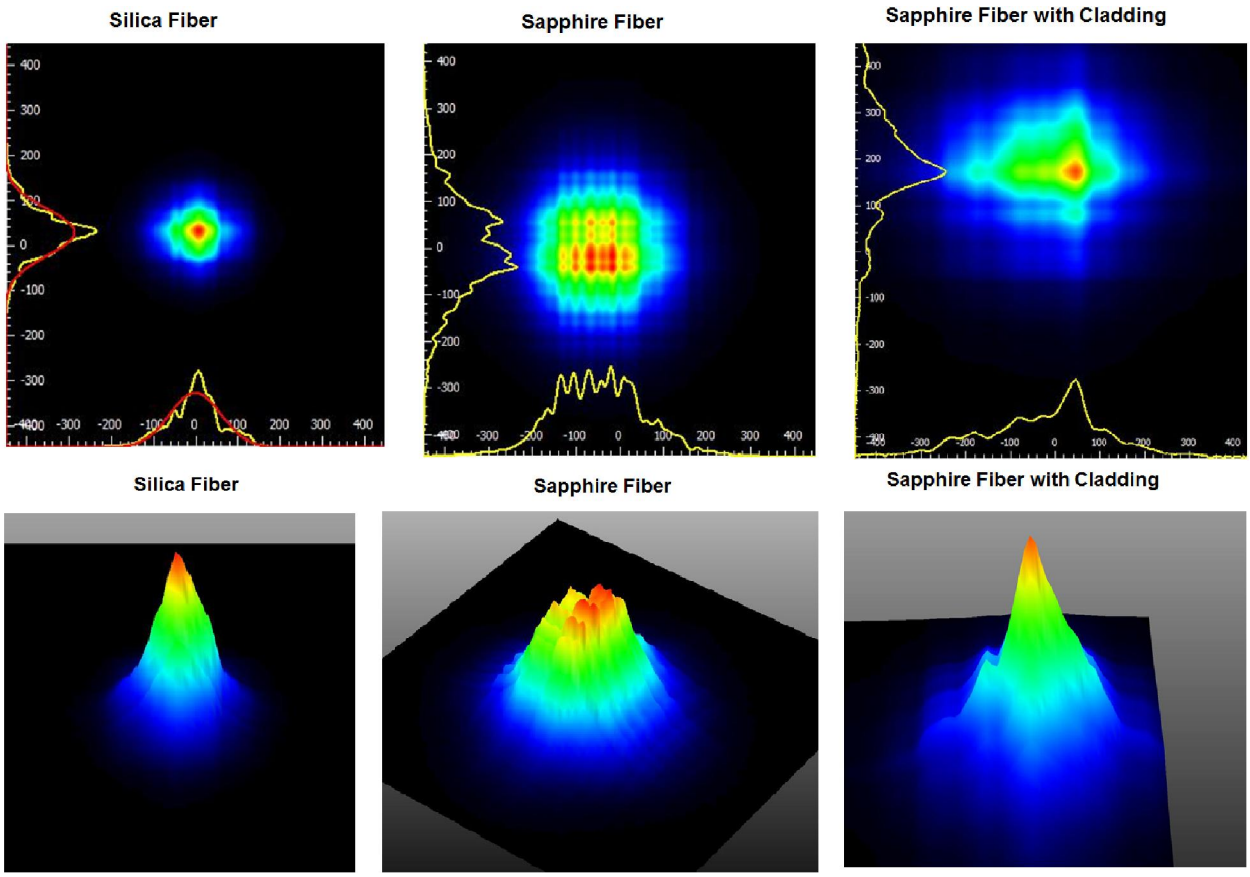

Figure 91: Pictures taken with our IR camera of different transmission profiles for the three different optical fibers that we tested

With the dark box images indicating that the cladded sapphire fiber had nearly single mode light transmission characteristics, the cladded sapphire fiber was attached to the OBR to determine if the cladded fiber was capable of producing distributed temperature measurements. A screenshot from the OBR of the cladded sapphire fiber's backscattered light amplitude versus position along the fiber can be seen in Figure 92. Lead silica fiber (corning SMF-28+) was fusion spliced to sapphire fiber using a customized OFS Fitel fusion splicer to cut down on cost, because sapphire fiber is expensive. Collaborating with Fitel, we were able to adjust the fusion splicer to splice single mode silica fiber with sapphire fiber with estimated coupling losses of less than 3db. The first spike in reflectance (at ~ 4.075m) is from the splice between the single mode silica fiber and the cladded sapphire fiber. The second spike in reflectance (at ~ 4.325m) is from the end of the cladded sapphire fiber. The cladded sapphire fiber displays a reflected amplitude between 4.075m and 4.335m that is above the noise floor of 120 dB, which is the value of the reflected amplitude for positions greater than ~ 4.4m. The reflected amplitude was not larger than the noise floor in similar measurements that we made using virgin sapphire fiber instead of reactor irradiated fiber. The defects from the fast neutron damage created enough scattering sites in the cladded sapphire fiber to create a backscatter signal above the noise floor, allowing the fiber to potentially be successfully used with the OBR to readout distributed temperature measurements.

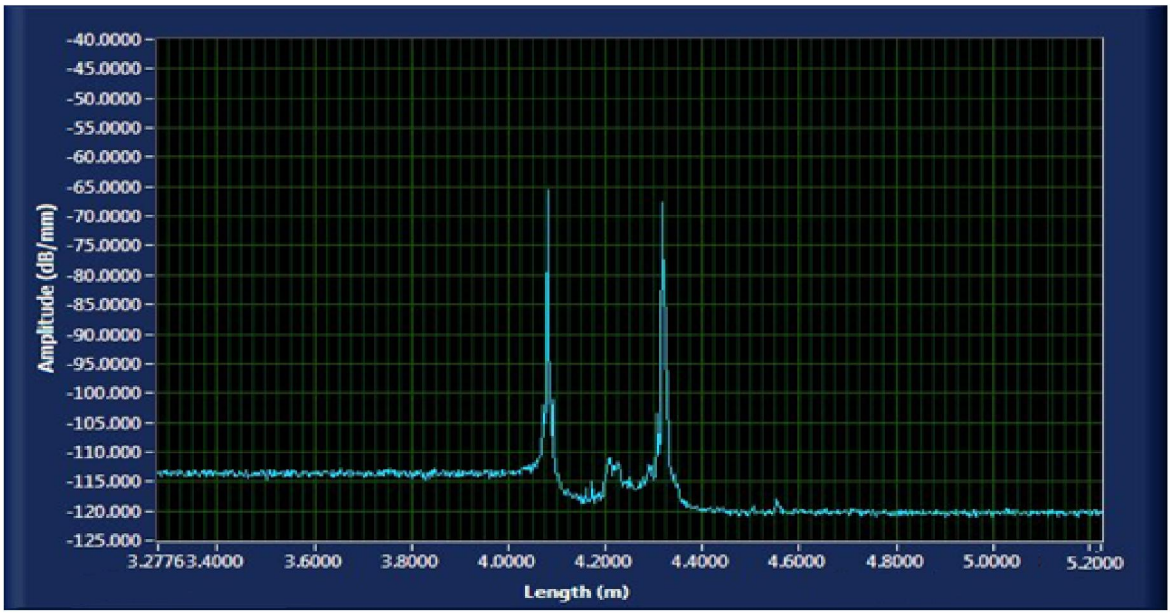

Figure 92: Screenshot from the OBR of the reflected amplitude of light in the cladded sapphire optical fiber as a function of position along the fiber.

A short time duration heating test of the cladded sapphire fiber was conducted using a hot plate to determine if the cladded sapphire fiber could be successfully used to produce temperature measurements, using the OFDR sensing technique. An aluminum plate was thermally cantilevered on a hot plate and the fiber was strung along the top of the aluminum plate as shown in Figure 93. A k-type thermocouple was placed near the fiber for comparison, at a point above the hotplate (length ~ 4.25m). Multiple temperature measurements were made with the OBR and thermocouple every 150 seconds during the duration of the test.

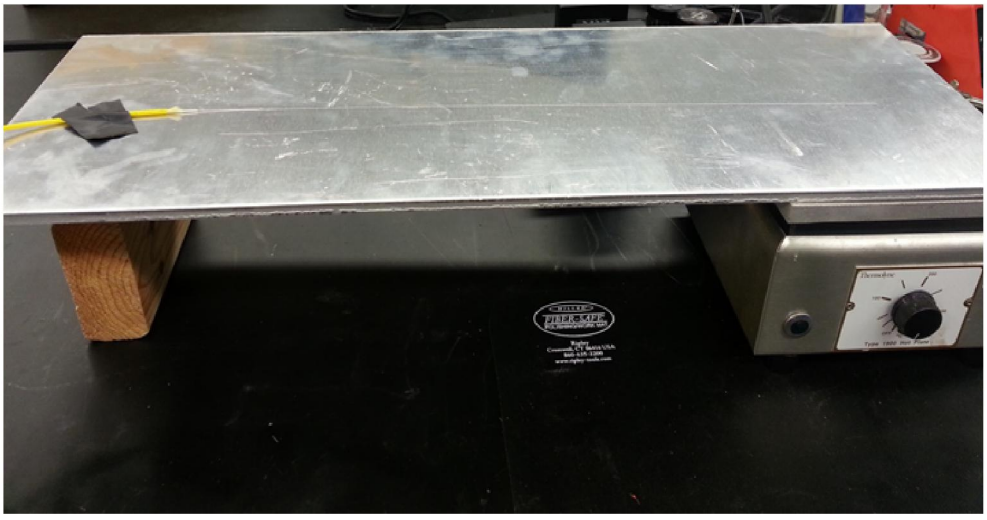

Figure 93: Photograph of the Li-6 cladded sapphire optical fiber strung along the length of a thermally cantilevered aluminum plate.

The hot plate was heated up to 100 °C creating a distinctive temperature profile along the thermally cantilevered aluminum plate. The fiber and thermocouple temperatures are plotted versus time in Figure 94. The fiber temperature is plotted for the point in the fiber nearest to the thermocouple (length ~ 4.25m). Error bars on the sapphire measurements in Figure 94 represent the standard deviation of the precision of the measurements; the accuracy of the OBR measurements of the sapphire fiber is still being investigated. Figure 95 shows the distributed temperature measurements made by the sapphire fiber on the thermally cantilevered aluminum plate as a function of time during the experiment.

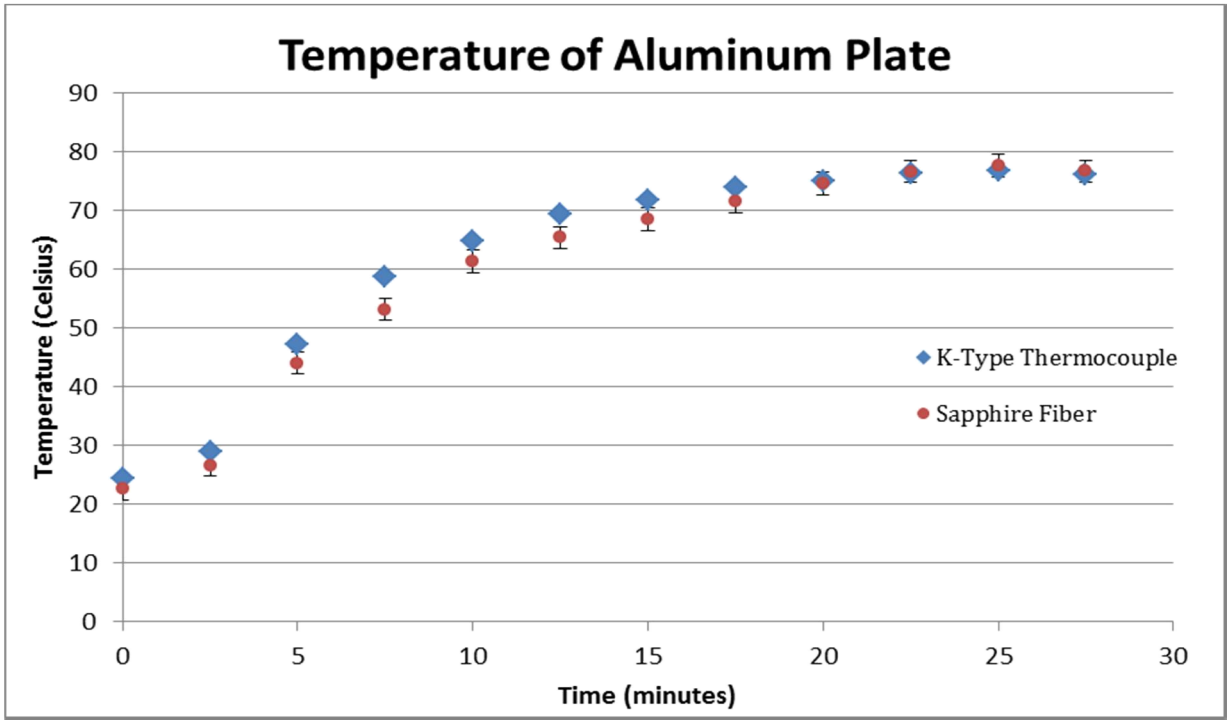

Figure 94: Graph of the temperature vs time for the cladded sapphire fiber and a k-type thermocouple placed on an aluminum plate above a hotplate, as the hotplate was turned on at time=0 with the hotplate set to 100 °C. The fiber temperature is plotted for the point in the fiber nearest to the thermocouple (length ~ 4.25m).

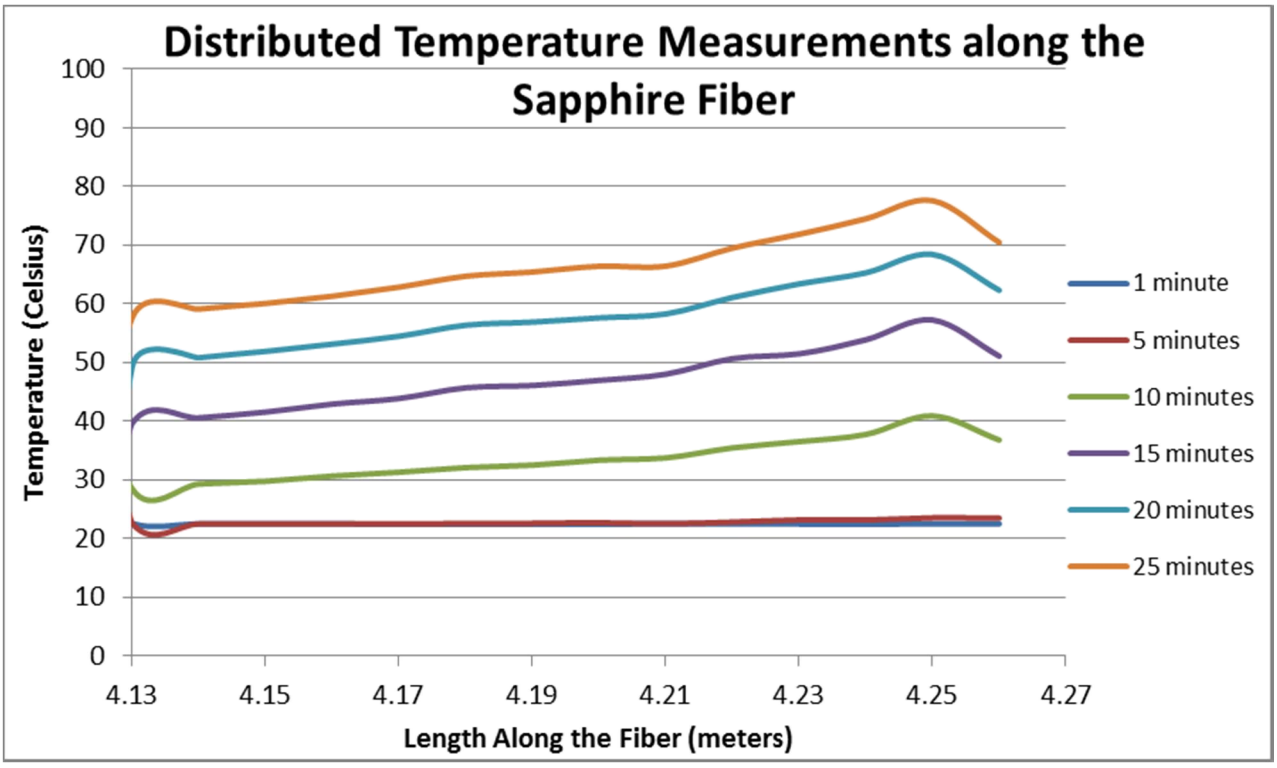

Figure 95: Distributed temperature measurements of the sapphire fiber as a function of distance along the fiber with time as a parameter for the experiment corresponding to the data presented in Figure 94.

The temperature measurements in Figure 94 indicate that the cladded fiber and the thermocouple record a similar temperature versus time history. The thermocouple was spaced about an inch away from the fiber, which could account for discrepancy between the measurements. Figure 95 shows the spatial temperature profile of the plate along the length of the cladded fiber as the plate was heated with time as a parameter. The temperature profile resembles what one might expect from a heated cantilevered beam. The goal of this test was not to determine the accuracy of the cladded sapphire fiber measurement, but rather to determine if a measurement could be made, and if so, if it was reasonable. The data from Figure 95 appears reasonable, although more work is needed to determine the accuracy of the cladded sapphire fiber measurements.

9.3.4 High Temperature Testing of Sapphire Optical Fiber Sensors

Having determined that temperature could be measured using cladded sapphire fiber and the OBR, a test was devised to determine the temperature limits of the ion implanted cladding and the limits of the OFDR sensing technique in cladded sapphire optical fiber. The cladded sapphire fiber was spliced to a single mode silica extension fiber and connected to the OBR. The sapphire fiber was placed into a tube furnace and the furnace was ramped to 1500 °C. The furnace was held

at 1500 °C for 24 hours, before the furnace was cooled back to room temperature. The light transmission through the cladded sapphire fiber after it was heated can be seen below in Figure 96.

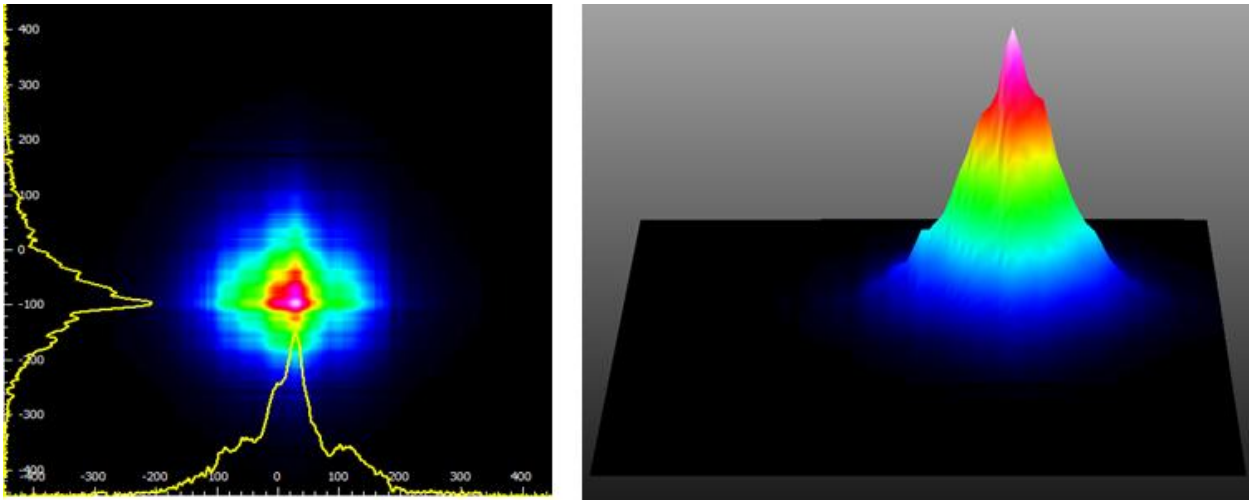

Figure 96: Transmission profiles taken with an IR camera for the cladded sapphire fiber that was heated treated

The transmission profile of the heated sapphire fiber indicates that the cladding of the sapphire has potentially held up to the higher temperatures and is still causing the reduction of light modes in the fiber. Unfortunately, our distributed temperature measurements failed (around 600 C) during the experiment and so we do not have a second confirmation of the amount of light modes in the fiber. The reason for the distributed sensing failure in the cladded sapphire fiber was due to either a change in the defects in the core of the fiber or a miss calibration of the OBR. The OBR is calibrated to the thermal expansion limits of glass fiber and so when the sapphire expanded, the software in the OBR might not have been able to track its larger expansion. The second possible cause for the failure is the annealing of the point defects in the sapphire fiber that the OBR uses to make temperature measurements from. The point defects in the sapphire fiber caused from the fast neutron damage are likely to have a much lower annealing threshold than that of the implanted ions. Unfortunately, Luna does not allow people to change the OBR software and so we approached this problem in regards to the annealing of the point defects in the sapphire fiber core. To overcome the annealing of the point defects, intentional high temperature defects were added to the core of the sapphire fiber.

A Bragg grating is an intentional cluster of defects in an optical fiber that cause a change in the index of refraction which causes a reflection of the light in an optical fiber. Bragg gratings are typically used in silica glass fibers as either temperature sensors or light filters. The Bragg gratings in silica optical fiber are traditionally created with a UV laser that creates defects in the core of the fiber from a photosensitive reaction between the core and the UV laser resulting in a change in the index of refraction. Unfortunately, these gratings typically recombine and anneal out of the fiber at temperatures around 800 C. Recently, a breakthrough in Bragg gratings has been made by using a femtosecond laser instead of a UV laser. The femtosecond laser creates a grating by the compaction and dilation of the fiber structure from the bright and dark fringes of a femtosecond laser interference pattern. The high energy pulse of the femtosecond laser causes the atoms to vaporize in the bright fringe and resettle in the dark fringes of the optical pattern [33]. The displacement damage of the femtosecond grating requires more thermal energy to anneal out than that of the UV

gratings at high temperatures. Researchers have started to use this technique in sapphire optical fiber also and have been able to produce temperature stable Bragg gratings in sapphire optical fiber up to 1500 C [34]. Due to the multimodal nature of sapphire fiber, only one Bragg grating can be analyzed as a temperature sensor in a sapphire fiber. With the cladding technique that OSU developed, reading out multiple Bragg gratings in a sapphire fiber is possible. Theoretically, a cladded sapphire fiber with femtosecond Bragg gratings inscribed in it could produce distributed temperature measurements up to 1500 C.

FemtoFiber Tec is a German company that produces femtosecond Bragg gratings in sapphire optical fiber and OSU has ordered multiple sapphire fibers with Bragg gratings inscribed in it. Upon the delivery of this fiber, OSU placed a cladding in the fiber using the Li-6/Neutron reaction so that all of the gratings can be read out. With an internal cladding placed in the sapphire fiber with the femtosecond Bragg gratings, the fiber was attached to the OBR to see if the fiber could be readout. A screenshot from the OBR of the cladded sapphire fiber's backscattered light amplitude versus position along the fiber can be seen in Figure 97.

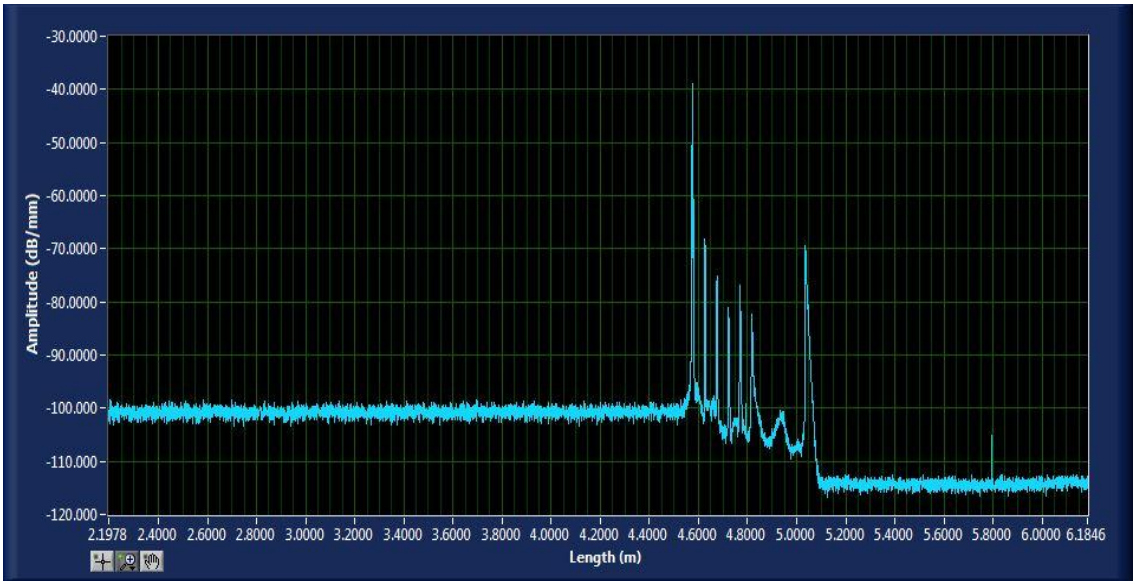

Figure 97: Screenshot from the OBR of the reflected amplitude of light in the cladded sapphire optical fiber as a function of position along the fiber.

The first spike in reflectance (at ~ 4.575m) is from the splice between the single mode silica fiber and the cladded sapphire fiber. The spike in reflectance from the end of the sapphire fiber is located at 5.05m. The 5 spikes in reflectance between the fiber splice and the end of the fiber are the femtosecond Bragg gratings. The high reflectance of the gratings should ensure a high signal to noise ratio compared to that of the cladded only sapphire fiber. To test the fiber's ability to measure distributed temperature measurements, an aluminum plate was thermally cantilevered on a hot plate and the fiber was strung along the top of the aluminum plate. A k-type thermocouple was placed near the fiber for comparison, at a point closest to the 4th grating in the sapphire fiber (the gratings are numbered from left to right in Figure 97). The temperature measurements from each Bragg grating in the cladded sapphire fiber can be seen below in Figure 98.

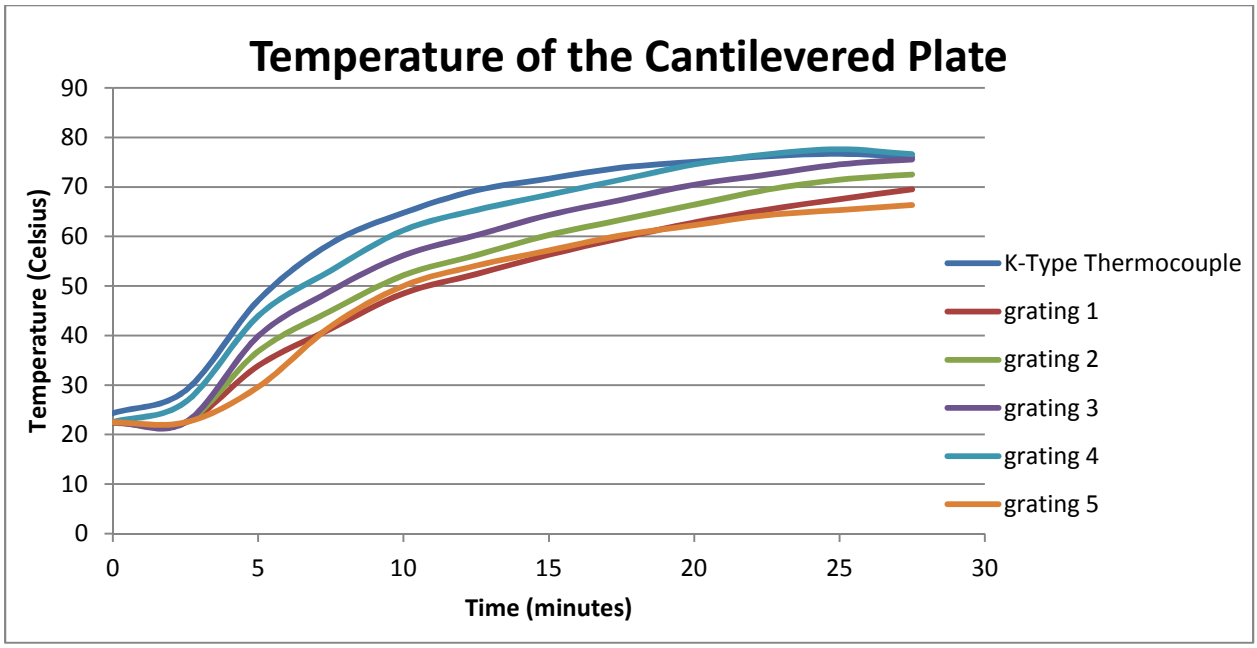

Figure 98: Distributed temperature measurements of the sapphire fiber as a function of distance along the fiber with time as a parameter for the experiment corresponding to the data

The hot plate was heated up to 100 °C creating a distinctive temperature profile along the thermally cantilevered aluminum plate. The temperature measurements produced by the Bragg gratings in the sapphire fiber and the thermocouple attached to the aluminum plate can be seen in Figure 98. The temperature measurements from the gratings have a very similar heating profile to that of the thermocouple indicating that the fiber sensing is working properly. The temperature readings are slightly off from that of the thermocouple as the location of the placement of the thermocouple next to the fiber was not accurately measured. With the Bragg gratings producing reasonable temperature measurements along the sapphire fiber, a higher temperature test was devised.

Since OSU had to take on the Lambda Instruments part of the project by building sapphire sensors and a readout system, the timing of the experiments were delayed and full testing of the sensors could not be fully accomplished by the end of the project. The radiation tests of the sapphire sensors were completed in full but the temperature tests were limited to only a 1000 C testing (the project originally specified for temperature testing of sapphire sensors to 1500 C).

From our heated sapphire transmission testing (see Chapter 9.3.1), we know that at 1300 C and above, the sapphire fiber losses its ability to transmit light if it is not in an inert atmosphere. In addition to the atmosphere problem, the OBR is calibrated for the expansion of silica fiber, and so at high temperatures, the OBR measurement could fail due to the sapphire fiber expanding significantly more than what the OBR is calibrated for. To avoid the two aforementioned problems, a test to only a 1000 C was contrived. The cladded sapphire fiber was spliced to a single mode silica extension fiber and connected to the OBR. The sapphire fiber was placed into a tube furnace and the furnace was ramped to 1000 °C in 100 degree steps. The temperature profile of the furnace can be seen in Figure 99.

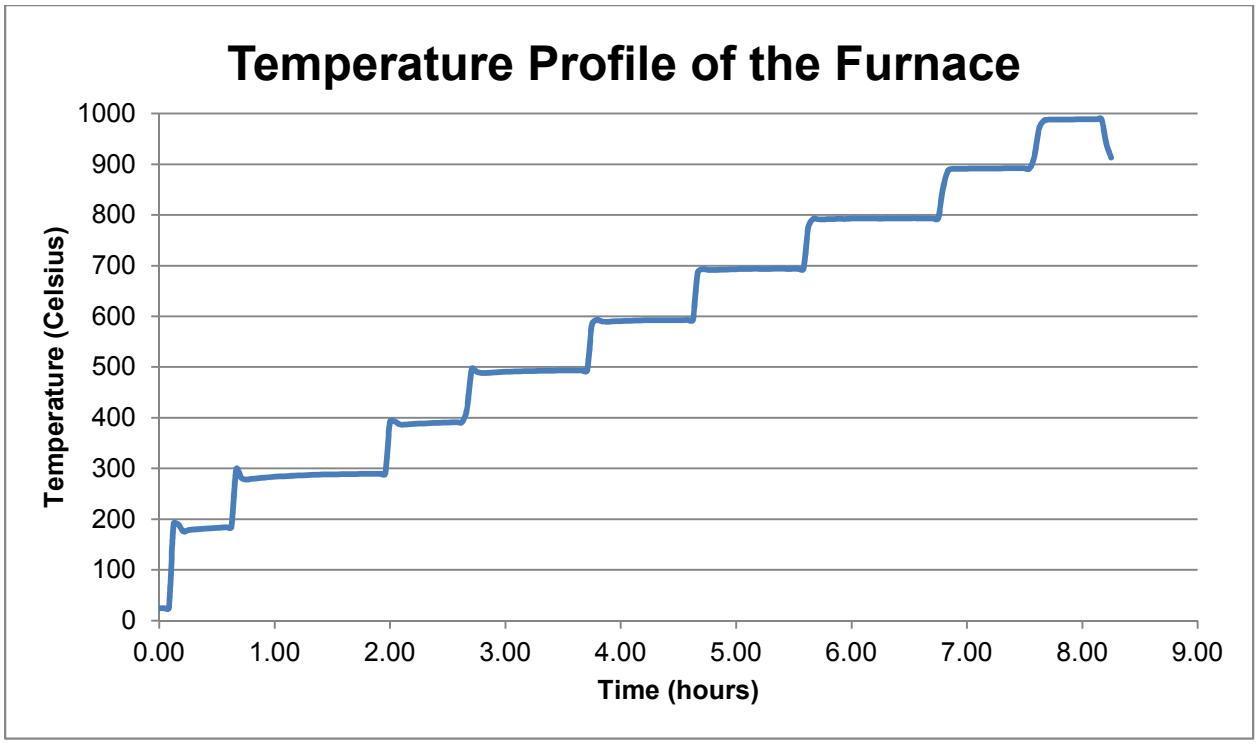

Figure 99: Temperature measurements, as a function of time, recorded by a K-type thermocouple of the air temperature inside of a tube furnace during an experiment involving the heating of sapphire sensors.

The temperature of the furnace was stepped up in 100 C steps and held for hour long increments to determine the temperature at which either the OBR calibration failed and or the gratings started to degrade. The temperature measurements from the grating closest to the thermocouple in the furnace can be seen in Figure 100. The temperature measurements from the sapphire Bragg grating had a strong correlation to the thermocouple measurements. The sapphire measurements produced a steady and relatively accurate temperature profile of the furnace during the entire duration of the experiment. The temperature measurements of the sapphire fiber differ from the thermocouple measurement in the low temperature range and this is due to a poor calibration of the sapphire expansion rate as a function of temperature. A crude correlation of the sapphire expansion rate as a function of temperature was applied to the sapphire measurements; an accurate correlation of the temperature and expansion rate of sapphire is recommended for future work. With the successful measurements of the sapphire gratings at high temperatures, the reflective backscatter from the gratings was measured to ensure that the sapphire gratings did not degrade in the high temperature environment.

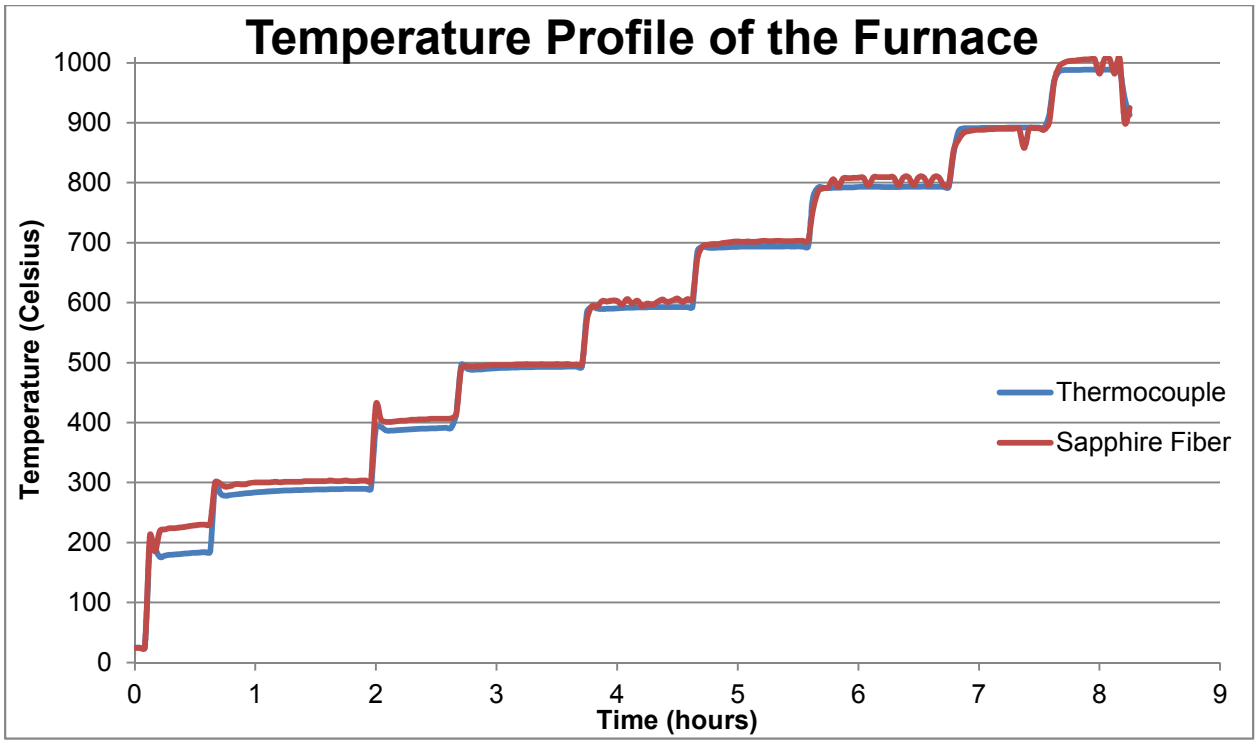

Figure 100: Temperature measurements, as a function of time, recorded by a K-type thermocouple and a Bragg grating inscribed in sapphire fiber of the air temperature inside of a tube furnace.

The reflected backscatter amplitude of the Bragg gratings before and after the high temperature experiment can be seen in Figure 101. The gratings appear to have been unaffected by the high temperatures during the experiment. A few of the gratings even had a higher reflective amplitude after the high temperature experiment. To confirm that the gratings are thermally stable during the entire experiment, the reflective amplitude was measured at every temperature step during the experiment (see Figure 102).

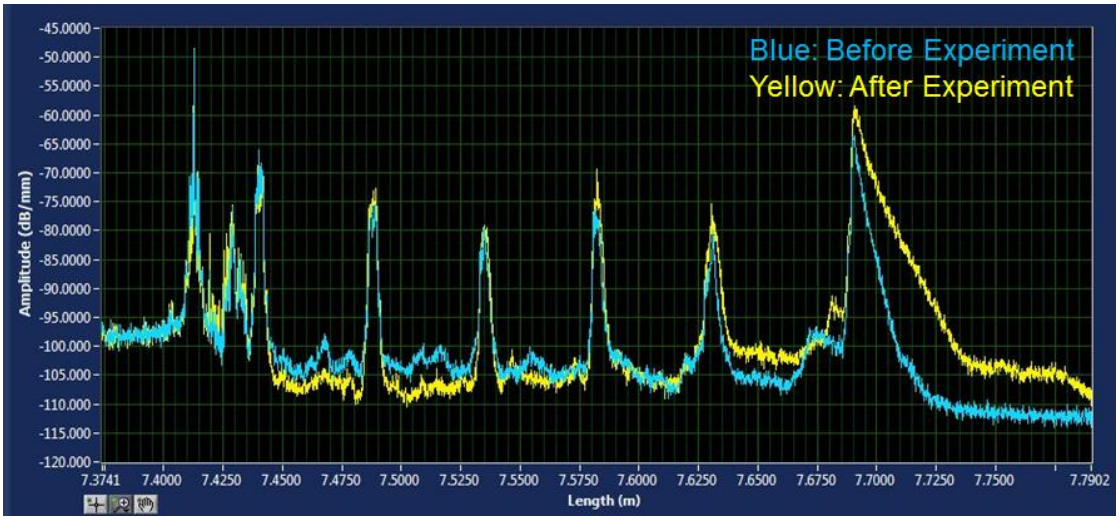

Figure 101: Screenshot from the OBR of the reflected amplitude of light off of the Bragg gratings in the cladded sapphire optical fiber as a function of time and position along the fiber.

The sapphire Bragg gratings exhibit an interesting phenomenon in regards to their reflective amplitude at higher temperatures (the reflective amplitude of the sapphire gratings can be seen in Figure 102). The gratings appear to decrease in their reflective strength yet increase in their physical size at high temperatures. The increase in the size of the gratings could be from the diffusion of defects from the gratings into to the nearby virgin sections of the fiber. The interesting phenomenon that happens is that upon cooling, the gratings return to their original physical size and reflective amplitude (see Figure 101). Another explanation for the widening of the gratings at high temperatures could be from a combination of a bulk refractive index change in the sapphire fiber at higher temperatures and thermal noise from the gratings in the fiber. The widening and decrease in the reflective amplitude of the sapphire gratings at high temperatures does not appear to affect the temperature measurements of the gratings but it is an interesting phenomenon and could help reveal in the future the physical characteristics of sapphire fiber at high temperatures.

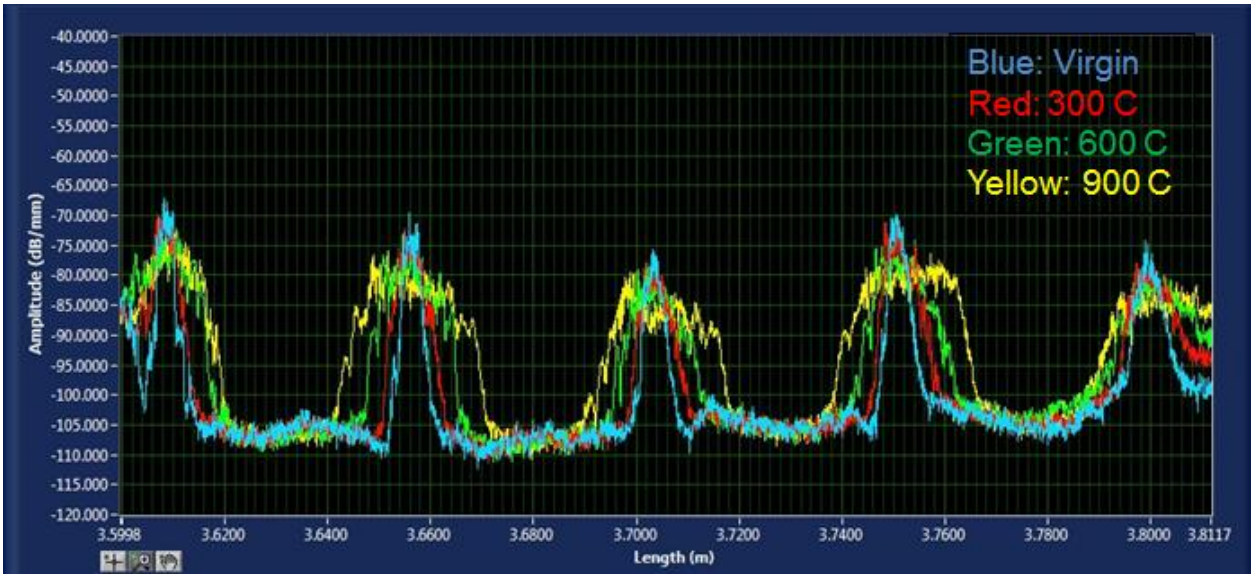

Figure 102: Screenshot from the OBR of the reflected amplitude of light off of the Bragg gratings in the cladded sapphire optical fiber as a function of temperature, time and position along the fiber.

In conclusion, the sapphire Bragg gratings were able to produce stable temperature measurements up to a 1000 C. Tests to higher temperatures and a more accurate calibration of the sapphire Bragg gratings is recommended for future work. The gratings showed no degradation in regards to their reflected backscatter amplitude to temperatures up to 1000 C. The sapphire Bragg grating sensors have great potential for producing accurate temperature measurements at temperatures higher than a 1000 C, unfortunately, time restrictions caused a reduction in the scope of our testing.

9.3.5 Gamma Ray Testing of Sapphire Optical Fiber Sensors

Following the high temperature tests, the cladded sapphire fiber, with inscribed femtosecond Bragg gratings, was tested for its radiation survivability. The radiation survivability tests consisted of two tests: a gamma ray only irradiation and a reactor irradiation (neutrons and gamma rays). The Ohio State Reactor Lab was used for both of these tests as the facility contains a

450 kW research reactor and a Co-60 irradiator. The Co-60 irradiator consisted of an array of Co-60 pins that encircle a 6" aluminum dry tube. The pins are submerged at the bottom of a pool of water to provide radiation shielding. The 6" aluminum tube extends from the Co-60 pins to a foot above the waterline of the pool. For testing in the Co-60 irradiator, samples were lowered down into the tube until they reach the Co-60 pins at the bottom of the tube.

The rig that was used to irradiate the sapphire fiber sensors can be seen below in Figure 103. The rig's purpose was to center the fibers in the irradiation tube and to provide strain relief to the fibers when they were lowered into the irradiator. The aluminum disks on the rig were used to ensure the fibers were free floating and did not snag or touch the tube upon insertion into the irradiator. The sapphire fiber sensors were fusion spliced to silica SMF-28 connection fiber (the yellow cabling seen on the right side of Figure 103) to provide enough length to connect to the OBR readout system located at the top of the pool top. The rig also contained two k-type thermocouples that were positioned to be at the centerline and at a foot above the Co-60 pins. A silica fiber was also included in the rig (and attached to the OBR) to provide a comparison between the silica fiber and the sapphire fiber sensors during the irradiation.

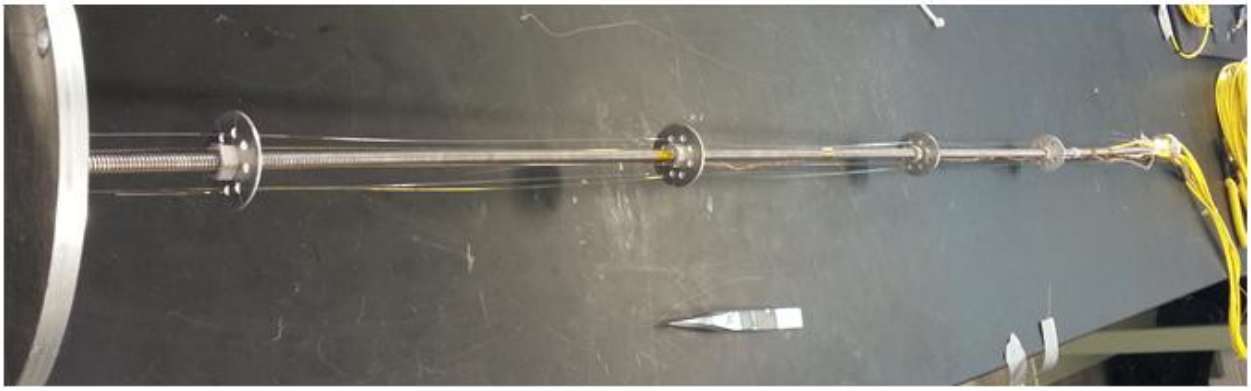

Figure 103: Photograph of the fiber rig used for the Co-60 irradiations.

The sapphire fiber sensors were placed into the Co-60 irradiator and irradiated for a total of 5 full days. The gamma dose of the irradiator is approximately 23.1 kRad per hour. Over the 5 days of irradiation, the sapphire sensors accumulated approximately 2.82 MRads. The sapphire sensors provided measurements every 10 minutes during the entire duration of the experiment. The backscatter reflectivity of the sapphire sensors can be seen below in Figure 104. Figure 104 is a graph produced by the OBR of the backscatter reflectivity of the sapphire fiber.

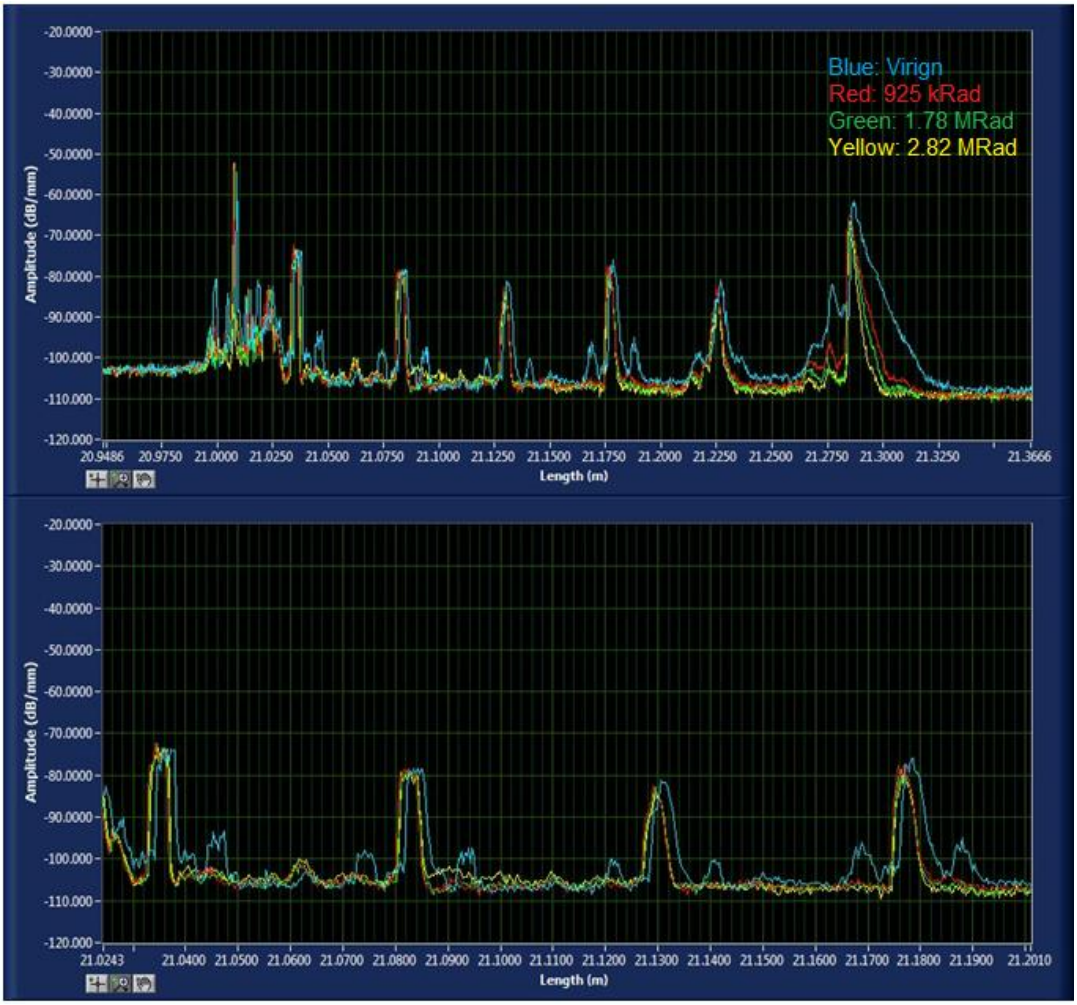

Figure 104: Screenshot from the OBR of the reflected amplitude of light off of the Bragg gratings in the cladded sapphire optical fiber as a function of gamma dose, time and position along the fiber.

The Bragg gratings appear to be unaffected by the gamma rays as their reflective amplitude never changes over the course of the experiment. Degradation of Bragg gratings, in terms of their reflective strength, in a gamma environment has been observed by multiple researchers, including the researchers on this project, but it appears the femtosecond gratings in the sapphire fiber are unaffected by the gamma environment. The locations of the gratings along the fiber appear to have shifted by around 1.5 mm. The fiber appears to have compressed by some mechanism. To determine if the sapphire fiber was compressing or rather the silica lead in fiber was compressing, a measurement of the sapphire fiber was made. The sapphire fiber length never changed, indicating that the silica lead in fiber was to blame for the 1.5 mm compression. The mechanism of the compression of the lead in fiber is still unknown, but it could be potentially effecting our temperature measurements which can be seen in Figure 105.

Figure 105: Thermocouple and sapphire Bragg grating measurements, as a function of time, of the air temperature in the Co-60 irradiator tube at the centerline of the Co-60 pins.

The measurements from the thermocouple and the sapphire fiber sensors show two different temperature profiles for the air temp of the Co-60 irradiator. Grating 2 is the Bragg grating in the sapphire fiber that is closest to the centerline of the Co-60 pins (the closest grating to the thermocouple location) yet the sapphire fiber measurement does not match the thermocouple measurement. The sapphire measurement shows an initial drop in temperature at the beginning of the experiment, which corresponds to the loading of the sapphire fibers into the Co-60 irradiator. After the initial drop, the temperature only changes by one degree Celsius during the entire duration of the experiment. The thermocouple measurements show a wider range of temperature fluctuations as there appears to be a diurnal trend of the temperature during the 5 days of irradiation in the Co-60 irradiator. This diurnal behavior could correspond to the air temperature inside of the Ohio State Reactor lab as the lab is not temperature controlled and the temperature does vary depending on time of day and the time of the year. There are two different heating mechanisms happening during this experiment: conductive heating between the fiber/thermocouple and the air in the irradiator tube and also the gamma heating of the fiber/thermocouple from the absorption of the gamma rays. The sapphire fiber has a lower gamma heating rate and a lower conductive heat transfer rate to the air than that of the thermocouple but we are not sure if it is significant enough to see the large discrepancies between the sapphire fiber and the thermocouple measurements.

The compaction of the lead in fiber could also be contributing to the discrepancy between the fiber and the thermocouple. The OBR works on the principle of tracking the position of defects in an optical fiber due to thermal expansion and correlating that change in position to a temperature. The compaction of the lead in fiber could have caused the sapphire measurements to be skewed as the sapphire fiber could have expanded due to gamma heating but it's overall position would have remained the same due to the lead in fiber compacting. The temperature measurements from the silica fiber are nearly identical to that of the sapphire fiber in which the temperature measurements only oscillate about one degree Celsius during the entire experiment. The silica fiber measurements also show a compaction in the lead in fiber. The interfering input

from the compaction of the lead in silica fiber is likely the reason for the inaccurate temperature measurements from the OBR. Nevertheless, this experiment shows that the sapphire sensors can withstand gamma rays and produce temperature measurements for the entire experiment. The accuracy and precision of the sapphire fiber temperature measurements still needs to be determined in future work. Following the irradiations in the gamma irradiator, the fibers and its rig were transferred from the Co-60 irradiator to the Ohio State Research Reactor.

9.3.6 Reactor Testing of Sapphire Optical Fiber Sensors

The sapphire fiber sensors and its rig were loaded into the Central Irradiation Facility (CIF) dry tube following the conclusion of the gamma only experiments. The CIF tube is a 1.25" ID aluminum tube that is situated in the middle of the OSURR core. The CIF tube bottom is in line with the bottom of the OSURR core and the top of the tube extends to about a foot above the waterline of the reactor pool. The fiber rig was lowered into the CIF dry tube and situated so that the sapphire fiber was in the middle of the OSURR core. The thermocouples on the rig were readjusted so that they sat at about the mid plane of the OSURR core and at a foot above the OSURR core. Figure 106 shows the CIF tube and its position relative to the OSURR core (the photo on the left shows the extension fiber exiting the top of the CIF tube).

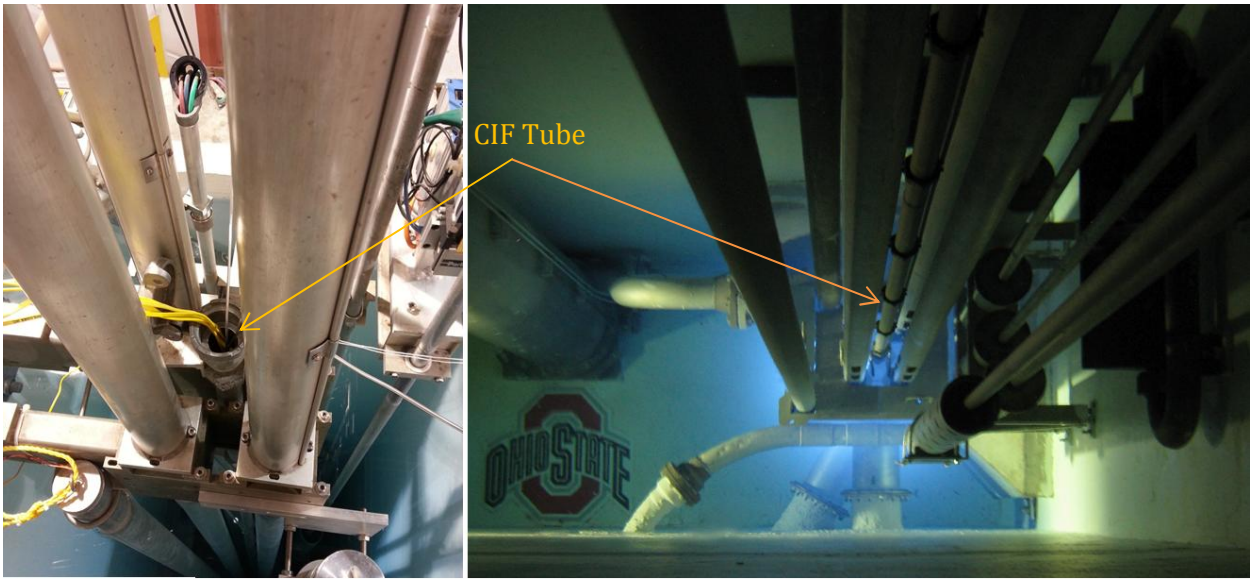

Figure 106: Photographs of the OSURR and the CIF Tube

The CIF tube has the highest neutron and gamma fluence of any irradiation location in the core. The neutron flux at full power (450 kW) is 2.3×10^{13} n/cm^2 – sec and the gamma does is around 92 MRad/hr. Since, this technology has never been tested in a nuclear reactor; we started our experiment with lower power levels and increased the power levels with every successful

irradiation. The Ohio State Research Reactor only operates during business hours each day and so the reactor can only be run for a maximum of 8 hours. This experiment occurred during the OSU Reactor Lab's busy season and so unfortunately, we had reduced hours for 3 of the 4 days of irradiation. Nonetheless, we still were able to accomplish our radiation fluence goals of 10^{18} n/cm^2 and a gamma dose of around 1 GRad. In Figure 107, the reactor power levels are shown for each day of irradiation. The first day of irradiation was a short 45 minute run in which the fiber was subjected to low power levels to determine if it could survive short doses. The second day was a two hour irradiation at mid-level power to determine its survivability for medium doses. The third day of irradiation was a full 8 hour day of two hours at 300 kW and 6 hours at full power. Following the third day, the OBR was recalibrated and the fourth day was a short 45 minute full power irradiation.

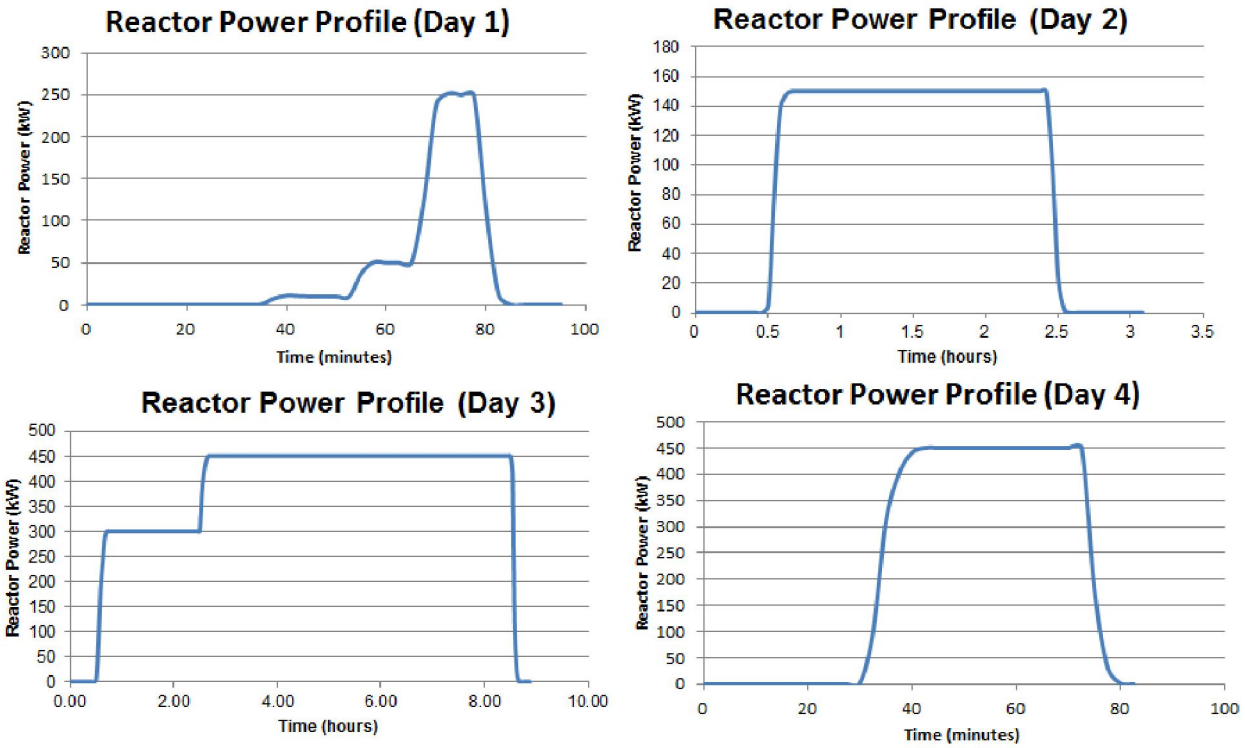

Figure 107: OSURR reactor power profiles as a function of time for each day of irradiation.

The degradation of Bragg gratings due to radiation has been well documented (in silica fibers) and so the main goal of these experiments is to determine how femtosecond Bragg gratings in sapphire fiber hold up to radiation. Any Bragg grating degradation could cause the temperature measurement from these gratings to become skewed or lost. The backscatter reflectivity of the sapphire Bragg gratings can be seen in Figure 108. The Bragg gratings appear to be completely unaffected by the gamma and neutron radiation from the reactor. The reflective amplitude from the sapphire Bragg gratings never changes over the course of the first two days of irradiation. The

non-degradation from the initial irradiations are a good sign for the radiation survivability of these sapphire sensors.

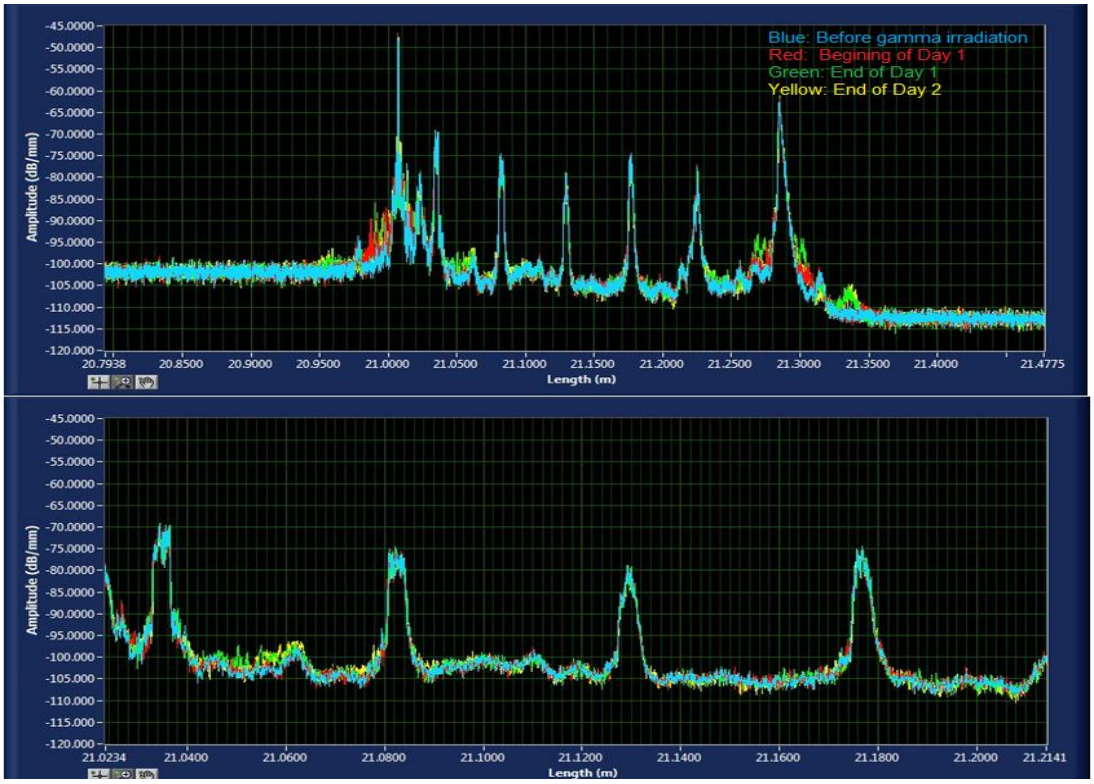

Figure 108: Screenshot from the OBR of the reflected amplitude of light off of the Bragg gratings in the cladded sapphire optical fiber as a function of radiation dose, time and position along the fiber.

The temperature measurements of the sapphire gratings were recorded and compared to the thermocouple measurements. Graphs of the thermocouple measurements and the sapphire fiber measurements can be seen in Figure 109 for the first two days of irradiation. The temperature increase seen from the thermocouple and the sapphire fiber measurements is due to the gamma and neutron heating of the air in the CIF tube and of the fiber and thermocouple themselves. The temperature increase is directly related to the power level of the reactor (increased radiation) which makes the thermocouple and fiber temperature profile (seen in Figure 109) reasonable. The thermocouple measurements and the sapphire grating measurements have a highly correlated profile to each other. The thermocouples were recording data every minute while the sapphire grating measurements occurred every 5 minutes. The difference in the data rate explains why the sapphire graph appears smoother than that of the thermocouple graph. The sapphire graph shows the temperature measurements for each grating with Grating 2 closest to the mid plane of the OSURR core. The temperature measurements of the gratings decrease along the fiber which is to be expected as the radiation is highest at the centerline of the core and decreases towards the bottom and top of the core. This correlation of temperature and radiation flux in the sapphire fiber could be exploited to make a distributed gamma thermometer for power reactors.

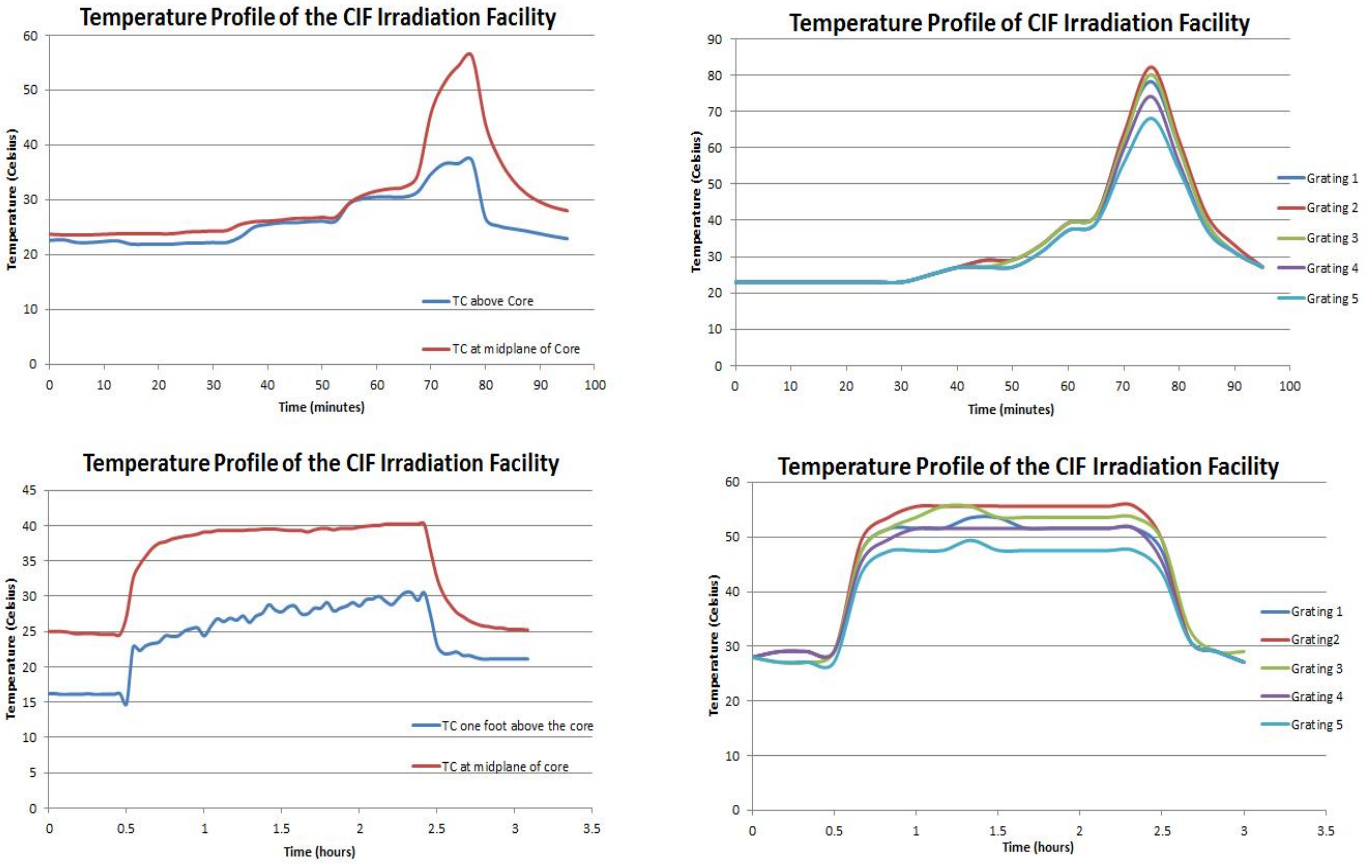

Figure 109: (Top, Left) Thermocouple measurements of the air temperature inside of the CIF Tube as a function of time during the first irradiation. (Top, Right) Sapphire Bragg grating measurements of the air temperature inside of the CIF Tube as a function of time during the first irradiation. (Bottom, Left) Thermocouple measurements of the air temperature inside of the CIF Tube as a function of time during the second day of irradiation. (Bottom, Right) Sapphire Bragg grating measurements of the air temperature inside of the CIF Tube as a function of time during the second day of irradiation.

The temperatures recorded by the sapphire Bragg gratings and the thermocouple does not match up, but their profile is nearly identical. The difference in their measurements could be from either the difference in heating rates due to gamma ray and neutron absorption or from the OBR not having a precise calibration of the sapphire fiber at higher temperatures. The insulating properties of the sapphire fiber could cause higher temperatures as the heat transfer rate from sapphire to air is less than that of the thermocouple heat transfer rate to the air. The main conclusion from the first two irradiations is that the sapphire fiber gratings survived and produced a reasonable temperature profile and measurement; the accuracy and precision of the sapphire measurements still needs further work.

The third day of irradiation was at full power and for 8 hours which produced significantly more radiation dose than that of the first two days of irradiations. The measurements for the thermocouples and the sapphire Bragg gratings for the third day of irradiation can be seen in Figure 110. The sapphire gratings produced temperature measurements at 300 kW but the jump to 450 kW caused three of the gratings to produce faulty measurements. These faulty measurements are

normally caused by either degradation of the Bragg grating or a miss calibration in the OBR readout system. The first two gratings (including the one in the highest radiation flux location) still produced temperature measurements and so it is likely something physical happening to the gratings in the sapphire fiber.

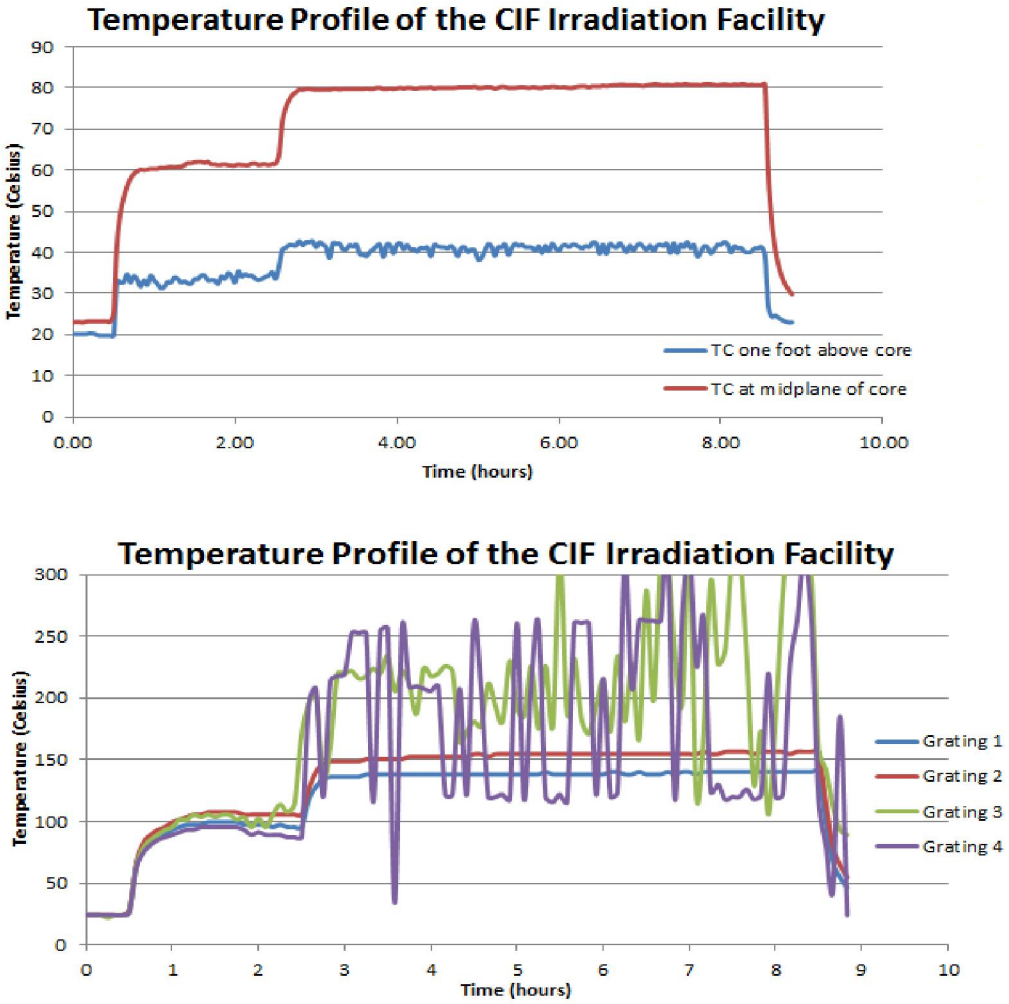

Figure 110: (Top) Thermocouple measurements of the air temperature inside of the CIF Tube as a function of time during the third day of irradiation. (Bottom) Sapphire Bragg grating measurements of the air temperature inside of the CIF Tube as a function of time during the third day of irradiation.

The backscatter reflectivity of the sapphire Bragg gratings can be seen in Figure 111 below. The gratings in the sapphire fiber do appear to have degraded but the mechanism for their degradation is not totally apparent. The radiation from the reactor was greatest at the Grating 1 and 2 position (these positions were closest to the mid plane of the core) and those two gratings showed the least degradation in terms of backscatter reflectivity. If the gratings were not being degraded by radiation, another cause for the loss in reflected amplitude off of the gratings is the lack of light reaching the gratings. If the light attenuation in the fiber is increasing, that could also

cause the effect seen in Figure 111. On the far left side of the graph in Figure 111, the lead in fiber (the length of fiber before the first spike in the backscatter reflectivity) shows an increase in reflective amplitude. This silica lead in fiber has been documented by multiple researchers to darken with radiation damage, causing extra light attenuation in the fiber. This could be the effect that is causing the light loss in the sapphire fiber but this is not totally conclusive, there could be a breakdown in the splice connection between the silica and sapphire fiber or even degradation in the sapphire cladding. Nonetheless, to test whether the gratings are degrading or if there is simply extra light loss to the sapphire fiber, the OBR was recalibrated and the gain increased on the laser source of the OBR.

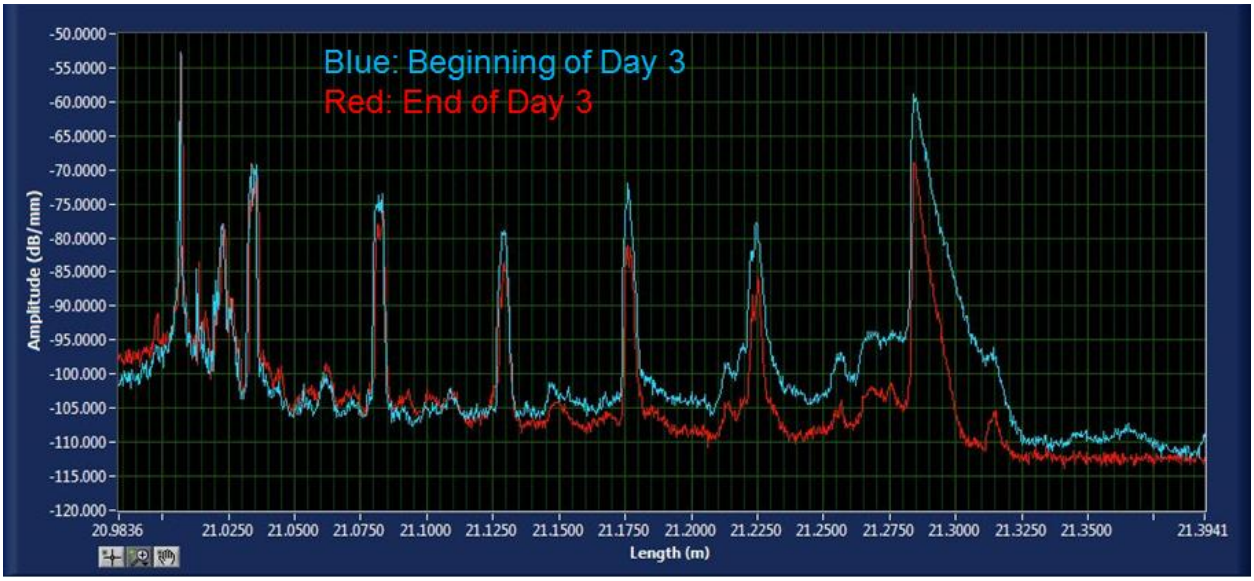

Figure 111: Screenshot from the OBR of the reflected amplitude of light off of the Bragg gratings in the cladded sapphire optical fiber as a function of radiation dose, time and position along the fiber.

The OBR was recalibrated following the third day of irradiation and a fourth irradiation at full power was conducted. The full power run for the fourth irradiation lasted only 45 minutes but it would show whether the sapphire sensors simply needed recalibrated or if the sapphire fiber sensors were truly damaged by the previous irradiations. The temperature measurements from the thermocouple and the sapphire Bragg gratings can be seen in Figure 112. The heating profiles of the thermocouples and the sapphire Bragg gratings look nearly identical, the temperature measurements are off but the profile is the same. All of the gratings were able to make temperature measurements for the entire irradiation which indicates that they sensors simply needed to be recalibrated.

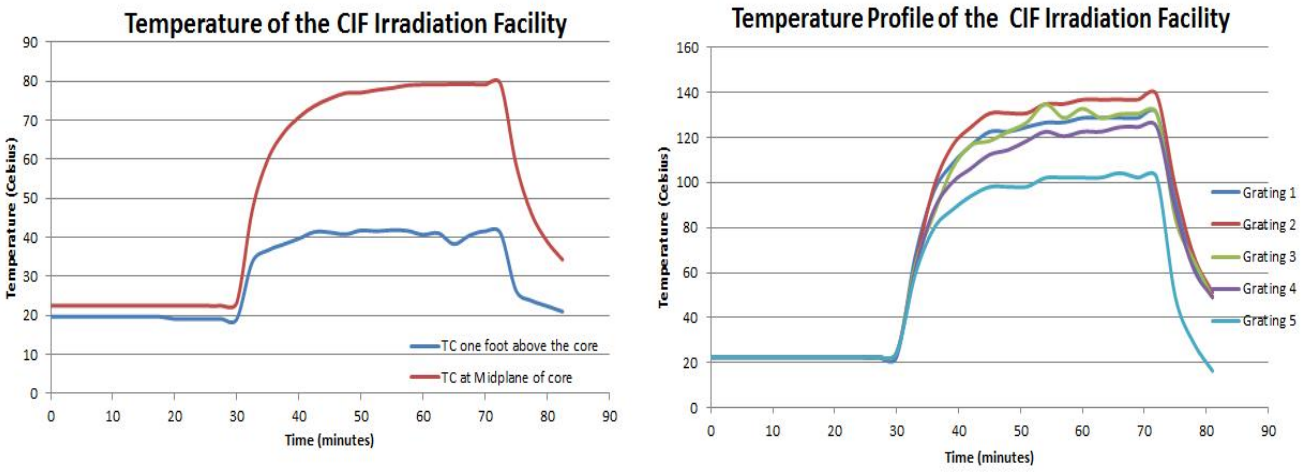

Figure 112: (Left) Thermocouple measurements of the air temperature inside of the CIF Tube as a function of time during the fourth day of irradiation. (Right) Sapphire Bragg grating measurements of the air temperature inside of the CIF Tube as a function of time during the fourth day of irradiation.

In conclusion, the sapphire Bragg gratings survived the irradiations in the OSURR and produced reasonable temperature measurements. The sapphire Bragg gratings were able to survive 1 GRad of gamma dose and a neutron fluence of 10^{18} n/cm^2 without showing degradation of the gratings. The lead in silica fiber did exhibit darkening which affected our results during the third day but recalibrating and or having a longer sapphire fiber to avoid putting the silica fiber in the radiation field, can help with ensuring accurate sapphire sensor measurements. The survivability of these sapphire sensors in a higher radiation flux environment or even to a higher radiation fluence is something that still needs to be tested and would require a test reactor such as HFIR or ATR. The survivability testing of the sapphire sensors was successful but the accuracy and precision of these sensors still needs to be determined.

10 Summary, Conclusions

In the computational portion of this project, we have completed all of the modeling tasks for this project; our model simulates the radiation damage in sapphire fibers, the evolution of that damage as a function of temperature and distance and the damage effects on the broadband optical attenuation in the fibers. Our model is broken down into 3 different models: a damage model, the damage evolution and the optical absorption from damage. The damage model consists of a MCNP model of the fiber irradiation furnace located inside the Ohio State University Research Reactor (OSURR) to model neutron interactions in the sapphire fibers. We have characterized the radiation field in the OSURR in standard terms, including the neutron flux energy spectra and the displacement damage rates (displacement damage and ionization rates due to both neutrons and gamma rays). Neutron-PKA interactions were modeled using both the MCNP and SPECTER-ANL software code packages to determine the distributions of primary knock-on atom (PKA) position, energy, and direction, as well as the PKA generation rates in the sapphire fibers. Displacement and ionization dose rates from neutrons were determined using MCNP simulations. Dose rates from gamma radiation in the OSURR were measured using an Mg-walled ion chamber. PKA transport and defect generation modeling was performed using the TRIM and Marlowe software code packages. The generation rates of both aluminum and oxygen Frenkel pairs were determined as a function of location in the sapphire fiber. Immediate defect recombination can be accounted for using recombination radii.

To understand the formation and evolution of point defects as a function of temperature and stoichiometry in sapphire, DFT calculations were used to determine the formation energies of the V_O, V_{Al}, $V_{2O,b}$, $V_{2O,c}$, O_i, AVOID pair, Al_O, and Al_i defects. Elemental chemical potentials of oxygen and aluminum in sapphire were calculated using a newer method that overcomes issues associated with a common method used previously in the literature. Formation energies were calculated in stoichiometric and nonstoichiometric sapphire using both the CCCP and heat of formation methods. The nonstoichiometric results showed that the constitutional defects shift from AVOID pairs in the O-rich limiting case, to $V_{2O,b}$ pairs in the Al-rich case. Incorporating phonon calculations with the DFT formation energies, formation free energies were calculated as a function of temperature for all of the point defect species. The dominant defect combination was found to be temperature dependent, with two distinct transitions between 200 and 2000 K. Up to 800 K, combinations of V_O and AVOID pairs are dominant, with the addition of the V_{Al} at 800 K. At even higher temperature, the V_{Al} replaces the AVOID pairs to pair with V_O as the dominant combination. A second transition occurs at 1800 K, where the $V_{2O,c}$ replaces the V_O to combine with V_{Al} as the dominant defects. This result is unprecedented, and emphasizes the potential issues sapphire fiber optics can face under reactor conditions.

With the formation of point defects as a function of temperature understood, the evolution of point defect concentrations in sapphire were studied using a rate theory model. The model solved a series of partial differential equations that defined the relationship between defect concentration, time, and temperature. Formation energies calculated using the constitutional defect method were used in the model to predict defect concentrations in nonstoichiometric sapphire, while free energies calculated using the CCCP method were used for stoichiometric sapphire. Results from previously calculated neutronics models were also used to account for prior irradiation damage, and a continuous generation of point defects due to constant irradiation. Concentration profiles of the considered defect species were determined in O-rich, Al-rich, and stoichiometric sapphire. For the O-rich limiting case, AVOID pairs were found to have the highest concentration present, while V_O was highest for the Al-rich case. As seen in the results for

formation energies, a combination of V_{2O} and AVOID pairs have the highest concentration in stoichiometric sapphire. Additionally, there is an increase in both the V_O and V_{2O} concentrations near the fiber surface, which could result from oxygen leaving the material. To gain a better understanding of this behavior, future research could be conducting using a free boundary condition at the fiber surface that does not fix the defect concentrations at their equilibrium value.

With the energetics and kinetics of the point defects determined, the effects on the optical properties of sapphire were determined. Using DFT calculations, the frequency-dependent dielectric function and absorption coefficient associated with individual point defects were calculated. The absorption coefficient values were then used to calculate the attenuation spectrum, which is directly related to signal loss in fiber optic materials. All point defect species were found to be optically active in the UV to low-visible spectrum range, with the exception of the V_{Al} which is active in the IR near 2000 nm. The AVOID and $V_{2O,c}$ have the strongest magnitude peaks in attenuation of all considered defect species. A total defect attenuation spectrum was calculated by normalizing the individual spectra against the defect concentration values for stoichiometric sapphire at varying temperatures and summing them together. The resulting spectrum shows two main regions of optical activity, the largest being in the UV/low-visible range with a sharp peak at 356 nm, and the lesser in the IR with a peak near 1300 nm. The 356 nm peak is attributed to a combination of the strong peaks of the AVOID and $V_{2O,b}$ pairs, while the peak near 1300 nm is associated with the tails of those peaks in conjunction with the broad peak of the V_{Al}. A general trend was also established between decreasing attenuation with increasing temperature, indicative of defect recombination occurring during thermal annealing. To better connect these results to experimental observations at high temperature in the IR wavelength range, future research could look at the addition of thermal scattering effects attributed to the point defects in sapphire.

In the experimental portion of this project, measurements of the sapphire fiber's ability to transmit light at high temperatures and in a high radiation field were made. In addition to the transmission testing, sapphire fiber sensors were also tested to high temperatures and high radiation fluence to determine their survivability and potential use in next-Gen reactors. The first part of the project involved the creation of high temperature furnaces and a fiber transmission readout system. Furnaces were fabricated in order to perform high temperature irradiation experiments. A high temperature (1600 °C maximum) low-activation furnace from MHI, Inc. with a $MoSi_2$ heating element was fabricated to perform heated irradiation experiments inside a 7 inch diameter dry tube facility at the OSURR and other in lab heating tests. Other furnaces were built to accommodate the variety of sapphire transmission and sensor testing for this project. A fiber transmission readout system was built to analyze the light transmission characteristics of sapphire optical fiber over the light wavelengths of 450 – 2200 nm.

Optical transmission experiments with sapphire fibers were performed under the following conditions: during heating in the absence of radiation up to 1500 °C, during Co-60 gamma irradiation while heating to temperatures up to 1000 °C, during reactor irradiation at room temperature and finally reactor irradiation at temperatures up to 1000°C.

Heated optical transmission experiments were performed at temperatures up to 1500 °C. During the initial experiments, the attenuation in the sapphire fiber continued to degrade without reaching a steady-state value as the fiber was heated at temperatures above 1300 °C. Analyzing the heated fiber under an optical microscope, the surface of the fiber appeared to have "bubbles" forming. Subsequent images using an SEM and a TEM microscope confirmed the formation of "bubbles" on and below the surface of the heated sapphire fiber. Composition analyses of the heated sapphire fiber surface discovered that the sapphire fiber was interacting with water vapor in the air at high temperatures and forming a type of aluminum hydroxide on the surface of the fiber. To confirm this hypothesis, heated optical transmission tests were performed in an inert environment up to 1500 C. The transmission results from the heated inert tests showed very

minimal added attenuation in the IR range and a steady state increase in the visible light range at 1500 C. Analyzing the sapphire fiber after the inert heating tests, the fiber showed no signs of aluminum hydroxide formation on its surface. In conclusion, in order for sapphire optical fiber to operate at temperatures above 1300 C, an inert atmosphere is needed for the fiber.

An optical transmission experiment was also performed during which sapphire fibers were irradiated with Co-60 gamma rays, while a portion of one of the fibers was heated to temperatures up to 1000 °C. Gamma radiation caused a seemingly broadband increase in the attenuation of the sapphire fiber that saturated at ~4-5 dB after accumulating an absorbed dose of ~9 MRad. Heating a portion of one of the fibers to 200 °C decreased the radiation-induced attenuation. Heating to higher temperatures, while continuing to accumulate dose, resulted in a slight increase in the attenuation. This increase was likely due to a combination of continued accumulation of dose, and possibly thermally-induced attenuation at higher temperatures.

The heated reactor irradiation experiments consisted of in-situ measurements of the optical transmission in commercially available 100 μm diameter sapphire optical fibers during exposure to reactor irradiation at various reactor power levels and at various temperatures. During the first heated reactor irradiation experiment, sapphire fibers were first irradiated at approximately room temperature at reactor power levels of 10, 30, and 90% reactor power. The fibers were then irradiated at 90% power while holding the temperature constant at 300 °C. Fitting the slope of the added attenuation vs. time data showed that the slope of the linear increase in added attenuation during constant power irradiation increased proportionally with increasing reactor power. This finding is consistent with the idea that reactor irradiation generates displacement damage from high energy neutrons, and very little defect recombination is taking place near room temperature. The furnace that was used to heat the fibers during irradiation failed during the second day of the first heated reactor irradiation experiment, after operating at 300 °C during 90% power reactor irradiation for about an hour. For this reason, a second heated reactor irradiation experiment was performed using the ThermCraft furnace.

During the second heated reactor irradiation experiment, two sapphire fibers were irradiated for two days, with approximately 8 hours spent each day at 10% reactor power. The temperature of the furnace was held constant during irradiation at four different temperatures for a period of about 4 hours at each temperature. The tested temperatures included room temperature (with gamma heating of the furnace interior up to 34 °C), and 300, 600, and 1000 °C. One of the two sapphire fibers (referred to as the exterior sapphire fiber, which was loaded outside of the furnace insulation) was irradiated under the same conditions as the interior (heated) fiber, except at a much lower temperature. The results of the second heated irradiation experiment were difficult to interpret, because the periods of time during which the fibers were irradiated at constant temperature were relatively short. It appeared as though there were transient effects taking place due to the combined effects of temperature and irradiation. In general, during reactor irradiation, the increase in added attenuation in the interior sapphire fiber was significantly less than that observed in the exterior sapphire fiber. The added attenuation at 1300 and 1550 nm remained less than ~1 dB in both the interior and exterior sapphire fibers throughout the entire experiment. However, it was difficult to predict the long-term performance of sapphire fibers under irradiation at high temperature based on the data obtained in the second heated reactor irradiation experiment, since the data appeared to be dominated by transient effects.

Because of the significance of the transient effects that were observed during the limited time that the fibers were irradiated at constant reactor power and constant temperature during the second heated reactor irradiation experiment, a third heated reactor irradiation experiment was performed. During the third heated reactor irradiation experiment, the same two sapphire fibers that were used in the second heated reactor irradiation experiment were irradiated at constant power (30% reactor power) for approximately 8 hours for each temperature that was tested (59,

300, 600, and 1000 °C). The added attenuation in the interior and exterior sapphire fibers during the experiment generally showed dynamic behavior similar to what was observed in the first reactor irradiation experiment. The added attenuation showed a linear increase with increasing time at constant reactor power for each of the temperatures that were tested. The added attenuation data in the interior sapphire fiber at 650 nm were fit for each constant temperature irradiation period, during the third heated irradiation experiment, to determine the slope of the added attenuation as a function of temperature, for constant (30%) reactor power. The rate of increase of the added attenuation during constant power reactor irradiation monotonically decreased with increasing temperature up to 1000 °C, with the most significant decrease occurring between 300 and 600 °C.

For the sapphire fiber sensing portion of this project, Lambda Instruments, Inc., an industrial partner on this project, was supposed to develop a sensor readout system and software application for interrogating sapphire fiber-based temperature and strain sensors. The system was supposed to be completed and delivered for the final testing of this project but Lambda Instruments Inc. were unable to make and deliver such a system. The sapphire Faby-Perot sensor testing will thus not be completed for this project but OSU has recently developed a new type of sapphire fiber that allows for distributed temperature sensing. This new type of sapphire sensor will be used for the sensor testing in lieu of the Fabry-Perot sensors.

OSU developed a method of creating a near single mode sapphire optical fiber which enabled the sapphire optical fiber to produce distributed temperature measurements using the OFDR sensing technique. With a single mode sapphire fiber created, OSU inscribed Bragg gratings every 6 cm along the entire fiber to act as high temperature sensors. These sapphire sensors were tested under the following environments: during heating in the absence of radiation up to 1000 °C, during Co-60 gamma irradiation at room temperature and finally during reactor irradiation at room temperature.

The sapphire Bragg grating sensors were ramped to 1000 °C, in 100 °C steps, in a tube furnace. The sapphire Bragg gratings were able to produce stable and accurate temperature measurements at every temperature tested. The gratings showed zero degradation in regards to their reflected backscatter amplitude to temperatures up to 1000 C. The sapphire Bragg grating sensors have great potential for producing accurate temperature measurements at temperatures higher than a 1000 C, unfortunately, time restrictions caused a reduction in the scope of our testing. Tests to higher temperatures and a more accurate calibration of the sapphire Bragg gratings is recommended for future work.

Following the high temperature tests, the cladded sapphire fiber with inscribed femtosecond Bragg gratings was tested for its radiation survivability. The radiation survivability tests consisted of two tests: a gamma ray only irradiation and a reactor irradiation (neutrons and gamma rays). The Ohio State Reactor Lab was used for both of these tests as the facility contains a 450 kW research reactor and a Co-60 irradiator. The Co-60 irradiator consists of an array of Co-60 pins that encircle a 6" aluminum tube. For testing in the Co-60 irradiator, the sapphire sensors were lowered down into the tube until they reach the centerline of the Co-60 pins. A silica fiber and a thermocouple were also placed at the centerline of the Co-60 pins to provide a comparison for the sapphire sensor measurements.

The sapphire fiber sensors were placed into the Co-60 irradiator and irradiated for a total of 5 full days. The gamma dose of the irradiator is approximately 23.1 kRad per hour. Over the 5 days of irradiation, the sapphire sensors accumulated approximately 2.82 MRads. The sapphire Bragg gratings were unaffected by the gamma rays as their reflective amplitude never changed over the course of the experiment and the gratings produced a constant temperature measurement. The measurements from the thermocouple and the sapphire fiber sensors showed two different temperature profiles for the air temp of the Co-60 irradiator. The sapphire measurement showed

an initial drop in temperature at the beginning of the experiment, which corresponded to the loading of the sapphire fibers into the Co-60 irradiator. After the initial drop, the temperature only changed by one degree Celsius during the entire duration of the experiment. The thermocouple measurements showed a wider range of temperature fluctuations (±15 C) and a diurnal trend of the temperature during the 5 days of irradiation in the Co-60 irradiator. The discrepancy between the sapphire fiber sensors and the thermocouple is caused by either the poor heat transfer rate between the air and the fiber or the compaction of the lead fiber. The lead in fiber for the sapphire sensors compacted by 1.5 mm which could cause an interfering input to the temperature sensing mechanism of the sapphire fiber. Nevertheless, this experiment showed that the sapphire sensors can withstand gamma rays and produce temperature measurements for the entire experiment. The accuracy and precision of the temperature measurements still needs to be determined in future work.

Following the irradiations in the gamma irradiator, the sapphire fiber sensors were transferred into the Central Irradiation Facility (CIF) dry tube located in the Ohio State Research Reactor. The CIF tube is a 1.25" ID aluminum tube that is situated in the middle of the OSURR core. The fiber was lowered into the CIF dry tube and situated so that the sapphire fiber was in the middle of the OSURR core. Thermocouples were added as a comparison for the sapphire fiber measurements and were positioned at the mid plane of the OSURR core and at a foot above the OSURR core. This experiment occurred during the OSU Reactor Lab's busy season and so unfortunately, we had reduced hours for 3 of the 4 days of irradiation. The first day of irradiation was a short 45 minute run in which the fiber was subjected to low power levels to determine if it could survive short doses. The second day was a two hour irradiation at mid-level power to determine its survivability for medium doses. The third day was of irradiation was a full 8 hour day of two hours at 300 kW and 6 hours at full power. Following the third day, the OBR was recalibrated and the fourth day was a short 45 minute full power irradiation.

The sapphire Bragg gratings appeared to have survived the irradiations in the OSURR and produced reasonable temperature measurements. The sapphire Bragg gratings were able to survive 1 GRad of gamma dose and a neutron fluence of 10^{18} n/cm^2 without showing degradation of the gratings. The lead in silica fiber did exhibit darkening which affected our results during the third day but recalibrating and or having a longer sapphire fiber to avoid putting the silica fiber in the radiation field, can help with ensuring accurate sapphire sensor measurements. The survivability testing of the sapphire sensors was successful but the accuracy and precision of these sensors still needs to be determined.

Bibliography

[1] G. J. Dienes, D. O. Welch, C. R. Fischer, R. D. Hatcher, O. Lazareth and M. Samberg, "Shell-model calculation of some point-defect properties in a-Al2O3," *Physical Review B,* vol. 11, no. 8, pp. 3060-3070, 1975.

[2] C. R. A. Catlow, R. James, W. C. Mackrodt and R. F. Stewart, "Defect energetics in a-Al2O3 and rutile TiO2," *Physical Review B,* vol. 25, no. 2, pp. 1006-1026, 1982.

[3] R. W. Grimes, "Solution of MgO, CaO, and TiO2 in a-Al2O3," *Journal of the American Ceramic Society,* vol. 77, pp. 378-384, 1994.

[4] K. P. D. Lagerlof and R. W. Grimes, "The Defect Chemistry of Sapphire (a-Al2O3)," *Acta Materialia,* vol. 46, no. 16, pp. 5689-5700, 1998.

[5] K. J. W. Atkinson, R. W. Gromes, M. R. Levy, Z. L. Coull and T. English, "Accommodation of Impurities in a-Al2O3, a-Cr2O3 and a-Fe2O3," *Journal of the European Ceramic Society,* vol. 23, pp. 3059-3070, 2003.

[6] P. W. M. Jacobs and E. A. Kotomin, "Defect energies for pure corundum and for corundum doped with transition metal ions," *Philisophical Magazine A,* vol. 68, pp. 695-709, 1993.

[7] P. W. M. Jacobs and E. A. Kotomin, "Theory of Point Defects and Vacancy Motion in Corundum Crystals," *Journal of Solid State Chemistry,* vol. 106, pp. 27-34, 1993.

[8] K. Matsunaga, T. Tanaka, T. Yamamoto and Y. Ikuhara, "First-principles calculations of intrinsic defects in Al2O3," *Physical Review B,* vol. 68, p. 085110, 2003.

[9] Y. N. Xu, Z. Gu, X. F. Zhong and W. Y. Ching, "Ab initio calculations for the neutral and charged O vacancy in sapphire," *Physical Review B,* vol. 56, no. 12, pp. 7277-7284, 1997.

[10] A. A. Sokol, A. Walsh and C. A. Catlow, "Oxygen interstitial structures in close-packed metal oxides," *Chemical Physics Letters,* vol. 492, pp. 44-48, 2010.

[11] I. Tanka, K. Tatsumi, M. Nakano and H. Adachi, "First-Principles Calculations of Anion Vacancies in Oxides and Nitrides," *Journal of the American Ceramic Society,* vol. 85, pp. 68-74, 2002.

[12] D. Liu, S. J. Clark and J. Robertson, "Oxygen vacancy levels and electron transport in Al2O3," *Applied Physics Letters,* vol. 96, p. 032905, 2010.

[13] N. D. M. Hine, K. Frensch, W. M. C. Foulkes and M. W. Finnis, "Supercell size scaling of density functional theory formation energies of charged defects," *Physical Review B,* vol. 79, p. 024112, 2009.

[14] J. R. Weber, A. Janotti and C. G. Van de Walle, "Point defects in Al2O3 and their impact on gate stacks," *Microelectronic Engineering,* vol. 86, pp. 1756-1759, 2009.

[15] J. R. Weber, A. Janotti and C. G. Van de Walle, "Native defects in Al2O3 and their impact on III-V/Al2O3 metal-oxide-semiconductor-based devices," *Journal of Applied Physics,* vol. 109, p. 033715, 2011.

[16] E. Iguchi, K. Otake, T. Yamamoto and H. Nishikawa, "Calculations of collision cascades in oxide ceramics MgO and a-Al2O3," *Journal of Nuclear Materials,* vol. 169, pp. 55-63, 1989.

[17] M. Lee and E. Farnum, "The effect of neutron energy on defect production in alumina," *Nuclear Instruments and Methods in Physics Research B,* vol. 102, pp. 113-118, 1995.

[18] F. Mota, C. Ortiz, R. Vila, N. Casal, A. Garcia and A. Ibarra, "Calculation of damage function of Al2O3 in irradiation facilities for fusion reactor applications," *Journal of Nuclear Materials,* vol. 442, no. 1-3, pp. S699-S704, 2013.

[19] D. W. Yergeau and R. W. Dutton, "*Alamode*: A LAyered MOdel Development Environment for simulation of impurity diffusion in semiconductors," http://www.tcad.stanford.edu/tcad/programs/alamode-97.08.19/alamode.html, 1997.

[20] L. Torpo, M. Marlo, T. E. M. Staab, R. M. Niminen, J. Phys. Condens. Mat. **13**, 6203 (2001)

[21] W. Windl, Process Simulation for Silicon Nanoelectronic Devices, in Handbook of Theoretical and Computational Nanotechnology, edited by M. Rieth and W. Schommers (American Scientific Publishers, Stevenson Ranch, CA, 2006), Chapter 132, p. 137-209.

[22] W. M. C. Foulkes, N. D. M. Hine, K. Frensch, M. W. Finnis, and A. H. Heuer, "Point Defects and Diffusion in α-Al2O3," International Conference on Quantum Monte Carlo in the Apuan Alps V, 2009

[23] G. Kresse, M. Marsman, J. Furthmüller, *VASP the* GUIDE, Universität Wien

[24] M. Gajdoš, K. Hummer, G. Kresse, J. Furthmüller, F. Bechstedt, Phys. Rev. B **73**, 045112 (2006)

[25] K. H. Lee, J. H. Crawford, Phys. Rev. B **15**, 4065 (1997)

[26] G. J. Pogatshnik, Y. Chen, Transactions on Nucler Science **34**, 1709 (1987)

[27] S. V. Solov'ev, I. I. Milman, A. I. Syurdo, Physics of the Solid State **54**, 726 (2012)

[28] B. D. Evans, M. Stapelbroek, Phys. Rev. B **18**, 7089 (1978)

[29] L. S. Welch, A. E. Hughes, G. P. Pells, J. Phys. C: Solid St. Phys. **13**, 1805 (1979)

[30] D.K. Gifford, B.J. Soller, M.S. Wolfe, M.E. Froggatt, ECOC 2005: 31st European Conference on Optical Communication Vol. 3 (2005) 511- 512.

[31] E. J. Opila, D. L. Myers, "Alumina Volatility in Water Vapor at Elevated Temperatures". J. Am. Ceram. Soc., Vol 87 (2004), pp. 1701–1705.

[32] S. William, H. Mengbing, M. Thomas and X. Hua, "Optical mode confinement and selection in single-crystal sapphire fibers by formation of nanometer scale cavities with hydrogen ion implantation," *Journal of Applied Physics ,* 2013.

[33] Mihailov, S. J., Smelser, C. W., Lu, P., Walker, R. B., Grobnic, D., Ding, H. & Unruh, J. (2003). Fiber Bragg gratings made with a phase mask and 800-nm femtosecond radiation. *Optics letters*, *28*(12), 995-997.

[34] Grobnic, D., Mihailov, S. J., Smelser, C. W., & Ding, H. (2004). Sapphire fiber Bragg grating sensor made using femtosecond laser radiation for ultrahigh temperature applications. *IEEE Photonics Technology Letters*, *16*(11), 2505-2507